The development of micro-alloyed magnesium-zinc based ternary alloy

Dissertation

Zur Erlangung des akademischen Grades

Doktor der Ingenieurwissenschaften

(Dr.-Ing.)

Der Technischen Fakultät

Der Christian-Albrechts-Universität zu Kiel

Vorgelegt von

Pingli Jiang

Aus

Hunan, VR China

Kiel 2020

Gutachtern der Dissertation

1. Gutachter: Prof. Dr. Mikhail Zheludkevich

2. Gutachter: Prof. Dr. Regine Willumeit-Römer

3. Gutachter: Prof. Dr. Stephan Wulfinghoff

4. Gutachter: Prof. Dr. rer. nat. Franz Faupel

Vorsitzender des Promotionsausschusses:

Prof. Dr. Stephan Wulfinghoff

Tag der mündlichen Prüfung:

8th July 2020

Eidesstattliche Erklärung

Hiermit erkläre ich, dass die beigefügte Dissertation, abgesehen von der Beratung durch die Betreuerin, nach Inhalt und Form meine eigene Arbeit ist.

Die Arbeit, ganz oder zum Teil, wurde nie schon einer anderen Stelle im Rahmen eines Prüfungsverfahrens vorgelegt und ist abgesehen, von den im Anhang angegebenen Veröffentlichungen, nicht anderweitig zur Veröffentlichung vorgelegt worden.

Außerdem ist die Arbeit unter Einhaltung der Regeln guter wissenschaftlicher Praxis der Deutschen Forschungsgemeinschaft entstanden.

Geesthacht, den 30. 04. 2020

Pingli Jiang

Table of contents

Abstract

Magnesium (Mg) alloys have been widely studied for applications in 3C and transport areas. However, the intrinsically high susceptibility to corrosion and the inadequate ductility at room temperature largely limit their wider practical applications. The poor creep resistance of commonly commercial magnesium-aluminum (Mg-Al) based alloys at elevated temperature drives the demand for Al-free Mg alloys, among which magnesium-zinc system (Mg-Zn) shows great potential for the development of low-cost Mg alloys with higher strength and good corrosion performance.

In this thesis, low-Zn containing Mg-Zn alloys micro-alloyed with different ternary alloying elements were developed and comprehensively studied, aiming at achieving a good combination of corrosion performance and mechanical properties. By investigating the influence of ternary alloying elements on the microstructures and corrosion behavior of Mg0.5Zn0.2X and Mg4Zn0.2X alloys (in *wt.*%), Mg0.5Zn0.2Ca, Mg0.5Zn0.2Ge and Mg4Zn0.2Sn alloys were identified as promising alloys with possible good combination of corrosion performance and mechanical strength. Afterwards, hot extrusion at different speed was applied to the three alloys to further improve corrosion resistance and strength. The extrusion speed showed little influence on the corrosion resistance of the three optimized alloys because of the slight alternation of the microstructures. Affected by the chemistry of the bulk materials, the corrosion rates of Mg0.5Zn0.2Ge and Mg4Zn0.2Sn alloys were reduced after extrusion while that of Mg0.5Zn0.2Ca alloy was not clearly affected. The corrosion mechanism of Mg0.5Zn0.2Ge alloy changed from localized corrosion to uniform corrosion after extrusion owing to the refined microstructure and the increased participation of Zn in the corrosion product layer. In comparison, both as-cast and extruded Mg0.5Zn0.2Ca alloys revealed uniform corrosion, while Mg4Zn0.2Sn alloys in both conditions suffered from localized corrosion in corrosive electrolytes due to the heterogeneous microstructures. Deionized water based sodium chloride (NaCl) solutions at different concentrations did not affect the corrosion mechanism of the alloys, while artificial tap water based NaCl solution significantly enhanced the corrosion resistance of the alloys owing the formation of an additional calcium carbonate layer on the top of the primary oxide/hydroxide layer. The stronger textures of Mg0.5Zn0.2Ge and Mg4Zn0.2Sn alloys conferred higher tensile strength but higher mechanical anisotropy on the alloys compared with Mg0.5Zn0.2Ca alloy. The tensile properties of all alloys deteriorated with exposure time in salt spray because of corrosion, especially when localized corrosion happened. However, the variation tendency of the tensile properties was closely related to the corrosion resistance of the alloys in salt fog. The fatigue behavior (S-N curves) of the optimized alloys deviated from near-linear trend in air. In the presence of corrosive electrolytes, the fatigue lives and fatigue limits of the alloys decreased. Again, the corrosion fatigue behavior of the alloys were strongly related to the corrosion behavior in different solutions, especially for Mg4Zn0.2Sn alloy. The susceptibility of the alloys to stress corrosion cracking (SCC) in four different electrolytes were studied by constant load tests. Mg0.5Zn0.2Ca and Mg4Zn0.2Sn alloys were resistant to SCC in all environments. While Mg0.5Zn0.2Ge alloy exhibited susceptibility to SCC in all environments, especially in deionized water. This was because of the different corrosion products/substrate interfaces formed in different solutions, which influenced the development of cracks.

The results emphasized the influence of corrosion on the fatigue behavior and mechanical properties of Mg-Zn alloys, and also highlighted the importance of the investigation of the overall properties (corrosion, mechanical, fatigue and stress corrosion properties) of Mg alloys during practical alloy development.

Zusammenfassung

Magnesiumlegierungen sind für die Anwendungen in 3C- und Transportbereichen umfassend untersucht worden. Allerdings begrenzt die hohe Anfälligkeit für Korrosion und unzureichende Duktilität bei Raumtemperatur deren vielfältige praktische Anwendungen weitgehend. Die niedrige Kriechbeständigkeit von kommerziell basierten Magnesium-Aluminium Legierungen (Mg-Al) bei erhöhten Temperaturen fördert die Nachfrage nach Al-freien Mg-Legierungen, wobei das Magnesium-Zink-System (Mg-Zn) ein großes Potenzial für die Entwicklung der preiswerteren Mg-Legierungen mit höherer Festigkeit und eine hohe Korrosionsbeständigkeitsleistung aufweist.

In dieser Arbeit wurden Mg-Zn-Legierungen mit niedrigem Zn-Gehalt mit verschiedenen ternären Legierungselementen mikrolegiert, entwickelt und eingehend untersucht. Das Ziel ist eine gute Kombination von Korrosionsverhalten und mechanischen Eigenschaften zu gewährleisten. Durch die Untersuchung des Einflusses von ternären Legierungselementen auf der Mikrostruktur und das Korrosionsverhalten von Mg0,5Zn0,2X und Mg4Zn0,2X Legierungen (in Gew.%) wurden Mg0,5Zn0,2Ca, Mg0,5Zn0,2Ge und Mg4Zn0,2Sn Legierungen als vielversprechende Legierungen mit einer möglichen guten Kombination aus Korrosionsverhalten und mechanischer Festigkeit identifiziert. Anschließend wurden die drei Legierungen mit unterschiedlicher Geschwindigkeit warmstranggepresst, um Korrosionsbeständigkeit und Festigkeit weiter zu verbessern. Die Strangpressgeschwindigkeit zeigte aufgrund der leichten Veränderung der Mikrostruktur nur einen geringen Einfluss auf die Korrosionsbeständigkeit der drei optimierten Legierungen. Die Chemie des Schüttgut-Materials könnte die Korrosionsrate beeinflussen. Die Korrosionsraten der Mg0,5Zn0,2Ge- und Mg4Zn0,2Sn-Legierungen waren nach dem Strangpressen reduziert, während die der Mg0,5Zn0,2Ca Legierung nicht deutlich beeinträchtigt wurde. Der Korrosionsmechanismus der Mg0,5Zn0,2Ge Legierung änderte sich nach dem Strangpressen von lokaler Korrosion zu Flächenkorrosion wegen der verfeinerten Mikrostruktur und der erhöhten Beteiligung von Zn in der Korrosionsproduktschicht. Im Vergleich wiesen sowohl Gusszustand als auch stranggepresste Mg0,5Zn0,2Ca Legierungen flächenmäßige Korrosion auf, während Mg4Zn0,2Sn Legierungen in beiden Zuständen aufgrund der heterogenen Mikrostruktur bei korrosiven Lösungen lokale Korrosion zeigten. Deionisierte Natriumchlorid-Lösungen (in verschiedenen NaCl Konzentrationen) beeinträchtigten nicht den Korrosionsmechanismus der Legierungen, während die künstliche Leitungsnatriumchlorid NaCl-Lösung deutlich die Korrosionsbeständigkeit der Legierungen aufgrund der Bildung einer zusätzlichen Kalziumkarbonatschicht auf der Oberseite der primären Oxid-/Hydroxidschicht verbesserte.

Zusammenfassung

Darüber hinaus bewirkten die stärkeren Texturen der Mg0,5Zn0,2Ge und Mg4Zn0,2Sn Legierungen eine höhere Zugfestigkeit, aber auch eine höhere mechanische Anisotropie der Legierungen im Vergleich zur Mg0,5Zn0,2Ca Legierung. Die Zugfestigkeitseigenschaften aller Legierungen verringerten sich aufgrund von Korrosion mit der Einwirkungszeit im Salzsprühnebel, insbesondere, wenn lokale Korrosion auftrat. Die Schwankungsneigung der Zugeigenschaften stand jedoch in engem Zusammenhang mit der Korrosionsbeständigkeit der Legierungen im Salzsprühnebel. Das Ermüdungsverhalten (in den S-N-Kurven) der optimierten Legierungen wich von dem fast linearen Trendverlauf in Luft ab. In Gegenwart von korrosiven Elektrolyten nahm die Ermüdungsdauer und die Ermüdungsgrenzen der Legierungen ab. Auch hier war das Korrosionsermüdungsverhalten der Legierungen eindeutig mit dem Korrosionsverhalten in verschiedenen Lösungen verbunden, insbesondere bei der Mg4Zn0,2Sn Legierung. Die Anfälligkeit der Legierungen zur Spannungsrisskorrosion (SCC) wurde in vier verschiedenen Elektrolyten durch Dauerbelastungstests untersucht. Die Mg0,5Zn0,2Ca und Mg4Zn0,2Sn Legierungen waren widerstandsfähig gegen SCC in allen Umgebungen, im Gegensatz dazu war die Mg0,5Zn0,2Ge Legierung für SCC in allen Umgebungen anfällig, besonders in deionisiertem Wasser. Dies erfolgte aufgrund der unterschiedlichen Korrosionsprodukte/Substrat-Grenzflächen, die in verschiedenen Lösungen gebildet wurden und die Entwicklung von Rissen begünstigten.

Allen Untersuchungen lag der Schwerpunkt auf den Einfluss der Korrosion auf das Ermüdungsverhalten und die mechanischen Eigenschaften von Mg-Zn-Legierungen zugrunde, sowie die Bedeutung der Untersuchung der allgemeinen Eigenschaften (Korrosion, mechanische, Ermüdungs- und Spannungskorrosionseigenschaften) von Mg-Legierungen im Verlauf der praktischen Legierungsentwicklung.

1. Introduction

The renewed interest in magnesium (Mg) alloys stimulated by the high demand for weight-saving since the late 1990s [1] failed to promote much wider practical applications of Mg alloys in the past 20 years because of the poor corrosion resistance and inadequate mechanical properties of Mg alloys [2]. Many efforts have been made and some improvement has been achieved by developing new alloys, applying wrought processes, designing novel Mg-based materials (e.g. Mg-based metal matrix composite) and preparing protective coatings on the surfaces [3-8]. Among them, alloying addition turned out to be one of the most effective strategies to enhance both corrosion resistance and mechanical properties of Mg alloys [9]. The remarkable response to age hardening of Mg-Zn system attracted great attention for the development of low-cost Mg alloys with improved properties [10, 11]. Alloying with calcium (Ca), yttrium (Y), rare-earth elements (RE), manganese (Mn) and silicon (Si) etc. has been widely studied [12-16]. However, most of them focused only on one or two aspects of the alloys. For example, excellent tensile properties of Mg-Zn-Y alloys can be achieved by adjusting the microstructures with addition of different amounts of Zn and Y. Nevertheless, enhanced mechanical properties usually were obtained at the sacrifice of corrosion performance due to the higher amounts of alloying elements required and the formation of intermetallic phases [17, 18]. In practical applications, a good combination of corrosion resistance and mechanical properties is vital since the service environment of the material usually is harsh and corrosion can result in serious deterioration of mechanical properties or even sudden failure of the material [19].

Previous studies revealed that the added amount of Zn should be below 4 *wt.*% to achieve a good combination of corrosion resistance and mechanical properties of Mg-Zn alloys [20, 21]. Moreover, Hofstetter et al. [22, 23] have developed a high-strength low-alloy Mg-Zn-Ca alloy with Zn and Ca concentration below 1 *wt.*% through extrusion processing, achieving a good combination of excellent mechanical properties and good corrosion resistance. However, the corrosion mechanism of the alloy was not thoroughly understood.

Therefore, in present work, a comprehensive study of low-Zn containing Mg-Zn-X alloys was carried out, with an emphasis on the relationship/interaction between corrosion resistance and mechanical properties of the alloys.

2. State of Art

The state of art about the study of Mg-Zn system has been overviewed in following publication [24].

Review

The Corrosion Performance and Mechanical Properties of Mg-Zn Based Alloys—A Review

Pingli Jiang [1,*], Carsten Blawert [1] and Mikhail L. Zheludkevich [1,2]

[1] Magnesium Innovation Centre (MagIC), Institute of Materials Research, Helmholtz-Zentrum Geesthacht, Max-Planck Str.1, Geesthacht 21502, Germany; carsten.blawert@hzg.de (C.B.); mikhail.zheludkevich@hzg.de (M.L.Z.)
[2] Faculty of Engineering, University of Kiel, Kaiserstrasse 2, 24143 Kiel, Germany
* Correspondence: pingli.jiang@hzg.de

Received: 12 February 2020; Accepted: 21 April 2020; Published: 23 April 2020

Abstract: Magnesium alloys have shown great potential for applications as both structural and biomedical materials due to their high strength-to-weight ratio and good biodegradability and biocompatibility, respectively. Among them, Mg-Zn based alloys are attracting increasing interest for both applications. As such, this article provides a review of the corrosion performance and mechanical properties of Mg-Zn based alloys, including the influence of environment and processing on both of them. The strategies for tailoring corrosion resistance and/or mechanical properties by microstructure adjustment and surface treatment are discussed.

Keywords: magnesium alloys; zinc; corrosion performance; mechanical property

1. Introduction

Magnesium (Mg) alloys have drawn increasing attention during the past two decades for applications in the automotive, aerospace, and electronics industries due to their high specific strength and stiffness, low density, good castability, and machinability [1-4]. In addition, they have also been considered as attractive candidates for application as biodegradable implant materials because of their mechanical properties that are similar to those of natural bone, good biodegradability, and inherent biocompatibility [5-9]. To expand the application scope of Mg alloys, alloying is one of the most effective strategies for the further enhancement of mechanical properties and corrosion performance [10].

Magnesium–aluminum (Mg-Al) based alloys are the most widely studied and used Mg alloys due to their excellent castability, reasonable mechanical properties at room temperature, and good corrosion resistance [11]. However, the mechanical properties of Mg-Al based alloys significantly decrease as temperature rises above 130 °C, above which softening of the β-$Mg_{17}Al_{12}$ phases, precipitated at grain boundaries, results in poor creep resistance [12,13]. Additionally, Al has been reported to be a neurotoxicant, and the accumulation of Al can induce various neurological disorders during the degradation of Mg-Al alloys in the human body [14]. Therefore, the development of Al-free Mg alloys is desired.

Zinc (Zn) is the second most common alloying element for commercial Mg alloys [15,16]. Zn alloying additions can lead to a higher free corrosion potential of the MgZn alloy compared to that of pure Mg, reduce the corrosion rate, and improve the mechanical properties through a solid solution hardening mechanism [17,18]. Moreover, in comparison with Mg-Al series alloys, the presence of heat-resistant intermetallics results in the much higher creep resistance and the better

Corros. Mater. Degrad. **2020**, *1*, 7; doi:10.3390/cmd1020007 www.mdpi.com/journal/cmd

tensile properties of Mg-Zn-Al alloys at elevated temperatures [19,20]. Furthermore, Zn is one of the essential trace elements for the human body and is crucial for many biological functions, such as the immune system and sense of smell and taste [21]. Thus, the Mg-Zn system shows great potential as a low-cost Mg alloy alternative with high strength in industrial applications, and has attracted increasing interest for medical applications.

Motivated by the new trend of biomedical applications for Mg-Zn based alloys, the objective of this article is to provide a review of the corrosion performance and mechanical properties of Mg-Zn based alloys developed for both industrial and biomedical applications. Potentials or relative Volta potentials of some secondary phases in Mg-Zn based alloys and the corrosion rates and mechanical properties of Mg-Zn based alloys summarized from publications are compared in Tables A1 and A2 in the Appendix. The influence of environment and processing on the corrosion behavior and mechanical properties of Mg-Zn based alloys are also reviewed. The strategies for improving the properties of Mg-Zn based alloys are discussed based on microstructure design and surface modification. Finally, typical applications are shortly summarized.

2. Binary Mg-Zn Alloys

2.1. Mg-Zn System

The maximum solid solubility of Zn in Mg is considered to be relatively high at high temperatures [22,23], e.g., 2.5 at.% (6.2 wt.%) at 325 °C, as indicated by the binary Mg-Zn phase diagram proposed by Okamoto et al. [24] and shown in Figure 1. However, with decreasing temperature, only 0.6 at.% (1.6 wt.%) Zn remains soluble in the Mg matrix and contributes to solid solution strengthening [22,25,26]. Excess Zn will form intermetallic phases. In the Mg-Zn system, five intermetallic phases, namely $Mg_{51}Zn_{20}$ (previously denoted as Mg_7Zn_3 [27]), MgZn, Mg_2Zn_3 (previously denoted as Mg_4Zn_7 [28,29]), $MgZn_2$, and Mg_2Zn_{11}, exist. The primary Mg_7Zn_3 phase has a body-centered orthorhombic structure [30]. The crystal structures of MgZn, $MgZn_2$, and Mg_2Zn_{11} are base-centered monoclinic [31], hexagonal [32], and cubic [33], respectively. However, the structure of the Mg_4Zn_7 phase is under debate, assumed to be a triclinic structure by Gallot and Graf [34], but reported to be a base-centered monoclinic structure by Gao and Nie [31]. It is believed that the Mg_xZn_y intermetallics can provide a pronounced age hardening effect [35-37], but they are detrimental to the corrosion resistance of the alloy due to accelerated cathodic reaction rates [38-40].

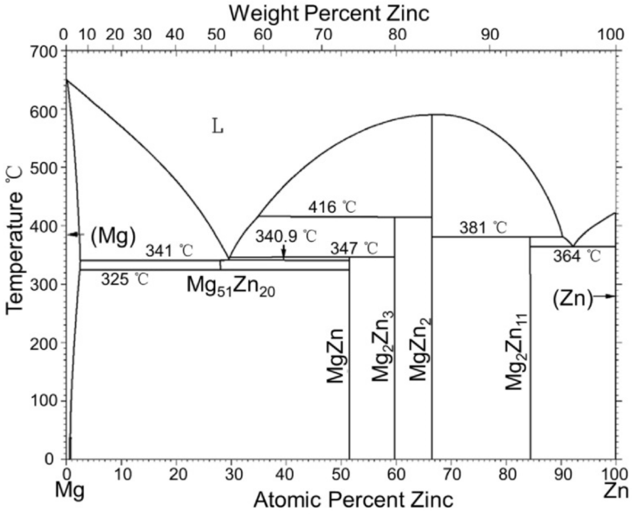

Figure 1. The binary Mg-Zn phase diagram [24] (with permission from Springer Nature and Copyright Clearance Center).

2.2. Influence of Zn Content on the Corrosion and Mechanical Properties of Binary Mg-Zn Alloys

Addition of Zn as an alloying element can refine the grain size and improve the corrosion resistance and mechanical properties of Mg [10,41]. Compared with pure Mg and high-purity AZ31 alloy, almost one order of magnitude improvement of corrosion resistance can be achieved by small additions of Zn (1 wt.%) [10,42]. Since the electrode potential of Zn (–0.762 V vs. Standard Hydrogen Electrode) is higher than that of Mg (–2.372 vs. Standard Hydrogen Electrode), and Zn is known to have a high hydrogen evolution over-potential, the improved corrosion resistance is presumably attributed to the reduced hydrogen evolution kinetics by Zn in solid solution [42]. It was also suggested that Zn can increase the tolerance limits of impurities (iron (Fe), copper (Cu), nickel, and cobalt) in Mg, which enhances the corrosion resistance of Mg via weakening of the galvanic corrosion between impurities and Mg [1,43,44]. In addition, Gu et al. [45] have reported that the corrosion resistance of as-cast Mg1Zn (in wt.%) alloy is higher compared to several other binary Mg alloys alloyed with the same amount (Ag, Al, In, Mn, Si, Sn, Y, and Zr). Generally, the corrosion resistance and mechanical properties of Mg-Zn binary alloys strongly depend on Zn content. When the added amount of Zn is lower than 5 wt.%, an increase in Zn content enhances the general and localized corrosion resistance of as-cast Mg-Zn alloys in simulated body fluid (SBF) at 37 °C, which is due to the refinement of grain size and the facilitated formation of protective surface film induced by Zn [10,41,46]. However, much higher levels of Zn (up to 7 wt.%) can result in the formation of a significant amount of secondary phases. As a result, severe localized corrosion occurs due to the galvanic effect between intermetallics and matrix, and, consequently, a decrease of the overall corrosion resistance is found [10,47,48]. Opposite results have been reported by Kubàsek et al [42,49], showing that the corrosion rates of Mg-Zn binary alloys increase with increasing Zn amount in the range of 0–6 wt.% when testing is performed in either simple sodium chloride (NaCl) solution or simulated body fluid. This finding is ascribed to the increased galvanic effect due to the increase in volume fraction of secondary phases.

The yield (YS) and ultimate tensile strength (UTS) of binary Mg-Zn alloys increase with increasing Zn content when Zn wt.% is in the range of 0–4 wt.% [10,22,46,50]. This is a combined result of fine grain strengthening [51-53], solid solution strengthening [25,26,54], and precipitation hardening effects [54,55]. Nevertheless, when alloying with higher amounts of Zn, plenty of secondary phases will form at the grain boundaries. They will result in the increased dislocation density and act as new crack sources [10]. Consequently, the tensile strength of the alloy can be significantly reduced.

Binary Mg-Zn alloys with much higher amounts of Zn (>10 wt.%) produced by using powder metallurgy have only been studied by Yang et al. [55]. High Zn content (>10 wt.%) causes the formation of large-size secondary phases and undissolved Zn particles, which results in severe pitting and localized corrosion due to the formation of galvanic cells, thus reducing the corrosion resistance of the alloys (corrosion current density: 16.9 μA cm^{-2} for Mg6Zn alloy, 54.2 μA cm^{-2} for Mg14.5Zn alloy, 80.3 μA cm^{-2} for Mg20.3Zn alloy, 132.2 μA cm^{-2} for Mg40.3Zn alloy). The compression strength increases with increasing Zn content, but reaches the highest value when Zn content reaches 14.5 wt.% (373.5 MPa for M6Zn alloy, 396.5 MPa for Mg14.5Zn alloy, 371.7 MPa for Mg20.3Zn alloy, 354.6 MPa for Mg40.3Zn alloy). Above this value, further addition of Zn is detrimental because large-size secondary phases and Zn particles formed in the alloy could act as crack sources [56].

Considering the aforementioned dependence of a good combination of mechanical properties and corrosion resistance on Zn content, Zhang et al. [22] have suggested that the Zn content of MgZn alloys should be limited to 4 wt.%. Figure 2 depicts the influence of Zn content on the corrosion rate and tensile properties of Mg-Zn binary alloys, summarizing the data provided in the literature. This shows that, as Zn content varies, the corrosion rate of MgZn alloy changes differently between different reports (Figure 2). One of the reasons might be the fact that other influences besides the Zn content do affect the corrosion rate. The most obvious is the electrolyte composition, which was not the same in all of the experiments (see Table A2 in Appendix). Two other important influence factors are the microstructure of the alloy (e.g., grain size and distribution of secondary phases) and the impurity levels of the tested alloys. Generally, more secondary phases and more impurities would lead to faster corrosion and severer localized corrosion of the alloy. In contrast, an average tendency can be observed for the influence of Zn content on tensile properties. The yield and ultimate tensile strength increase while elongation to fracture decreases with increasing Zn content in the range of 0–4 wt.%. It can be noted that studies about binary Mg-Zn alloys are still quite limited and many inconsistencies exist, suggesting that more systematic studies are needed.

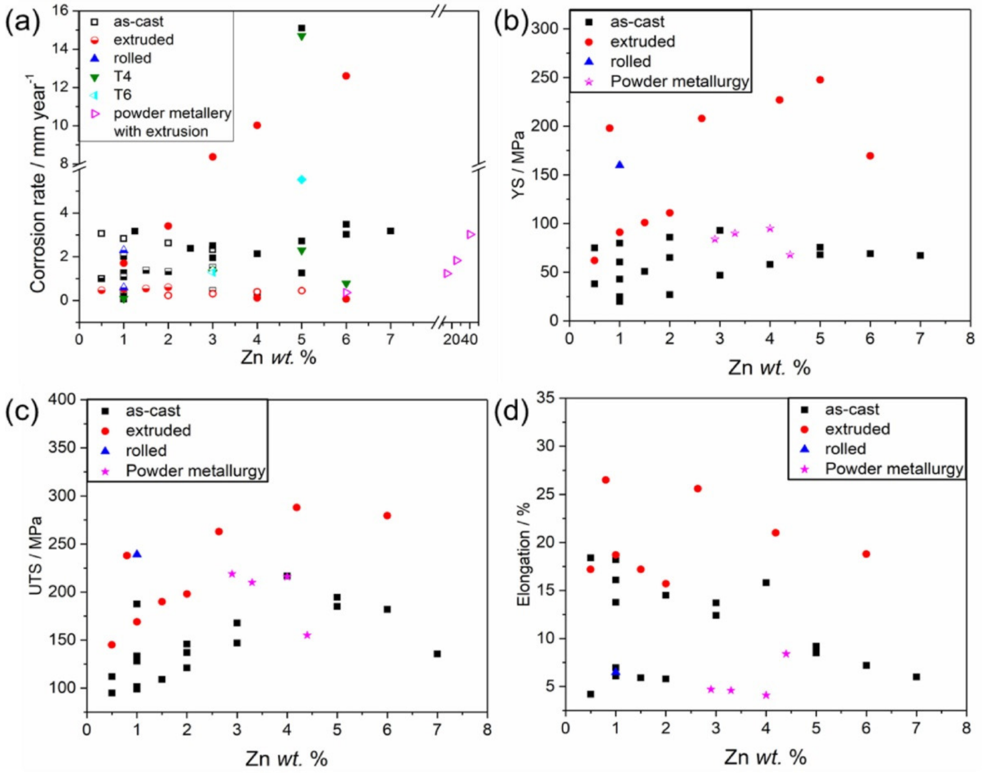

Figure 2. Influence of Zn wt.% on (**a**) corrosion rate (solid symbols refer to corrosion rate of Mg alloys measured by gravimetric method (P_w), half-up open symbols refer to corrosion rate of Mg alloys measured by hydrogen evolution (P_H), and open symbols refer to corrosion rate of Mg alloys evaluated from corrosion current density (P_i)), (**b**) yield strength, (**c**) ultimate tensile strength, and (**d**) elongation to fracture of binary Mg-Zn alloys reproduced from the literature [10,22,26,40-42,45-50,54,56-61].

3. Ternary Mg-Zn-X Alloys

Superior combinations of corrosion resistance and mechanical properties of as-cast Mg-Zn based alloys can often be improved by the addition of a third alloying element or microstructure modification via heat treatment or mechanical processing.

3.1. Influence of Microstructure on the Corrosion and Mechanical Properties

Microstructural features, such as grain size, volume fraction, and distribution of secondary phases, generally play an important role in the corrosion behavior of Mg alloys. It is widely accepted that refined grain size is beneficial to the corrosion resistance of Mg alloys in neutral and alkaline sodium chloride (NaCl) corrosive electrolytes [62-67]. However, large residual stresses, which can be introduced during grain refinement, can be detrimental to the corrosion resistance of Mg [63,64]. Song et al. have reported that the influence of secondary phases on corrosion behavior of Mg alloys depends on the amount and distribution of the secondary phases [1,68,69]. They can either act as a galvanic cathode to accelerate the corrosion rate, or as a continuous barrier with higher corrosion resistance (compared with the Mg matrix) when exposed to the corrosive environment after the dissolution of the top Mg matrix (Figure 3). Lu et al. [70] have studied the combined influence of secondary phases and grain size on the corrosion of as-cast and heat-treated Mg3Zn0.3Ca (in wt.%) alloy. The results (Figure 4) indicate that both the volume fraction of secondary phases and grain size are important for controlling the corrosion of the alloy. When the influence of grain size is dominating the corrosion process of the alloy, the large grain size would lead to the increase of the corrosion rate. Vice versa, when the secondary phase volume fraction is high, it overrules the beneficial effect of fine grain size.

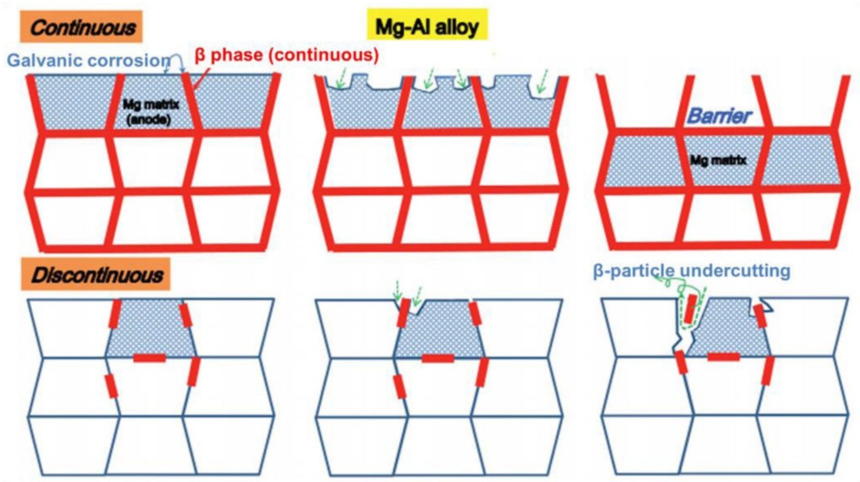

Figure 3. Influence of distribution of secondary phases on corrosion behavior of Mg alloys (AZ91D alloy as representative) [71] (with permission from Elsevier and Copyright Clearance Center).

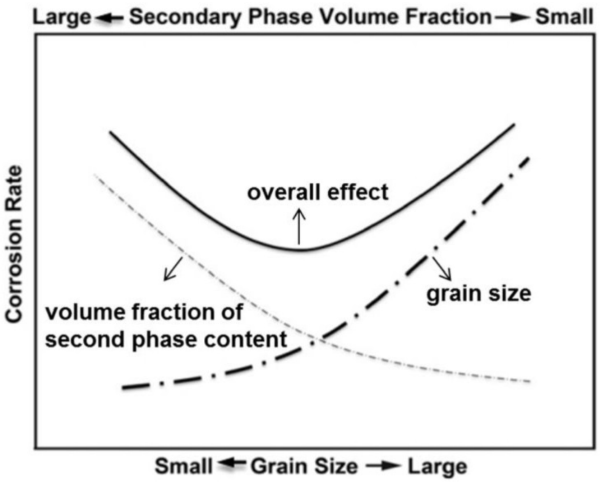

Figure 4. Schematic illustration showing the effect of volume fraction of secondary phases and grain size on the corrosion rate of Mg3Zn0.3Ca alloy [70] (with permission from Elsevier and Copyright Clearance Center).

3.1.1. Mg-Zn-Ca Alloys

Due to their good biocompatibility, Mg-Zn-Ca alloys have attracted attention in research of Mg alloys for biomedical devices. Calcium (Ca) behaves as an effective grain refiner for MgZn alloys [5,72,73]. The phase formation depends on the contents of Zn and Ca (especially the Zn/Ca ratio), and affects the corrosion performance of the alloy. It has been pointed out that eutectic α-Mg + Mg_2Ca + $Ca_2Mg_6Zn_3$ phase precipitates when Zn/Ca atomic ratio is lower than 1.2, while α-Mg + $Ca_2Mg_6Zn_3$ eutectic phase is formed when Zn/Ca atomic ratio is higher than 1.2 [5,74]. A new phase $Ca_2Mg_5Zn_{13}$ has also been reported in the case of Mg6Zn1Ca (in wt.%) alloy [23]. Mg_2Ca and $Ca_2Mg_6Zn_3$ phases usually distribute along the grain boundary and form interdendritic interstices in as-cast Mg-Zn-Ca alloys. A segregation of Zn may occur in the vicinity of Mg_2Ca phase, consequently protecting this area (Mg_2Ca phase) against corrosion [75,76]. Mg_2Ca is more active than α-Mg matrix, while $Ca_2Mg_6Zn_3$ is nobler than α-Mg [75,77]. Therefore, $Ca_2Mg_6Zn_3$ phase with discontinuous distribution can act as a cathode site, accelerating galvanic corrosion of the matrix, but can act as a barrier when the $Ca_2Mg_6Zn_3$ phase is continuously distributed in the microstructure, e.g., along the grain boundary [75].

When the content of Ca is lower than 1 wt.%, alloying additions of Ca improve the corrosion resistance of Mg-Zn alloys by forming compounds with elemental impurities and thus purifying the melts, while more addition of Ca leads to the formation of secondary phases and thus results in increased pitting corrosion with increasing overall corrosion rate [5,22,59,73,75]. It has been reported that $Ca_2Mg_6Zn_3$ and $Ca_2Mg_5Zn_{13}$ phases have strengthening effects [16,78,79]. Thereby, grain refinement and precipitate strengthening would contribute to an improvement in mechanical properties of Mg-Zn-Ca alloys. Nevertheless, with increasing Ca content, Mg_2Ca and $Ca_2Mg_6Zn_3$ phases continuously precipitate along the grain boundary, which is detrimental to the tensile properties of the alloy, since Mg_2Ca is a brittle phase and can produce crack sources that can lead to brittle failure [5,22,80,81].

Increasing the Zn content promotes the corrosion of Mg-Zn-Ca alloys because, as aforementioned, nobler $Ca_2Mg_6Zn_3$ secondary phases form and thus accelerate galvanic corrosion [7,23,82]. However, the yield and tensile strength of the alloy can be enhanced with the increase of the Zn content when Zn concentration is in the range of 0–4.0 wt.%, which is due to the solid solution hardening and precipitation strengthening effects [7,23]. Nevertheless, more Zn addition would result in decline of mechanical properties of Mg-Zn-Ca alloys and change the fracture type from ductile to brittle [23].

On the basis of the above discussion, the corrosion and mechanical properties of Mg-Zn-Ca alloys can be optimized by adjusting the content of Zn and Ca, influencing the microstructure. Geng et al. studied Mg4ZnCa (in wt.%) alloys with micro-alloying addition of 0.2 wt.% Ca (corrosion and mechanical properties) [6] and 0.5 wt.% Ca (only mechanical property) [16], respectively. The corrosion properties of Mg4Zn0.2Ca alloys are similar to those of high-purity Mg in SBF. In addition, both of these two alloys exhibit good mechanical properties, especially Mg4Zn0.5Ca, which shows a good balance between tensile strength and ductility. The tensile strength and elongation to fracture are 185 MPa and 12.5% for Mg4Zn0.2Ca alloy and 211 MPa and 17% for Mg4Zn0.5Ca alloy, respectively [6,16]. Furthermore, tensile strength and elongation to fracture can be further enhanced by extrusion. The integrity of the alloy with 0.2Ca is still given even after immersion for 30 days in SBF, and the mechanical properties are still high enough (ultimate strength: 220 MPa, yield strength: 160 MPa, ductility: 8.3) for bone fixture applications.

3.1.2. Mg-Zn-Y Alloys

The solubility of Zn in the Mg matrix is greatly decreased when Y is incorporated as an alloying addition. This decrease is believed to be a result of the interaction between Zn and Y [53]. Ternary MgZnY phases would precipitate firstly at grain boundaries because of the higher eutectic temperature of ternary phases compared with that of binary phases [83]. The phase constituency in Mg-Zn-Y alloys is strongly dependent on the weight ratio of Zn to Y for both low (2 wt.%) and high (≥ 3 wt.%) Zn-containing systems [53,83,84]. When the Zn/Y weight ratio is lower than 1.5, $Mg_{12}ZnY$ phase precipitates (X-phase or LPSO phase—long period stacking ordered phase). When the Zn/Y weight ratio is 1.5–2, $Mg_3Zn_3Y_2$ phase (W-phase, dendritic phase) forms in the interdendritic region. When the Zn/Y ratio increases to 2–2.5, Mg_3Zn_6Y phase (I-phase, icosahedral quasicrystal phase) begins to form and co-exists with W-phase. When the Zn/Y ratio is 5–7, only I-phase forms in the Mg-Zn-Y alloy. However, with further increase of the Zn/Y ratio (~10), the composition is close to that of the binary Mg-Zn system; thus, mainly binary MgZn phases form [84,85]. Those secondary phases are electrochemically nobler than the α-Mg matrix and can thus be effective cathode sites when the alloys are exposed to corrosive environments, resulting in pitting corrosion at the secondary phase/α-Mg interface. With similar sizes and volume fractions of intermetallic particles, MgZnY alloys with a single secondary phase (e.g. Mg_3Zn_6Y I-phase) exhibit better corrosion resistance than those with two secondary phases (e.g. $Mg_3Zn_3Y_2$ W-phase and Mg_3Zn_6Y I-phase) [53,86]. Generally, with the increase of volume fraction of secondary phases with discontinuous distribution, the corrosion properties of the alloys would deteriorate, since the effective cathode area increases [87-89]. However, continuous distribution and moderate volume fraction of secondary phases can hinder the corrosion propagation [87,88]. For example, Mg97Zn1Y2 alloy (continuous distribution, volume fraction of secondary phases: 30.4%) has higher corrosion resistance compared with Mg98.5Zn0.5Y1 alloy (discontinuous distribution, volume fraction of secondary phases: 11.5%), Mg94Zn2Y4 alloy (continuous distribution, volume fraction of secondary phases: 55.4%) and Mg88Zn4Y8 alloy (continuous distribution, volume fraction of secondary phases:, 63.2%) [87]. Li et al. [88] have studied the influence of volume fraction of LPSO phases on the corrosion resistance of Mg0.9Zn1.6Y, Mg2.1Zn5.2Y, and Mg3.1Zn7.6Y (all in wt.%) alloys in 0.1 M NaCl solution. It has been revealed that the Volta potential difference at the LPSO phase/α-Mg interface could be up to 250 mV (Figure 5b). As a result, severe micro-galvanic corrosion preferentially occurs at the LPSO/α-Mg interfaces. Then, the corrosion progresses along the boundary of LPSO phases instead of in the α-Mg matrix (Figures 5c and 5d). A new phase (currently cannot be indexed) has been found in the Raman spectra of the corrosion products forming on LPSO phases besides magnesium hydroxide ($Mg(OH)_2$).

The mechanical properties of Mg-Zn-Y alloys also largely rely on the phase constituency. The presence of stable I-phase is beneficial for the mechanical properties of Mg-Zn-Y alloys, especially at elevated temperatures [90-92], due to the low interfacial energy between the I-phase and α-Mg matrix. The yield and tensile strengths of the alloys increase with increasing volume fraction of I-phase [84,90,93]. W-phase also contributes to the strength, but not as effectively as I-phase. However, W-phase has a better softening effect than I-phase, which is beneficial for the ductility of the alloys [53,94]. Many reports have demonstrated that the LPSO phases are effective for strengthening of Mg alloys [88,95-102]. Kawamura et al. have firstly reported a Mg97Zn1Y (in at.%) alloy with high yield strength of 610 MPa, usable ductility (5%), and a yield strength of 300 MPa at 473 K due to the presence of LPSO phase [103]. The strengthening mechanisms of LPSO phase were attributed to four mechanisms: 1) increased critical resolved shear stress (CRSS) of the basal plane, 2) activated non-basal slip, 3) kinking bands on LPSO formed during the deformation process, and 4) a coherent LPSO/Mg interface along the basal and prismatic planes [104–106]. However, the improvement of strength is slight (the ultimate strength is only increased from 141 MPa to 148 MPa) when the volume fraction of LPSO phases exceeds 20.3%, and even declines with much higher LPSO phase concentration because of the large length and thickness of the LPSO phases [88,96]. The influences of different phases on the mechanical properties of Mg-Zn-Y alloys are summarized in Table 1. In addition to the abovementioned influence of phase constituency, conditions of the alloys should also be taken into serious consideration during the optimization of mechanical properties.

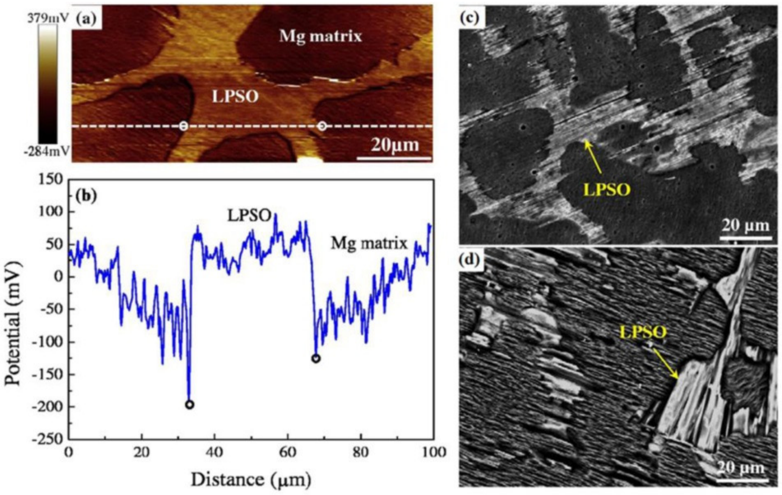

Figure 5. Scanning kelvin probe force microscopy (SKPFM) results of Mg3.1Zn7.6Y (in wt.%) alloy: (**a**) Surface Volta potential map and (**b**) line-profile analysis of relative Volta potential through the LPSO phase in (**a**). Scanning electron microscopy (SEM) surface morphologies of Mg3.1Zn7.6Y alloy after immersion in 0.1 M NaCl solution for (**c**) 2 h and (**d**) 4 h [88] (with permission from Elsevier and Copyright Clearance Center).

Table 1. Summary of mechanical properties of Mg-Zn-Y alloys containing different secondary phases.

Composition	Condition	Containing phases	Mechanical Properties (Room Temperature)			Refs.
			YS / MPa	UTS / MPa	Elongation / %	
Mg97Zn1Y2 (at.%)	Rapidly solidified powder metallurgy	LPSO phase	610	-	5	[103]
Mg97Zn1Y2 (at.%)	High-frequency induction melting + warm extrusion	LPSO phase	350	410	6	[98]
Mg97Zn1Y2 (at.%)	Conventional casting + extrusion	LPSO phase	-	400	12.5	[100]
Mg97Zn1Y2 (at.%)	Conventional casting + ECAP	LPSO phase	400	450	2.5	[102]
Mg3.1Zn7.6Y (wt.%)	Conventional casting	LPSO phase	107	148	3	[88]
Mg94Zn2Y4 (wt.%)	Conventional casting	LPSO phase	155	236	3.7	[96]
Mg94Zn3Y3 (wt.%)	Conventional casting + hot-rolling	LPSO phase + W-phase	380	-	6	[97]
Mg96Zn2Y2 (wt.%)	High-frequency induction melting + extrusion	LPSO phase + W-phase	390	420	5	[99]
Mg1.5Zn0.8Y (wt.%)	Conventional casting + hot-rolling	W-phase	178 *	225	18	[94]
Mg2Zn1.54Y (wt.%)	Conventional casting + extrusion	W-phase	214	266	27	[53]

Mg2Zn0.82Y (wt.%)	Conventional casting + extrusion	W-phase + I-phase	213	266	25	[53]
Mg2Zn0.36Y (wt.%)	Conventional casting + extrusion	I-phase	197	261	23	[53]
Mg96.27Zn3.3Y0.43 (at.%)	Rapidly solidified powder metallurgy + extrusion	I-phase	412	445	13	[107]
Mg95Zn4.3Y0.7 (at.%)	Conventional casting + hot-rolling	I-phase	220 *	370	19.7	[90]
Mg12Zn2.4Y (wt.%)	Conventional casting + hot-rolling	I-phase	189	286	21.3	[108]

* means 0.2% yield strength.

3.1.3. Mg-Zn-Mn Alloys

It is well known that manganese (Mn) is effective in combining with some heavy metal impurities, for example, Fe, thereby decreasing the galvanic corrosion between impurities and the Mg matrix [44]. When Mn is micro-alloyed (Mn wt.% < 1.0 wt.%) with the Mg-Zn system, Mn exists in a soluble state, and some binary MgZn phases precipitate with increase of Zn content in the range of 0 to 3 wt.% [109–112]. In addition, Mn in solid solution could stabilize the corrosion product layer formed when alloys corrode in corrosive environments by incorporating manganese as an oxide into the $Mg(OH)_2$ layer [51,112]. Rosalbino et al. [51] have found that Mg2Zn0.2Mn exhibits the best corrosion resistance in comparison with Mg2Zn0.2Ca, Mg2Zn0.2Si (all in wt.%), and AZ91 alloys, revealing a four-fold increase in polarization resistance over that of AZ91 alloy after exposure for 168 h in Ringer’s solution at 37 °C. Moreover, it has been reported by Abidin et al. [113] that the steady state corrosion rate of Mg2Zn0.2Mn (wt.%) alloy tested in Hank’s solution at 37 °C is much lower than that of high-purity Mg. However, this has been ascribed to a lower content of Fe impurity particles in the Mg2Zn0.2Mn alloy. In addition to $MgZn_2$ phase, additions of silicon (Si, 0–2 wt.%) into Mg-Zn-Mn alloys can induce the formation of Mg_2Si and Mn_5Si_3 phases, but only Mg_2Si phase influences the corrosion resistance of the alloy significantly [114]. The role of Mg_2Si phase on the corrosion property of the alloy depends on its morphology and volume fraction in the microstructure (Figure 6). When Mg_2Si is in Chinese script type (0.5 wt.% Si), the corrosion rate is higher than that in the polygonal type. However, when the morphology of Mg_2Si phase changes from Chinese script type to polygonal type with increasing Si content (1 wt.% and 2 wt.%), the corrosion resistance of the alloy increases again [114–116].

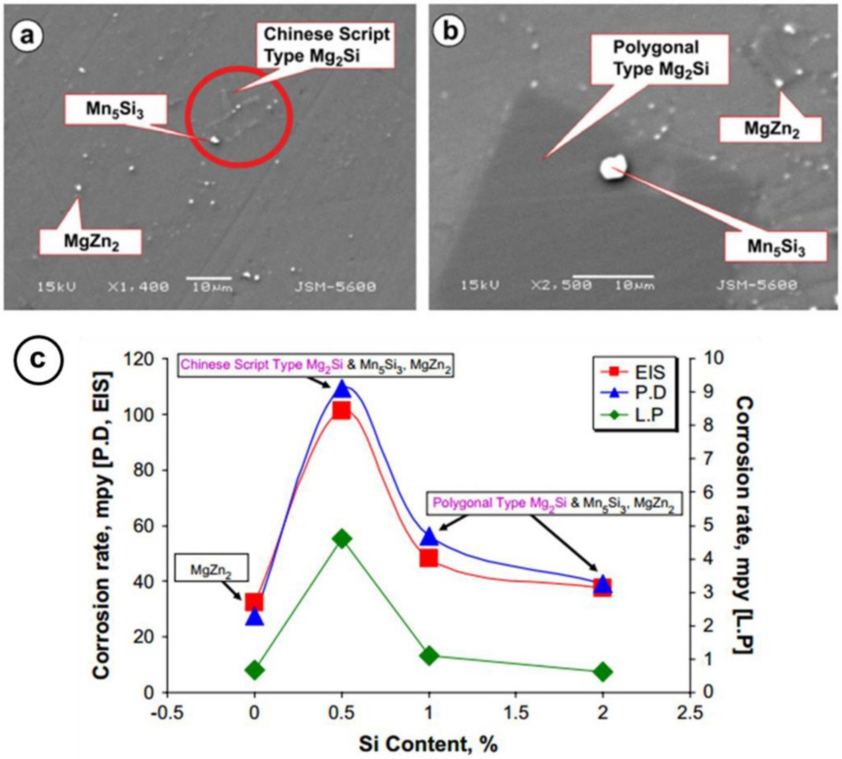

Figure 6. Microstructures of (**a**) Mg6Zn0.5Mn0.5Si and (**b**) Mg6Zn0.5Mn2Si alloys (wt.%) determined by SEM. (**c**) Influence of Mg_2Si phase on the corrosion rates of Mg6Zn0.5MnxSi (x= 0, 0.5, 1.0, 2.0; wt.%) alloys in 3.5% NaCl solution saturated with $Mg(OH)_2$ (EIS: Electrochemical impedance spectroscopy, P.D: Potentiodynamic polarization measurements, L.P: Linear polarization measurements) [114] (with permission from Elsevier and Copyright Clearance Center).

3.1.4. Representative Mg-Zn-RE and Mg-Zn-Zr Based Alloys

Generally, the addition of rare earth (RE) elements is beneficial for the mechanical properties of Mg alloys at elevated temperatures, and zirconium (Zr) is considered to behave as an effective grain refiner [117,118]. Thus, many efforts have been devoted to the development of RE/Zr-containing Mg alloys with fine grains. Representatively, Mg-Zn-RE (ZE) and Mg-Zn-Zr (ZK) alloys have been widely studied for automotive/aerospace and biomedical applications, especially commercial ZE41 and ZK60 alloys.

The corrosion resistance of ZE41 alloy is poor, with a corrosion rate twice as high as that of AZ91D and about thirteen times higher than that of pure Mg in 1 M NaCl solution [119]. Mg_7Zn_3RE (T-phase) and $Mg_{12}RE$ phases with nobler corrosion potential can precipitate along the grain boundaries, as well as inside of the grains, thereby inducing severe galvanic corrosion. As a result, the Mg matrix adjacent to the secondary phases will dissolve preferentially; then, pitting and intergranular corrosion can occur [118,120]. Caution should be paid during mass loss measurements because the T-phase could be dissolved by chromium-trioxide-based corrosion product removal solutions [121], thus leading to misleading results of corrosion rate. Furthermore, with micro-additions of Zr into ZE41 alloy, a so-called Zr-rich interaction zone can form within the grains and Zr-rich particles, together with some Zn and Fe precipitates can be found in those Zr-rich regions (shown in Figure 7) [121–123]. Consequently, the Zr-rich zones are also favorable sites for galvanic-driven localized corrosion attack (galvanic couple between the Zr-rich particles and the surrounding matrix).

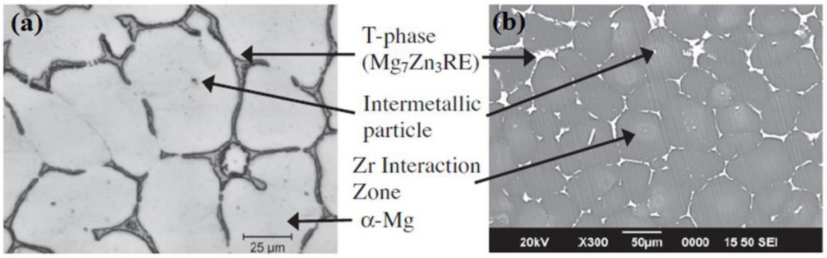

Figure 7. Microstructure of ZE41A alloy obtained by (**a**) optical micrograph and (**b**) SEM micrograph [122] (with permission from Elsevier and Copyright Clearance Center).

ZK60 alloy has wide engineering applications due to its good combination of tensile strength (≥ 250 MPa) and uniform elongation (≥ 15%) [124]. However, a piece of ϕ 28 mm × 5 mm specimen can degrade completely after 12 weeks of immersion in Hank's solution due to the galvanic corrosion between binary MgZn phases (Mg_7Zn_3 or $MgZn_2$) and the Mg matrix [125]. This fast degradation rate cannot meet the requirements of biomedical applications [126]. By optimizing the content of Zn (Mg3Zn0.6Zr, in wt.%) in Mg-Zn-Zr alloy, the corrosion rate of Mg-Zn-Zr alloy can be comparable to that of WE43 alloy, which exhibits good corrosion behavior relative to AZ31, AZ91, and LAE42 alloys [125,127]. The further addition of Y and/or neodymium (Nd) into Mg-Zn-Zr alloys results in the precipitation of less noble T-phase and/or W-phase, and leads to the formation of more a compact corrosion product layer with higher corrosion resistance [128,129]. It is quite often observed for Mg alloys that the protective film is denser when the overall corrosion rate is low. Too much and fast $Mg(OH)_2$ formation results in more compact films with coarse needle-like structures [130] The tensile properties of Mg-Zn-Zr alloys further alloyed with some rare earth elements (Nd, Gd, etc.) strongly depend on the microstructure of the alloy, i.e., the types and shapes of secondary phases [131–135]. For example, the addition of 2 wt.% Nd into Mg5Zn0.6Zr (in wt.%) alloy leads to the formation of a continuous network of intergranular phases, which significantly deteriorates the ultimate strength and elongation to fracture. However, the presence of discontinuous phases in Mg5Zn0.6Zr2Nd0.5Y (in wt.%) favors the ultimate strength and elongation to fracture [136].

Gadolinium (Gd) has a large solubility in Mg (23.49 wt.% at 548 ºC and 3.82 wt.% at 200 °C), but binary MgGd (Mg_5Gd or Mg_3Gd) phase and/or ternary MgZnGd ($Mg_3Gd_2Zn_3$) phase precipitate in the matrix when Gd is alloyed to the Mg-Zn system. Similar to the Mg-Zn-Y alloys, the phase constitutions of Mg-Zn-Gd alloys also strongly depend on the Zn/Gd atomic ratio [137]. Small amounts of Gd addition (1 wt.%) are beneficial to the corrosion resistance of the Mg1Zn (in wt.%) system. Furthermore, both Gd and Zn enrich in the Mg matrix surrounding the secondary phases, improving the corrosion resistance of the matrix [49]. Yang et al. [138,139] have studied the influence of varying Gd content (from 0.5 up to 5 wt.%) on the microstructures and mechanical properties of the Mg4.5Zn (in wt.%) system. It has been revealed that Gd can refine the grains when additions are less than 2 wt.%, and further increase of Gd content would cause increasing grains. The strength of the Mg4.5Zn alloy is improved with increasing Gd addition up to 2 wt.%, but deteriorates with further increase of Gd content. This is related to the effects of grain size, solid solubility of Zn and/or Gd, and the size and volume fraction of secondary phases.

3.1.5. Other Mg-Zn-X Alloys

Addition of strontium (Sr) can also refine the microstructure of Mg-Zn alloys in spite of its limited solubility in Mg (0.11 wt.% at 858 K), and the refinement effect increases with increasing Sr content (0.1–1 wt.%) due to precipitate formation [140,141]. Although nobler secondary phases (compared with Mg matrix) precipitate, the corrosion behavior of Mg4Zn1Sr (in wt.%) is superior to that of pure Mg [142]. Nevertheless, the corrosion rate of Mg-Zn-Sr alloy increases with the increase of either Zn or Sr contents due to the enhanced galvanic corrosion induced by the increased amount of secondary phases. In comparison, the strength of Mg-Zn-Sr alloys is improved when both Zn (2–6 wt.%) and Sr (0.2–1 wt.%) contents increase, because of the refined grains and homogeneously distributed secondary phases [140,143].

A few studies have also been carried out to investigate the influence of alloying with silver (Ag), Cu, germanium (Ge), etc. on the corrosion and/or mechanical properties of an Mg-Zn system. For example, Ben-Hamu et al. [144] have revealed that addition of Ag into an Mg6Zn (in wt.%) system is harmful to the corrosion resistance due to the galvanic coupling between $Ag_{17}Mg_{54}$ phases and the α-Mg matrix, but contributes to the hardness of the alloy. Minor additions of Cu (< 0.5 wt.%) into the Mg2Zn (in wt.%) system improves the corrosion resistance and tensile properties of the alloy, but higher addition levels are detrimental to both corrosion and tensile performance due to the increased volume fraction of secondary phases [145]. Liu et al. [146] and our recent study [147] have demonstrated that a small addition of Ge (≤ 0.5 wt.%) significantly improves the corrosion resistance and tensile strength of binary Mg-Zn alloys. Furthermore, the presence of Ge suppresses the kinetics of cathodic reactions and facilitates the incorporation of alloying elements into the corrosion product layer, which are beneficial for the corrosion resistance of Mg-Zn alloys. However, the amount of related work is too small to give a comprehensive overview.

3.2. Influence of Environment on the Corrosion Behavior

In addition to the galvanic coupling between secondary phases and the Mg matrix (influence of microstructure), the corrosion behavior of Mg alloys is also governed by surface product layers and their protective properties, which are significantly affected by the environment. Fang et al. [73] have studied the corrosion behavior of Mg1ZnxCa (x = 0.2, 0.5, 0.8 1.0; wt.%) alloys in SBF and 3.5 wt.% NaCl solutions, which reveals that Mg1Zn0.8Ca alloy is the most corrosion-resistant alloy in 3.5 wt.% NaCl solution, while Mg1Zn0.5Ca alloy has the best corrosion properties in SBF, demonstrating that the corrosion properties of the alloys are significantly influenced by the compositions of the corrosive media.

It is well known that the surface film formed on Mg alloys in aqueous solution is mainly composed of magnesium oxide (MgO) and $Mg(OH)_2$, and the film can be easily broken down by the penetration of chloride ions (Cl^-) [1]. Zhao et al. [119] have studied the corrosion behavior of ZE41 alloy in NaCl solutions at different pH and Cl^- concentrations. The incubation period to the onset of corrosion is shortened as pH decreases or Cl^- concentration increases. This is because corrosion predominantly happens at the uncovered regions or defects of the surface film, and the fraction of film-free surface of the alloy increases with decreasing pH and increasing Cl^- concentration. This phenomenon has been further confirmed by Johnston et al. [148] and Taltavull et al. [149], who investigate the corrosion behavior of ZE41 alloy in Hanks' solution at different pH and Cl^- concentrations buffered with bicarbonate. A more stable and thicker $Mg(OH)_2$ layer could be formed with increasing pH, since higher pH values mean that $Mg(OH)_2$ can precipitate at a lower magnesium ion (Mg^{2+}) concentration. The breakdown of the surface layer induced by Cl^- subsequently accelerates galvanic corrosion between the constituencies in the alloy.

Very few corrosion studies of Mg-Zn based alloys have been carried out in other salt solutions, such as sodium sulfate (Na_2SO_4) and ammonium nitrate (NH_4NO_3) solutions. The limited studies show that the corrosion rate of ZE41 alloy in Na_2SO_4 solution increases with increased concentration of Na_2SO_4 at each pH, and decreases with increased pH at each concentration of Na_2SO_4 [150]. In mixed solutions of NaCl and Na_2SO_4, the increased concentration of Na_2SO_4 also leads to a higher corrosion rate of ZE41 alloy [117]. Mg2.03Zn0.83Mn (in wt.%) alloy is more corrosion-resistant in 0.01 M Na_2SO_4 solution than in 0.01 M NH_4NO_3 solution [151]. As such, much more research is needed in order to get more general influence of those salt solutions on the corrosion behavior of Mg-Zn based alloys, and the application background should be specified when the corrosion of Mg-Zn based alloys is discussed or investigated.

In addition to immersion tests in salt solutions, salt spray tests are also commonly used to evaluate the corrosion resistance of Mg alloys. Under salt spray conditions, weight loss of Mg alloys is lower, and the pits formed on the sample surface are fewer and grow more slowly [152]. Generally, salt spray atmosphere is less deleterious in terms of general and pitting corrosion compared with solution immersion environments. The differences between salt spray tests and immersion tests come from the fact that a thin solution layer can be formed on the sample surface in salt spray tests, which can be considered as a stagnation, and subsequently results in rapid increase of local pH as Mg dissolves, whereas the immersion environment favors the diffusion of dissolved Mg ions, as well as the formation and growth of pits [152–154]. Therefore, interrupted salt spray and alternate immersion tests are suggested to comment on the normal corrosion of Mg-Zn alloys [57].

Direct comparison between the corrosion rates obtained from the two tests would not always be possible, since different concentrations of salt are usually used for each testing environment. Cao et al. [57] have tested the corrosion behavior of as-cast and heat-treated Mg5Zn (in wt.%) alloys in 3.5 wt.% NaCl solution saturated with $Mg(OH)_2$ at room temperature, as well as in spray of 5 wt.% NaCl solution at 35 °C. The general trend of corrosion rates is the same in the two kinds of tests. Corrosion rates of Mg5Zn alloys measured by weight loss after immersion and salt spray tests are comparable, and both of those two tests have demonstrated that heat treatment can improve the corrosion resistance of Mg5Zn alloy. Moreover, the corroded morphologies of Mg5Zn alloy are similar after immersion and salt spray tests. Zhao et al. [155] have studied the corrosion of ZE41 alloy in interrupted salt spray and solution immersion tests with 3 wt.% NaCl. When the interrupted salt spray period is 1 min for salt spray and 119 min for drying at 20 % humid conditions (duration for one week), the corrosion rate of ZE41 alloy is similar to the steady state corrosion rate in the solution immersion test. However, when the procedure is changed to be 15 min for salt spray and 105 min for drying (duration for 1 d), the corrosion rate of ZE41 alloy measured in interrupted salt spray tests is significantly lower than that measured in solution immersion for 1 day, revealing the importance of salt spray intervals to the corrosion tests of alloys.

In contrast to simple salt solutions, a variety of different corrosion products (e.g., calcium carbonate ($CaCO_3$), carbonated calcium phosphates ($Ca_{10}(PO_4)_6(OH)_6$ or $Ca_3(PO_4)_2{\cdot}3H_2O$), hydroxyapatite (HA), etc.) are formed on the surfaces of Mg alloys exposed to complex electrolytes, such as SBF. Usually, a simulated body solution contains appropriate inorganic components, a buffering system, and/or organic ingredients. Ringer's solution, Hanks' solution, phosphate-buffered saline (PBS), SBF, Dulbecco's modified Eagles medium (DMEM), Earle's balanced salt solution (EBSS), and minimum essential media (MEM) are frequently used for the in vitro investigation of the corrosion behavior of Mg alloys [46,52,113,126]. The typical chemical compositions of those simulated body fluids are listed in Table 2. The corrosion behavior of Mg alloys differs when different simulated body fluids are used due to the different compositions of the fluids and different corrosion products formed. In particular, the use and type of buffering agent plays a particularly significant role in determining the type of corrosion product formed [9,156]. For example, the corrosion resistance of ZK60 alloy in Hanks' solution is higher than in DMEM and DMEM + fetal bovine serum (FBS). In DMEM+FBS, the corrosion resistance of ZK60 alloy is the lowest compared to that in Hanks' solution and DMEM. The lower content of hydrocarbonate, as well as the absence of organic components in Hanks' solution, results in less protective corrosion products on the surface and the consequent faster corrosion occurring on ZK60 alloy. Additionally, in the presence of FBS, the interaction between proteins and corrosion products may affect the equilibrium of dissolution and regeneration of corrosion products, thus accelerating the corrosion of the alloy [126]. Jamesh et al. [124] have reported that the corrosion products formed on ZK60 alloy surface are $Ca_{10}(PO_4)_6(OH)_6$, $Ca_3(PO_4)_2{\cdot}3H_2O$, and $Mg(OH)_2$ in SBF, while $CaCO_3$ and $Mg(OH)_2$ predominate in the case of Ringer's solution. In addition, much more severe pitting and localized corrosion occurs on ZK60 samples immersed in SBF. Zander et al. [75] have further demonstrated that the influence of Zn content on the corrosion resistance of Mg-Zn-Ca alloys is more significant in

Hank's solution than in PBS, as indicated by the anodic polarization curves measured in Hanks' solution.

Table 2. The typical chemical compositions of simulated body fluids (in mM/L if not specified).

Ingredient	Ringer's Solution	Hanks' Solution	DMEM	EBSS	SBF	PBS	MEM	Blood Plasma
Mg^{2+}	-	0.8	0.81	0.4	1.0	-	0.4	1
Na^+	156	142	154	144	142	153	143	140
K^+	5.8	5.8	6.24	5.4	5.0	5.0	5.4	5
Ca^{2+}	2.2	2.5	1.8	1.8	2.5	-	1.8	2.5
Cl^-	164	145	118	125	109	140	125	100
HCO_3^-	2.4	4.2	44.05	26	27	-	26	22-30
$H_2PO_4^-$	-	0.4	1.04	1.0	-	2.0	0.9	0.8
HPO_4^{2-}	-	0.3	-	-	1.0	8.0	-	-
SO_4^{2-}	-	0.8	0.81	0.4	1.0	-	0.4	0.5
Glucose	-	-	5.55	5.6	-	-	5.6	5
Amino acid (g/L)		-	11.01 (mM/L)	-	-	-	0.95	Variable
Proteins (g/L)	-	-	-	-	-	-	-	35-50
Vitamins (mg/L)	-		-	-			8.1	Variable
Phenol red	-	-	-	0.03	-	-	0.03	-
Refs.	[51]	[113]	[126]	[157]	[158]	[158]	[157]	[157]

Normally, the corrosion rate of Mg alloy in vivo is around 1–5 times lower than that obtained in vitro [159]. For example, the corrosion rate of as-cast Mg3Zn1.34Ca (in wt.%) alloy in MEM is 4.718 mm/year, whilst that measured in vivo implanted in Lewis rats is only 0.786 mm/year after immersion or implantation for 7 d [157]. However, opposite results have also been reported. Extruded Mg6Zn corrodes faster in vivo (2.32 mm/year) than in SBF (average at 0.14 mm/year) [160]. As indicated in Table 2, the lower concentration of Cl^- in blood plasma (100 mM/L), compared to simulated physiological solutions such as Hank's solution (145 mM/L), generally contributes to slower corrosion of Mg alloy in vivo than in vitro. Additionally, the possible interaction between the complicated components in vivo (e.g., cells and proteins) and Mg may also contribute to the lower corrosion rate measured in vivo [157,159,161]. As already suggested by many researchers [157,162–164], much caution should be paid when choosing the appropriate simulated body fluid to evaluate the corrosion rates of Mg-Zn alloys in vitro to get results comparable to those in vivo.

The behavior of Mg alloys in aggressive environments under dynamic loading, including stress corrosion cracking (SCC) (applied tensile mechanical loading) and corrosion fatigue (CF) (applied cyclic loading), is also a critical concern for their applications. The combined action of stress and corrosive electrolytes can result in an unexpected premature failure of alloys at a loading below the designed value for static loading service conditions [165]. Generally, the corrosion rates of Mg alloys are significantly higher in corrosion fatigue tests than those measured in static immersion. The corrosion product layers can be broken due to the cyclic loading or the strain induced, which consequently promotes the penetration of corrosive electrolytes into the underlying metals and the occurrence of corrosion [166]. Furthermore, the corrosion rates of Mg alloys increase with increasing cyclic loading. Bian et al. [167] have studied the corrosion behavior of extruded Mg2Zn0.2Ca (in wt.%) alloy in SBF under static conditions and cyclic loading, revealing the effect of cyclic loading on the corrosion rate of the alloy mentioned above (Figure 8b). Moreover, it has been pointed out that a material that corroded more slowly in static immersion may exhibit a faster corrosion rate under cyclic loading conditions. This finding is often attributed to the stress-accumulating role of intermetallics due to the evolution of hydrogen at these locations. SCC of Mg alloys, which can occur in either the presence or absence of Cl^- [168], is often associated with hydrogen embrittlement. Under tensile loading in a corrosive environment, the rupture of surface film can be induced by an applied stress or localized corrosion, and can facilitate the initiation of cracks. This, in turn, allows the diffusion of hydrogen into the material [169,170]. The strain rate plays a critical role in the failure of alloys. Fast strain rate results in failure via mechanical overload as opposed to SCC. However, low strain rate increases the contact time of the alloy with the corrosive medium, thus facilitating the penetration of the electrolyte and the ingress of hydrogen [171]. Additionally, SCC can even occur in the presence of residual stress that accumulates during thermal–mechanical processing without externally applied stress. Jadari et al. [172] have observed that the fracture morphologies of extruded Mg2Zn1Zr (in wt.%) alloy, immersed in modified simulated body fluid (m-SBF) and then strained in air, are similar to those strained directly in m-SBF. The SCC of the pre-immersion sample is ascribed to the residual stress developed during the extrusion processing.

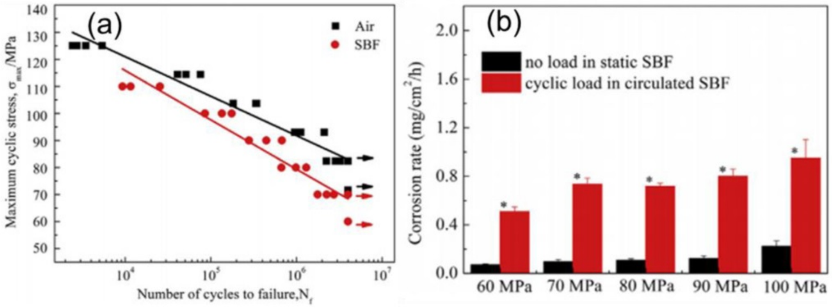

Figure 8. (**a**) Stress-life (S-N) curve of Mg2Zn0.2Ca alloy in air and in simulated body fluid (SBF). (**b**) Corrosion rate of Mg2Zn0.2Ca alloy measured in static SBF (static immersion) and under a cyclic loading in circulating SBF [167] (with permission from Elsevier and Copyright Clearance Center).

3.3. *Influence of Processing*

The influence of thermal and mechanical processing on corrosion and mechanical properties of Mg-Zn-X alloys is closely associated with the grain size and the distribution of precipitates within the microstructure. This results in significant differences in the performance compared to as-cast alloys.

Solid solution heat treatment is beneficial to the corrosion resistance of Mg-Zn-X alloys, especially when conducted at high temperatures or for relatively long time periods. Some secondary phases—for example, MgZn binary phase—could dissolve into the Mg matrix during solution treatment. Thus, dendrite structures would disappear, resulting in the formation of a homogenized microstructure [70,173,174]. With the decrease of volume fraction of secondary phases, micro-galvanic corrosion is reduced; thus, the corrosion resistance of the alloys is improved. However, solution treatment can increase grain size, which could decrease corrosion resistance of Mg-Zn-X alloys when the effect of grain size overwhelms that of secondary phases on corrosion of

Mg-Zn-X alloys [70]. In contrast, aging treatments facilitate the precipitation of secondary phases [58,142,173,175]. For example, rod-like metastable $MgZn_2$ secondary phases would precipitate both at the grain boundaries and inside the grains, inducing enhanced strength of the alloy due to the strengthening effect of this phase. With the increase of ageing time, the average volume fraction of precipitates increases. Guan et al. [142] have studied the development of microstructure and mechanical properties of rolled Mg4Zn1Sr (in wt.%) alloy with different aging times (0–16 h). The hardness, ultimate tensile strength, and elongation to fracture of Mg4Zn1Sr alloy increased as aging time increased, and reached their maximum after aging for 8 h at 175 ºC. This was attributed to the strengthening effect of the precipitated rod-like transition $MgZn_2$ phase. However, with further increase in aging time, the volume of rod-like $MgZn_2$ phases decreases, while the amount of particle-like flaky $MgZn_2$ phase and stable MgZn phase, which weaken the strengthening effect, increases. Therefore, mechanical properties of the alloy start to decrease. Ibrahim et al. [176] have also confirmed the influence of aging time on the microstructure and mechanical properties of Mg-Zn-Ca alloy. They have studied the microstructural, mechanical, and corrosion characteristics of Mg1.2Zn0.5Ca (in wt.%) alloy after solid solution treatment and with further aging treatment for different time. It has been demonstrated that when the age hardening duration increases to 2–5 h, both the mechanical properties and corrosion resistance of Mg1.2Zn0.5Ca alloy strengthen because of the refined microstructure and finely distributed $Mg_6Ca_2Zn_3$ precipitates. Further increases in aging time did not contribute to further enhancement of either mechanical or corrosion properties.

Wrought processing can introduce several effects, such as grain refinement and texture, conferring specific improved properties to Mg alloys. Extrusion treatment induces severe plastic deformation, simultaneously refines α-Mg grains by dynamic recrystallization, and produces highly dispersed precipitates. The refined microstructure is beneficial for the improvement of the corrosion resistance of Mg-Zn-X alloys [6,126]. Moreover, the tensile strength and ductility of Mg-Zn-X alloys can be enhanced by grain refinement strengthening, solid solution strengthening, and secondary phase strengthening during the extrusion process [6,16,96,160,177]. Extrusion parameters, such as extrusion temperature, speed, and ratio, have a significant influence on the microstructure and mechanical properties of Mg-Zn-X alloys (Figure 9). In general, with the increase of extrusion temperature, ratio, and speed, average grain size and area fraction of dynamic recrystallized (DRXed) grains increase. This is because the deformation heating, which occurs during the extrusion process, results in rise of temperature at the deformation zone. Concomitantly, the ultimate strength and yield strength decrease due to the coarsened microstructure [86,173,178–180]. Formation of precipitates also increases with elevated extrusion temperature because the diffusion of solute atoms is faster at higher temperatures [173,181]. However, the influence of extrusion temperature on the plastic deformation of Mg-Zn-X alloys is still under debate. Park et al. [179] and Zeng et al. [180] have reported increased elongation to fracture of MgZn(Mn)Ce/Gd and MgZnYZr alloys with increased extrusion temperature, while the relationship was reversed in the case of MgZnHo [178] and MgZnGd alloys [173]. Park et al. attribute the increased ductility of MgZn(Mn)Ce/Gd alloys to the suppression of {10-11}-{10-12} double twinning with increased area fraction of DRXed.

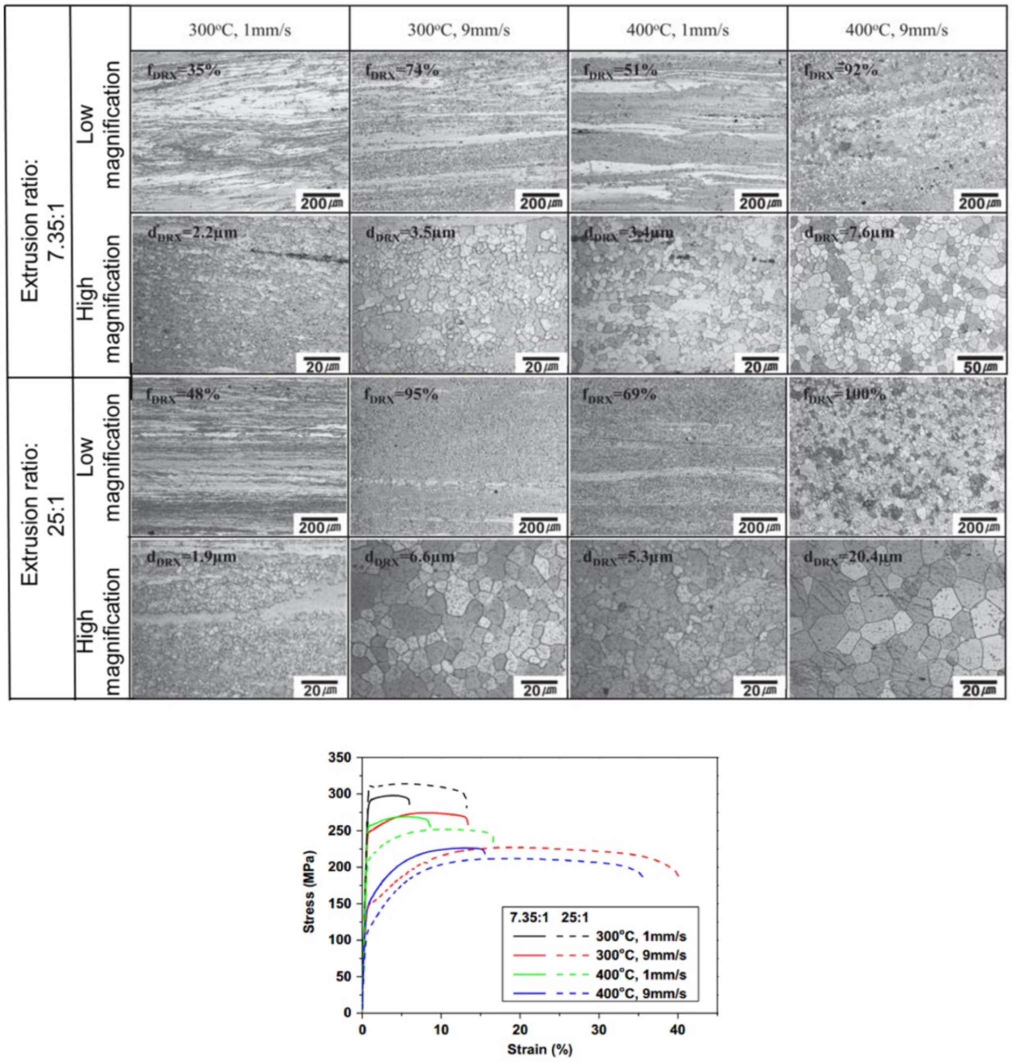

Figure 9. Effect of extrusion parameters (extrusion speed, ratio, and temperature) on the microstructure and mechanical properties of Mg2Zn1Mn0.5Ce alloy (in wt.%) (f_{DRX}: Area fraction of the recrystallized grains, d_{DRX}: Grain size of the recrystallized grains) [179] (with permission from Elsevier and Copyright Clearance Center).

It is believed that a weaker or non-basal texture is beneficial to the improvement of ductility of Mg sheets at room temperature, since the majority of grains in weaker basal or non-basal textures favor dislocation glide on the basal plane [182–184]. To control the texture, many processing technologies have been applied to Mg alloys. Rolling processes have been shown to be more effective in developing weaker or non-basal textures in Mg alloys compared with continuous extrusion, torsion extrusion, and equal channel angular extrusion [185]. The refined microstructure and uniformly dispersed fine secondary phases, formed during the rolling processing, contribute to enhanced yield strength and elongation to fracture of Mg-Zn-X alloys [101]. Lee et al. [186] have compared the recrystallization behavior of hot-rolled Mg3Zn0.5Ca alloy with that of hot-rolled Mg3Al1Zn alloy (both in wt.%). The results showed a totally different twins formation mode in Mg3Zn0.5Ca and Mg3Al1Zn alloys. Both compressive and secondary twins are generated in Mg3Zn0.5Ca alloy, while only tensile twins are observed in Mg3Al1Zn alloy. The presence of compressive and secondary twins leads to a weaker basal texture evolution in the Mg3Zn0.5Ca sheet. As a result, the hot-rolled Mg3Zn0.5Ca alloy exhibits much better formability than hot-rolled

Mg3Al1Zn alloy. The influences of rolling on the corrosion properties of Mg-Zn-X alloys are not widely studied. The increase of grain boundary area due to significantly refined microstructure after rolling can decrease the corrosion resistance of Mg3.0Zn (in wt.%) alloy in SBF [187].

Equal channel angular pressing (ECAP), which induces severe plastic deformation (SPD) by introducing an extremely large strain, is one of the most effective processing techniques for fabricating ultrafine-grained (UFG) Mg alloys. Compared with conventionally processed Mg alloys, ECAPed Mg alloys exhibit improved corrosion resistance and excellent mechanical properties [188–193]. Jiang et al. [188] have studied the influence of ECAP pass number on the corrosion resistance of as-cast ZE41A alloy in NaCl solution. Higher ECAP passes endow UFG ZE41A alloy with better corrosion resistance. The corrosion product layers formed on ECAPed ZE41A alloy, which has undergone 60 passes, are free of cracks compared to those formed on the ECAPed alloy surfaces with fewer passes. This can be explained by the decreased residual internal stress of the alloy, resulting from the complete DRX of the deformed microstructure formed after a high number of ECAP passes. ECAP processing of extruded ZK60 alloy is also beneficial for the reduction of the corrosion rate of the alloy in PBS solution [189]. The refinement and redistribution of precipitates during the ECAP process lead to a remarkable change in corrosion behavior from a localized to a more uniform mode. However, the influence of ECAP processing on the mechanical properties of Mg-Zn-X alloys differs with the initial conditions of the alloys. Zheng et al. [190] have compared the mechanical properties of as-cast and extruded Mg5Zn0.9Y0.2Zr (in wt.%) alloys after different passes of ECAP processing. Both the strength and elongation to fracture of as-cast Mg5Zn0.9Y0.2Zr alloy are significantly enhanced after ECAP processing, especially after an increased number of ECAP passes. This is attributed to the uniformly dispersed I-phase and refined grains formed during recrystallization. In contrast, for extruded Mg5Zn0.9Y0.2Zr alloy, the grain size is further refined after ECAP and the ductility is improved, while both yield strength and ultimate strength are reduced. This trend, also confirmed by other researchers [189,191,192], does not follow the Hall–Petch relation. It is explained by the intensive development of texture during ECAP. ECAP processing routes (shown in Figure 10), regarding the rotation of the billet between each pass, also have significant influence on the microstructure and mechanical properties of Mg alloys [193]. Route B_c (Figure 10b) is the most effective way to refine grains, while route A is the least effective one. The different strain paths can also result in different textures. Processing as route C would lead to the strongest texture of the alloys, with high-intensity basal planes inclining about 45º to the extrusion direction. As a result of the competition between grain refinement strengthening and texture softening effect, both yield strength and ultimate tensile strength of extruded Mg5.25Zn0.6Ca (in wt.%) alloy processed by ECAP with routes A and Bc increase, but decrease with route C.

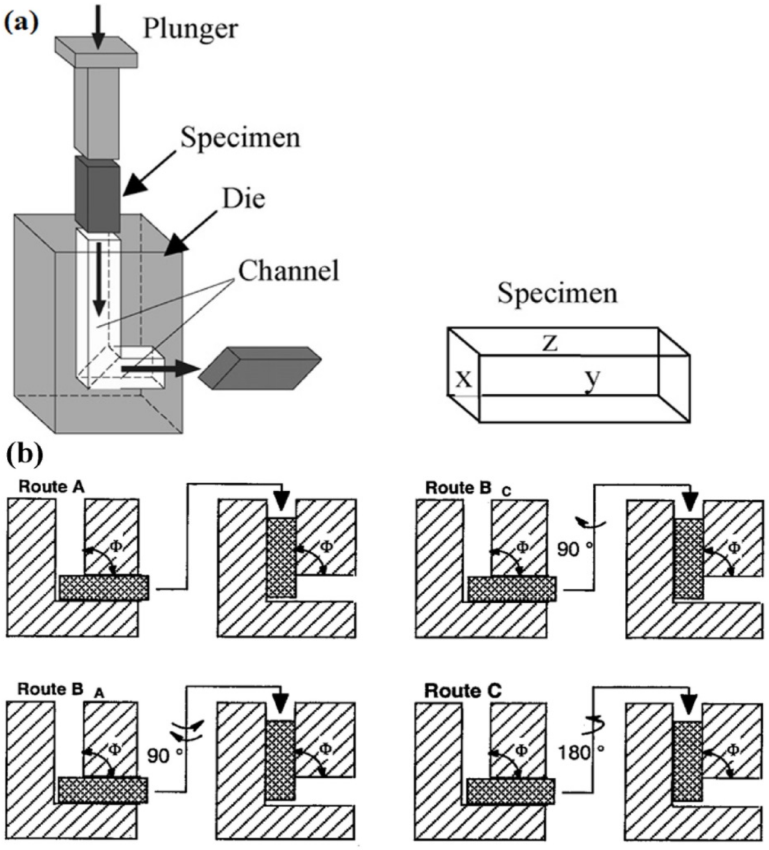

Figure 10. Schematic illustration for (**a**) equal channel angular pressing (ECAP) processing and (**b**) the rotation schemes for four ECAP routes [193,194] (with permission from Elsevier and Copyright Clearance Center).

4. Strategy to Improve Properties of Mg-Zn Based Alloys

In the previous chapters, it was demonstrated how alloying additions and thermal–mechanical treatments can be used to meet the requirements of different applications and expand the application field. However, microstructure adjustment by phase composition and unconventional fabrication approaches can also improve the corrosion performance and mechanical properties of Mg-Zn based alloys. Furthermore, surface treatment is effective for tailoring surface properties and corrosion resistance.

4.1. Microstructure Adjustment by Phase Composition

4.1.1. Magnesium-Based Metal Matrix Composites

Magnesium-based metal matrix composites (MMCs) have high specific stiffness and strength both at room and elevated temperature, as well as improved damping capacity and wear resistance compared to the conventional alloys. The fabrication of MMCs has been considered as an approach to tailor the corrosion rate of Mg alloys with enhanced mechanical properties. Therefore, they have attracted considerable attention as high-performance structural materials for applications in the automotive and aerospace industries [195–197]. Nunez-Lopez et al. [198,199] have studied the corrosion behavior of Mg-Zn-Cu (ZC71)/SiC_P (silicon carbide particles) metal matrix composite in salt spray tests at 25 °C, particularly the micro-galvanic corrosion between the reinforcement and the matrix. Compared with conventional ZC71 alloy, the local penetration rate recorded for ZC71/SiC_P composites is about three times higher, which is due to the formation of less protective corrosion products. However, the maximum depth of corrosion attack in the salt spray test is the greatest for extruded ZC71 alloy, which is believed to be a result of the more uniform distribution of eutectic Mg(Zn, Cu)$_2$ phases in the composite. This uniform distribution is ascribed to the effective nucleation sites of SiC$_P$ for precipitation of eutectic Mg(Zn, Cu)$_2$ phases. Additionally, no galvanic corrosion is detected in the vicinity of the reinforcement particles. Difficulty in forming protective corrosion product layers on SiC$_P$/ZK80A and SiC$_P$/ZK60A composites has also been revealed by Zucchi et al. using electrochemical impedance spectroscopy [200]. Nevertheless, dense corrosion product (Mg(OH)$_2$) layers can be formed on the surfaces of calcium-polyphosphate-reinforced ZK60A composites [201]. Compared with the porous and plate-like crystalline morphology of the Mg(OH)$_2$ formed on the surface of conventional ZK60A alloy, dense and plate-like Mg(OH)$_2$ is formed on the surface of the composite. This dense layer significantly slows down the corrosion of the composite. Nieh et al. [202] have reported superplasticity of a ZK60A composite reinforced by 17 vol.% SiC particles, with an elongation to failure of up to 350% at a very high strain rate of about 1 s^{-1}, which is due to the refined grain size of about 0.5 μm. The presence of fine SiC particles contributes to the refinement and stabilization of the microstructure of the composites at elevated temperature. Hu et al. [203] have also fabricated ZK51A matrix composites reinforced by SiC whiskers (SiCw) using a two-step squeeze casting process. The modulus and mechanical strength increase compared with unreinforced ZK51A alloy. Particularly, the increase in 0.2% offset yield strength and modulus of the composite is linearly proportional to the volume fraction of SiCw in the range of 0–0.2, demonstrating the load transfer strengthening mechanism. The adjustment of mechanical properties and corrosion rates of MMCs by choosing appropriate composites, such as HA [204,205], β-tricalcium phosphate (β-TCP) [206], and poly-L-lactic acid (PLLA) [207], also confers great potential as biomaterial candidates on MMCs. Yu et al. [208] have investigated the in vitro and in vivo degradation behavior of β-$Ca_3(PO_4)_2$/Mg6Zn (wt.%) composites in SBF and rabbits, respectively. The corrosion rate of 10% β-$Ca_3(PO_4)_2$/Mg6Zn composites significantly decreases compared with Mg6Zn alloy fabricated with the same processing route. This is explained by the decomposition of β-$Ca_3(PO_4)_2$ that favored the formation of protective insoluble phosphates and carbonates on the composite surfaces during immersion. Furthermore, in vivo tests indicate that the composites improve the concrescence of pre-broken bone tissues and exhibit good biocompatibility with vital organs like the hearts, livers, and kidneys of rabbits, even in the presence of hydrogen bubbles.

4.1.2. Magnesium Bulk Metallic Glasses

Magnesium bulk metallic glasses (BMGs), especially Mg-Zn-Ca glassy alloys, have been extensively studied as biodegradable materials. Their single-phase and chemically homogenous microstructures are beneficial for the improvement of both corrosion resistance and mechanical properties of Mg alloys [209]. The specific strength of Mg-Zn-Ca alloy in glass state (250–300 MPa cm^3/g) can be about 40% higher than those of traditional crystalline Mg alloys (around 220 MPa cm^3/g for die-casting AZ91D alloy) [210]. Gu et al. [211] have assessed the corrosion behavior of Mg66Zn30Ca4 and Mg70Zn25Ca5 (both in at.%) BMGs, and have revealed that the corrosion rate decreases compared to some previously reported Mg alloys, such as as-cast AZ91 alloy and as-rolled pure Mg. This was attributed to the absence of secondary phases in BMGs, which can induce galvanic corrosion and the dense corrosion products containing zinc oxide/hydroxide forming on Mg-Zn-Ca BMGs. Due to the absence of crystal slip systems in Mg-Zn-Ca BGMs, the single-phase and chemically homogeneous nature also results in a three-times-higher compressive strength compared to as-rolled pure Mg. Moreover, the cytocompatibility is improved, and good adherence and growth of MG63 cells occur on the Mg-Zn-Ca BMGs surface. However, glassy Mg-Zn-Ca alloys are extraordinarily brittle at room temperature, and the fabrication of BMGs usually requires high-purity raw materials to guarantee glass-forming ability (GFA). Wang et al. [209] have successfully synthesized Mg69Zn27Ca4 (in at.%) glassy alloy reinforced by ductile Fe particles by using industrial raw metallic elements. The GFA decreases due to the addition of Fe with the formation of ductile α-Mg and dendrite MgZn phases. Nevertheless, the compressive strength and fracture strain are enhanced.

4.2. Microstructure Adjustment by Production Technique

4.2.1. Squeeze Casting

Squeeze casting is a metal fabrication process in which the solidification of molten metal is accelerated by applying high pressure. It combines permanent mold casting with die forging. Compared with conventional casting process, such as die-casting, gravity casting or sand casting, squeeze casting processing can produce Mg alloys with finer microstructure, less porosity, longer die-life, and reduced microshrinkage. These merits confer both better corrosion resistance and mechanical properties on alloys fabricated by squeeze casting [212,213]. Mo et al. [214] have compared the microstructures and mechanical properties of Mg12Zn4Al0.5Ca (in wt.%) alloys fabricated by gravity and squeeze casting. The applied pressure used during squeeze casting limits the formation of shrinkage porosity. The refined microstructure obtained during the squeeze-cast process contributes to improved mechanical properties of components compared to those produced by gravity casting. The influence of squeeze casting processing parameters, such as pouring temperature, applied pressure, and dwell time, has also been investigated. Increasing applied pressure and dwell time (just before the ending of solidification) refine microstructure and promote cast densification, which consequently improves the mechanical properties of the alloy. However, as pouring temperature increases, cast densification is promoted and grain size is coarsened, which leads first to an increase, then to a decrease of the mechanical properties. The study of Doležal et al. [215] on Mg3Zn2Ca (in wt.%) alloy has also confirmed the grain refinement and the enhanced mechanical properties of Mg-Zn alloys produced by squeeze casting compared with those produced by gravity casting. Moreover, subsequent aging treatment can further improve the ultimate tensile strength and elongation to fracture due to the homogenization of microstructure.

4.2.2. Twin-Roll Casting

Twin-roll casting (TRC) processing reduces several production steps compared to the conventional production techniques by combining casting and hot rolling into a single step. This reduces manufacturing costs for commercial weight-saving applications of wrought Mg alloys. It has been revealed that TRC processing can provide much faster solidification speed, refine gain size, homogenize the microstructure, and reduce, or even remove, segregation of alloying elements [216–220]. Moreover, the basal texture can be reduced when Mg alloys are fabricated by TRC processing compared to the strong basal texture developed in hot rolling. Little attention has been paid to the corrosion behavior of Mg alloys fabricated by twin-roll casting. Oktay et al. [221] have compared the corrosion behavior of AZ31 sheets produced by twin-roll casting and conventional direct chill casting + rolling in 0.01 M NaCl and 0.5 M Na_2SO_4 solutions. The higher solidification rate during twin-roll casting results in much smaller and more homogenously distributed secondary phases in the alloy, which contributes to a slightly higher corrosion resistance of TRC AZ31 alloy in both Na_2SO_4 and NaCl solutions. Mg alloys produced by TRC have comparable or better mechanical properties to those of Mg alloys sheets produced by conventional ingot casting and subsequent hot rolling, but a better combination of yield strength and fracture elongation [222,223]. Park et al. [224] have compared the high-temperature superplastic deformation behavior of TRC-prepared Mg6Zn1Mn1Al (ZMA611) (in wt.%) and ingot cast AZ31 alloys. The TRC ZMA611 alloy exhibits larger fracture elongation than ingot cast AZ31 alloy at all testing temperatures and strain rates, which is caused by the presence of thermally stable Al_8Mn_5 dispersoid particles. Hou et al. [225] have compared the degradability and mechanical integrity of a TRC Mg0.7Zn0.6Ca alloy (in wt.%) before and after annealing. The results show that the residual strain and deformation twins restored in the as-rolled alloy lead to a slightly higher corrosion rate than that of the annealed one. For both alloys, sufficient mechanical support still exists after immersion in α-MEM + 10 % FBS for up to 42 days, with a residual YS and UTS that are more than 85% those of the pristine states. With further minor (0.1 wt.%) addition of Zr [226,227], the sheet exhibits excellent stretch formability at room temperature, slow corrosion rate (<0.25 mm/year, determined by a neutral salt spray test at room temperature), and a widely adjustable strength level (YS = 130–260 MPa, UTS = 210–300 MPa), which shows great potential in applications as both structural and biomedical materials.

4.2.3. Rapid Solidification

Compared with conventional ingot metallurgy (I/M), rapid solidification (RS) processing confers better corrosion and mechanical properties to Mg parts due to the refinement of grain and precipitate sizes, the extended solid solubility of alloying elements, and the homogeneous microstructure [228,229]. Zhang et al. [111] have compared the corrosion resistance (Figure 11) and mechanical properties of Mg6Zn1Mn (in wt.%) alloy fabricated by conventional casting and rapid solidification. In comparison to the formation of coarse dendrite cells (about 200 μm) in as-cast Mg6Zn1Mn alloy, extremely small dendrites with an average size of about 25 μm are formed in rapid solidification. The refinement of the dendritic microstructure consequently decreases the corrosion rate of Mg6Zn1Mn alloy in 3.5 wt.% NaCl solution by approximately one order of magnitude, and increases the ultimate strength from 335 MPa to 460 MPa. Xu et al. [230] have studied the influence of solidification rate on the microstructure and corrosion resistance of Mg20Zn1Ca (in wt.%) alloy. They have found that the grain size and precipitate size decrease with increased cooling rate. A continuous 3D network of secondary phases is formed under a cooling rate of 3000 ºC/min. Moreover, as a result of fast cooling, the contents of Zn and Ca in the Mg matrix are much higher than their equilibrium solid solubility in Mg. The supersaturations of Zn and Ca elements and the dispersed alloying elements due to homogeneous microstructure enhance the corrosion resistance of Mg20Zn1Ca alloy in PBS solution.

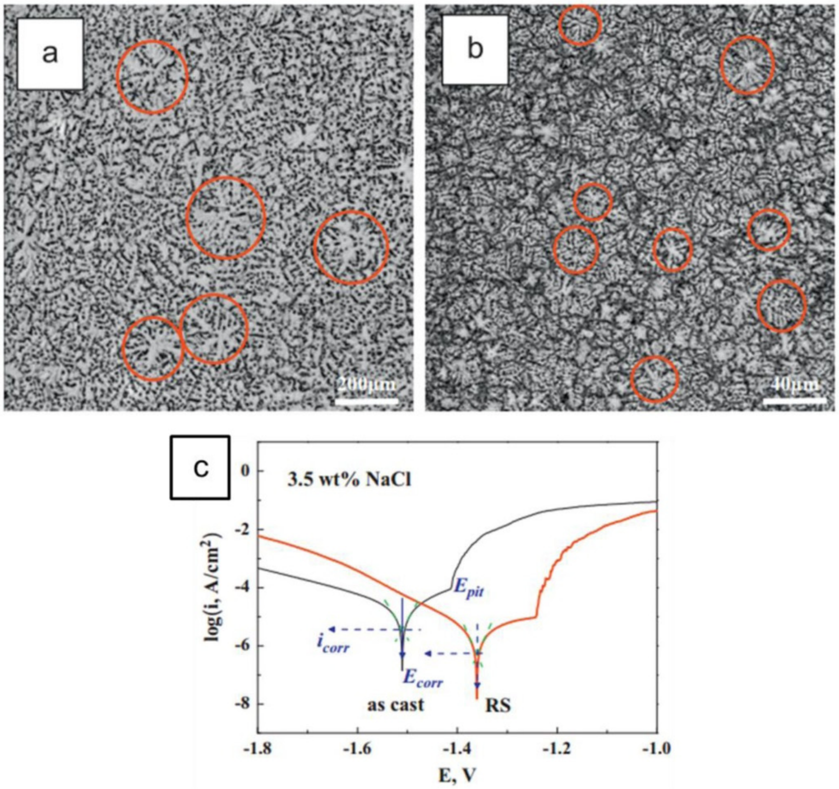

Figure 11. Comparison of the microstructure and corrosion behavior of Mg6Zn1Mn (in wt.%) alloy fabricated by conventional casting and rapid solidification. The microstructure of (**a**) as-cast and (**b**)

rapid solidification Mg6Zn1Mn alloys. (**c**) Potentiodynamic polarization curves of Mg6Zn1Mn alloy in 3.5% NaCl solution. [111] (with permission from Elsevier and Copyright Clearance Center).

4.3. Surface Treatments

Modification of the surface is another very popular strategy to improve the (corrosion) properties of Mg alloys in general and Mg-Zn based alloys in particular. However, the field is wide; here, it is only intended to give a short overview of the topic. For a deeper study of the topic, a range of reviews about surface treatments of Mg alloys are available [231–239].

There are a couple of different approaches and concepts to either improving the substrate by itself (e.g., surface alloying), to coating it with a more resistant material, and/or to separating the substrate material from the surrounding. However, no coating is perfect or will survive in service forever without defects. From this point of view, the substrate corrosion resistance is still an important factor. Good substrate corrosion resistance is a requirement for minimizing reactions at the interface when diffusion of ions and water through the layer or defects take place. The formation of corrosion products (mainly hydroxide formation) can cause severe volume increase and thus stresses at the interface, leading to blistering and flaking-off of the coatings. As-cast Mg-Zn based alloys are, from this point of view, not the best choice, but the newly developed wrought alloys with much lower Zn contents and additional micro-alloying elements (e.g., Ca, Zr, etc.) do offer substrates with good corrosion resistance and uniform corrosion without localized attack [147,226]. To guarantee good corrosion resistance, especially for wrought products, a sufficient cleaning (material removal) is the pre-requirement for any successful coating on Mg alloys. Removal of the undefined and contaminated surface oxide layer by etching has to be done, replacing it afterwards with a defined "passive" layer (conversion). The etching of Zn-rich alloys can result in Zn enrichment at the surface with problems to obtain such a uniform conversion layer. The latter is not a problem for most alloys with lower alloy content or the alloying elements in solid solution (Zn and other alloying elements <1 wt.% each).

After cleaning, depending on the application and the required properties, a wide set of treatments/coatings are available, ranging from metals to ceramics and polymers. To deposit them on Mg, a range of coating techniques is available:

- Chemical conversion coatings

- Chromates (restricted in use in most countries) [240]

- Chromate-free alternatives: Phosphate-permanganate, vanadates, molybdates, stannates, tungstates, fluorozirconate/titanate, and potassium-permanganate [241-252]

- Electro-chemical coatings

- Electroplating (Zn, Cu, Ni, Cr) [253-256]

- Anodizing [257,258]

- Plasma electrolytic oxidation (PEO) [259,260]

- Polymeric coatings/paints (e.g., Powder and E-Coat) and other non-metallic coatings (e.g., varnish, wax) [261–263]

- Physical techniques

- Physical vapor deposition [264-266]

- Plasma/laser surface treatments (alloying, cladding) [267-270]

- Thermal/plasma spraying [271]

Currently, the most industrially used processes for corrosion protection are conversion coatings in combination with paint or polymer top coats. The conversion treatment is the base for paint application, and should create a strong interface with good adhesion to the paint. There are chromate-free conversions available, and if more adhesion and better barrier properties are required, the chemical conversion layer can be replaced by anodizing/PEO coatings. The paint/polymer top coats can range from single- to multi-layer coatings according to the requirements of the applications and severity of the environment. Such combinations are sufficient for most of today's transport applications. The main challenge in coating development today is the integration of inhibitors into the coatings, offering release on demand, self-healing ability, and additional functionalities.

5. Applications of Mg-Zn Based Alloys

Mg-Zn based alloys have a long tradition in aerospace applications in helicopter, aircraft, and aeroengine components [272]. For example, ZE41 alloy is applied in the main transmission of Sikorsky UH60 Family (Blackhawk) and the turbofan of Pratt and Whitney Canada PW305. In addition, the tray of Rolls Royce is made from ELEKTRON ZRE1 alloy (Figure 12) [273]. In automotive applications, Mg4.2Zn1.2RE0.7Zr (ZE41A) and Mg6Zn2.7Cu0.25Mn (ZC63A) (both in wt.%) alloys have been used for functional prototypes due to the good pressure tightness of ZE41A alloy and the good elevated temperature properties of ZC63A alloy [274]. Moreover, ZK60 extruded at an extremely low extrusion rate is used for wheels and stems of racing cars and bicycles [275]. IMRA America Inc. [276] has developed a series of Mg8Zn5AlCa (in wt.%) alloys with a Ca content varying from 0.2 to 1.2 wt.% for automotive powertrain applications. The developed alloys showed a comparable or slightly better corrosion resistance than that of AZ91D alloy. The creep performance at 150 ºC and 35 MPa was decreased by almost one order of magnitude, while the tensile properties were comparable to or slightly better than those of AZ91D alloy. Volkswagen AG, Helmholtz-Zentrum Geesthacht, and Posco collaborated together to develop a new sheet alloy based on TRC Mg-Zn-Ca-Zr. The TRC Mg-Zn-Ca-Zr sheet reduced the forming temperatures from over 220 °C for a conventional AZ31 sheet to 160 °C, which means saving more energy and significantly simplified temperature control in a series-forming process. A tailgate was successfully produced as a demonstrator [227,277].

Figure 12. Tailgate for Volkswagen Passat utilizing a twin-roll-cast (TRC) Mg-Zn-Ca-Zr sheet [277] (pictures offered by Volkswagen. Copyright accessed).

Up to now, Mg-Zn based alloys have not been commercialized for clinical/medical applications, but a relatively high number of in vivo and in vitro studies have been carried out to investigate the feasibility of Mg-Zn based alloys as biomedical materials. He et al. [278,279] have comprehensively studied the in vitro and in vivo degradation behavior of extruded Mg6Zn (in wt.%) alloy. It exhibited better cell attachment, mineralization ability, and improved mRNA expression compared with PLLA. More importantly, considerable new bone formation is observed surrounding the implanted Mg6Zn alloy, and no adverse effect induced by hydrogen evolution is detected during the in vivo experiment. In addition, pathological analysis demonstrated that the in vivo degradation of Mg6Zn alloy did not harm the vital organs (heart, liver, kidney, and spleen) [278]. Guo et al. [60] have also studied the in vitro and in vivo histocompatibility of urinary implants made of Mg6Zn and pure Mg. The Mg6Zn alloy degrades faster than pure Mg in SBF, but exhibits better histocompatibility in the bladder compared to pure Mg after implantation for two weeks. Kraus et al. [280] have utilized online microfocus computed tomography (μCT) (Figure 13) to observe the interaction of implant and tissue performance by implanting Mg5Zn0.25Ca0.15Mn (in wt.%) pins into a growing rat skeleton. During degradation in a physiological environment, large amounts of Mg^{2+} are released into the surrounding tissue. As a result, magnesium hydroxide is formed, which consequently facilitates the accumulation of calcium phosphates and the formation of new bone around the implanted material. Although the Mg5Zn0.25Ca0.15Mn alloy starts to degrade immediately after the implantation and generates a massive volume of hydrogen gas (about 270 mm^3/d), the gas can be rapidly resorbed, and the bone recovers restitution after the complete degradation of the implanted pin. In addition, no inflammation is observed. These studies suggested that Mg-Zn based alloys have quite excellent in vivo biocompatibility and are promising candidates as biodegradable medical devices.

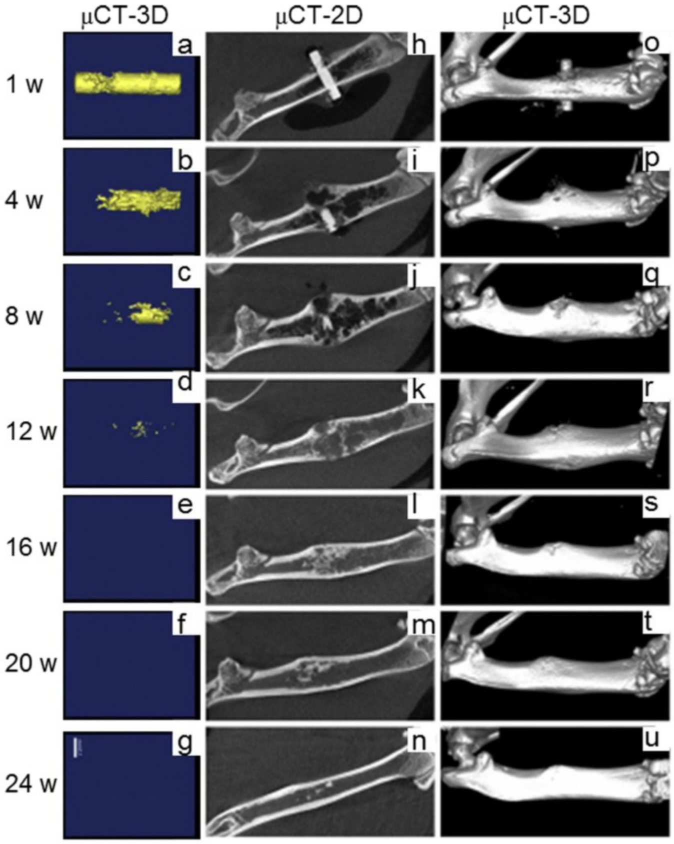

Figure 13. μCT reconstructions showing the degradation process of ZX50 pins and bone response [280]. (**a**-**g**) 3-D reconstruction of the degradation process of the pin, (**h**-**n**) 2-D slices of the degradation process of the pin and (**o**-**u**) 3-D displays of the bone response. The ZX50 pin fully degraded 12 weeks after implantation. The bone recovered restitution after the complete degradation of the implanted pin without observation of inflammation. (with permission from Elsevier and Copyright Clearance Center).

6. Summary

This review presents recent developments of Mg-Zn based alloys for both industrial and biomedical applications. Various attempts have been made to improve the corrosion resistance and mechanical properties of Mg-Zn based alloys, including alloying addition, processing, development of composites, etc. The new developments focus on wrought alloys rather than as-cast alloys.

Obvious composition–microstructure–properties relationships can be observed, especially for Mg-Zn-Y alloys. Some Mg-Zn based alloys show good potential for structural or biomedical applications—for example, Mg-Zn-Ca alloys as implants and new sheet materials for industrial wrought applications. On the other hand, inconsistent results between different studies can still be found, especially for the binary Mg-Zn system, which seems to offer no real potential for further developments. However, a good understanding of the binary Mg-Zn system is the basis for any further development of more complicated Mg-Zn-X alloys. Moreover, a satisfactory combination of high strength and good corrosion properties is difficult to be achieved, since more element addition usually results in a higher volume fraction of secondary phases, which is usually unfavorable for the corrosion performance. The combination of micro-alloying and wrought processing seems to be a promising way to solve this problem.

In summary, it can be stated that the current driving force for the development of Mg-Zn based alloys comes from two directions, both of which aim to prevent strong localized corrosion and to keep the corrosion rate of the alloy as low as possible. The first direction is the demand for new sheet material, mainly for industrial transport applications, and the second one is that of biomedical applications. Thus, the clear trend for the current ternary Mg-Zn-X and quaternary Mg-Zn-X-Y systems is to reduce the Zn content (less than 1 wt.%) and to improve strength by micro-alloying with ternary/quaternary alloying addition and wrought processing. In particular, the newly developed Mg-Zn-Ca-Zr sheet alloys [227,277] do have the potential to replace the currently most used AZ31 sheet alloys in many applications. To assure the biocompatibility and cytotoxicity, careful selection of bio-safe alloying elements and controlling of release rates of alloying elements within the safety range are of fundamental importance. However, more research is still needed for a better understanding of the Mg-Zn system and its interaction with other alloying elements to develop new Mg-Zn-X-Y alloys with better combinations of corrosion performance and mechanical properties.

Funding: This research was funded by China Scholarship Council (CSC), grant number 201606310043.

Acknowledgments: We would like to thank the China Scholarship Council (CSC) for a scholarship to Pingli Jiang (CSC No. 201606310043). The general discussion with colleagues in the department of Corrosion and Surface Technology, Helmholtz-Zentrum Geesthacht is also gratefully acknowledged.

Conflicts of Interest: The authors declare no conflict of interest. The funders had no role in the design of the study; in the collection, analyses, or interpretation of data; in the writing of the manuscript, or in the decision to publish the results.

Tables A1 and A2 can be found in the Appendix .

References

1. Song, G.L.; Atrens, A. Corrosion mechanisms of magnesium alloys. *Adv. Eng. Mater.* **1999**, *1*, 11–33.
2. Gusieva, K.; Davies, C.; Scully, J.; Birbilis, N. Corrosion of magnesium alloys: The role of alloying. *Int. Mater. Rev.* **2015**, *60*, 169–194.
3. Yang, Z.; Li, J.; Zhang, J.; Lorimer, G.; Robson, J. Review on research and development of magnesium alloys. *Acta Metall. Sin.* **2008**, *21*, 313–328.
4. Kulekci, M.K. Magnesium and its alloys applications in automotive industry. *Int. J. Adv. Manuf. Tech.* **2008**, *39*, 851–865.
5. Yin, P.; Li, N.F.; Lei, T.; Liu, L.; Ouyang, C. Effects of Ca on microstructure, mechanical and corrosion properties and biocompatibility of Mg–Zn–Ca alloys. *J. Mater. Sci. Mater. Med.* **2013**, *24*, 1365–1373.
6. Sun, Y.; Zhang, B.; Wang, Y.; Geng, L.; Jiao, X. Preparation and characterization of a new biomedical Mg–Zn–Ca alloy. *Mater. Des.* **2012**, *34*, 58–64.
7. Li, H.; Liu, D.; Zhao, Y.; Jin, F.; Chen, M. The influence of Zn content on the corrosion and wear performance of Mg-Zn-Ca alloy in simulated body fluid. *J. Mater. Eng. Perform.* **2016**, *25*, 3890–3895.
8. Li, N.; Zheng, Y. Novel magnesium alloys developed for biomedical application: A review. *J. Mater. Sci. Technol.* **2013**, *29*, 489–502.
9. Xin, Y.; Hu, T.; Chu, P. In vitro studies of biomedical magnesium alloys in a simulated physiological environment: A review. *Acta Biomater.* **2011**, *7*, 1452–1459.
10. Cai, S.; Lei, T.; Li, N.; Feng, F. Effects of Zn on microstructure, mechanical properties and corrosion behavior of Mg–Zn alloys. *Mater. Sci. Eng. C* **2012**, *32*, 2570–2577.
11. Bamberger, M.; Dehm, G. Trends in the development of new Mg alloys. *Annu. Rev. Mater. Res.* **2008**, *38*, 505–533.
12. Blum, W.; Zhang, P.; Watzinger, B.; Grossmann, B.; Haldenwanger, H. Comparative study of creep of the die-cast Mg-alloys AZ91, AS21, AS41, AM60 and AE42. *Mater. Sci. Eng. A* **2001**, *319*, 735–740.
13. Han, Q.; Kad¶, B.K.; Viswanathan, S. Design perspectives for creep-resistant magnesium die-casting alloys. *Philos. Mag.* **2004**, *84*, 3843–3860.
14. El-Rahman, S.S.A. Neuropathology of aluminum toxicity in rats (glutamate and GABA impairment). *Pharmacol. Res.* **2003**, *47*, 189–194.
15. Xia, X.; Davies, C.; Nie, J.; Birbilis, N. Influence of composition and processing on the corrosion of magnesium alloys containing binary and ternary additions of zinc and strontium. *Corrosion* **2014**, *71*, 38–49.
16. Geng, L.; Zhang, B.; Li, A.; Dong, C. Microstructure and mechanical properties of Mg–4.0Zn–0.5Ca alloy. *Mater. Lett.* **2009**, *63*, 557–559.
17. Haferkamp, H.; Bach, F.W.; Kaese, V.; Möhwald, K.; Niemeyer, M.; Schreckenberger, H.; Tai, P.T. Magnesium Corrosion–Processes, Protection of Anode and Cathode. In *Magnesium-alloys and technology*. Kainer, K., Ed. Wiley-VCH: Weiheim, Germany, 2003; pp. 226-241.
18. Mordike, B.; Lukác, P., Physical metallurgy. In *Magnesium technology: Metallurgy, design data, applications.* Friedrich, H.E.; Mordike, B., Eds. Springer: Berlin, Germany, 2006; pp. 76.
19. Shi, Z.-Z.; Zhang, W.-Z. Investigation on the microstructure of a τ-Mg32 (Al, Zn) 49 strengthened Mg–Zn–Al alloy with relatively low Zn content. *Phase Transitions* **2012**, *85*, 41–51.

20. Zhang, J.; Li, Z.-S.; Guo, Z.-X.; Pan, F.-S. Solidification microstructural constituent and its crystallographic morphology of permanent-mould-cast Mg-Zn-Al alloys. *T. Nonferr. Metal Soc.* **2006**, *16*, 452–458.
21. Tapiero, H.; Tew, K.D. Trace elements in human physiology and pathology: Zinc and metallothioneins. *Biomed. Pharmacother.* **2003**, *57*, 399–411.
22. Zhang, B.; Wang, Y.; Geng, L. Research on Mg-Zn-Ca alloy as degradable biomaterial. In *Biomaterials-Physics and Chemistry*. Pignatello, R., Ed. InTech: London, UK, 2011; pp. 183–204.
23. Zhang, B.; Hou, Y.; Wang, X.; Wang, Y.; Geng, L. Mechanical properties, degradation performance and cytotoxicity of Mg–Zn–Ca biomedical alloys with different compositions. *Mater. Sci. Eng. C* **2011**, *31*, 1667–1673.
24. Okamoto, H. Comment on Mg-Zn (magnesium-zinc). *J. Phase Equilib.* **1994**, *15*, 129–130.
25. Witte, F.; Hort, N.; Vogt, C.; Cohen, S.; Kainer, K.U.; Willumeit, R.; Feyerabend, F. Degradable biomaterials based on magnesium corrosion. *Curr. Opin. Solid State Mater. Sci.* **2008**, *12*, 63–72.
26. Somekawa, H.; Osawa, Y.; Mukai, T. Effect of solid-solution strengthening on fracture toughness in extruded Mg–Zn alloys. *Scripta Mater.* **2006**, *55*, 593–596.
27. Ohno, M.; Schmid-Fetzer, R. Mg-rich phase equilibria of Mg–Mn–Zn alloys analyzed by computational thermochemistry. *ZMetl* **2006**, *97*, 526–532.
28. Tsai, A.-P.; Murakami, Y.; Niikura, A. The Zn-Mg-Y phase diagram involving quasicrystals. *Philos. Mag. A* **2000**, *80*, 1043–1054.
29. Bhan, S.; Lal, A. The Mg-Zn-Zr system (magnesium-zinc-zirconium). *J. Phase Equilib.* **1993**, *14*, 634–637.
30. Higashi, I.; Shiotani, N.; Uda, M.; Mizoguchi, T.; Katoh, H. The crystal structure of Mg51Zn20. *J. Solid State Chem.* **1981**, *36*, 225–233.
31. Gao, X.; Nie, J. Structure and thermal stability of primary intermetallic particles in an Mg–Zn casting alloy. *Scripta Mater.* **2007**, *57*, 655–658.
32. Komura, Y.; Tokunaga, K. Structural studies of stacking variants in Mg-base Friauf–Laves phases. *Acta Crystallogr. Sect. B* **1980**, *36*, 1548–1554.
33. Samson, S. Die Kristallstruktur von Mg2Zn11-Isomorphie zwischen Mg2Zn11 und Mg2Cu6Al5. *Acta Chem. Scand.* **1949**, *3*, 835–843.
34. Gallot, J.; Graf, R. X-Ray Investigation of the Equilibrium Phase in a 60% Zinc Containing Magnesium-Zinc Alloy. *Comptes Rendus Acad. Sci.* **1966**, *262*, 1219–1222.
35. Chun, J.; Byrne, J. Precipitate strengthening mechanisms in magnesium zinc alloy single crystals *J. Mater. Sci. Mater. Med.* **1969**, *4*, 861–872.
36. Cáceres, C.; Blake, A. The Strength of Concentrated Mg–Zn Solid Solutions. *Phys. Status Solidi. A* **2002**, *194*, 147–158.
37. Clark, J. Transmission electron microscopy study of age hardening in a Mg-5 wt.% Zn alloy. *Acta Metall.* **1965**, *13*, 1281–1289.
38. Kirkland, N.T.; Staiger, M.P.; Nisbet, D.; Davies, C.H.; Birbilis, N.. Performance-driven design of biocompatible Mg alloys. *JOM* **2011**, *63*, 28–34.
39. Makar, G.; Kruger, J. Corrosion studies of rapidly solidified magnesium alloys. *J. Electrochem. Soc.* **1990**, *137*, 414–421.
40. Song, Y.; Han, E.-H.; Shan, D.; Yim, C.D.; You, B.S. The effect of Zn concentration on the corrosion behavior of Mg–xZn alloys. *Corros. Sci.* **2012**, *65*, 322–330.

41. Bakhsheshi-Rad, H.; Hamzah, E.; Fereidouni-Lotfabadi, A.; Daroonparvar, M.; Yajid, M.; Mezbahul-Islam, M.; Kasiri-Asgarani, M.; Medraj, M., 41.Microstructure and bio-corrosion behavior of Mg–Zn and Mg–Zn–Ca alloys for biomedical applications. *Mater. Corros.* **2014**, *65*, 1178–1187.

42. Kubasek, J.; Vojtech, D.; Pospisilova, I. Structural and corrosion characterization of biodegradable Mg-Zn alloy castings. *Kovove Mater.* **2012**, *50*, 415–424.

43. Lu, Y.; Bradshaw, A.; Chiu, Y.-L.; Jones, I. The role of β1′ precipitates in the bio-corrosion performance of Mg–3Zn in simulated body fluid. *J. Alloys Compd.* **2014**, *614*, 345–352.

44. Avedesian, M.M.; Baker, H. *ASM Speciality Handbook: Magnesium and Magnesium Alloys*; ASM International: Novelty, OH, USA, 1999; Volume 59, p. 60.

45. Gu, X.; Zheng, Y.; Cheng, Y.; Zhong, S.; Xi, T. In vitro corrosion and biocompatibility of binary magnesium alloys. *Biomaterials* **2009**, *30*, 484–498.

46. Koç, E.; Kannan, M.B.; Ünal, M.; Candan, E. Influence of zinc on the microstructure, mechanical properties and in vitro corrosion behavior of magnesium–zinc binary alloys. *J. Alloys Compd.* **2015**, *648*, 291–296.

47. Song, Y.; Han, E.-H.; Shan, D.; Yim, C.D.; You, B.S. The role of second phases in the corrosion behavior of Mg–5Zn alloy. *Corros. Sci.* **2012**, *60*, 238–245.

48. Bakhsheshi-Rad, H.; Hamzah, E.; Medraj, M.; Idris, M.; Lotfabadi, A.; Daroonparvar, M.; Yajid, M. Effect of heat treatment on the microstructure and corrosion behaviour of Mg–Zn alloys. *Mater. Corros.* **2014**, *65*, 999–1006.

49. Kubasek, J.; Vojtěch, D. Structural characteristics and corrosion behavior of biodegradable Mg–Zn, Mg–Zn–Gd alloys. *J. Mater. Sci. Mater. Med.* **2013**, *24*, 1615–1626.

50. Peng, Q.; Li, X.; Ma, N.; Liu, R.; Zhang, H. Effects of backward extrusion on mechanical and degradation properties of Mg–Zn biomaterial. *J. Mech. Behav. Biomed.* **2012**, *10*, 128–137.

51. Rosalbino, F.; De Negri, S.; Saccone, A.; Angelini, E.; Delfino, S. Bio-corrosion characterization of Mg–Zn–X (X= Ca, Mn, Si) alloys for biomedical applications. *J. Mater. Sci. Mater. Med.* **2010**, *21*, 1091–1098.

52. Zhang, E.; Yang, L. Microstructure, mechanical properties and bio-corrosion properties of Mg–Zn–Mn–Ca alloy for biomedical application. *Mater. Sci. Eng. A* **2008**, *497*, 111–118.

53. Zhang, E.; He, W.; Du, H.; Yang, K. Microstructure, mechanical properties and corrosion properties of Mg–Zn–Y alloys with low Zn content. *Mater. Sci. Eng. A* **2008**, *488*, 102–111.

54. Boehlert, C.; Knittel, K. The microstructure, tensile properties, and creep behavior of Mg–Zn alloys containing 0–4.4 wt.% Zn. *Mater. Sci. Eng. A* **2006**, *417*, 315–321.

55. Yan, Y.; Cao, H.; Kang, Y.; Yu, K.; Xiao, T.; Luo, J.; Deng, Y.; Fang, H.; Xiong, H.; Dai, Y. Effects of Zn concentration and heat treatment on the microstructure, mechanical properties and corrosion behavior of as-extruded Mg-Zn alloys produced by powder metallurgy. *J. Alloys Compd.* **2017**, *693*, 1277–1289.

56. Zhang, S.; Li, J.; Song, Y.; Zhao, C.; Zhang, X.; Xie, C.; Zhang, Y.; Tao, H.; He, Y.; Jiang, Y. In vitro degradation, hemolysis and MC3T3-E1 cell adhesion of biodegradable Mg–Zn alloy. *Mater. Sci. Eng. C* **2009**, *29*, 1907–1912.

57. Cao, F.; Shi, Z.; Song, G.-L.; Liu, M.; Atrens, A. Corrosion behaviour in salt spray and in 3.5% NaCl solution saturated with $Mg(OH)_2$ of as-cast and solution heat-treated binary Mg–X alloys: X= Mn, Sn, Ca, Zn, Al, Zr, Si, Sr. *Corros. Sci.* **2013**, *76*, 60–97.

58. Liu, X.-B.; Shan, D.-Y.; Song, Y.-W.; Han, E.-H. Effects of heat treatment on corrosion behaviors of Mg-3Zn magnesium alloy. *T. Nonferr. Metal Soc.* **2010**, *20*, 1345–1350.

59. Chen, X.-B.; Kirkland, N.; Krebs, H.; Thiriat, M.; Virtanen, S.; Nisbet, D.; Birbilis, N. In vitro corrosion survey of Mg–x Ca and Mg–3Zn–y Ca alloys with and without calcium phosphate conversion coatings. *Corros. Eng. Sci. Techn.* **2012**, *47*, 365–373.

60. Zhang, S.; Zheng, Y.; Zhang, L.; Bi, Y.; Li, J.; Liu, J.; Yu, Y.; Guo, H.; Li, Y. In vitro and in vivo corrosion and histocompatibility of pure Mg and a Mg-6Zn alloy as urinary implants in rat model. *Mater. Sci. Eng. C* **2016**, *68*, 414–422.

61. Ha, H.-Y.; Kang, J.-Y.; Yang, J.; Yim, C.D.; You, B.S. Limitations in the use of the potentiodynamic polarisation curves to investigate the effect of Zn on the corrosion behaviour of as-extruded Mg–Zn binary alloy. *Corros. Sci.* **2013**, *75*, 426–433.

62. Ralston, K.; Birbilis, N. Effect of grain size on corrosion: A review. *Corrosion* **2010**, *66*, 075005–075005-075013.

63. op't Hoog, C.; Birbilis, N.; Estrin, Y. Corrosion of pure Mg as a function of grain size and processing route. *Adv. Eng. Mater.* **2008**, *10*, 579–582.

64. Birbilis, N.; Zhang, M.X.; Estrin, Y. Surface grain size effects on the corrosion of magnesium. In *Key Engineering Materials*; Hoog, C.O.T., Birbilis, N., Zhang, M.X., Eds.; Trans Tech Publ.: Zürich, Switzerland, 2008; pp. 229–240.

65. Ambat, R.; Aung, N.N.; Zhou, W. Evaluation of microstructural effects on corrosion behaviour of AZ91D magnesium alloy. *Corros. Sci.* **2000**, *42*, 1433–1455.

66. Ben-Hamu, G.; Eliezer, D.; Shin, K.; Cohen, S. The relation between microstructure and corrosion behavior of Mg–Y–RE–Zr alloys. *J. Alloys Compd.* **2007**, *431*, 269–276.

67. Birbilis, N.; Ralston, K.; Virtanen, S.; Fraser, H.; Davies, C. Grain character influences on corrosion of ECAPed pure magnesium. *Corros. Eng. Sci. Techn.* **2010**, *45*, 224–230.

68. Zhao, M.-C.; Liu, M.; Song, G.; Atrens, A. Influence of the β-phase morphology on the corrosion of the Mg alloy AZ91. *Corros. Sci.* **2008**, *50*, 1939–1953.

69. Song, G.; Atrens, A.; Dargusch, M. Influence of microstructure on the corrosion of diecast AZ91D. *Corros. Sci.* **1998**, *41*, 249–273.

70. Lu, Y.; Bradshaw, A.; Chiu, Y.; Jones, I. Effects of secondary phase and grain size on the corrosion of biodegradable Mg–Zn–Ca alloys. *Mater. Sci. Eng. C* **2015**, *48*, 480–486.

71. Jeong, Y.; Kim, W. Enhancement of mechanical properties and corrosion resistance of Mg–Ca alloys through microstructural refinement by indirect extrusion. *Corros. Sci.* **2014**, *82*, 392–403.

72. Zhang, B.; Wang, Y.; Geng, L.; Lu, C. Effects of calcium on texture and mechanical properties of hot-extruded Mg–Zn–Ca alloys. *Mater. Sci. Eng. A* **2012**, *539*, 56–60.

73. Fang, D.; Li, X.; Li, H.; Peng, Q. Electrochemical corrosion behavior of backward extruded Mg-Zn-Ca alloys in different media. *Int. J. Electrochem. Sci* **2013**, *8*, 2551–2565.

74. Bohlen, J.; Nürnberg, M.R.; Senn, J.W.; Letzig, D.; Agnew, S.R. The texture and anisotropy of magnesium–zinc–rare earth alloy sheets. *Acta Mater.* **2007**, *55*, 2101–2112.

75. Zander, D.; Zumdick, N.A., Influence of Ca and Zn on the microstructure and corrosion of biodegradable Mg–Ca–Zn alloys. *Corros. Sci.* **2015**, *93*, 222–233.

76. Cha, P.-R.; Han, H.-S.; Yang, G.-F.; Kim, Y.-C.; Hong, K.-H.; Lee, S.-C.; Jung, J.-Y.; Ahn, J.-P.; Kim, Y.-Y.; Cho, S.-Y. Biodegradability engineering of biodegradable Mg alloys: Tailoring the electrochemical properties and microstructure of constituent phases. *Sci. Rep.* **2013**, *3*, 2367.

77. Südholz, A.; Kirkland, N.; Buchheit, R.; Birbilis, N. Electrochemical properties of intermetallic phases and common impurity elements in magnesium alloys, *Electrochem. Solid-State Lett.* **2011**, 14, C5–C7.

78. Gao, X.; Zhu, S.; Muddle, B.; Nie, J. Precipitation-hardened Mg–Ca–Zn alloys with superior creep resistance. *Scripta Mater.* **2005**, *53*, 1321–1326.
79. Oh, J.; Ohkubo, T.; Mukai, T.; Hono, K., TEM and 3DAP characterization of an age-hardened Mg–Ca–Zn alloy. *Scripta Mater.* **2005**, *53*, 675–679.
80. Liu, D.; Guo, C.; Chai, L.; Sherman, V.R.; Qin, X.; Ding, Y.; Meyers, M.A. Mechanical properties and corrosion resistance of hot extruded Mg–2.5 Zn–1Ca alloy. *Mater. Sci. Eng. B* **2015**, *195*, 50–58.
81. Chino, Y.; Kobata, M.; Iwasaki, H.; Mabuchi, M. Tensile properties from room temperature to 673 K of Mg-0.9 mass% Ca alloy containing lamella Mg2Ca. *Mater. Trans.* **2002**, *43*, 2643–2646.
82. Jang, Y.; Tan, Z.; Jurey, C.; Xu, Z.; Dong, Z.; Collins, B.; Yun, Y.; Sankar, J. Understanding corrosion behavior of Mg–Zn–Ca alloys from subcutaneous mouse model: Effect of Zn element concentration and plasma electrolytic oxidation. *Mater. Sci. Eng. C* **2015**, *48*, 28–40.
83. Shao, G.; Varsani, V.; Fan, Z. Thermodynamic modelling of the Y–Zn and Mg–Zn–Y systems. *Calphad* **2006**, *30*, 286–295.
84. Lee, J.Y.; Kim, D.H.; Lim, H.K.; Kim, D.H. Effects of Zn/Y ratio on microstructure and mechanical properties of Mg-Zn-Y alloys. *Mater. Lett.* **2005**, *59*, 3801–3805.
85. Nam, S.; Kim, W.; Kim, D.; Kim, T. Microstructure and corrosion behavior of rapidly solidified Mg-Zn-Y alloys. *Met. Mater. Int.* **2013**, *19*, 205–209.
86. Asgharzadeh, H.; Yoon, E.; Chae, H.; Kim, T.; Lee, J.; Kim, H. Microstructure and mechanical properties of a Mg–Zn–Y alloy produced by a powder metallurgy route. *J. Alloys Compd.* **2014,** 586, S95–S100.
87. Zhang, J.; Xu, J.; Cheng, W.; Chen, C.; Kang, J. Corrosion behavior of Mg–Zn–Y alloy with long-period stacking ordered structures. *J. Mater. Sci. Technol.* **2012**, *28*, 1157–1162.
88. Li, C.; Xu, D.; Zeng, Z.; Wang, B.; Sheng, L.; Chen, X.-B.; Han, E. Effect of volume fraction of LPSO phases on corrosion and mechanical properties of Mg-Zn-Y alloys. *Mater. Des.* **2017**, *121*, 430–441.
89. Zhao, X.; Shi, L.-l.; Xu, J. Mg–Zn–Y alloys with long-period stacking ordered structure: In vitro assessments of biodegradation behavior. *Mater. Sci. Eng. C* **2013**, *33*, 3627–3637.
90. Bae, D.; Lee, M.; Kim, K.; Kim, W.; Kim, D. Application of quasicrystalline particles as a strengthening phase in Mg–Zn–Y alloys. *J. Alloys Compd.* **2002**, *342*, 445–450.
91. Xu, D.; Han, E. Effects of icosahedral phase formation on the microstructure and mechanical improvement of Mg alloys: A review. *Progr. Nat. Sci.* **2012**, *22*, 364–385.
92. Singh, A.; Watanabe, M.; Kato, A.; Tsai, A. Microstructure and strength of quasicrystal containing extruded Mg–Zn–Y alloys for elevated temperature application. *Mater. Sci. Eng. A* **2004**, *385*, 382–396.
93. Bae, D.; Kim, S.; Kim, D.; Kim, W. Deformation behavior of Mg–Zn–Y alloys reinforced by icosahedral quasicrystalline particles. *Acta Mater.* **2002**, *50*, 2343–2356.
94. Chino, Y.; Sassa, K.; Mabuchi, M. Texture and stretch formability of a rolled Mg–Zn alloy containing dilute content of Y. *Mater. Sci. Eng. A* **2009**, *513*, 394–400.
95. Lu, F.; Ma, A.; Jiang, J.; Yang, D.; Zhou, Q. Review on long-period stacking-ordered structures in Mg-Zn-RE alloys. *Rare Metals* **2012**, *31*, 303–310.
96. Zhao, X.; Shi, L.-l.; Xu, J. Biodegradable Mg–Zn–Y alloys with long-period stacking ordered structure: Optimization for mechanical properties. *J. Mech. Behav. Biomed.* **2013**, *18*, 181–190.
97. Itoi, T.; Inazawa, T.; Yamasaki, M.; Kawamura, Y.; Hirohashi, M. Microstructure and mechanical properties of Mg--Zn--Y alloy sheet prepared by hot-rolling. *Mater. Sci. Eng. A* **2013**, *560*, 216–223.

98. Kawamura, Y.; Yamasaki, M. Formation and mechanical properties of Mg97Zn1RE2 alloys with long-period stacking ordered structure. *Mater. Trans.* **2007**, *48*, 2986–2992.

99. Yoshimoto, S.; Yamasaki, M.; Kawamura, Y. Microstructure and mechanical properties of extruded Mg-Zn-Y alloys with 14H long period ordered structure. *Mater. Trans.* **2006**, *47*, 959–965.

100. Chen, B.; Lin, D.; Zeng, X.; Lu, C. Effects of yttrium and zinc addition on the microstructure and mechanical properties of Mg–Y–Zn alloys. *J. Mater. Sci. Mater. Med.* **2010**, *45*, 2510–2517.

101. Itoi, T.; Suzuki, T.; Kawamura, Y.; Hirohashi, M. Microstructure and mechanical properties of Mg-Zn-Y rolled sheet with a Mg12ZnY phase. *Mater. Trans.* **2010**, *51*, 1536–1542.

102. Chen, B.; Lin, D.; Zeng, X.; Lu, C. Microstructure and mechanical properties of ultrafine grained Mg97Y2Zn1 alloy processed by equal channel angular pressing. *J. Alloys Compd.* **2007**, *440*, 94–100.

103. Kawamura, Y.; Hayashi, K.; Inoue, A.; Masumoto, T. Rapidly solidified powder metallurgy Mg97Zn1Y2Alloys with excellent tensile yield strength above 600 MPa. *Mater. Trans.* **2001**, *42*, 1172–1176.

104. Matsuda, M.; Ando, S.; Nishida, M. Dislocation structure in rapidly solidified Mg97Zn1Y2 alloy with long period stacking order phase. *Mater. Trans.* **2005**, *46*, 361–364.

105. Shao, X.; Yang, Z.; Ma, X. Strengthening and toughening mechanisms in Mg–Zn–Y alloy with a long period stacking ordered structure. *Acta Mater.* **2010**, *58*, 4760–4771.

106. Hagihara, K.; Yokotani, N.; Umakoshi, Y. Plastic deformation behavior of Mg12YZn with 18R long-period stacking ordered structure. *Intermetallics* **2010**, *18*, 267–276.

107. Mora, E.; Garcés, G.; Onorbe, E.; Pérez, P.; Adeva, P. High-strength Mg–Zn–Y alloys produced by powder metallurgy. *Scripta Mater.* **2009**, *60*, 776–779.

108. Lee, J.Y.; Lim, H.K.; Kim, D.H.; Kim, W.T.; Kim, D.H. Effect of volume fraction of qusicrystal on the mechanical properties of quasicrystal-reinforced Mg–Zn–Y alloys. *Mater. Sci. Eng. A* **2007**, *449*, 987–990.

109. Liu, D.-B.; Wu, B.; Wang, X.; Chen, M.-F. Corrosion and wear behavior of an Mg–2Zn–0.2 Mn alloy in simulated body fluid. *Rare Metals* **2015**, *34*, 553–559.

110. Yin, D.-s.; Zhang, E.-l.; Zeng, S.-y. Effect of Zn on mechanical property and corrosion property of extruded Mg-Zn-Mn alloy. *T. Nonferr. Metal Soc.* **2008**, *18*, 763–768.

111. Zhang, H.; Zhang, D.; Ma, C.; Guo, S. Improving mechanical properties and corrosion resistance of Mg-6Zn-Mn magnesium alloy by rapid solidification. *Mater. Lett.* **2013**, *92*, 45–48.

112. Rosalbino, F.; De Negri, S.; Scavino, G.; Saccone, A. Microstructure and in vitro degradation performance of Mg–Zn–Mn alloys for biomedical application. *J. Biomed. Mater. Res. A* **2013**, *101*, 704–711.

113. Abidin, N.I.Z.; Atrens, A.D.; Martin, D.; Atrens, A. Corrosion of high purity Mg, Mg2Zn0. 2Mn, ZE41 and AZ91 in Hank's solution at 37 °C. *Corros. Sci.* **2011**, *53*, 3542–3556.

114. Ben-Hamu, G.; Eliezer, D.; Shin, K. The role of Mg2Si on the corrosion behavior of wrought Mg–Zn–Mn alloy. *Intermetallics* **2008**, *16*, 860–867.

115. Lisitsyn, V.; Ben-Hamu, G.; Eliezer, D.; Shin, K. The role of Ca microalloying on the microstructure and corrosion behavior of Mg–6Zn–Mn–(0.5–2) Si alloys. *Corros. Sci.* **2009**, *51*, 776–784.

116. Lisitsyn, V.; Ben-Hamu, G.; Eliezer, D.; Shin, K. Some particularities of the corrosion behaviour of Mg–Zn–Mn–Si–Ca alloys in alkaline chloride solutions. *Corros. Sci.* **2010**, *52*, 2280–2290.

117. Dinodi, N.; Shetty, A.N. Electrochemical investigations on the corrosion behaviour of magnesium alloy ZE41 in a combined medium of chloride and sulphate. *J. Magnes. Alloy.* **2013**, *1*, 201–209.

118. Zhao, M.C.; Liu, M.; Song, G.-L.; Atrens, A. Influence of Microstructure on Corrosion of As-cast ZE41. *Adv. Eng. Mater.* **2008**, *10*, 104–111.

119. Zhao, M.-C.; Liu, M.; Song, G.-L.; Atrens, A. Influence of pH and chloride ion concentration on the corrosion of Mg alloy ZE41. *Corros. Sci.* **2008**, *50*, 3168–3178.

120. Kannan, M.B.; Blawert, C.; Dietzel, W. Electrochemical corrosion behaviour of ZE41 and QE22 magnesium alloys. In *Materials Science Forum*; Dieringa, H., Hort, N., Kainer, K.U., Eds.; Trans Tech Publ.: Zürich, Switzerland, 2011; pp. 385–388.

121. Neil, W.; Forsyth, M.; Howlett, P.; Hutchinson, C.; Hinton, B. Corrosion of magnesium alloy ZE41−The role of microstructural features. *Corros. Sci.* **2009**, *51*, 387–394.

122. Neil, W.; Forsyth, M.; Howlett, P.; Hutchinson, C.; Hinton, B. Corrosion of heat treated magnesium alloy ZE41. *Corros. Sci.* **2011**, *53*, 3299–3308.

123. Coy, A.; Viejo, F.; Skeldon, P.; Thompson, G. Susceptibility of rare-earth-magnesium alloys to micro-galvanic corrosion. *Corros. Sci.* **2010**, *52*, 3896–3906.

124. Jamesh, M.I.; Wu, G.; Zhao, Y.; McKenzie, D.R.; Bilek, M.M.; Chu, P.K. Electrochemical corrosion behavior of biodegradable Mg–Y–RE and Mg–Zn–Zr alloys in Ringer's solution and simulated body fluid. *Corros. Sci.* **2015**, *91*, 160–184.

125. Huan, Z.; Leeflang, M.; Zhou, J.; Fratila-Apachitei, L.; Duszczyk, J. In vitro degradation behavior and cytocompatibility of Mg–Zn–Zr alloys. *J. Mater. Sci. Mater. Med.* **2010**, *21*, 2623–2635.

126. Gu, X.; Li, N.; Zheng, Y.; Ruan, L. In vitro degradation performance and biological response of a Mg–Zn–Zr alloy. *Mater. Sci. Eng. B* **2011**, *176*, 1778–1784.

127. Witte, F.; Kaese, V.; Haferkamp, H.; Switzer, E.; Meyer-Lindenberg, A.; Wirth, C.; Windhagen, H. In vivo corrosion of four magnesium alloys and the associated bone response. *Biomaterials* **2005**, *26*, 3557–3563.

128. Gao, J.-C.; Sha, W.; Qiao, L.-Y.; Yong, W. Corrosion behavior of Mg and Mg-Zn alloys in simulated body fluid. *T. Nonferr. Metal Soc.* **2008**, *18*, 588–592.

129. Chang, J.-W.; Duo, J.; Xiang, Y.-Z.; Yang, H.-Y.; Ding, W.-J.; Peng, Y.-H. Influence of Nd and Y additions on the corrosion behaviour of extruded Mg-Zn-Zr alloys. *Int. J. Min. Metal Mater.* **2011**, *18*, 203.

130. Campos, M.D.R.S.; del Rosario, M. *The Role of Intermetallic Phases in the Corrosion of Magnesium-Rare Earth Alloys*; Technische Universität Hamburg-Harburg: Hamburg, Germany, 2016.

131. Liu, L.; Chen, X.; Pan, F.; Wang, Z.; Liu, W.; Cao, P.; Yan, T.; Xu, X., Effect of Y and Ce additions on microstructure and mechanical properties of Mg–Zn–Zr alloys, *Mater. Sci. Eng. A* **2015**, *644*, 247–253.

132. Wu, W.; Wang, Y.; Zeng, X.; Chen, L.; Liu, Z. Effect of neodymium on mechanical behavior of Mg-Zn-Zr magnesium alloy. *J. Mater. Sci. Lett.* **2003**, *22*, 445–447.

133. Yu, H.; Hongge, Y.; Jihua, C.; Bin, S.; Yi, Z.; Yanjin, S.; Zhaojie, M. Effects of minor Gd addition on microstructures and mechanical properties of the high strain-rate rolled Mg–Zn–Zr alloys. *J. Alloys Compd.* **2014**, *586*, 757–765.

134. Wang, J.; Song, P.; Gao, S.; Wei, Y.; Pan, F. Influence of Y on the phase composition and mechanical properties of as-extruded Mg–Zn–Y–Zr magnesium alloys. *J. Mater. Sci. Mater. Med.* **2012**, *47*, 2005–2010.

135. He, S.; Peng, L.; Zeng, X.; Ding, W.; Zhu, Y. Comparison of the microstructure and mechanical properties of a ZK60 alloy with and without 1.3 wt.% gadolinium addition. *Mater. Sci. Eng. A* **2006**, *433*, 175–181.

136. Li, Q.; Wang, Q.; Wang, Y.; Zeng, X.; Ding, W. Effect of Nd and Y addition on microstructure and mechanical properties of as-cast Mg–Zn–Zr alloy. *J. Alloys Compd.* **2007**, *427*, 115–123.

137. Liu, Y.; Yuan, G.; Zhang, S.; Zhang, X.; Lu, C.; Ding, W. Effects of Zn/Gd ratio and content of Zn, Gd on phase constitutions of Mg alloys. *Mater. Trans.* **2008**, *49*, 941–944.

138. Yang, J.; Xiao, W.; Wang, L.; Wu, Y.; Wang, L.; Zhang, H. Influences of Gd on the microstructure and strength of Mg–4.5 Zn alloy. *Mater. Charact.* **2008**, *59*, 1667–1674.

139. Yang, J.; Wang, L.; Wang, L.; Zhang, H. Microstructures and mechanical properties of the Mg–4.5 Zn–xGd (x= 0, 2, 3 and 5) alloys. *J. Alloys Compd.* **2008**, *459*, 274–280.

140. Li, H.; Peng, Q.; Li, X.; Li, K.; Han, Z.; Fang, D. Microstructures, mechanical and cytocompatibility of degradable Mg–Zn based orthopedic biomaterials. *Mater. Des.* **2014**, *58*, 43–51.

141. Lai, H.; Li, J.; Li, J.; Zhang, Y.; Xu, Y. Effects of Sr on the microstructure, mechanical properties and corrosion behavior of Mg-2Zn-xSr alloys. *J. Mater. Sci. Mater. Med.* **2018**, *29*, 87.

142. Guan, R.-G.; Cipriano, A.F.; Zhao, Z.-Y.; Lock, J.; Tie, D.; Zhao, T.; Cui, T.; Liu, H. Development and evaluation of a magnesium–zinc–strontium alloy for biomedical applications—Alloy processing, microstructure, mechanical properties, and biodegradation. *Mater. Sci. Eng. C* **2013**, *33*, 3661–3669.

143. Brar, H.S.; Wong, J.; Manuel, M.V. Investigation of the mechanical and degradation properties of Mg–Sr and Mg–Zn–Sr alloys for use as potential biodegradable implant materials. *J. Mech. Behav. Biomed.* **2012**, *7*, 87–95.

144. Ben-Hamu, G.; Eliezer, D.; Kaya, A.; Na, Y.; Shin, K. Microstructure and corrosion behavior of Mg–Zn–Ag alloys. *Mater. Sci. Eng. A* **2006**, *435*, 579–587.

145. Lotfpour, M.; Emamy, M.; Dehghanian, C.; Tavighi, K. Influence of Cu addition on the structure, mechanical and corrosion properties of Cast Mg-2% Zn alloy. *J. Mater. Eng. Perform.* **2017**, *26*, 2136–2150.

146. Liu, R.; Zeng, Z.; Scully, J.; Williams, G.; Birbilis, N. Simultaneously improving the corrosion resistance and strength of magnesium via low levels of Zn and Ge additions. *Corros. Sci.* **2018**, *140*, 18–29.

147. Jiang, P.; Blawert, C.; Hou, R.; Scharnagl, N.; Bohlen, J.; Zheludkevich, M.L. Microstructural influence on corrosion behavior of MgZnGe alloy in NaCl solution. *J. Alloys Compd.* **2019**, *783*, 179–192.

148. Johnston, S.; Shi, Z.; Atrens, A. The influence of pH on the corrosion rate of high-purity Mg, AZ91 and ZE41 in bicarbonate buffered Hanks' solution. *Corros. Sci.* **2015**, *101*, 182–192.

149. Taltavull, C.; Shi, Z.; Torres, B.; Rams, J.; Atrens, A. Influence of the chloride ion concentration on the corrosion of high-purity Mg, ZE41 and AZ91 in buffered Hank's solution. *J. Mater. Sci. Mater. Med.* **2014**, *25*, 329–345.

150. Dinodi, N.; Shetty, A.N. Investigation of influence of medium ph and sulfate ion concentrations on corrosion behavior of magnesium alloy ZE41. *Surf. Eng. Appl. Elect.* **2014**, *50*, 149–156.

151. Natarajan, S.; Ravikiran, V. Evaluation of electrochemical and surface characteristics of conversion coatings on ZM21 magnesium alloy. *Surf. Eng.* **2006**, *22*, 287–293.

152. Martin, H.J.; Horstemeyer, M.; Wang, P.T. Comparison of corrosion pitting under immersion and salt-spray environments on an as-cast AE44 magnesium alloy. *Corros. Sci.* **2010**, *52*, 3624–3638.

153. Song, W.; Martin, H.J.; Hicks, A.; Seely, D.; Walton, C.A.; Lawrimore II, W.B.; Wang, P.T.; Horstemeyer, M. Corrosion behaviour of extruded AM30 magnesium alloy under salt-spray and immersion environments. *Corros. Sci.* **2014**, *78*, 353–368.

154. Walton, C.A.; Martin, H.J.; Horstemeyer, M.; Wang, P.T. Quantification of corrosion mechanisms under immersion and salt-spray environments on an extruded AZ31 magnesium alloy. *Corros. Sci.* **2012**, *56*, 194–208.

155. Zhao, M.-C.; Schmutz, P.; Brunner, S.; Liu, M.; Song, G.-l.; Atrens, A. An exploratory study of the corrosion of Mg alloys during interrupted salt spray testing. *Corros. Sci.* **2009**, *51*, 1277–1292.

156. Gonzalez, J.; Hou, R.Q.; Nidadavolu, E.P.; Willumeit-Römer, R.; Feyerabend, F. Magnesium degradation under physiological conditions–Best practice. *Bioact. Mater.* **2018**, *3*, 174–185.

157. Walker, J.; Shadanbaz, S.; Kirkland, N.T.; Stace, E.; Woodfield, T.; Staiger, M.P.; Dias, G.J. Magnesium alloys: Predicting in vivo corrosion with in vitro immersion testing. *J. Biomed. Mater. Res. B Appl. Biomater.* **2012**, *100*, 1134–1141.

158. Hänzi, A.C.; Gerber, I.; Schinhammer, M.; Löffler, J.F.; Uggowitzer, P.J. On the in vitro and in vivo degradation performance and biological response of new biodegradable Mg–Y–Zn alloys. *Acta Biomater.* **2010**, *6*, 1824–1833.

159. Sanchez, A.H.M.; Luthringer, B.J.; Feyerabend, F.; Willumeit, R. Mg and Mg alloys: How comparable are in vitro and in vivo corrosion rates? A review. *Acta Biomater.* **2015**, *13*, 16–31.

160. Zhang, S.; Zhang, X.; Zhao, C.; Li, J.; Song, Y.; Xie, C.; Tao, H.; Zhang, Y.; He, Y.; Jiang, Y. Research on an Mg–Zn alloy as a degradable biomaterial. *Acta Biomater.* **2010**, *6*, 626–640.

161. Seuss, F.; Seuss, S.; Turhan, M.; Fabry, B.; Virtanen, S. Corrosion of Mg alloy AZ91D in the presence of living cells. *J. Biomed. Mater. Res. B Appl. Biomater.* **2011**, *99*, 276–281.

162. Hou, R.; Willumeit-Römer, R.; Garamus, V.M.; Frant, M.; Koll, J.; Feyerabend, F. Adsorption of Proteins on Degradable Magnesium-Which Factors are Relevant? *ACS Appl. Mater. Inter.* **2018**, *10*, 42175–42185.

163. Willumeit, R.; Fischer, J.; Feyerabend, F.; Hort, N.; Bismayer, U.; Heidrich, S.; Mihailova, B. Chemical surface alteration of biodegradable magnesium exposed to corrosion media. *Acta Biomater.* **2011**, *7*, 2704–2715.

164. Yamamoto, A.; Hiromoto, S. Effect of inorganic salts, amino acids and proteins on the degradation of pure magnesium in vitro. *Mater. Sci. Eng. C* **2009**, *29*, 1559–1568.

165. Raman, R.S.; Jafari, S.; Harandi, S.E. Corrosion fatigue fracture of magnesium alloys in bioimplant applications: A review. *Eng. Fract. Mech.* **2015**, *137*, 97–108.

166. Gu, X.; Zhou, W.; Zheng, Y.; Cheng, Y.; Wei, S.; Zhong, S.; Xi, T.; Chen, L. Corrosion fatigue behaviors of two biomedical Mg alloys–AZ91D and WE43–in simulated body fluid. *Acta Biomater.* **2010**, *6*, 4605–4613.

167. Bian, D.; Zhou, W.; Liu, Y.; Li, N.; Zheng, Y.; Sun, Z. Fatigue behaviors of HP-Mg, Mg–Ca and Mg–Zn–Ca biodegradable metals in air and simulated body fluid. *Acta Biomater.* **2016**, *41*, 351–360.

168. Shi, Z.; Hofstetter, J.; Cao, F.; Uggowitzer, P.J.; Dargusch, M.S.; Atrens, A. Corrosion and stress corrosion cracking of ultra-high-purity Mg5Zn. *Corros. Sci.* **2015**, *93*, 330–335.

169. Choudhary, L.; Raman, R.S. Mechanical integrity of magnesium alloys in a physiological environment: Slow strain rate testing based study. *Eng. Fract. Mech.* **2013**, *103*, 94–102.

170. Winzer, N.; Atrens, A.; Dietzel, W.; Song, G.; Kainer, K. Stress corrosion cracking in magnesium alloys: Characterization and prevention. *JOM* **2007**, *59*, 49–53.

171. Prabhu, D.B.; Dhamotharan, S.; Kumar, G.S.; Gopalakrishnan, P.; Ravi, K. Stress corrosion cracking of biodegradable Mg-4Zn alloy in simulated body fluid at different strain rates-a fractographic investigation. *Mater. Sci. Eng. A* **2018.**

172. Jafari, S.; Raman, R.S.; Davies, C.H. Stress corrosion cracking of an extruded magnesium alloy (ZK21) in a simulated body fluid. *Eng. Fract. Mech.* **2018**, *201*, 47–55.

173. Yuan, G.; Liu, Y.; Ding, W.; Lu, C. Effects of extrusion on the microstructure and mechanical properties of Mg–Zn–Gd alloy reinforced with quasicrystalline particles. *Mater. Sci. Eng. A* **2008**, *474*, 348–354.

174. Shi, Z.; Song, G.; Atrens, A. Corrosion resistance of anodised single-phase Mg alloys. *Surf. Coat. Tech.* **2006**, *201*, 492–503.

175. Zhang, J.; Ma, Q.; Pan, F. Effects of trace Er addition on the microstructure and mechanical properties of Mg–Zn–Zr alloy. *Mater. Des.* **2010**, *31*, 4043–4049.

176. Ibrahim, H.; Klarner, A.D.; Poorganji, B.; Dean, D.; Luo, A.A.; Elahinia, M. Microstructural, mechanical and corrosion characteristics of heat-treated Mg-1.2 Zn-0.5 Ca (wt%) alloy for use as resorbable bone fixation material. *J. Mech. Behav. Biomed.* **2017**, *69*, 203–212.

177. Xu, D.; Han, E.-H.; Liu, L.; Xu, Y. Influence of higher Zn/Y ratio on the microstructure and mechanical properties of Mg-Zn-Y-Zr alloys, *Metall. Mater. Trans. A* **2009**, *40*, 1727–1740.

178. Singh, A.; Somekawa, H.; Mukai, T., Compressive strength and yield asymmetry in extruded Mg–Zn–Ho alloys containing quasicrystal phase. *Scripta Mater.* **2007**, *56*, 935–938.

179. Park, S.H.; You, B.S.; Mishra, R.K.; Sachdev, A.K. Effects of extrusion parameters on the microstructure and mechanical properties of Mg–Zn–(Mn)–Ce/Gd alloys. *Mater. Sci. Eng. A* **2014**, *598*, 396–406.

180. Zeng, X.; Zhang, Y.; Lu, C.; Ding, W.; Wang, Y.; Zhu, Y. Precipitation behavior and mechanical properties of a Mg–Zn–Y–Zr alloy processed by thermo-mechanical treatment. *J. Alloys Compd.* **2005**, *395*, 213–219.

181. Kim, I.; Bae, D.; Kim, D. Precipitates in a Mg–Zn–Y alloy reinforced by an icosahedral quasicrystalline phase. *Mater. Sci. Eng. A* **2003**, *359*, 313–318.

182. Mackenzie, L.; Davis, B.; Humphreys, F.; Lorimer, G. The deformation, recrystallisation and texture of three magnesium alloy extrusions. *Mater. Sci. Technol.* **2007**, *23*, 1173–1180.

183. Agnew, S.; Horton, J.; Lillo, T.; Brown, D. Enhanced ductility in strongly textured magnesium produced by equal channel angular processing. *Scripta Mater.* **2004**, *50*, 377–381.

184. Chino, Y.; Lee, J.-S.; Sassa, K.; Kamiya, A.; Mabuchi, M. Press formability of a rolled AZ31 Mg alloy sheet with controlled texture. *Mater. Lett.* **2006**, *60*, 173–176.

185. Yan, H.; Chen, R.; Han, E. Room-temperature ductility and anisotropy of two rolled Mg–Zn–Gd alloys. *Mater. Sci. Eng. A* **2010**, *527*, 3317–3322.

186. Lee, J.-Y.; Yun, Y.-S.; Suh, B.-C.; Kim, N.-J.; Kim, W.-T.; Kim, D.-H. Comparison of static recrystallization behavior in hot rolled Mg–3Al–1Zn and Mg–3Zn–0.5 Ca sheets. *J. Alloys Compd.* **2014**, *589*, 240–246.

187. Nayak, S.; Bhushan, B.; Jayaganthan, R.; Gopinath, P.; Agarwal, R.; Lahiri, D. Strengthening of Mg based alloy through grain refinement for orthopaedic application. *J. Mech. Behav. Biomed.* **2016**, *59*, 57–70.

188. Jiang, J.; Aibin, M.; Saito, N.; Zhixin, S.; Dan, S.; Fumin, L.; Nishida, Y.; Donghui, Y.; Pinghua, L. Improving corrosion resistance of RE-containing magnesium alloy ZE41A through ECAP. *J. Rare Earth.* **2009**, *27*, 848–852.

189. Mostaed, E.; Hashempour, M.; Fabrizi, A.; Dellasega, D.; Bestetti, M.; Bonollo, F.; Vedani, M. Microstructure, texture evolution, mechanical properties and corrosion behavior of ECAP processed ZK60 magnesium alloy for biodegradable applications. *J. Mech. Behav. Biomed.* **2014**, *37*, 307–322.

190. Zheng, M.Y.; Xu, S.W.; Qiao, X.G.; Gan, W.M.; Wu, K.; Kamado, S.; Kojima, Y.; Brokmeier, H.G. Equal channel angular pressing of magnesium alloy containing quasicrystal phase. In *Materials Science Forum*; Horita, Z., Ed.; Trans Tech Publ.: Zürich, Switzerland, 2006; pp. 527–532.

191. Mostaed, E.; Vedani, M.; Hashempour, M.; Bestetti, M. Influence of ECAP process on mechanical and corrosion properties of pure Mg and ZK60 magnesium alloy for biodegradable stent applications. *Biomaterials* **2014,** 4, e28283.

192. Tong, L.; Zheng, M.; Chang, H.; Hu, X.; Wu, K.; Xu, S.; Kamado, S.; Kojima, Y. Microstructure and mechanical properties of Mg–Zn–Ca alloy processed by equal channel angular pressing. *Mater. Sci. Eng. A* **2009**, *523*, 289–294.

193. Tong, L.; Zheng, M.; Hu, X.; Wu, K.; Xu, S.; Kamado, S.; Kojima, Y. Influence of ECAP routes on microstructure and mechanical properties of Mg–Zn–Ca alloy. *Mater. Sci. Eng. A* **2010**, *527*, 4250–4256.

194. Stolyarov, V.V.; Zhu, Y.T.; Alexandrov, I.V.; Lowe, T.C.; Valiev, R.Z. Influence of ECAP routes on the microstructure and properties of pure Ti. *Mater. Sci. Eng. A* **2001**, *299*, 59–67.

195. Witte, F.; Feyerabend, F.; Maier, P.; Fischer, J.; Störmer, M.; Blawert, C.; Dietzel, W.; Hort, N. Biodegradable magnesium–hydroxyapatite metal matrix composites. *Biomaterials* **2007**, *28*, 2163–2174.

196. Poddar, P.; Srivastava, V.; De, P.; Sahoo, K. Processing and mechanical properties of SiC reinforced cast magnesium matrix composites by stir casting process. *Mater. Sci. Eng. A* **2007**, *460*, 357–364.

197. Saravanan, R.; Surappa, M. Fabrication and characterisation of pure magnesium-30 vol.% SiCP particle composite. *Mater. Sci. Eng. A* **2000**, *276*, 108–116.

198. Nunez-Lopez, C.; Skeldon, P.; Thompson, G.; Lyon, P.; Karimzadeh, H.; Wilks, T. The corrosion behaviour of Mg alloy ZC71/SiCp metal matrix composite. *Corros. Sci.* **1995**, *37*, 689–708.

199. Nunez-Lopez, C.; Habazaki, H.; Skeldon, P.; Thompson, G.; Karimzadeh, H.; Lyon, P.; Wilks, T. An investigation of microgalvanic corrosion using a model magnesium-silicon carbide metal matrix composite. *Corros. Sci.* **1996**, *38*, 1721–1729.

200. Zucchi, F.; Trabanelli, G.; Grassi, V.; Frignani, A. Corrosion behavior in sodium sulfate and sodium chloride solutions of SiCp reinforced magnesium alloy metal matrix composites. *Corrosion* **2004**, *60*, 362–368.

201. Feng, A.; Han, Y. Mechanical and in vitro degradation behavior of ultrafine calcium polyphosphate reinforced magnesium-alloy composites. *Mater. Des.* **2011**, *32*, 2813–2820.

202. Nieh, T.; Schwartz, A.; Wadsworth, J. Superplasticity in a 17 vol.% SiC particulate-reinforced ZK60A magnesium composite (ZK60/SiC/17p). *Mater. Sci. Eng. A* **1996**, *208*, 30–36.

203. Lianxi, H.; Erde, W. Fabrication and mechanical properties of SiCw/ZK51A magnesium matrix composite by two-step squeeze casting. *Mater. Sci. Eng. A* **2000**, *278*, 267–271.

204. Liu, D.-B.; Chen, M.-F.; Ye, X.-Y. Fabrication and corrosion behavior of HA/Mg-Zn biocomposites. *Front. Mater. Sci.* **2010**, *4*, 139–144.

205. Ye, X.; Chen, M.; Yang, M.; Wei, J.; Liu, D. In vitro corrosion resistance and cytocompatibility of nano-hydroxyapatite reinforced Mg–Zn–Zr composites. *J. Mater. Sci. Mater. Med.* **2010**, *21*, 1321–1328.

206. He, S.-Y.; Yue, S.; Chen, M.-F.; Liu, D.-B.; Ye, X.-Y. Microstructure and properties of biodegradable β-TCP reinforced Mg-Zn-Zr composites. *T. Nonferr. Metal Soc.* **2011**, *21*, 814–819.

207. Cifuentes, S.C.; Frutos, E.; González-Carrasco, J.L.; Muñoz, M.; Multigner, M.; Chao, J.; Benavente, R.; Lieblich, M. Novel PLLA/magnesium composite for orthopedic applications: A proof of concept. *Mater. Lett.* **2012**, *74*, 239–242.

208. Yu, K.; Chen, L.; Zhao, J.; Li, S.; Dai, Y.; Huang, Q.; Yu, Z. In vitro corrosion behavior and in vivo biodegradation of biomedical β-$Ca_3(PO_4)_2$/Mg–Zn composites, *Acta Biomater.* **2012**, *8*, 2845–2855.

209. Wang, J.; Huang, S.; Wei, Y.; Guo, S.; Fusheng, P. Enhanced mechanical properties and corrosion resistance of a Mg–Zn–Ca bulk metallic glass composite by Fe particle addition. *Mater. Lett.* **2013**, *91*, 311–314.

210. Gu, X.; Shiflet, G.; Guo, F.; Poon, S. Mg–Ca–Zn bulk metallic glasses with high strength and significant ductility. *J. Mater. Res.* **2005**, *20*, 1935–1938.

211. Gu, X.; Zheng, Y.; Zhong, S.; Xi, T.; Wang, J.; Wang, W. Corrosion of, and cellular responses to Mg–Zn–Ca bulk metallic glasses. *Biomaterials* **2010**, *31*, 1093–1103.

212. Kamado, S.; Ikeya, N.; Rudi, R.S.; Araki, T.; Kojima, Y. Application of semi-solid forming to Mg-Zn-Al-Ca alloys. In *Materials Science Forum*; Kojima, Y., Aizawa, T., Kamado, S., Eds.; Trans Tech Publ.: Zürich, Switzerland, 2000; pp. 205–214.

213. Blawert, C.; Morales, E.D.; Dietzel, W.; Kainer, K.U. Comparison of corrosion properties of squeeze cast and thixocast MgZnRE alloys. In *Materials Science Forum*; Ke, W., Han, E.H., Han, Y.F., Eds.; Trans Tech Publ.: Zürich, Switzerland, 2005; pp. 697–700.

214. Mo, W.; Zhang, L.; Wu, G.; Zhang, Y.; Liu, W.; Wang, C. Effects of processing parameters on microstructure and mechanical properties of squeeze-cast Mg–12Zn–4Al–0.5 Ca alloy. *Mater. Des.* **2014**, *63*, 729–737.

215. Doležal, P.; Zapletal, J.; Fintová, S.; Trojanová, Z.; Greger, M.; Roupcová, P.; Podrábský, T. Influence of processing techniques on microstructure and mechanical properties of a biodegradable Mg-3Zn-2Ca alloy. *Materials* **2016**, *9*, 880.

216. Chen, H.-M.; Yu, H.-S.; Kang, S.-B.; Min, G.-H.; Jin, Y.-X. Effect of rolling temperature on microstructure and texture of twin roll cast ZK60 magnesium alloy. *T. Nonferr. Metal Soc.* **2010**, *20*, 2086–2091.

217. Park, S.S.; Bae, G.; Kang, D.; Jung, I.-H.; Shin, K.; Kim, N.J. Microstructure and tensile properties of twin-roll cast Mg–Zn–Mn–Al alloys. *Scripta Mater.* **2007**, *57*, 793–796.

218. Wang, S.-R.; Min, W.; Kang, S.-B.; Cho, J.-H. Microstructure comparison of ZK60 alloy under casting, twin roll casting and hot compression. *T. Nonferr. Metal Soc.* **2010**, *20*, 763–768.

219. Watari, H.; Davey, K.; Rasgado, M.; Haga, T.; Izawa, S.. Semi-solid manufacturing process of magnesium alloys by twin-roll casting. *J. Mater. Process. Technol.* **2004**, *155*, 1662–1667.

220. Park, S.S.; Park, W.-J.; Kim, C.; You, B.; Kim, N.J. The twin-roll casting of magnesium alloys. *JOM* **2009**, *61*, 14.

221. Oktay, G.; Ürgen, M. Corrosion behaviour of magnesium AZ31 sheet produced by twin roll casting. *Corros. Eng. Sci. Techn.* **2015**, *50*, 380–389.

222. Mendis, C.; Bae, J.; Kim, N.; Hono, K. Microstructures and tensile properties of a twin roll cast and heat-treated Mg–2.4 Zn–0.1 Ag–0.1 Ca–0.1 Zr alloy. *Scripta Mater.* **2011**, *64*, 335–338.

223. Kim, N. Critical assessment 6: Magnesium sheet alloys: Viable alternatives to steels? *Mater. Sci. Technol.* **2014**, *30*, 1925–1928.

224. Park, S.S.; Bae, G.; Kang, D.; You, B.; Kim, N.J. Superplastic deformation behavior of twin-roll cast Mg–6Zn–1Mn–1Al alloy. *Scripta Mater.* **2009**, *61*, 223–226.

225. Hou, R.; Victoria-Hernandez, J.; Jiang, P.; Willumeit-Römer, R.; Luthringer-Feyerabend, B.; Yi, S.; Letzig, D.; Feyerabend, F. In vitro evaluation of the ZX11 magnesium alloy as potential bone plate: Degradability and mechanical integrity. *Acta Biomater.* **2019**, *97*, 608–622.

226. Victoria-Hernández, J.; Yi, S.; Klaumünzer, D.; Letzig, D. Recrystallization behavior and its relationship with deformation mechanisms of a hot rolled Mg-Zn-Ca-Zr alloy. *Mater. Sci. Eng. A* **2019**, *761*, 138054.

227. Klaumünzer, D.; Marx, A.; Schauerte, O.; Wollenberg, A.; Letzig, D.; Yi, S.; Victoria-Hernández, J.; Uggowitzer, P.; Knwon, O.-D.; Kim, J.J., et al. Magneisum alloy sheet produced by twin roll casting. EP3205736A1, 22 August 2018.

228. Yamasaki, M.; Hayashi, N.; Izumi, S.; Kawamura, Y. Corrosion behavior of rapidly solidified Mg–Zn–rare earth element alloys in NaCl solution. *Corros. Sci.* **2007**, *49*, 255–262.

229. Shuai, C.; Yang, Y.; Wu, P.; Lin, X.; Liu, Y.; Zhou, Y.; Feng, P.; Liu, X.; Peng, S. Laser rapid solidification improves corrosion behavior of Mg-Zn-Zr alloy. *J. Alloys Compd.* **2017**, *691*, 961–969.

230. Xu, Z.; Smith, C.; Chen, S.; Sankar, J. Development and microstructural characterizations of Mg–Zn–Ca alloys for biomedical applications. *Mater. Sci. Eng. B* **2011**, *176*, 1660–1665.

231. Hornberger, H.; Virtanen, S.; Boccaccini, A. Biomedical coatings on magnesium alloys–a review. *Acta Biomater.* **2012**, *8*, 2442–2455.

232. Chen, X.; Yang, H.Y.; Abbott, T.; Easton, M.A.; Birbilis, N. Corrosion-resistant electrochemical platings on magnesium alloys: A state-of-the-art review. *Corrosion* **2012**, *68*, 518–535.

233. Singh, A.; Harimkar, S.P. Laser surface engineering of magnesium alloys: A review. *JOM* **2012**, *64*, 716–733.

234. Yang, J.; Cui, F.-z.; Lee, I.S.; Wang, X. Plasma surface modification of magnesium alloy for biomedical application. *Surf. Coat. Tech.* **2010,** 205, S182–S187.

235. Gray, J.; Luan, B. Protective coatings on magnesium and its alloys—A critical review. *J. Alloys Compd.* **2002**, *336*, 88–113.

236. Hu, R.-G.; Zhang, S.; Bu, J.-F.; Lin, C.-J.; Song, G.-L. Recent progress in corrosion protection of magnesium alloys by organic coatings. *Prog. Org. Coat.* **2012**, *73*, 129–141.

237. Chen, X.; Birbilis, N.; Abbott, T. Review of corrosion-resistant conversion coatings for magnesium and its alloys. *Corrosion* **2011**, *67*, 035005–035001-035005-035016.

238. Wang, J.; Tang, J.; Zhang, P.; Li, Y.; Wang, J.; Lai, Y.; Qin, L. Surface modification of magnesium alloys developed for bioabsorbable orthopedic implants: A general review. *J. Biomed. Mater. Res. B Appl. Biomater.* **2012**, *100*, 1691–1701.

239. Uddin, M.; Hall, C.; Murphy, P. Surface treatments for controlling corrosion rate of biodegradable Mg and Mg-based alloy implants. *Sci. Technol. Adv. Mat.* **2015**, *16*, 053501.

240. Pommiers-Belin, S.; Frayret, J.; Uhart, A.; Ledeuil, J.; Dupin, J.-C.; Castetbon, A.; Potin-Gautier, M. Determination of the chemical mechanism of chromate conversion coating on magnesium alloys EV31A. *Appl. Surf. Sci.* **2014**, *298*, 199–207.

241. Yong, Z.; Zhu, J.; Qiu, C.; Liu, Y. Molybdate/phosphate composite conversion coating on magnesium alloy surface for corrosion protection. *Appl. Surf. Sci.* **2008**, *255*, 1672–1680.

242. Yang, K.; Ger, M.; Hwu, W.; Sung, Y.; Liu, Y. Study of vanadium-based chemical conversion coating on the corrosion resistance of magnesium alloy. *Mater. Chem. Phys.* **2007**, *101*, 480–485.

243. Zhao, M.; Wu, S.; Luo, J.; Fukuda, Y.; Nakae, H. A chromium-free conversion coating of magnesium alloy by a phosphate–permanganate solution. *Surf. Coat. Tech.* **2006**, *200*, 5407–5412.

244. Lee, Y.; Chu, Y.; Li, W.; Lin, C. Effect of permanganate concentration on the formation and properties of phosphate/permanganate conversion coating on AZ31 magnesium alloy. *Corros. Sci.* **2013**, *70*, 74–81.

245. Zhang, H.; Yao, G.; Wang, S.; Liu, Y.; Luo, H. A chrome-free conversion coating for magnesium–lithium alloy by a phosphate–permanganate solution. *Surf. Coat. Tech.* **2008**, *202*, 1825–1830.

246. Hu, J.; Li, Q.; Zhong, X.; Zhang, L.; Chen, B. Composite anticorrosion coatings for AZ91D magnesium alloy with molybdate conversion coating and silicon sol–gel coatings. *Prog. Org. Coat.* **2009**, *66*, 199–205.

247. Li, K.; Liu, J.; Lei, T.; Xiao, T. Optimization of process factors for self-healing vanadium-based conversion coating on AZ31 magnesium alloy. *Appl. Surf. Sci.* **2015**, *353*, 811–819.

248. Niu, L.; Chang, S.-H.; Tong, X.; Li, G.; Shi, Z. Analysis of characteristics of vanadate conversion coating on the surface of magnesium alloy. *J. Alloys Compd.* **2014**, *617*, 214–218.

249. Lin, C.; Lin, H.; Lin, K.; Lai, W. Formation and properties of stannate conversion coatings on AZ61 magnesium alloys. *Corros. Sci.* **2006**, *48*, 93–109.

250. Li, Z.; Dai, C.-l.; Liu, Y.-l.; ZHU, J. Study of Silicate and Tungstate Composite Conversion Coating on Magnesium Alloy. *Eletroplating and Pollution Control* **2007**, *27*, 16.

251. Yang, Y.; Tsai, C.; Huang, Y.; Lin, C. Formation mechanism and properties of titanate conversion coating on AZ31 magnesium alloy. *J. Electrochem. Soc.* **2012,** 159, C226–C232.

252. Jian, S.-Y.; Chu, Y.-R.; Lin, C.-S. Permanganate conversion coating on AZ31 magnesium alloys with enhanced corrosion resistance. *Corros. Sci.* **2015**, *93*, 301–309.

253. Zhang, X.; Liang, J.; Liu, B.; Peng, Z. Preparation of superhydrophobic zinc coating for corrosion protection. *Colloids Surf. Physicochem. Eng. Aspects* **2014**, *454*, 113–118.

254. Park, B.C. Method of preparing copper plating layer having high adhesion to magnesium alloy using electroplating. US7368047B2, 6 May 2008.

255. Macary, R.L. Method of chrome plating magnesium and magnesium alloys. US8152985B2, 10 April 2012.

256. Zhang, Z.; Yu, G.; Ouyang, Y.; He, X.; Hu, B.; Zhang, J.; Wu, Z. Studies on influence of zinc immersion and fluoride on nickel electroplating on magnesium alloy AZ91D. *Appl. Surf. Sci.* **2009**, *255*, 7773–7779.

257. Song, G.-L.; Shi, Z. Corrosion mechanism and evaluation of anodized magnesium alloys. *Corros. Sci.* **2014**, *85*, 126–140.

258. Blawert, C.; Dietzel, W.; Ghali, E.; Song, G. Anodizing treatments for magnesium alloys and their effect on corrosion resistance in various environments. *Adv. Eng. Mater.* **2006**, *8*, 511–533.

259. Lu, X.; Blawert, C.; Kainer, K.U.; Zheludkevich, M.L. Investigation of the formation mechanisms of plasma electrolytic oxidation coatings on Mg alloy AM50 using particles. *Electrochim. Acta* **2016**, *196*, 680–691.

260. Lu, X.; Blawert, C.; Huang, Y.; Ovri, H.; Zheludkevich, M.L.; Kainer, K.U. Plasma electrolytic oxidation coatings on Mg alloy with addition of SiO_2 particles. *Electrochim. Acta* **2016**, *187*, 20–33.

261. Shao, Y.; Huang, H.; Zhang, T.; Meng, G.; Wang, F. Corrosion protection of Mg–5Li alloy with epoxy coatings containing polyaniline. *Corros. Sci.* **2009**, *51*, 2906–2915.

262. Truong, V.-T.; Lai, P.; Moore, B.; Muscat, R.; Russo, M. Corrosion protection of magnesium by electroactive polypyrrole/paint coatings. *Synthetic Met.* **2000**, *110*, 7–15.

263. Wong, H.M.; Yeung, K.W.; Lam, K.O.; Tam, V.; Chu, P.K.; Luk, K.D.; Cheung, K.M. A biodegradable polymer-based coating to control the performance of magnesium alloy orthopaedic implants. *Biomaterials* **2010**, *31*, 2084–2096.

264. Hoche, H.; Groß, S.; Oechsner, M. Development of new PVD coatings for magnesium alloys with improved corrosion properties. *Surf. Coat. Tech.* **2014**, *259*, 102–108.

265. Wu, G.; Zeng, X.; Yuan, G. Growth and corrosion of aluminum PVD-coating on AZ31 magnesium alloy. *Mater. Lett.* **2008**, *62*, 4325–4327.

266. Altun, H.; Sen, S. The effect of PVD coatings on the corrosion behaviour of AZ91 magnesium alloy. *Mater. Des.* **2006**, *27*, 1174–1179.

267. Gao, Y.-l.; Wang, C.-S.; Yao, M.; Liu, H.-B. The resistance to wear and corrosion of laser-cladding Al2O3 ceramic coating on Mg alloy. *Appl. Surf. Sci.* **2007**, *253*, 5306–5311.

268. Ignat, S.; Sallamand, P.; Grevey, D.; Lambertin, M. Magnesium alloys laser (Nd: YAG) cladding and alloying with side injection of aluminium powder. *Appl. Surf. Sci.* **2004**, *225*, 124–134.

269. Kim, J.; Lee, S.; Park, J.; Kim, H. Laser surface modification of Ti and TiC coatings on magnesium alloy. *Phys. Met. Metallogr.* **2014**, *115*, 1389–1394.

270. Qian, J.; Yin, Y.; Li, T.; Hu, X.; Wang, C.; Li, S. Structure, micro-hardness and corrosion behaviour of the Al–Si/Al_2O_3 coatings prepared by laser plasma hybrid spraying on magnesium alloy. *Vacuum* **2015**, *117*, 55–59.

271. Waterman, J.; Staiger, M. Coating systems for magnesium-based biomaterials—State of the art. In *Magnesium Technology 2011*; Neelameggham, A.R.; Mathaudhu, S.N., Eds. Springer: Berlin/Heidelberg, Germany, 2011; pp. 403–408.

272. Aghion, E.; Bronfin, B. Magnesium alloys development towards the 21st century. In *Materials Science Forum*; Kojima, Y., Aizawa, T., Kamado, S., Eds.; Trans Tech Publ.: Zürich, Switzerland, 2000; pp. 19–30.

273. Luo, A.A., Magnesium casting technology for structural applications, *J. Magnes. Alloy.* **2013**, *1*, 2–22.

274. Luo, A.; Renaud, J.; Nakatsugawa, I.; Plourde, J. Magnesium castings for automotive applications. *JOM* **1995**, *47*, 28–31.

275. Powell, B.; Luo, A.; Krajewski, P. Magnesium alloys for lightweight powertrains and automotive bodies. In *Advanced Materials in Automotive Engineering*, Rowe, J., Ed. Elsevier: Amsterdam, The Netherlands, 2012; pp 150-209.

276. Luo, A.; Shinoda, T. A new magnesium alloy for automotive powertrain applications. *SAE Trans.* **1998**, *107*, 86–94.

277. Klaumünzer, D.; Hernandez, J.V.; Yi, S.; Letzig, D.; Kim, S.-h.; Kim, J.J.; Seo, M.H.; Ahn, K. Magnesium Process and Alloy Development for Applications in the Automotive Industry. In *Magnesium Technology 2019*, Springer: Berlin/Heidelberg, Germany, 2019; pp. 15–20.

278. He, Y.; Tao, H.; Zhang, Y.; Jiang, Y.; Zhang, S.; Zhao, C.; Li, J.; Zhang, B.; Song, Y.; Zhang, X. Biocompatibility of bio-Mg-Zn alloy within bone with heart, liver, kidney and spleen. *Chin. Sci. Bull.* **2009**, *54*, 484–491.

279. Chen, D.; He, Y.; Tao, H.; Zhang, Y.; Jiang, Y.; Zhang, X.; Zhang, S. Biocompatibility of magnesium-zinc alloy in biodegradable orthopedic implants. *Int. J. Mol. Med.* **2011**, *28*, 343–348.

280. Kraus, T.; Fischerauer, S.F.; Hänzi, A.C.; Uggowitzer, P.J.; Löffler, J.F.; Weinberg, A.M. Magnesium alloys for temporary implants in osteosynthesis: In vivo studies of their degradation and interaction with bone. *Acta Biomater.* **2012**, *8*, 1230–1238.

281. Ben-Hamu, G.; Eliezer, D.; Shin, K. Influence of Si, Ca and Ag addition on corrosion behaviour of new wrought Mg–Zn alloys. *Mater. Sci. Technol.* **2006**, *22*, 1213–1218.

282. Ben-Hamu, G.; Eliezer, D.; Shin, K. The role of Si and Ca on new wrought Mg–Zn–Mn based alloy. *Mater. Sci. Eng. A* **2007**, *447*, 35–43.

283. Wang, L.-X.; Song, R.-B.; Cai, C.-H.; Li, J.-Y. Enhanced Strength and Corrosion Resistance of Mg–2Zn–0.6Zr Alloy with Extrusion. *Acta Metall. Sin.-Engl.* **2019**, *32*, 10–22.

284. Baek, S.-M.; Kim, B.; Park, S.S. Influence of Intermetallic Particles on the Corrosion Properties of Extruded ZK60 Mg Alloy Containing Cu. *Metals* **2018**, *8*, 323.

285. Zhang, Y.; Li, J.; Li, J. Microstructure, mechanical properties, corrosion behavior and film formation mechanism of Mg-Zn-Mn-xNd in Kokubo's solution. *J. Alloys Compd.* **2018**, *730*, 458–470.

286. Zhang, Y.; Li, J.; Li, J. Effects of microstructure transformation on mechanical properties, corrosion behaviors of Mg-Zn-Mn-Ca alloys in simulated body fluid. *J. Mech. Behav. Biomed.* **2018**, *80*, 246–257.

287. Zhang, Y.; Li, J.; Li, J. Effects of Calcium addition on phase characteristics and corrosion behaviors of Mg-2Zn-0.2 Mn-xCa in simulated body fluid. *J. Alloys Compd.* **2017**, *728*, 37–46.

288. Buzolin, R.; Mohedano, M.; Mendis, C.; Mingo, B.; Tolnai, D.; Blawert, C.; Kainer, K.; Pinto, H.; Hort, N. As cast microstructures on the mechanical and corrosion behaviour of ZK40 modified with Gd and Nd additions. *Mater. Sci. Eng. A* **2017**, *682*, 238–247.

289. Zheng, Y.; Li, Y.; Chen, J.; Zou, Z. Effects of tensile and compressive deformation on corrosion behaviour of a Mg–Zn alloy. *Corros. Sci.* **2015**, *90*, 445–450.

290. Gao, J.; Guan, S.; Ren, Z.; Sun, Y.; Zhu, S.; Wang, B. Homogeneous corrosion of high pressure torsion treated Mg–Zn–Ca alloy in simulated body fluid. *Mater. Lett.* **2011**, *65*, 691–693.

291. Liu, D.; Liu, Y.; Huang, Y.; Song, R.; Chen, M. Effects of solidification cooling rate on the corrosion resistance of Mg–Zn–Ca alloy. *Progr. Nat. Sci.* **2014**, *24*, 452–457.

292. Tong, L.; Zheng, M.; Xu, S.; Kamado, S.; Du, Y.; Hu, X.; Wu, K.; Gan, W.; Brokmeier, H.; Wang, G. Effect of Mn addition on microstructure, texture and mechanical properties of Mg–Zn–Ca alloy. *Mater. Sci. Eng. A* **2011**, *528*, 3741–3747.

293. Homma, T.; Mendis, C.; Hono, K.; Kamado, S. Effect of Zr addition on the mechanical properties of as-extruded Mg–Zn–Ca–Zr alloys. *Mater. Sci. Eng. A* **2010**, *527*, 2356–2362.

294. Cao, J.; Laws, K.; Birbilis, N.; Ferry, M. Potentiodynamic polarisation study of bulk metallic glasses based on the Mg–Zn–Ca ternary system. *Corros. Eng. Sci. Techn.* **2012**, *47*, 329–334.

295. Wang, J.; Wei, Y.; Guo, S.; Huang, S.; Zhou, X.; Pan, F. The Y-doped MgZnCa alloys with ultrahigh specific strength and good corrosion resistance in simulated body fluid. *Mater. Lett.* **2012**, *81*, 112–114.

296. Wang, J.; Li, Y.; Huang, S.; Wei, Y.; Xi, X.; Cai, K.; Pan, F. Effects of Y on the Microstructure, Mechanical and Bio-corrosion Properties of Mg–Zn–Ca Bulk Metallic Glass. *J. Mater. Sci. Technol.* **2014**, *30*, 1255–1261.

297. Wang, Y.; Tan, M.J.; Pang, J.; Wang, Z.; Jarfors, A.W. In vitro corrosion behaviors of Mg67Zn28Ca5 alloy: From amorphous to crystalline. *Mater. Chem. Phys.* **2012**, *134*, 1079–1087.

298. Ramya, M.; Sarwat, S.G.; Udhayabanu, V.; Subramanian, S.; Raj, B.; Ravi, K. Role of partially amorphous structure and alloying elements on the corrosion behavior of Mg–Zn–Ca bulk metallic glass for biomedical applications. *Mater. Des.* **2015**, *86*, 829–835.

299. Yamasaki, M.; Izumi, S.; Kawamura, Y. Development of High Strength and Highly Corrosion-Resistant Bulk Nanocrystalline Mg-Zn-Y Alloys with Long Period Stacking Ordered Phase. *ECS Trans.* **2009**, *16*, 81–88.

300. Izumi, S.; Yamasaki, M.; Kawamura, Y. Relation between corrosion behavior and microstructure of Mg–Zn–Y alloys prepared by rapid solidification at various cooling rates. *Corros. Sci.* **2009**, *51*, 395–402.

301. Xu, D.; Tang, W.; Liu, L.; Xu, Y.; Han, E. Effect of W-phase on the mechanical properties of as-cast Mg–Zn–Y–Zr alloys. *J. Alloys Compd.* **2008**, *461*, 248–252.

302. Pérez, P.; Onofre, E.; Cabeza, S.; Llorente, I.; Del Valle, J.; García-Alonso, M.; Adeva, P.; Escudero, M., Corrosion behaviour of Mg–Zn–Y–Mischmetal alloys in phosphate buffer saline solution. *Corros. Sci.* **2013**, *69*, 226–235.

303. Wang, S.; Xu, D.; Chen, X.; Han, E.; Dong, C. Effect of heat treatment on the corrosion resistance and mechanical properties of an as-forged Mg–Zn–Y–Zr alloy. *Corros. Sci.* **2015**, *92*, 228–236.

304. Fei, S.; Wang, C.-Q.; Zhang, Z.-M. Microstructures, corrosion and mechanical properties of as-cast Mg–Zn–Y–(Gd) alloys. *T. Nonferr. Metal Soc.* **2015**, *25*, 2172–2180.

305. Singh, A.; Nakamura, M.; Watanabe, M.; Kato, A.; Tsai, A. Quasicrystal strengthened Mg–Zn–Y alloys by extrusion. *Scripta Mater.* **2003**, *49*, 417–422.

306. Wang, J.; Song, P.; Gao, S.; Huang, X.; Shi, Z.; Pan, F. Effects of Zn on the microstructure, mechanical properties, and damping capacity of Mg–Zn–Y–Zr alloys. *Mater. Sci. Eng. A* **2011**, *528*, 5914–5920.

307. Song, R.; Liu, D.-B.; Liu, Y.-C.; Zheng, W.-B.; Zhao, Y.; Chen, M.-F. Effect of corrosion on mechanical behaviors of Mg-Zn-Zr alloy in simulated body fluid. *Front. Mater. Sci.* **2014**, *8*, 264–270.

308. Hong, D.; Saha, P.; Chou, D.-T.; Lee, B.; Collins, B.E.; Tan, Z.; Dong, Z.; Kumta, P.N. In vitro degradation and cytotoxicity response of Mg–4% Zn–0.5% Zr (ZK40) alloy as a potential biodegradable material. *Acta Biomater.* **2013**, *9*, 8534–8547.

309. Liu, W.; Dong, J.; Zhang, P.; Yao, Z.; Zhai, C.; Ding, W. High cycle fatigue behavior of as-extruded ZK60 magnesium alloy. *J. Mater. Sci. Mater. Med.* **2009**, *44*, 2916.

310. Zhang, Y.; Zeng, X.; Liu, L.; Lu, C.; Zhou, H.; Li, Q.; Zhu, Y. Effects of yttrium on microstructure and mechanical properties of hot-extruded Mg–Zn–Y–Zr alloys. *Mater. Sci. Eng. A* **2004**, *373*, 320–327.

311. Yu, W.; Liu, Z.; He, H.; Cheng, N.; Li, X. Microstructure and mechanical properties of ZK60–Yb magnesium alloys. *Mater. Sci. Eng. A* **2008**, *478*, 101–107.

312. Yamasaki, M.; Anan, T.; Yoshimoto, S.; Kawamura, Y. Mechanical properties of warm-extruded Mg–Zn–Gd alloy with coherent 14H long periodic stacking ordered structure precipitate. *Scripta Mater.* **2005**, *53*, 799–803.

313. Yuan, G.; Liu, Y.; Lu, C.; Ding, W. Effect of quasicrystal and Laves phases on strength and ductility of as-extruded and heat treated Mg–Zn–Gd-based alloys. *Mater. Sci. Eng. A* **2008**, *472*, 75–82.

314. Zhang, E.; Yin, D.; Xu, L.; Yang, L.; Yang, K. Microstructure, mechanical and corrosion properties and biocompatibility of Mg–Zn–Mn alloys for biomedical application. *Mater. Sci. Eng. C* **2009**, *29*, 987–993.

315. Zhang, Y.; Li, J.; Lai, H.; Xu, Y. Effect of Homogenization on Microstructure Characteristics, Corrosion and Biocompatibility of Mg-Zn-Mn-xCa Alloys. *Materials* **2018**, *11*, 227.

316. Zhang, Y.; Li, J.-y.; Liaw, P.K.; Xu, Y.-z.; Lai, H.-y. Effects of heat treatment on the mechanical properties and corrosion behaviour of the Mg-2Zn-0.2 Mn-xNd alloys. *J. Alloys Compd.* **2018**, *769*, 552–565.

317. He, R.; Liu, R.; Chen, Q.; Zhang, H.; Wang, J.; Guo, S. In vitro degradation behavior and cytocompatibility of Mg-6Zn-Mn alloy. *Mater. Lett.* **2018**, *228*, 77–80.

318. Guangyin, Y.; Manping, L.; Wenjiang, D.; Inoue, A. Microstructure and mechanical properties of Mg–Zn–Si-based alloys. *Mater. Sci. Eng. A* **2003**, *357*, 314–320.

319. Mengqi, C.; Ziquan, L.; Jinsong, L.; Menghui, W.; Beibei, S.; Bijun, W. Corrosion Behavior of as-Cast Mg-6Zn-4Si Alloy with Sr Addition. *Rare Metal Mat. Eng.* **2017**, *46*, 2405–2410.

320. Jihua, C.; Zhenhua, C.; Hongge, Y.; Fuquan, Z.; Yingliang, C. Effects of Sn and Ca additions on microstructure, mechanical properties, and corrosion resistance of the as-cast Mg-Zn-Al-based alloy. *Mater. Corros.* **2008**, *59*, 934–941.

321. Xiao, W.; Jia, S.; Wang, L.; Wu, Y.; Wang, L. The microstructures and mechanical properties of cast Mg–Zn–Al–RE alloys. *J. Alloys Compd.* **2009,** 480, L33–L36.

322. Yang, M.; Pan, F. Effects of Sn addition on as-cast microstructure, mechanical properties and casting fluidity of ZA84 magnesium alloy. *Mater. Des.* **2010**, *31*, 68–75.

323. Jayalakshmi, S.; Kailas, S.V.; Seshan, S.; Fleury, E. Properties of squeeze cast Mg-6Zn-3Cu alloy and its saffil alumina short fibre reinforced composites. *J. Mater. Sci. Mater. Med.* **2006**, *41*, 3743–3752.

3. Motivation and Objectives

Considering the need for the development of Al-free Mg alloys and the poor corrosion resistance of currently commercial Mg-Zn alloys, development of new Mg-Zn alloys with enhanced corrosion resistance is desired. Alloying is one of the most effective strategies for improving both corrosion resistance and mechanical properties of Mg alloys and great efforts have been made for the Mg-Zn system. However, the results or conclusions of different studies are controversial, even for the simplest Mg-Zn binary alloys, and most studies focused only on one or two specific aspects of Mg alloys. Therefore, the motivation of this thesis is to comprehensively investigate the properties of low-Zn containing Mg-Zn alloys micro-alloyed with different ternary alloying elements and to further improve the properties of Mg-Zn-X alloys by wrought processing. The objectives of this study are focused on:

(1) screening and understanding the influence of the ternary alloying elements on the microstructure and corrosion behavior of low-Zn containing Mg-Zn system to identify alloys with suitable corrosion performance,

(2) studying the influence of extrusion process and extrusion speed on the microstructures and corrosion performance of selected Mg-Zn-X alloys,

(3) understanding the corrosion mechanisms of optimized Mg-Zn-X alloys in different corrosive electrolytes,

(4) evaluating the overall properties of optimized Mg-Zn-X alloys, including corrosion properties, mechanical properties and integrity, fatigue and corrosion fatigue behavior and the sensitivity to stress corrosion cracking.

4. Experimental

4.1 Materials preparation

4.1.1 Conventional gravity casting

Raw materials with commercial purity were used in this study. They were magnesium (Mg) (99.96 %), zinc (Zn) (99.995 %), aluminum (Al) (99.9966 %), calcium (Ca) (99.9 %), gallium (Ga) (99.900 %), cerium (Ce) (99.000 %), gadolinium (Gd) (99.000 %), yttrium (Y) (99.000 %), germanium (Ge) (99.99 %) and tin (Sn) (99.963 %), respectively. Al was selected as the counterpart since it is the most commonly used alloying element for Mg alloys. Ca is a typical alloying element for Mg alloys aiming to improve the corrosion resistance of Mg-Zn based alloys. Ce, Gd and Y were frequently considered rare earth elements while Ga, Ge and Sn were rarely considered alloying elements. A micro-alloyed and a low-Zn containing systems were compared in this work, i.e. Mg0.5ZnX system and Mg4ZnX (both in *wt.*%) system. For all ternary alloying elements, 0.2 *wt.*% micro-addition was considered. For the first screening of the alloys to identify those with relatively better corrosion resistance, cylindrical alloy bars in a size of Φ 18 mm × 180 mm were prepared by conventional gravity casting using an electrical resistance furnace. Pure alloying metals were melted in a boron nitride coated stainless steel crucible under a protective atmosphere of argon and sulfur hexafluoride at 760 °C. The melts were stirred for 5 min before being casted into a steel mould preheated to 200 °C and subsequently cooled in air.

4.1.2 Indirect chill casting

For the extrusion of the selected alloys, indirect chill casting [25] was performed in order to provide a homogeneous microstructure. The melts were poured into a thin walled steel mould (r × R × h = 30 mm × 35 mm × 230 mm) which has been preheated to 680 °C. Subsequently, the melts were incubated at 680 °C for 2 minutes and then immersed into flowing water at a rate of 10 mm/s.

4.1.3 Indirect extrusion

For the indirect extrusion of selected alloys, the as-chill cast alloys were machined to billets of 49 mm in diameter and 150 mm in height. The billets were homogenized for 24 h and quenched with warm water. The homogenization temperature for each alloy was chosen according to the related ternary phase diagram (shown in Figure 4.1) calculated by Pandat at the aim to adjust a homogenous microstructure (without second phases) as much as possible. Currently, there is no Mg-Zn-Ge ternary phase diagram available. Since the chemical properties of Ge are similar to those of Sn, the homogenization temperature of Mg0.5Zn0.2Ge alloy was set to be the same as that of Mg4Zn0.2Sn alloy. Therefore, the homogenization temperature was 370 °C for Mg0.5Zn0.2Ca alloy and 320 °C for Mg0.5Zn0.2Ge and Mg4Zn0.2Sn alloys, respectively. The billets were preheated at 375 °C for 1 h before extrusion and then placed into a container preheated to 375 °C. Subsequently, indirect extrusion was carried out at speeds of 0.6, 2.2 and 4.4 mm/s. The extrusion ratio was 25:1 and a round bar with 10 mm in diameter was formed.

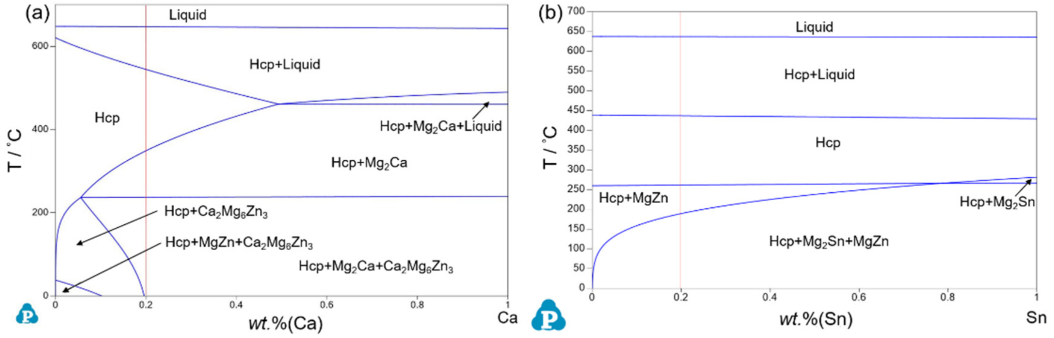

Figure 4.1 Phase diagram of (a) Mg0.5Zn-Ca and (b) Mg4Zn-Sn systems calculated by Pandat.

Table 4.1 Chemical compositions of the alloys studied (X: ternary alloying element).

Fabrication	**alloy**	**Composition (*wt.*%)**							
		X	**Zn**	**Fe**	**Cu**	**Ni**	**Mn**	**Si**	**Mg**
Gravity casting	Mg0.5Zn	-	0.45	0.0043	0.0014	0.0007	0.034	0.0310	Bal.
	Mg0.5Zn0.2Al	0.23	0.48	0.0016	0.0016	< 0.0002	0.021	0.0186	Bal.
	Mg0.5Zn0.2Ca	0.14	0.47	0.0026	0.0012	0.0007	0.034	0.0330	Bal.
	Mg0.5Zn0.2Ce	0.23	0.50	0.0024	0.0016	< 0.0002	0.021	0.0213	Bal.
	Mg0.5Zn0.2Ga	0.24	0.50	0.0020	0.0016	< 0.0002	0.022	0.0200	Bal.
	Mg0.5Zn0.2Gd	0.15	0.48	0.0064	0.0018	< 0.0002	0.022	0.0218	Bal.
	Mg0.5Zn0.2Ge	0.22	0.54	0.0012	0.0016	< 0.0002	0.021	0.0165	Bal.
	Mg0.5Zn0.2Sn	0.14	0.50	0.0041	0.0017	< 0.0002	0.021	0.0205	Bal.
	Mg0.5Zn0.2Y	0.10	0.49	0.0016	0.0017	< 0.0002	0.021	0.0218	Bal.
	Mg4Zn	-	3.87	0.0077	0.0011	0.0004	0.029	0.0331	Bal.
	Mg4Zn0.2Al	0.29	3.81	0.0018	0.0016	< 0.0002	0.021	0.0178	Bal.
	Mg4Zn0.2Ca	0.13	4.11	0.0045	0.0012	0.0005	0.029	0.0302	Bal.
	Mg4Zn0.2Ce	0.24	3.75	0.0009	0.0016	< 0.0002	0.020	0.0142	Bal.
	Mg4Zn0.2Ga	0.24	3.83	0.0022	0.0015	< 0.0002	0.020	0.0172	Bal.
	Mg4Zn0.2Gd	0.14	3.94	0.0011	0.0017	< 0.0002	0.020	0.0191	Bal.
	Mg4Zn0.2Ge	0.20	4.36	0.0021	0.0016	< 0.0002	0.020	0.0165	Bal.
	Mg4Zn0.2Sn	0.18	3.66	0.0011	0.0015	< 0.0002	0.020	0.0111	Bal.
	Mg4Zn0.2Y	0.18	3.89	0.0007	0.0017	< 0.0002	0.022	0.0155	Bal.
Indirect chill casting	Mg0.5Zn0.2Ca	0.19	0.45	0.0018	0.0017	0.0010	0.036	0.0162	Bal.
	Mg0.5Zn0.2Ge	0.20	0.49	0.0017	0.0017	0.0010	0.036	0.0158	Bal.
	Mg4Zn0.2Sn	0.22	3.92	0.0017	0.0015	0.0007	0.030	0.0133	Bal.
Indirect extrusion	Mg0.5Zn0.2Ca	0.23	0.47	0.0018	0.0014	0.0008	0.031	0.0089	Bal.
	Mg0.5Zn0.2Ge	0.20	0.49	0.0012	0.0014	0.0007	0.029	0.0093	Bal.
	Mg4Zn0.2Sn	0.17	3.77	0.0018	0.0014	0.0004	0.028	0.0069	Bal.

The chemical compositions of the studied alloys were determined by spark optical emission spectroscopy (Spectrolab M9, Spectro Ametek, Germany), as listed in Table 4.1. Micro X-ray fluorescence (M4 TRONADO, Bruker, Germany) and atomic absorption spectrometer (240FS AA, Agilent, United States) were also used for the analysis of some specific elements (e.g. Sn and Ge etc.) that could not be determined by spark optical emission spectroscopy.

4.2 Microstructure analysis

4.2.1 Sample preparation

Sample discs or rectangular samples were cut from the alloy bars (gravity casted or extruded alloys) or billets (indirect chill casted alloys). Before use, the specimens were mounted in epoxy resin and then successively wet ground with silicon carbide (SiC) abrasive papers from 500 to 2500 grit. Between each grinding step, the samples were rinsed with ethanol and dried by warm airflow. Afterwards, the ground samples were polished with 1 μm non-aqueous diamond suspension and colloidal silica suspension (OPS) to provide a mirror face.

4.2.2 Optical microscopy (OM)

To reveal the grains and grain boundaries, the polished mirror face was chemically etched with an etchant composed of 150 mL ethanol, 20 mL deionized water, 6.5 mL acetic acid and 4 - 5 g picric acid. Afterwards, the specimens were immediately rinsed with ethanol to stop the etching process and dried with warm airflow. Finally, the microstructure of the alloy was observed with a light optical microscope (Leica DM2500 M, Leica Microsystems, Germany) with a Color View software imaging system. The average grain size of the alloys was estimated by AnalySIS pro (version 5.0) software applying the method of line intercept using random straight line drawn through the micrograph.

4.2.3 Scanning electron microscopy (SEM) and Energy dispersive X-ray spectroscopy (EDS)

A scanning electron microscope (SEM) (Vega 3 SB, TESCAN Brno, Czech Republic) equipped with energy dispersive X-ray spectroscopy (EDS) (Eumex) was also utilized to analyze the microstructure and chemical compositions of the different constituents in the alloys. Both secondary electron (SE) and backscattering electron (BSE) modes were used. Latter was especially applied to facilitate the observation of second phases. The acceleration voltage was 15 kV, 20 kV or 30 kV for EDS analysis, depending on the energy of characteristic X-ray of the specific alloying element.

4.2.4 X-ray Diffraction (XRD)

X-ray diffraction (XRD) was performed on a diffractometer (D8 Advance, Bruker, Germany) equipped with Cu Kα radiation to determine the second phases precipitated in the alloys. The measurements were carried out at a voltage of 40 kV and a current of 40 mA with a step size of 0.01° and 2 s for each step from $2\theta = 20°$ to 80°.

The texture of the extruded alloys was measured by XRD (X'pert Pro, Panalytical, Netherlands) at 40 kV voltage and 40 mA current using Cu Kα radiation. Six pole figures (00.2), (10.0), (11.0), (10.1), (10.2) and (10.3) were measured on cross sections of the extruded bars with a sample tilt of 70°. An MTEX toolbox was used to analyze the obtained data and to reveal the inverse pole figure parallel to the extrusion direction in order to reveal the orientation distribution of the sample.

4.3 Corrosion characterization

4.3.1 Scanning kelvin probe force microscopy (SKPFM)

The Volta potential differences between different second phases and α-Mg matrix were measured by scanning kelvin probe force microscopy (SKPFM) (NanoWizard, JPK Instruments AG, Germany). SKPFM allows the imaging of the surface potential on a broad range of materials in nanoscale. It measures the contact potential difference between the specimen and the probe. During the measurement, the topography information is collected in the first pass through the mechanical excitation of the cantilever. While in the second pass, the electric surface potential is acquired by retracing the collected topography at a set lift height from the sample surface. In this process, the cantilever is excited electrically by applying a voltage to the probe tip. Silicon probe (Budget sensors Multi75E-G, Innovative Solutions Bulgaria Ltd., Bulgaria) coated with Cr/Pt conductive coating was used. The force constant and resonance frequency of the probe are 3 N/m and 75 kHz, respectively. Electric connection was achieved using a conductive tape between the grounded AFM sample stage and the specimen. The distance between the probe and sample surface was set as 100 nm during the collection of potential signal. The Volta potential difference map was collected with a resolution of 512 × 512 pixels. Tests were immediately carried out for the polished samples to avoid oxidation of the surfaces. All measurements were performed under open air condition at ambient temperature. JPKSPM Data Processing software was used for data analysis.

4.3.2 Electrochemical measurements

The corrosion behavior of the studied alloys were studied by electrochemical measurements using a Gill AC potentiostat/frequency response analyzer system (Gill AC, ACM Instruments, United Kingdom). A typical three-electrode cell (about 330 mL) composed of platinum mesh as the auxiliary electrode, Ag/AgCl electrode as the reference electrode and specimen as the working electrode was used. The exposed area of the sample was 0.5 cm^2. All measurements were carried out under atmospheric condition with magnetic stirring at a speed of 200 rpm. The room temperature was air-conditioned at about 21 ± 1 °C. In the present study, three corrosive electrolytes, 0.9 *wt.*% sodium chloride (NaCl) solution prepared with deionized water (DIW), 0.5 *wt.*% NaCl solution prepared with DIW and 0.5 *wt.*% NaCl solution prepared with artificial tap water (ATW), were used. The composition of the artificial tap water was 165 mg/L $CaCl_2$, 125 mg/L $NaHCO_3$, 15 mg/L $MgSO_4$ and 0.07 mg/L $NaNO_3$, designed according to our lab tap water offered by the local water supplier [26]. The pH and conductivity of the artificial tap water were about 7.4 and 510 µS/cm, respectively.

Samples for electrochemical studies were only ground up to 1200 grit. For extruded alloys, the face perpendicular to the extrusion direction was used for all corrosion studies.

At least four replicates were performed for each test for repeatability.

Open circuit potential (OCP) measurements

Open circuit potential (OCP) is the potential in a working electrode comparative to the reference electrode when there is no potential or current applied to the cell. In current study, the OCP measurements were performed for 5 min before an electrochemical impedance spectroscopy test and for 30 min before a potentiodynamic polarization test to reach a relatively stable potential.

Electrochemical impedance spectroscopy (EIS) measurements

Electrochemical impedance spectroscopy (EIS) measurements were performed to reveal the corrosion process and follow the evolution of the interfacial layer on metal surface during exposure to a corrosive electrolyte. EIS studies were carried out at OCP with an alternating potential amplitude of 10 mV rms over a frequency range of 30000 to 0.1 Hz with 70 data points. The impedance spectra were collected at fixed time intervals of 5 min, 1 h, 3 h, 6 h, 8 h, 12 h, 24 h and 48 h of exposure. Usually, Nyquist and Bode plots are the popular data presentations of EIS. In Nyquist plot (Figure 4.2a), the real part correlates with the imaginary part of the impedance (Z). Each point on the Nyquist plot is the impedance at one frequency. Note that the imaginary part is negative in Nyquist plot. In Bode plot (Figure 4.2b), the absolute values of the impedance and the phase shift are correlated with the applied frequency. An electrical equivalent circuit model is commonly used to fit and analyze the EIS data, which contains common electrical elements such as capacitors and resistors. Each element in the model has a physical explanation for the electrochemistry of the system. For example, the electrical equivalent circuit shown in Figure 4.3 was used to fit the impedance spectra shown in Figure 4.2. The spectra reveals two time constants, composed of the resistance (R_f) and capacitance (C_f) of the surface film and charge transfer resistance (R_{ct}) and double layer capacitance (C_{dl}) of the double electrical layer due to the corrosion process at the interface of the alloy and the electrolyte. R_s is the solution resistance between the reference electrode and the working electrode. The impedance spectra were analyzed using ZView software. The Chi-squared of the fitting was less than 0.001 to guarantee the reliability of the results.

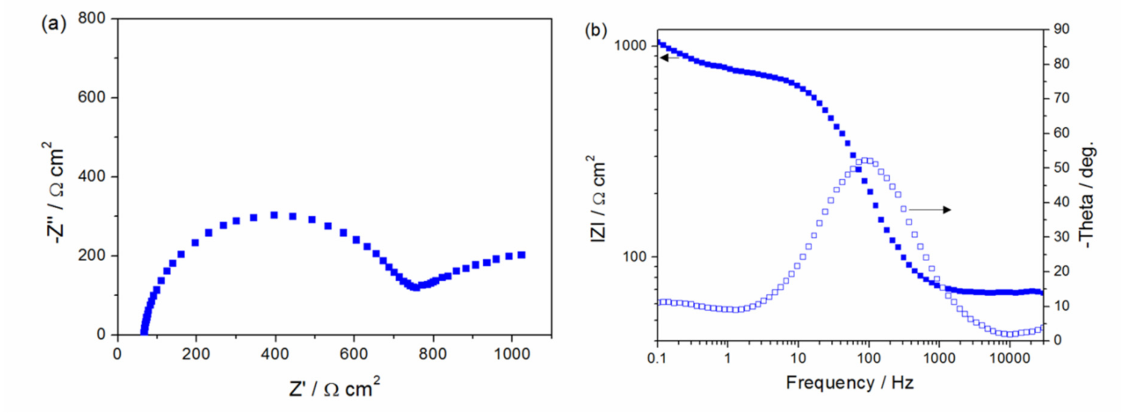

Figure 4.2 Example of an EIS spectra consisting of (a) Nyquist plot and (b) Bode plot.

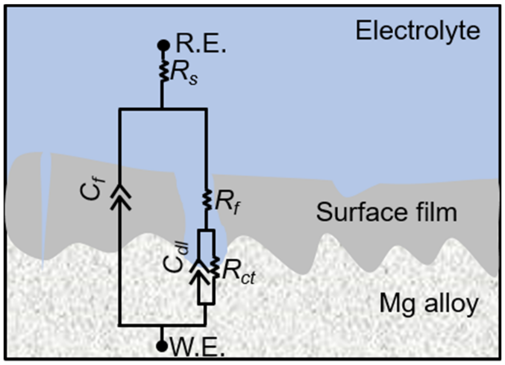

Figure 4.3 Schematic presentation of the electrical equivalent circuit used to fit the impedance spectrum shown in Figure 4.2.

Potentiodynamic polarization measurements

Potentiodynamic polarization measurements were performed to study the difference between the instantaneous polarization response kinetics of the studied alloys. An external voltage is applied to polarize the sample with the potentiostat. Two opposite electrochemical processes take place at the anode and cathode. At the anode, oxidation of the metal takes place, e.g. $Mg \rightarrow Mg^{2+} + 2e^-$. At the cathode, reduction takes place. When the potential is sufficiently negative, water reduction may take place in aqueous environment: $2H_2O + e^- \rightarrow H_2 + 2OH^-$, which is the usual case during the dissolution of Mg alloys. Apart from that, oxygen reduction can also occur: $O_2 + 2H_2O + 4e^- \rightarrow 4OH^-$. The corrosion rate (*CR*) and corrosion current density

(i_{corr}) were analyzed by extrapolating the cathodic branch to the intersection with the vertical through the corrosion potential (E_{corr}). The anodic branch is strongly affected by IR-drops because of the nearly non-polarizable nature of Mg. Thus only the cathodic branch is considered for the fitting of the polarization curves. All potentiodynamic polarization tests were conducted starting from -150 mV relative to the open circuit potential at a scanning rate of 0.2 mV s^{-1}.

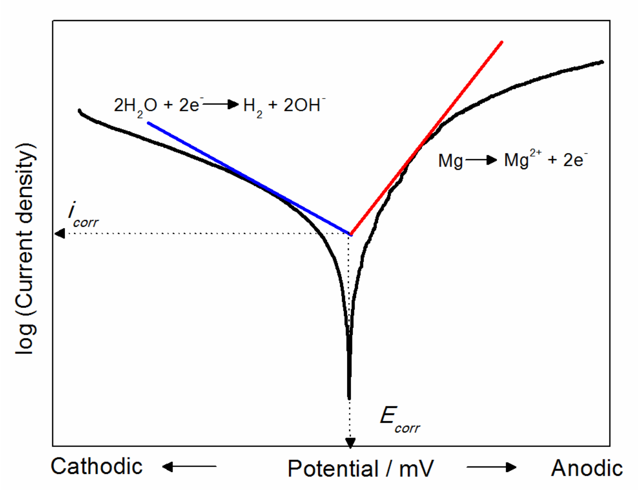

Figure 4.4 Schematic presentation of the determination of i_{corr} for Mg alloys from an experimental polarization curve.

4.3.3 Drop corrosion test

Drop corrosion tests were carried out to understand the local corrosion mechanisms of the studied Mg-Zn-X alloys and reveal the role of each constituent in the alloy during immersion in electrolyte. Firstly, SEM was utilized to determine typical positions of average microstructure features on polished specimens. Then, a droplet of NaCl solution was put on the surface of the specimen for different durations (up to 6 h). Afterwards, the specimen was rinsed with deionized water and dried by compressed air stream. The corroded surface was immersed in 180 g/L chromium trioxide (CrO_3) cleaning solution to remove the corrosion products, subsequently rinsed with ethanol and deionized water. Finally, the corroded surface after removal of corrosion products was examined by SEM again. A possible solubility of the second phases of the studied alloys in CrO_3 solution was checked by immersing the surface of a polished specimen in CrO_3 solution without corrosion and observing the surface with SEM before and after cleaning.

4.3.4 Immersion test

Another time extended immersion test was performed on ground samples in NaCl solutions at room temperature for 48 h. After immersion, the surface and cross-sectional morphologies were examined by SEM. Samples for cross-sectional characterizations were prepared by vertically mounting the corroded specimens in epoxy resin. Before observation with SEM, the mounted samples were mechanically ground with SiC papers and then polished in a mixture of non-aqueous diamond suspension and OPS. Cross-sectional element mapping was carried out with EDS to determine the distribution of element in the corrosion product layer. The applied acceleration voltage was 20 kV. The mapping was done at a resolution of 256 × 191 pixels and an acquisition time of 80 ms per pixel.

The phase compositions of corrosion products after immersion were determined by XRD in grazing incidence geometry at an incidence angle of 3° with a voltage of 40 kV and a current of 40 mA. The measurements were performed from $2\theta = 15°$ to $85°$ with a step size of 0.02° and 1 s for each step. The data was analyzed by using Bruker EVA software with PDF-2 release 2015 RDB.

4.3.5 Hydrogen evolution tests

A holistic assessment of the corrosion rates of the studied alloys were conducted by hydrogen evolution tests. The tests were performed in 350 mL NaCl solutions for 168 h at room temperature. A simple set-up (shown in Figure 4.5) was built with an inverted funnel and a burette above the specimen to collect hydrogen bubbles. The specimen (ground until 1200 grit) with a surface area of about 8 cm^2 was hung below the funnel with a small plastic screw and fishing wire. The average corrosion rate of each alloy at the end of the test was calculated by converting the volume of collected hydrogen into materials loss (1 mL H_2 gas = 0.001007 g dissolved Mg) using the following equation:

$$CR = \frac{87600 \times 0.001007 \times \Delta V}{\rho \cdot A \cdot t}$$

Where ΔV is the volume of H_2 in mL, A represents the exposed surface area in cm^2, t is the immersion duration in h, ρ is the density of the material in $g \cdot cm^{-3}$ and 87600 is the conversion factor to obtain the corrosion rate in mm/year.

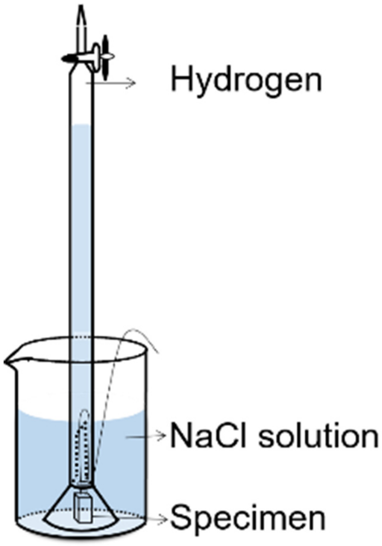

Figure 4.5 Schematic presentation of the set-up for hydrogen evolution tests.

4.3.6 Mechanical properties and integrity

The tensile and compressive properties of extruded (optimized) alloys were investigated before the study of mechanical integrity. Both tensile and compressive tests were conducted by a 50-kN static materials testing machine (Zwick/Roell Z050, Zwick GmbH & Co KG, Germany) at room temperature with a constant initial strain rate of 10^{-3} s^{-1} along the extrusion direction. The geometry of specimens for the tests is displayed in Figure 4.6. At least 3 samples were tested for repeatability. Fracture surfaces after tensile tests were examined by SEM in both SE and BSE modes.

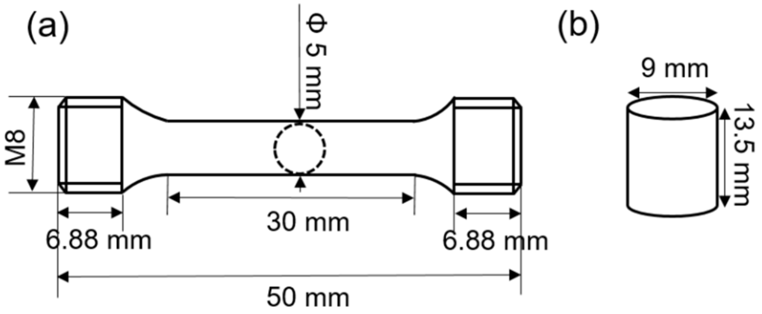

Figure 4.6 Geometry of specimens for (a) tensile and (b) compressive tests.

To study the mechanical integrity (only tensile properties) of optimized alloys, specimens were exposed to neutral salt spray for different time intervals (up to 42 days) according to ASTM B117 standard before the tensile tests. Only the gauge length parts were exposed for salt spray and the screw threads of the specimens were protected from corrosion with protective wax (beeswax/gum rosin= 9/7 in weight ratio). The corrosion exposure treatments were carried out in a salt spray chamber (Weiss SC/KWT 450-1000, Weiss Technik, Austria) at 35 °C with the fog generated from 5 *wt.*% NaCl solution. Macroscopic surface morphologies of specimens after salt spray tests were recorded by an OM equipped with a digital camera (Leica D-LUX 3, Leica Camera, Germany). Afterwards, tensile tests were carried out with the corroded specimens after the removal of the protective wax. For statistic purpose, at least 3 samples were measured. Fracture surfaces of corroded specimens were also checked by SEM.

4.3.7 Fatigue and corrosion fatigue behavior

An electrodynamic test system (MTS Acumen, MTS Systems Corporation, United States) was utilized to study the fatigue and corrosion fatigue behavior of optimized alloys. Figure 4.7 displays the geometry of the specimens for fatigue testing. An axial sinusoidal loading was applied at a frequency of 30 Hz. Normally, the test was continued until the specimen failed completely. If the specimen survived at one stress amplitude for up to 10^7 cycles, the measurement finished automatically. Consequently, this stress level was defined as the fatigue limit of the alloy. Fractural morphologies were studied by SEM in both SE and BSE modes to examine the initiation and growth of fatigue cracks.

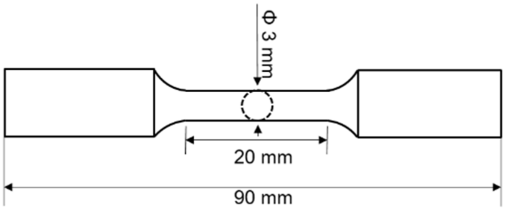

Figure 4.7 Geometry of specimens for fatigue and corrosion fatigue tests.

The corrosion fatigue behavior of optimized alloys was compared in two corrosive electrolytes at room temperature: 0.5 *wt.*% NaCl solutions prepared with DIW and ATW. The tests were conducted using a dynamic circulation system which consisted of a pump and an acrylic chamber. 800 mL solution was used for each test. The flow speed of the solution was controlled at 10 mL/min by using a clip on the tube to avoid the disturbance of too fast flow speed on the formation of the surface layer during testing. All corrosion fatigue tests started from the stress amplitude of the fatigue limit of a specific alloy in air. After the tests, fractured surfaces were cleaned in CrO_3 solution to remove the corrosion products and find the initiation sites of fatigue cracks.

4.3.8 Constant load test (stress corrosion cracking)

Constant load tests of the optimized alloys were carried out by deadweight load frames to characterize the susceptibility of the alloys to stress corrosion cracking (SCC). Four different corrosive electrolytes were used: DIW, ATW, 0.5 *wt.*% NaCl solutions prepared with DIW and ATW. During the tests, specimens were exposed to alternate cycles of 10 min immersion and 50 min drying at a loading of about 70 % of the yield strength of the specific alloy (100 MPa for Mg0.5Zn0.2Ca alloy, 125 MPa for Mg0.5Zn0.2Ge alloy and 110 MPa for Mg4Zn0.2Sn alloy). Loss of the electrolytes due to evaporation was replenished by topping up with deionized water. The standard testing duration was 30 days. Macroscopic surface appearance of tested samples were recorded with OM. If the specimen survived the entire testing duration, tensile test was further conducted on the specimen. If the specimen failed within 30 days, cross sections of the failed samples were checked by SEM.

5. Results

In order to investigate the influence of the ternary alloying element on Mg0.5Zn0.2X and Mg4Zn0.2X systems, the microstructures and corrosion behavior of Mg0.5Zn0.2X and Mg4Zn0.2X alloys were studied. Subsequently, the screened alloys with promising corrosion properties were extruded to further optimize the corrosion performance. The influence of extrusion speed was also investigated. Finally, a comprehensive investigation on the overall properties of the optimized alloys were carried out, including corrosion performance in different corrosive electrolytes, mechanical properties and integrity, fatigue and corrosion fatigue behavior and susceptibility to stress corrosion cracking.

5.1 Screening of as-cast Mg0.5Zn0.2X alloys

Second phases will precipitate when the solid solubility limit of the added alloying element in Mg is exceeded or when the solidification process is non-equilibrium. The maximum solubility of Zn and the added ternary elements in Mg is presented in Table 5.1. The formation of possible phases in Mg-Zn-X system is also displayed.

Table 5.1 Solid solutions and second phases of the studied Mg-Zn-X systems.

	Solid solubility in Mg (*wt.*%)		**Phases in Mg-Zn-X ternary system**	**Ref.**
	high temperature	**low temperature**		
Zn	6.4	1.6 (RT)	Mg_7Zn_3, MgZn, Mg_2Zn_3, $MgZn_2$, Mg_2Zn_{11}	[27-30]
Al	12.7	5 (250 °C)	$Mg_5Zn_2Al_2$, $Mg_{32}(Al, Zn)_{49}$, MgZn, $Mg_{17}Al_{12}$	[31, 32]
Ca	1.34	0.2 (RT)	Mg_2Ca, $Ca_2Mg_6Zn_3$, $Ca_2Mg_5Zn_{13}$	[33-35]
Ce	0.38	0.04 (200 °C)	$Mg_{12}Ce$, $Ce_2Mg_{53}Zn_{45}$, $CeMg_7Zn_{12}$	[36-38]
Ga	8.5	5 (300 °C)	Mg_5Ga_2, Mg_2Ga, MgGa, $MgGa_2$, Mg_2Ga_5	[39-42]
Gd	23.49	3.82 (200 °C)	$(Mg, Zn)_3Gd$, Mg_xZn_y	[43]
Ge	0.009	-	Mg_xZn_y, Mg_2Ge	[44]
Sn	14.85	0.17 (RT)	Mg_xZn_y, Mg_2Sn	[45, 46]
Y	12.0	2.5 (200 °C)	Mg_3Zn_3Y, Mg_3Zn_6Y, $Mg_{12}ZnY$, Mg_xZn_y	[16, 47, 48]

RT: room temperature

5.1.1 Microstructure

X-ray diffraction (XRD)

The phase compositions of as-cast Mg0.5Zn0.2X alloys were firstly determined by XRD, shown in Figure 5.1. The diffraction pattern of Mg0.5Zn0.2Ca alloy reveals a weak peak of Mg_2Ca phase and that of Mg0.5Zn0.2Ge alloy shows the peaks of Mg_2Ge phase besides the peaks of α-Mg phase. However, in the cases of the other alloys, only α-Mg phase peaks can be observed. Slight shift is observed for some α-Mg phase peaks in the diffraction patterns of some ternary Mg0.5Zn0.2X alloys, e.g. Mg0.5Zn0.2Y alloy, which can result from the mismatch of the atomic radius of the ternary alloying element compared with that of Mg.

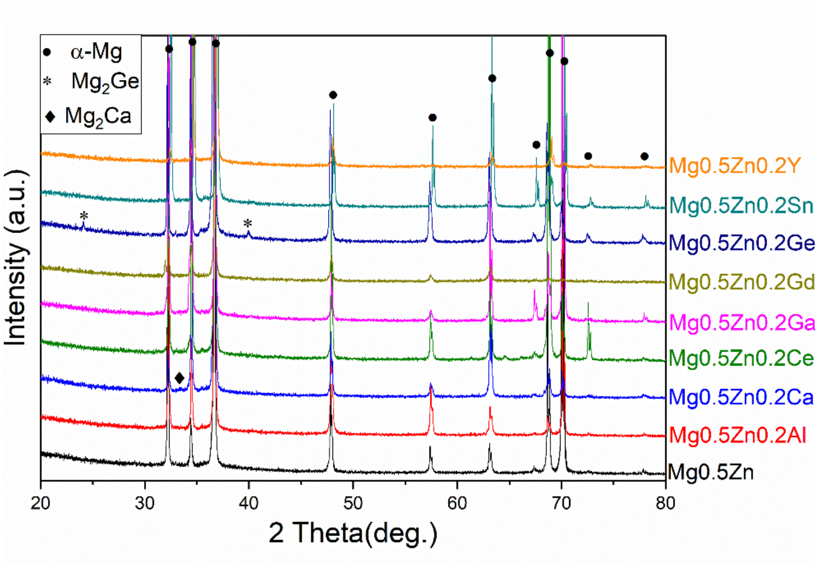

Figure 5.1 Phase compositions of as-cast Mg0.5Zn0.2X alloys determined by XRD.

Scanning electron microscopy (SEM) and energy dispersive X-ray spectroscopy (EDS)

The microstructures of as-cast Mg0.5Zn0.2X alloys are shown in Figure 5.2. In general, a small volume fraction of second phases is distributed on the grain boundaries and interdendritic spacings for all Mg0.5Zn0.2X alloys due to the low alloying addition amount. The morphologies of the second phases can be divided into four groups. For the first group composed of Mg0.5Zn (Figure 5.2a), Mg0.5Zn0.2Al (Figure 5.2b), Mg0.5Zn0.2Ce (Figure 5.2d), Mg0.5Zn0.2Ga (Figure 5.2e) and Mg0.5Zn0.2Sn (Figure 5.2h) alloys, fine spherical phases are observed. Eutectic phase exists in the microstructure of the second group containing only Mg0.5Zn0.2Ca alloy (Figure 5.2c). The bright and grey part of the eutectic phase shown in BSE images are marked as ‘A’ and ‘B’ (as denoted in the inserted image in Figure 5.2c) respectively for distinguishing. The third group consisting of Mg0.5Zn0.2Gd (Figure 5.2f) alloy contains both fine spherical and irregular phases. While in the last group including Mg0.5Zn0.2Ge (Figure 5.2g) and Mg0.5Zn0.2Y (Figure 5.2i) alloys, the second phases are in rod-like morphologies.

Since no second phases were detected by XRD for the studied as-cast Mg0.5Zn0.2X alloys except for Mg0.5Zn0.2Ca and Mg0.5Zn0.2Ge alloys, EDS point analysis was conducted on the second phases and the α-Mg matrix to clarify the expected second phase compositions. However, the EDS analysis results can be strongly affected by the size and penetration depth of the electron beam. As a result, the compositions of the second phases can only be qualitatively determined.

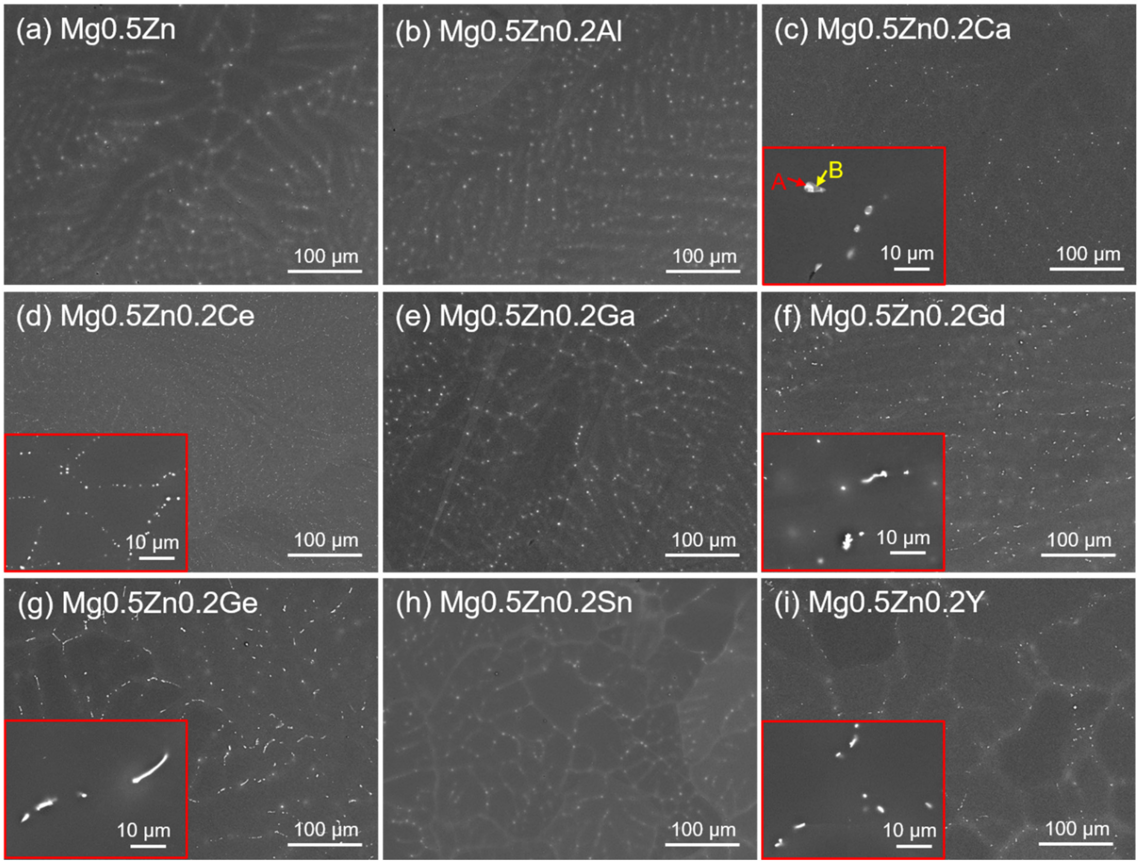

Figure 5.2 Microstructures imaged by SEM in BSE mode of as-cast Mg0.5Zn0.2X alloys.

According to the EDS analysis results listed in Table 5.2, silicon (Si) can be found in the second phases of several alloys with a relatively high variation while not detected in the α-Mg matrices. This can be a result of the contamination of Si from the casting process.

For as-cast Mg0.5Zn alloy, the Mg/Zn atomic ratio of the Mg-Zn binary phases is about 8:1. Considering the small size of these precipitates and the detection limitation of EDS analysis, these small spherical particles are simply referred as Mg_xZn_y phases.

The second phases in the microstructure of as-cast Mg0.5Zn0.2Al alloy contain 2.3 *at.*% Zn and 1.4 *at.*% Al, showing a Zn/Al atomic ratio at about 1.6, which can be $Mg_5Zn_2Al_2$ ternary phases according to the reported phase constituency for Mg-Zn-Al system listed in Table 5.1.

In the microstructure of as-cast Mg0.5Zn0.2Ca alloy, the bright phase 'A' contains higher content of Zn while the grey phase 'B' has a higher concentration of Ca. The atomic ratio of Zn to Ca for phase 'A' is about 1.7, which is close to the ideal ratio of 1.5 for the $Ca_2Mg_6Zn_3$ ternary phase. For the phase 'B', although a relatively higher content of Zn is detected compared to the α-Mg matrix, it is speculated to be Mg_2Ca phase according to the XRD result. Cha et al. [49] have reported that Zn can dissolve in Mg_2Ca phase and consequently stabilize this naturally active phase. Thus, the as-cast Mg0.5Zn0.2Ca alloy is composed of $Ca_2Mg_6Zn_3$ and Mg_2Ca eutectic phase, which is consistent with the reported references [49, 50],

For as-cast Mg0.5Zn0.2Ce alloy, a higher content of Ce (1.4 *at.*%) compared to Zn (0.6 *at.*%) is detected for the intermetallic particles. According to Table 5.1, those spherical phases are considered to be $Mg_{12}Ce$ phases.

Little work has been reported about the Mg-Zn-Ga system. However, considering the much higher contents of both Zn and Ga in the precipitates, it is supposed that these second phases may be Mg-Zn-Ga ternary phases, referred as Mg(Zn, Ga) phases.

Those irregular-shaped particles in as-cast Mg0.5Zn0.2Gd alloy have a composition of 0.3 *at.*% Zn and 0.9 *at.*% Gd. However, the content of Zn in the second phases is the same as the concentration of Zn in the Mg matrix, indicating that those particles should be binary Mg-Gd phases.

The rod-like precipitates in as-cast Mg0.5Zn0.2Ge alloy contain a high concentration of Ge (5.8 *at.*%) while a similar Zn content (0.2 *at.*%) to that of the Mg matrix, indicating that they are Mg_2Ge phases. This is in good agreement with the X-ray diffraction pattern of the alloy. Similarly shaped Mg_2Ge precipitates were also detected by other research groups [51-53]. Actually, a few spherical Mg_xZn_y phases also exist in Mg0.5Zn0.2Ge alloys.

As reported for the Mg-Zn-Sn system [54-56], no ternary phases can be formed, only binary Mg-Zn and/or Mg_2Sn phases. Consequently, the higher content of Zn (1.0 *at.*%) in the second phases compared to that of Sn (0.3 *at.*%) suggests that the particles may be Mg_xZn_y phases.

It has been revealed that the phase constituency in Mg-Zn-Y system is strongly dependent on the Zn/Y weight ratio for both low and high Zn containing alloys [16, 47, 57]. For the studied Mg0.5Zn0.2Y alloy, the Zn/Y weight ratio is 2.5. Theoretically, both $Mg_3Zn_3Y_2$ and Mg_3Zn_6Y exist in the alloy with this composition. However, the EDS results reveal that the atomic content of Y is 10.7 times higher than that of Zn in the precipitates of Mg0.5Zn0.2Y alloy, which is not representative of any reported ternary Mg-Zn-Y phases.

Table 5.2 Chemical compositions of different constituents in the microstructures of as-cast Mg0.5Zn0.2X alloys determined by EDS.

As-cast alloy	**Element**	**Second phase**		**α-Mg matrix**	
		at.%	***wt.%***	***at.%***	***wt.%***
Mg0.5Zn	Mg	84.9 ± 3.7	71.4 ± 6.4	99.9 ± 0.0	99.6 ± 0.0
	Zn	11.0 ± 3.6	24.6 ± 6.6	0.1 ± 0.0	0.4 ± 0.0
	Si	4.1 ± 1.7	4.0 ± 1.6	-	-
Mg0.5Zn0.2Al	Mg	90.9 ± 2.1	86.7 ± 1.9	99.5 ± 0.0	99.1 ± 0.0
	Zn	2.3 ± 0.6	5.9 ± 1.5	0.2 ± 0.0	0.5 ± 0.0
	Al	1.4 ± 0.2	1.4 ± 0.2	0.3 ± 0.0	0.4 ± 0.0
	Si	5.4 ± 2.6	6.0 ± 2.9	-	-

As-cast alloy	**Element**	**A-bright phase**		**B-grey phase**		**α-Mg matrix**	
		at.%	*wt.%*	*at.%*	*wt.%*	*at.%*	*wt.%*
Mg0.5Zn0.2Ca	Mg	83.8 ± 3.0	69.4 ± 4.6	85.9 ± 4.2	76.6 ± 6.1	99.6 ± 0.0	99.0 ± 0.0
	Zn	10.0 ± 1.6	22.1 ± 3.0	3.2 ± 1.1	7.5 ± 2.3	0.3 ± 0.0	0.8 ± 0.0
	Ca	6.2 ± 1.7	8.5 ± 2.2	10.9 ± 3.4	15.9 ± 4.4	0.1 ± 0.0	0.2 ± 0.0

As-cast alloy	**Element**	**Second phase**		**α-Mg matrix**	
		at.%	*wt.%*	*at.%*	*wt.%*
Mg0.5Zn0.2Ce	Mg	98.0 ± 0.4	91.0 ± 1.8	99.9 ± 0.0	99.7 ± 0.0
	Zn	0.6 ± 0.4	1.4 ± 0.9	0.1 ± 0.0	0.2 ± 0.0
	Ce	1.4 ± 0.4	7.6 ± 2.2	0.0 ± 0.0	0.1 ± 0.0
Mg0.5Zn0.2Ga	Mg	94.0 ± 2.7	88.0 ± 3.7	99.9 ± 0.0	99.7 ± 0.1
	Zn	2.0 ± 0.6	5.1 ± 1.4	0.1 ± 0.0	0.2 ± 0.1
	Ga	1.6 ± 0.8	4.3 ± 1.9	0.0 ± 0.0	0.1 ± 0.0
	Si	2.4 ± 2.8	2.6 ± 3.0	-	-
Mg0.5Zn0.2Gd	Mg	96.5 ± 1.4	91.5 ± 2.9	99.7 ± 0.1	99.1 ± 0.2
	Zn	0.3 ± 0.1	0.7 ± 0.2	0.3 ± 0.1	0.7 ± 0.1
	Gd	0.9 ± 0.3	5.3 ± 1.9	0.0 ± 0.0	0.2 ± 0.0
	Si	2.3 ± 1.1	2.5 ± 1.2	-	-
Mg0.5Zn0.2Ge	Mg	92.3 ± 1.4	82.4 ± 2.9	99.7 ± 0.0	99.3 ± 0.1
	Zn	0.2 ± 0.1	0.4 ± 0.2	0.2 ± 0.0	0.4 ± 0.0
	Ge	5.8 ± 1.1	15.5 ± 2.6	0.1 ± 0.0	0.3 ± 0.1
	Si	1.7 ± 0.4	1.7 ± 0.4	-	-
Mg0.5Zn0.2Sn	Mg	94.0 ± 1.8	90.8 ± 2.2	99.8 ± 0.0	99.5 ± 0.0
	Zn	1.0 ± 0.5	2.4 ± 1.4	0.1 ± 0.0	0.4 ± 0.0
	Sn	0.3 ± 0.0	1.5 ± 0.2	0.1 ± 0.0	0.1 ± 0.0
	Si	4.7 ± 1.8	5.3 ± 2.0	-	-
Mg0.5Zn0.2Y	Mg	96.5 ± 0.7	88.6 ± 2.2	99.9 ± 0.1	99.6 ± 0.1
	Zn	0.3 ± 0.1	0.8 ± 0.3	0.1 ± 0.0	0.3 ± 0.1
	Y	3.2 ± 0.7	10.6 ± 2.1	0.0 ± 0.0	0.1 ± 0.0

5.1.2 Corrosion performance

Open circuit potential (OCP) measurements

Addition of different ternary alloying elements affects the electrochemical properties of Mg0.5Zn system to different extent due to the formation of different solid solution and second phases. The OCP curves of Mg0.5Zn0.2X alloys after immersion in 0.9 *wt.*% NaCl solution for 30 min are displayed in Figure 5.3. Except Mg0.5Zn0.2Gd alloy, the OCP values of Mg0.5Zn0.2X alloys are lower than those of Mg0.5Zn alloy throughout the whole measurement. The curve of Mg0.5Zn0.2Sn alloy develops similarly to that of Mg0.5Zn alloy. The potential rapidly increases within less than 200 s and soon reaches a stable value during the rest testing period. The potential of Mg0.5Zn0.2Al, Mg0.5Zn0.2Ga and Mg0.5Zn0.2Gd alloys steeply climbs within the initial 100 s and then fluctuates with extended immersion time. Especially for Mg0.5Zn0.2Al alloy, a relatively bigger variation of the potential values is noticed during the measurement. Interestingly, the OCP values of Mg0.5Zn0.2Ca, Mg0.5Zn0.2Ce, Mg0.5Zn0.2Ge and Mg0.5Zn0.2Y alloys firstly drop within the initial 50 s and then gradually increase with prolonged immersion. The initial decrease of the OCP values may be due to the diffusion of the electrolyte into the oxide/hydroxide surface film formed in air or during the grinding process.

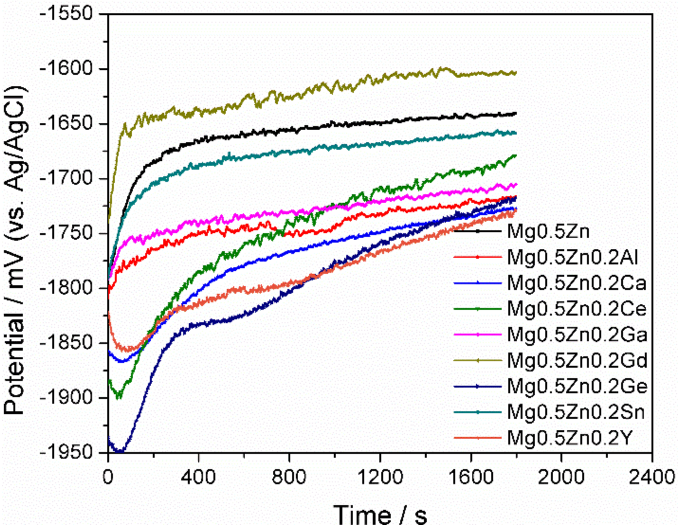

Figure 5.3 Open circuit potential curves of as-cast Mg0.5Zn0.2X alloys after immersion in 0.9 *wt.*% NaCl solution for 30 min at room temperature.

Potentiodynamic polarization measurements

Figure 5.4 depicts the potentiodynamic polarization curves for Mg0.5Zn0.2X alloys after conditioning at OCP in 0.9 *wt.*% NaCl solution for 30 min and 48 h at room temperature. At shorter conditioning time, the corrosion potentials shift negatively compared with Mg0.5Zn alloy after the addition of Al, Ca, Ce, Ga, Sn and Y. Especially, the addition of 0.2 *wt*.% Ca results in the largest potential shift of more than 100 mV. In contrast, the corrosion potentials of Mg0.5Zn0.2Gd and Mg0.5Zn0.2Ge alloys are more positive than that of Mg0.5Zn alloy. When the conditioning time increased to 48 h, the corrosion potentials of all alloys become more positive than those tested at shorter conditioning time. Moreover, only the corrosion potential of Mg0.5Zn0.2Gd alloy is still more positive than that of Mg0.5Zn alloy. For the anodic branches of the curves, the anodic current densities of Mg0.5Zn, Mg0.5Zn0.2Ce, Mg0.5Zn0.2Ga, Mg0.5ZnGd and Mg0.5Zn0.2Sn alloys steeply increase as the applied potential increases. Interestingly, a film breakdown potential is observed on the anodic polarization curves for Mg0.5Zn0.2Ca, Mg0.5Zn0.2Al, Mg0.5Zn0.2Ge and Mg0.5Zn0.2Y alloys. Especially, an extended low-current plateau region can be clearly observed on the anodic curves of Mg0.5Zn0.2Ca and Mg0.5Zn0.2Ge alloys, indicating that protective corrosion product films are formed on the alloy surfaces after 48 h and retard the anodic dissolution of the alloys.

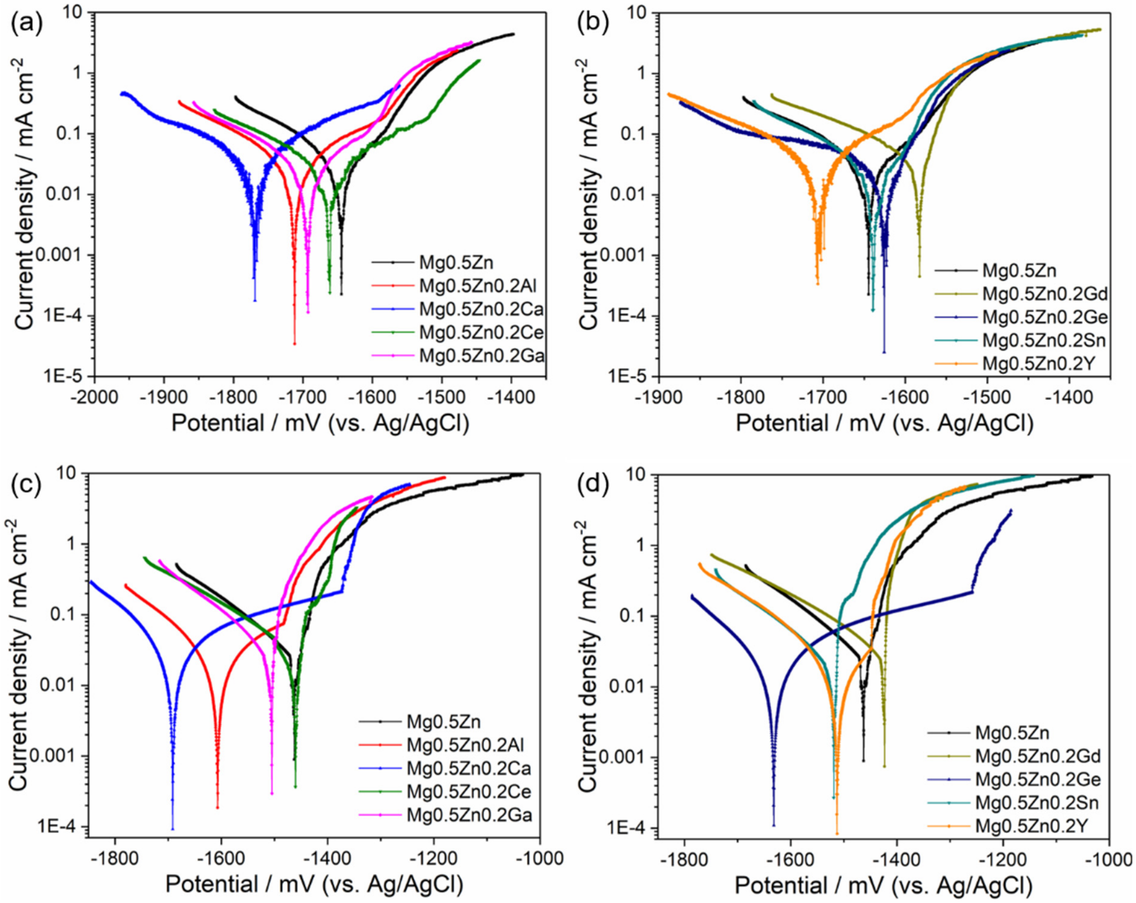

Figure 5.4 Potentiodynamic polarization curves of as-cast Mg0.5Zn0.2X alloys after OCP conditioning for (a, b) 30 min and (c, d) 48 h in 0.9 *wt.*% NaCl solution under ambient condition.

Table 5.3 presents the corrosion rates (*CR*) and corrosion current densities (i_{corr}) of Mg0.5Zn0.2X alloys derived from Figure 5.4. The corrosion rates are also summarized in Figure 5.5 to give a more intuitive comparison. However, the calculated corrosion rates and i_{corr} values inferred from the polarization curves of Mg alloys sometimes are not in accordance with those from other techniques and may not reflect the actual corrosion rates of Mg alloys. This is because of the unique 'negative difference effect' of Mg alloys during its dissolution and some other parasitic chemical/electrochemical reactions may concurrently occur at the Mg alloy surface [58, 59]. Actually, the most useful aspect of potentiodynamic polarization measurements of Mg alloys is to determine the relative changes in the branches that represent the anodic and cathodic kinetics [60]. Therefore, the calculated corrosion rates from polarization curves in this study are only used for a semi-quantitative approximation, which are combined with electrochemical impedance spectroscopy and hydrogen evolution results to clarify the corrosion properties of the alloys. When conditioned for 30 min, the corrosion rates of Mg0.5Zn0.2Ca, Mg0.5Zn0.2Ce and Mg0.5Zn0.2Ga alloys are lower than that of Mg0.5Zn alloy. When the conditioning time increased to 48 h, the corrosion rate of Mg0.5Zn0.2Ge alloy turns out to be the lowest one at 0.27 mm/year. In addition, Mg0.5Zn0.2Al, Mg0.5Zn0.2Ca, Mg0.5Zn0.2Ga, Mg0.5Zn0.2Sn and Mg0.5Zn0.2Y also show a lower corrosion rate than Mg0.5Zn alloy. The low-current plateau regions of Mg0.5Zn0.2Ca and Mg0.5Zn0.2Ge alloys extend over 250 mV.

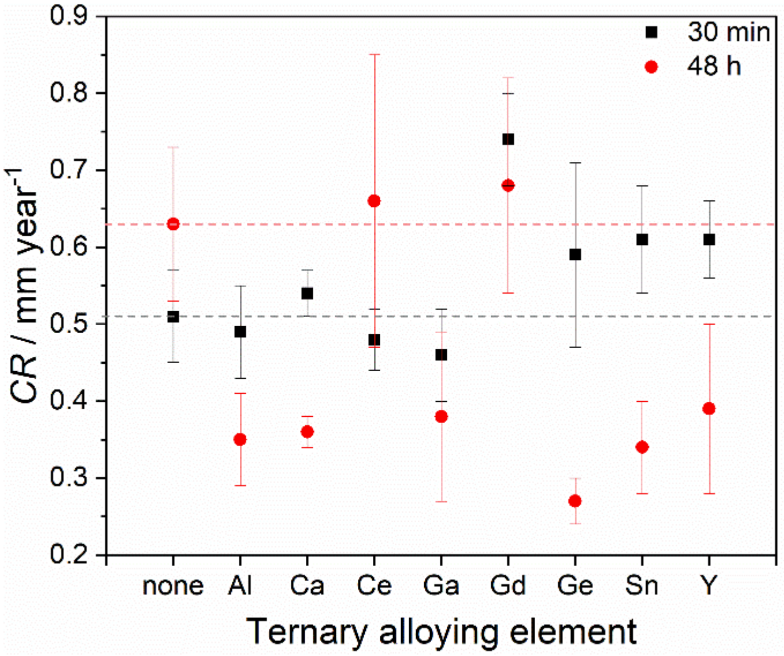

Figure 5.5 Comparison of the corrosion rates of as-cast Mg0.5Zn0.2X alloys calculated from the potentiodynamic polarization curves after conditioning at OCP for 30 min and 48 h in 0.9 *wt.*% NaCl solution.

Table 5.3 Measured and calculated parameters for the potentiodynamic curves of as-cast Mg0.5Zn0.2X alloys.

Conditioning time	**As-cast alloy**	***CR* / mm year^{-1}**	**i_{corr} / mA cm^{-2}**	**E_{corr} / mV**	**E_{bd} / mV**
30 min	Mg0.5Zn	0.51 ± 0.06	0.021 ± 0.004	-1647 ± 12	-
	Mg0.5Zn0.2Al	0.49 ± 0.06	0.021 ± 0.003	-1706 ± 7	-
	Mg0.5Zn0.2Ca	0.54 ± 0.03	0.023 ± 0.001	-1770 ± 17	-
	Mg0.5Zn0.2Ce	0.48 ± 0.04	0.021 ± 0.002	-1657 ± 6	-
	Mg0.5Zn0.2Ga	0.46 ± 0.06	0.020 ± 0.003	-1693 ± 13	-
	Mg0.5Zn0.2Gd	0.74 ± 0.06	0.032 ± 0.003	-1588 ± 4	-
	Mg0.5Zn0.2Ge	0.59 ± 0.12	0.026 ± 0.005	-1637 ± 12	-
	Mg0.5Zn0.2Sn	0.61 ± 0.07	0.027 ± 0.003	-1665 ± 20	-
	Mg0.5Zn0.2Y	0.61 ± 0.05	0.027 ± 0.002	-1701 ± 4	-
48 h	Mg0.5Zn	0.63 ± 0.1	0.028 ± 0.005	-1461 ± 22	-
	Mg0.5Zn0.2Al	0.35 ± 0.06	0.015 ± 0.002	-1571 ± 27	-1484 ± 54
	Mg0.5Zn0.2Ca	0.36 ± 0.02	0.016 ± 0.001	-1686 ± 23	-1416 ± 56
	Mg0.5Zn0.2Ce	0.66 ± 0.19	0.029 ± 0.008	-1462 ± 9	-
	Mg0.5Zn0.2Ga	0.38 ± 0.11	0.016 ± 0.004	-1520 ± 12	-
	Mg0.5Zn0.2Gd	0.68 ± 0.14	0.030 ± 0.006	-1436 ± 22	-
	Mg0.5Zn0.2Ge	0.27 ± 0.03	0.012 ± 0.001	-1627 ± 5	-1348 ± 61
	Mg0.5Zn0.2Sn	0.34 ± 0.06	0.015 ± 0.003	-1533 ± 12	-
	Mg0.5Zn0.2Y	0.39 ± 0.11	0.017 ± 0.005	-1542 ± 21	-1455 ± 33

Electrochemical impedance spectroscopy (EIS) measurements

Figure 5.6 exhibits the evolution of impedance spectra of as-cast Mg0.5Zn0.2X alloys with immersion time in 0.9 *wt.*% NaCl solution. Generally, the spectra can be divided into three groups according to the characteristics of the development: the first group contains Mg0.5Zn, Mg0.5Zn0.2Ce, Mg0.5Zn0.2Ga, Mg0.5Zn0.2Gd, Mg0.5Zn0.2Sn and Mg0.5Zn0.2Y alloys, the second group includes only Mg0.5Zn0.2Al alloy, while the third group consists of Mg0.5Zn0.2Ca and Mg0.5Zn0.2Ge alloys.

For the alloys in the first group, the Nyquist plots show two well-defined capacitive semicircles within 1 h, one in the high frequency region and another one in the middle frequency area. The capacitive loop at the high frequency region relates to the corrosion product films, while the loop at the middle frequency area owes to the electrochemical double layer capacitance connected in parallel to the charge transfer reaction at the interface of the metal surface and the electrolyte. However, with extended exposure in the corrosive electrolyte, the capacitive loop in the middle frequency range becomes less visible with some points scatter at lower frequencies, suggesting local active dissolution happens on the alloy surfaces. The impedance values fluctuate with immersion time at a low value (less than 500 Ω cm^2 except that of Mg0.5Zn0.2Sn alloy at 48 h).

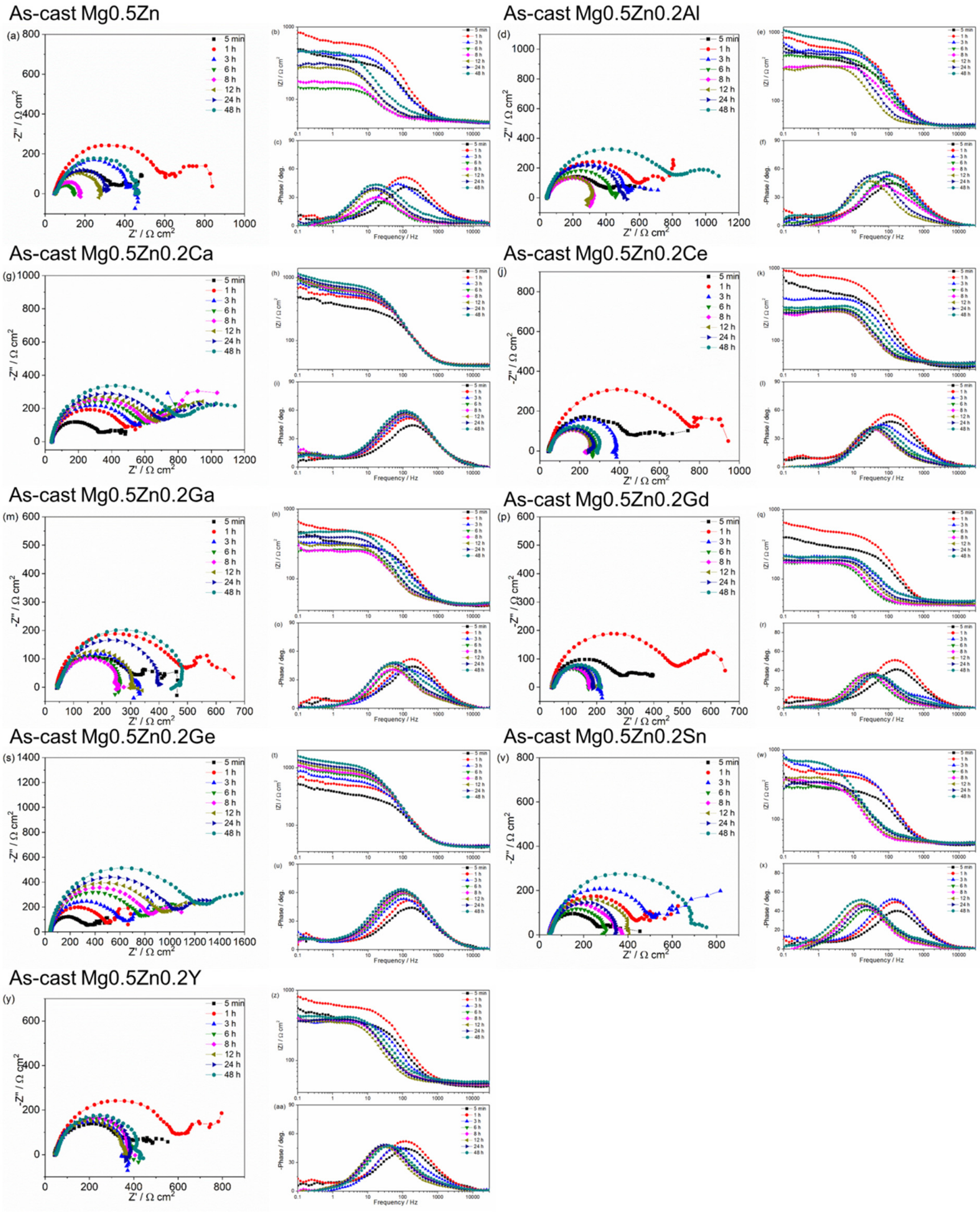

Figure 5.6 EIS spectra of as-cast Mg0.5Zn0.2X alloys tested in 0.9 *wt.*% NaCl solution for up to 48 h.

In the case of Mg0.5Zn0.2Al alloy (the second group), similar phenomenon is also observed. Active dissolution dominates the corrosion process after immersion for 3 h and the impedance value gradually decreases with prolonged immersion to be only about 300 Ω cm^2. However, after 12 h, the impedance value continually increases with exposure and the spectrum develops as two well-defined capacitive loops again at 48 h. This suggests that the corrosion product film formed on the surface of Mg0.5Zn0.2Al loses its protection to the substrate at the beginning but the active dissolution of the material is then retarded by the further formation or development of corrosion products.

Interestingly, for Mg0.5Zn0.2Ca and Mg0.5Zn0.2Ge alloys, the impedance spectra exhibit two well-defined relaxation processes throughout the entire measurement. In addition, the diameters of the capacitive loops gradually increase with immersion time. This suggests that the surface films formed on Mg0.5Zn0.2Ca and Mg0.5Zn0.2Ge alloys sufficiently protect the underneath substrates and the protective abilities of the films are enhanced with continued exposure. This is in good agreement with the polarization curves of Mg0.5Zn0.2Ca and Mg0.5Zn0.2Ge alloys after 48 h.

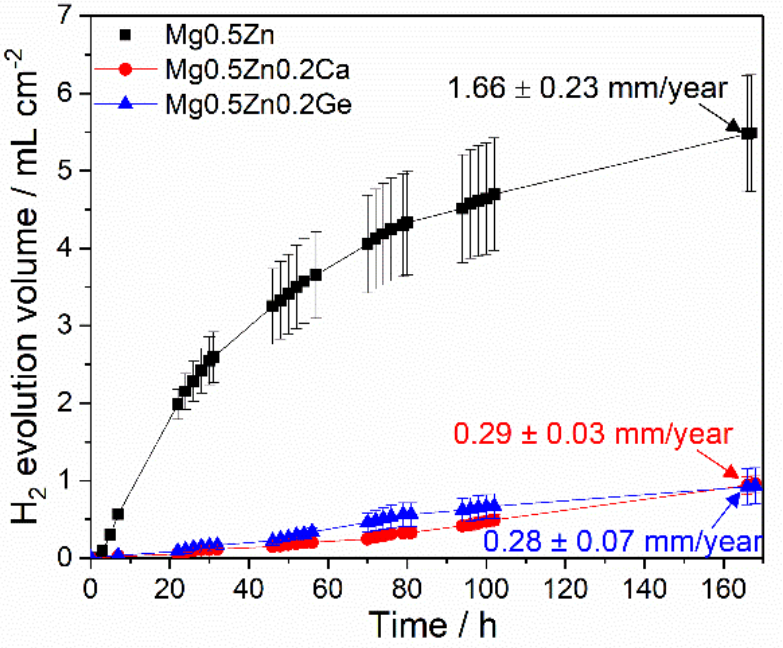

Figure 5.7 Hydrogen evolution results of as-cast Mg0.5Zn, Mg0.5Zn0.2Ca and Mg0.5Zn0.2Ge alloys after immersion in 0.9 *wt.*% NaCl solution for 168 h at room temperature.

By combining the potentiodynamic polarization curves and the impedance spectra, it is revealed that the corrosion properties of as-cast Mg0.5Zn0.2Ca and Mg0.5Zn0.2Ge alloys are the best during exposure to 0.9 *wt.*% NaCl solution among all as-cast Mg0.5Zn0.2X alloys, even better than the counterpart Mg0.5Zn0.2Al alloy. In order to confirm and provide a more holistic assessment of the corrosion rates of these two alloys, hydrogen evolution tests were conducted for Mg0.5Zn0.2Ca and Mg0.5Zn0.2Ge alloys for up to 168 h using Mg0.5Zn alloy as a reference, shown in Figure 5.7. Significant difference of hydrogen volume can be noted between Mg0.5Zn and Mg0.5Zn0.2Ca or Mg0.5Zn0.2Ge alloys. The evolved hydrogen volume of Mg0.5Zn0.2Ca and Mg0.5Zn0.2Ge alloys are similar and low while Mg0.5Zn alloy exhibits the greatest hydrogen evolution volume. The average corrosion rates calculated according to the collected hydrogen volume for Mg0.5Zn, Mg0.5Zn0.2Ca and Mg0.5Zn0.2Ge alloys after 168 h of immersion in 0.9 *wt.*% NaCl solution are 1.66 ± 0.23 mm/year, 0.29 ± 0.03 mm/year and 0.28 ± 0.07 mm/year, respectively. Significant improvement of corrosion resistance can be observed after the addition of Ca and Ge into Mg0.5Zn system. Therefore, Mg0.5Zn0.2Ca and Mg0.5Zn0.2Ge alloys were selected as the promising Mg0.5Zn0.2X alloys for further studies.

5.2 Screening of as-cast Mg4Zn0.2X alloys

5.2.1 Microstructure

Figure 5.8 presents the X-ray diffraction patterns of Mg4Zn0.2X alloys. However, only α-Mg phase is detected in Mg4Zn0.2X alloys except for Mg4Zn0.2Ge alloy. For Mg4Zn0.2Ge alloy, Mg_2Ge phase peaks are also observed. Considering the solid solubility of Zn and the ternary alloying elements in Mg listed in Table 5.1, more precipitates are expected in Mg4Zn0.2X alloys. The absent peaks of possible second phases may be a result of the detection limitation by resolution of XRD.

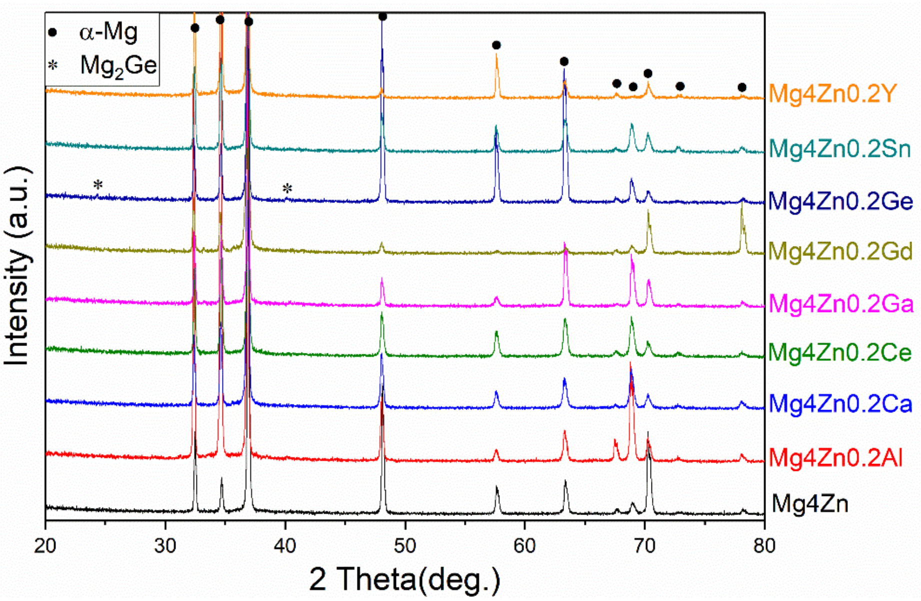

Figure 5.8 Phase compositions of as-cast Mg4Zn0.2X alloys determined by XRD.

The microstructures of Mg4Zn0.2X alloys are shown in Figure 5.9. Apparently, a higher volume fraction and larger sized second phases are formed when Zn content increases from 0.5 *wt.*% to 4 *wt.*% (compared with the micrographs of Mg0.5Zn0.2X alloys displayed in Figure 5.2). Moreover, obvious segregation of heavier element (Zn) at the particle-free interdendritic regions can be observed, indicated by the brighter contrast of those areas compared to the nearby α-Mg matrix in BSE images.

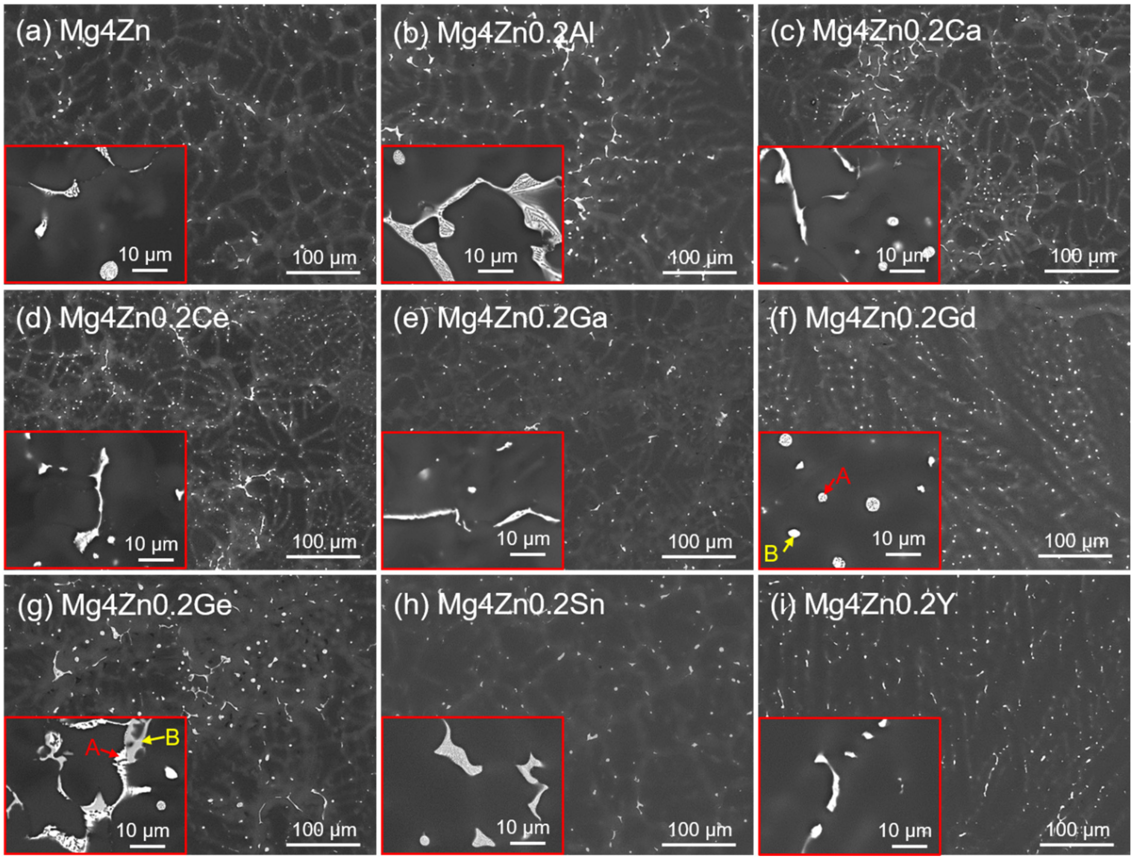

Figure 5.9 Microstructures imaged by SEM in BSE mode of as-cast Mg4Zn0.2X alloys.

The morphologies of the precipitates in the microstructures of Mg4Zn (Figure 5.9a), Mg4Zn0.2Al (Figure 5.9b) and Mg4Zn0.2Sn (Figure 5.9h) alloys are similar. Divorced eutectic compounds in irregular and circular shapes exist on the grain boundaries or interdendrite interstices. In comparison, stripe-like and granular integral second phases are noticed in Mg4Zn0.2Ca (Figure 5.9c), Mg4Zn0.2Ce (Figure 5.9d), Mg4Zn0.2Ga (Figure 5.9e) and Mg4Zn0.2Y (Figure 5.9i) alloys. Two distinct second phases are observed in Mg4Zn0.2Gd (Figure 5.9f) and Mg4Zn0.2Ge (Figure 5.9g) alloys. For Mg4Zn0.2Gd alloy, two kinds of granular particles exist in the microstructure. However, one is similar to those in Mg4Zn, Mg4Zn0.2Al and Mg4Zn0.2Sn alloys in divorced eutectic morphology (marked as 'A'), while another one is in integral type (marked as 'B'). In the case of Mg4Zn0.2Ge alloy, besides the irregular and circular divorced eutectic compounds (marked as ‘A’), another grey second phase (marked as ‘B’) is co-existing with the irregular divorced eutectic compounds.

EDS analysis was carried out to study the phase constituents in as-cast Mg4Zn0.2X alloys due to the limitation of XRD measurement (Table 5.4). Although the second phases are in two morphologies (irregular/stripe and circular shapes) in the alloys except those distinct different phases in Mg4Zn0.2Gd and Mg4Zn0.2Ge alloys, the EDS results indicate that the compositions of these irregular/stripe and circular particles are similar. As expected, a much higher content of Zn is detected in the brighter second phase-free interdendritic regions compared to the grey matrix dendrites. It is even higher than the solid solubility of Zn in Mg at room temperature, indicating the supersaturation of Zn at these places.

According to the atomic percentage composition, it seems that those second phases in Mg4Zn alloy are Mg_7Zn_3. However, due to the contribution of the α-Mg in the eutectic phase (α-Mg + Mg_xZn_y phase) and the underlying α-Mg matrix, the real concentration of Mg in the second phases analyzed by EDS can be largely affected. Based on the EDS and XRD results reported by Cai et al. [61], those Mg-Zn binary phases should be MgZn phases, which are formed by the decomposition of Mg_7Zn_3 phases at the eutectic temperature (325 °C). Similar results have also been reported in refs. [21, 62, 63].

For Mg4Zn0.2Al alloy, the morphologies of the second phases are almost the same as those of Mg4Zn alloy and the Mg/Zn atomic ratio is close to that of the second phase in Mg4Zn alloy. However, much higher concentration of Al is detected in second phases compared to the α-Mg matrix. Therefore, the particles in Mg4Zn0.2Al alloy are referred as Mg(Zn, Al) phases.

Given the 18.9 *at.*% content of Zn and 2.4 *at.*% content of Ca in the intermetallics of Mg4Zn0.2Ca alloy, the Zn/Ca atomic ratio of 7.9 is close to the ideal Zn/Ca ratio of 6.5 for $Ca_2Mg_5Zn_{13}$ phase in Mg-Zn-Ca system. Similar result (the morphology and phase constituency) is reported by Zhang et al. in the study of Mg4Zn1Ca (*wt.*%) alloy [27].

The stripe-like and granular precipitates in Mg4Zn0.2Ce alloy contain 18.0 *at.*% Zn and 1.7 *at.*% Ce, showing a Zn/Ce atomic ratio of 10.5, which may be $CeMg_7Zn_{12}$ ternary phase according to the phase constituency of Mg-Zn-Ce system.

Similar contents of Zn and Mg are revealed for the second phases in Mg4Zn0.2Ga alloy compared to those of Mg4Zn alloy. Those phases are thought to be MgZn phases despite the slightly higher concentration of Ga in the particles than that of the particle-free interdentritic area and the α-Mg matrix. The higher content of Ga in MgZn phase may be a result of the dissolution of Ga in the phase. It is noted that the morphology of the phase has been changed from divorced eutectic type to integral mode, which may be the effect of Ga.

Table 5.4 Chemical compositions of different constituents in the microstructures of as-cast Mg4Zn0.2X alloys determined by EDS.

As-cast Alloy	**Location**	**Element**					
		Mg		**Zn**		**alloying element**	
		at.%	***wt.%***	***at.%***	***wt.%***	***at.%***	***wt.%***
Mg4Zn (4Z)	EP	77.9 ± 3.0	56.9 ± 4.2	22.1 ± 3.0	43.1 ± 42	-	-
	BI	98.0 ± 0.3	94.8 ± 0.7	2.0 ± 0.3	5.2 ± 0.7	-	-
	α-Mg matrix	99.6 ± 0.0	98.8 ± 0.1	0.4 ± 0.0	1.2 ± 0.1	-	-
4Z-0.2Al	EP	79.7 ± 1.9	60.3 ± 2.8	19.1 ± 1.9	38.7 ± 2.7	1.2 ± 0.2	1.0 ± 0.1
	BI	97.6 ± 0.6	94.3 ± 1.3	2.1 ± 0.5	5.4 ± 1.2	0.3 ± 0.1	0.3 ± 0.1
	α-Matrix	99.3 ± 0.1	98.4 ± 0.2	0.5 ± 0.1	1.3 ± 0.1	0.2 ± 0.0	0.3 ± 0.0
4Z-0.2Ca	EP	78.7 ± 3.0	59.1 ± 4.4	18.9 ± 3.3	37.9 ± 5.0	2.4 ± 1.5	3.0 ± 1.8
	BI	98.2 ± 0.2	95.4 ± 0.6	1.7 ± 0.2	4.5 ± 0.6	0.1 ± 0.0	0.1 ± 0.0
	α-Matrix	99.6 ± 0.0	98.9 ± 0.1	0.4 ± 0.1	1.0 ± 0.1	0.0 ± 0.0	0.1 ± 0.0
4Z-0.2Ce	SP	80.3 ± 6.7	58.7 ± 9.1	18.0 ± 6.1	34.2 ± 7.7	1.7 ± 0.6	7.1 ± 1.5
	BI	98.2 ± 0.2	95.1 ± 0.6	1.8 ± 0.2	4.8 ± 0.6	0.0 ± 0.0	0.1 ± 0.0
	α-Matrix	99.5 ± 0.1	98.5 ± 0.1	0.5 ± 0.1	1.4 ± 0.1	0.0 ± 0.0	0.1 ± 0.0
4Z-0.2Ga	SP	77.1 ± 5.6	56.2 ± 7.8	22.4 ± 5.8	42.8 ± 8.2	0.5 ± 0.4	1.0 ± 0.9
	BI	98.0 ± 0.5	94.7 ± 1.4	1.8 ± 0.5	4.9 ± 1.3	0.2 ± 0.0	0.4 ± 0.1
	α-Matrix	99.4 ± 0.1	98.4 ± 0.4	0.5 ± 0.1	1.4 ± 0.3	0.1 ± 0.0	0.2 ± 0.1
4Z-0.2Gd	A-EP	79.2 ± 5.2	59.1 ± 7.9	20.7 ± 5.3	40.7 ± 8.0	0.1 ± 0.0	0.2 ± 0.1
	B-integral phase*	73.8 ± 7.9	49.5 ± 10.3	14.1 ± 7.7	23.9 ± 11.6	5.0 ± 1.7	21.2 ± 6.4
	α-Matrix	99.1 ± 0.0	97.7 ± 0.1	0.8 ± 0.0	2.2 ± 0.1	0.1 ± 0.0	0.1 ± 0.1
4Z-0.2Ge	A-bright EP	79.4 ± 2.9	59.1 ± 4.4	20.4 ± 2.9	40.5 ± 4.3	0.2 ±0.0	0.4 ±0.1
	B-integral phase*	86.1 ± 2.7	70.6 ±4.6	1.4 ± 0.3	3.2 ± 0.6	9.7 ± 2.1	23.6 ±4.0
	BI	97.9 ± 0.4	94.6 ±0.9	2.0 ± 0.4	5.2 ± 1.0	0.1 ± 0.0	0.2 ± 0.0
	α-Matrix	99.4 ± 0.0	98.5 ± 0.1	0.5 ± 0.0	1.3 ± 0.0	0.1 ± 0.0	0.2 ± 0.1
4Z-0.2Sn	EP	77.9 ± 1.1	56.6 ± 1.6	22.0 ± 1.4	43.1 ± 1.6	0.1 ± 0.0	0.3 ± 0.1
	BI	98.0 ± 0.2	94.7 ± 0.5	1.9 ± 0.2	4.9 ± 0.4	0.1 ± 0.0	0.4 ± 0.0
	α-Mg	99.4 ± 0.1	98.4 ± 0.3	0.5 ± 0.1	1.4 ± 0.3	0.1 ± 0.0	0.2 ± 0.0
4Z-0.2Y	SP	87.4 ± 1.9	71.9 ± 3.6	12.2 ± 1.7	26.8 ± 3.2	0.4 ± 0.3	1.3 ± 1.1
	α-Matrix	99.0 ± 0.0	97.5 ± 0.0	0.9 ± 0.0	2.4 ± 0.0	0.0 ± 0.0	0.1 ± 0.0

Note: EP: Eutectic phase, SP: Second phase, BI: Bright interdendrite.
* This phase contains a small amount of Si (for Mg4Zn0.2Gd: 7.1 ± 2.6 (*at.*%) or 5.4 ± 1.8 (*wt.*%), for Mg4Zn0.2Ge: 2.8 ± 0.5 (*at.*%) or 2.6 ± 0.3 (*wt.*%)).

For Mg4Zn0.2Gd alloy, two distinct phases are revealed. The divorced granular particles (phase A) displaying similar morphologies to those in Mg4Zn alloy also show similar contents of Mg and Zn, suggesting that they are MgZn phases. The concentration of Gd in these phases is the same as that in the Mg matrix, further confirming the formation of MgZn phases. While for the integral phases (phase B), a much higher content of Gd is detected. Moreover, the Zn/Gd atomic ratio is 2.8 and very close to the ideal ratio of 3 for the $(Mg, Zn)_3Gd$ ternary phase in the Mg-Zn-Gd system. Therefore, phase B is considered to be $(Mg, Zn)_3Gd$ phase.

Similar phenomenon is also observed for Mg4Zn0.2Ge alloy. Those divorced eutectic phases exhibit similar contents of Mg and Zn as those of Mg4Zn alloy, with a close concentration of Ge to that of the α-Mg matrix. Therefore, phase A should be MgZn phase. In comparison, phase B shows much higher concentration of Ge and the content of Zn in that phase is even slightly lower than that of the supersaturated interdendritic region. Consequently, those grey integral phases are Mg_2Ge phases, which are detected by XRD.

A same amount of Sn is revealed in the α-Mg matrix, particle-free interdendritic area as well as in the second phases. Additionally, the concentrations of Mg and Zn in the divorced eutectic phases are really close to those in Mg4Zn alloy, indicating that they are MgZn phases.

The Zn/Y weight ratio is 20 for the studied Mg4Zn0.2Y alloy, under which circumstance mainly binary Mg-Zn phases would form [16]. EDS analysis shows that the precipitates contain 87.4 *at.*% Mg, 12.2 *at.*% Zn and 0.4 *at.*% Y, suggesting that they are MgZn phases with some dissolved Y.

5.2.2 Volta potential difference

Figure 5.10 illustrates the Volta potential distribution across typical precipitates in Mg4Zn0.2X alloys, which was measured to facilitate the understanding of the corrosion behavior of the alloys and the influence of phase constituency on the corrosion behavior. During the polishing process, the softer Mg matrix was removed preferentially, resulting in harder precipitates protruding the average surface. In the Volta potential map, the bright region corresponds to a more positive potential, while the dark area corresponds to a more negative potential.

Obviously, according to the Volta potential map in Figure 5.10, all second phases precipitated in Mg4Zn0.2X alloys exhibit a higher Volta potential compared with the surrounding matrix, indicating that these second phases are nobler than the α-Mg matrix. Moreover, slightly higher Volta potential can also be noted for the matrix surrounding the second phases when compared with the matrix that is a bit further away from the second phases. This is especially obvious in the Volta potential map of Mg4Zn and Mg4Zn0.2Sn alloys. Consequently, it can be speculated that the second phases would be the most stable when the alloy is immersed in corrosive electrolyte, followed by Zn-rich interdendritic regions and the α-Mg dendrites (matrix). Galvanic couples may be formed between intermetallics as possible cathodes with both intermetallic-free regions (Zn-rich interdendritic region and α-Mg matrix) as possible anode and between Zn-rich interdendritic area (cathode) and normal α-Mg matrix (anode).

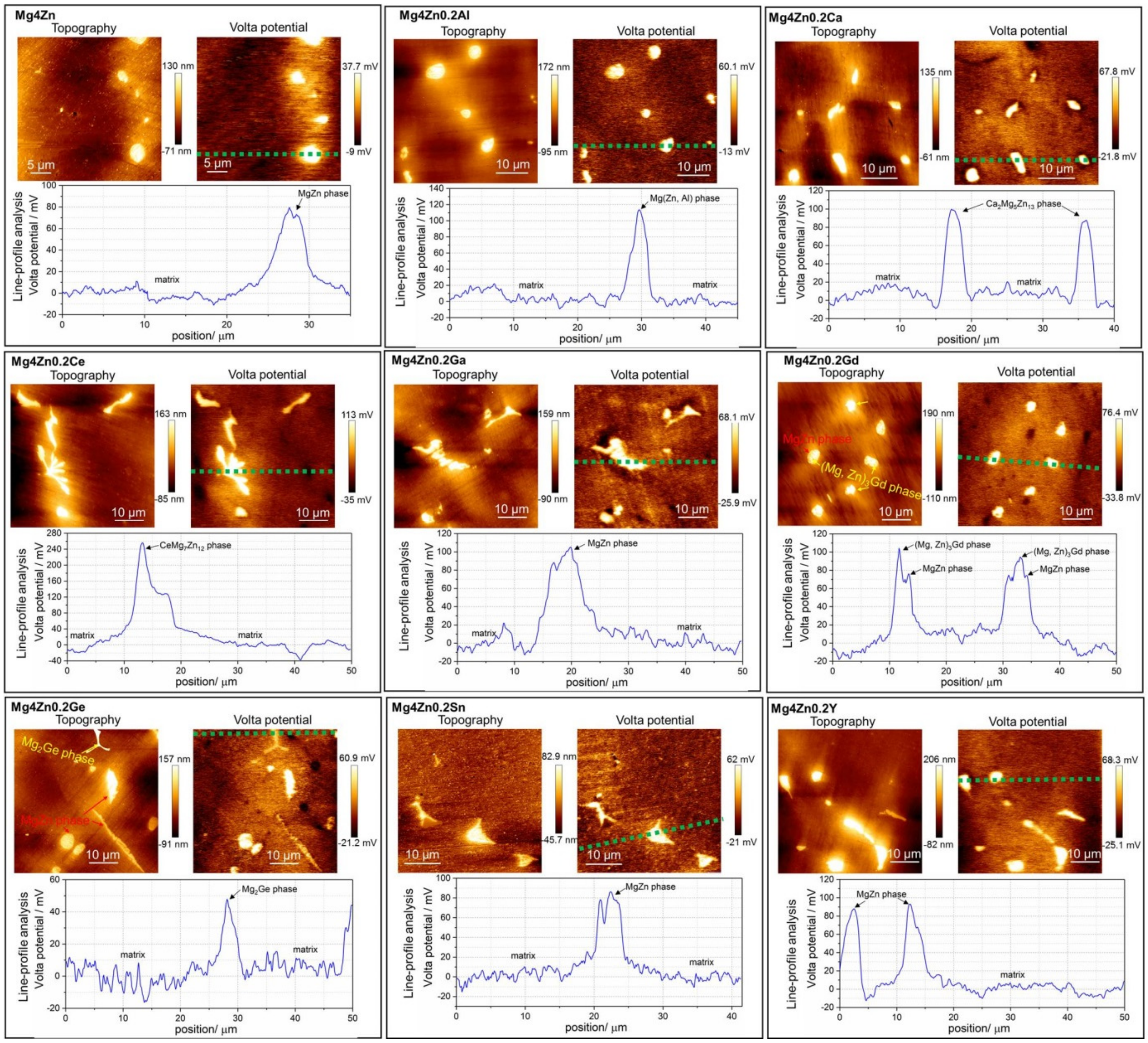

Figure 5.10 SKPFM studies of as-cast Mg4Zn0.2X alloys including topography map, surface Volta potential map and line-profile analysis of relative Volta potential through second phases.

Interestingly, the MgZn and (Mg, Zn)$_3$Gd phases in Mg4Zn0.2Gd alloy measured by SKFPM present co-existing morphology instead of the separated characteristic in the inserted image of Figure 5.9f. Actually, similar MgZn-(Mg, Zn)$_3$Gd co-existing phases were also observed by SEM with high magnification, as shown in Figure 5.11.

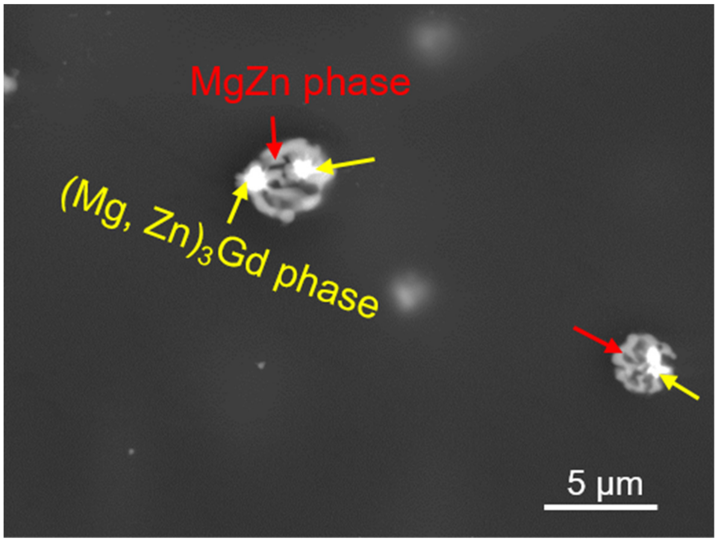

Figure 5.11 Co-existing MgZn-(Mg, Zn)$_3$Gd phases in as-cast Mg4Zn0.2Gd alloy imaged by SEM in BSE mode.

Table 5.5 Average Volta potential difference between second phases and the α-Mg matrix.

As-cast alloy	Second phase	Relative Volta potential / mV
Mg4Zn	MgZn	81 ± 16
Mg4Zn0.2Al	Mg(Zn, Al)	111 ± 16
Mg4Zn0.2Ca	$Ca_2Mg_5Zn_{13}$	91 ± 13
Mg4Zn0.2Ce	$CeMg_7Zn_{12}$	226 ± 60
Mg4Zn0.2Ga	MgZn	96 ± 16
Mg4Zn0.2Gd	MgZn	85 ± 13
	(Mg, Zn)$_3$Gd	123 ± 22
Mg4Zn0.2Ge	MgZn	86 ± 11
	Mg_2Ge	48 ± 7
Mg4Zn0.2Sn	MgZn	86 ± 26
Mg4Zn0.2Y	MgZn	95 ± 16

The average Volta potential difference between the second phases and the matrix is listed in Table 5.5, combined with the information of phase constituency as well. It is revealed that the $CeMg_7Zn_{12}$ phase in Mg4Zn0.2Ce alloy has the highest Volta potential difference of 226 ± 60 mV, successively followed by (Mg, Zn)$_3$Gd phase (123 ± 22 mV) in Mg4Zn0.2Gd alloy and Mg(Zn, Al) (111 ± 16 mV) phase in Mg4Zn0.2Al alloy, respectively. In contrast, the Volta potential difference of Mg_2Ge phase in Mg4Zn0.2Ge alloy is the lowest one with 48 ± 7 mV. The Volta potential difference of MgZn phase in Mg4Zn alloy is 81 ± 16 mV, close to that of MgZn phases in Mg4Zn0.2Gd, Mg4Zn0.2Ge and Mg4Zn0.2Sn alloys. However, the Volta potential difference of MgZn phase in Mg4Zn0.2Ga (96 ± 16 mV) and Mg4Zn0.2Y (95 ± 16 mV) alloys is relatively higher, which is even close to that of the $Ca_2Mg_5Zn_{13}$ phase (91 ± 13) in Mg4Zn0.2Ca alloy. This can be explained by the dissolution of Ga and Y in the MgZn phases as revealed above by the EDS analysis. Normally, the higher the Volta potential difference is, the stronger the micro-galvanic effect can be. As a result, the strongest galvanic corrosion can be expected in Mg4Zn0.2Ce alloy while the galvanic couple should be weak in Mg4Zn0.2Ge alloy. However, herein caution should be paid because SKPFM measurements were carried out in air, while the corrosion tests were performed in aqueous solution. Moreover, the potential values measured by SKPFM are useful for determining the relative local cathode sites but is confined to kinetic interpretations [64]. Last but not least, the volume fraction, distribution and number of species of second phases can also significantly affect the corrosion performance of alloys in corrosive electrolyte. For example, alloys with single second phase normally exhibit better corrosion resistance than alloys with two kinds of second phases [47, 65].

5.2.3 Corrosion performance

Open circuit potential (OCP) measurements

The OCP curves of as-cast Mg4Zn0.2X alloys after immersion in 0.9 *wt.*% NaCl solution for 30 min are shown in Figure 5.12. All curves reveal similar characteristic. The OCP values gradually increase with extended immersion time throughout the entire testing period. After about 200 s, except that of Mg4Zn0.2Ca alloy, the potential of the other Mg4Zn0.2X alloys is higher than that of Mg4Zn alloy.

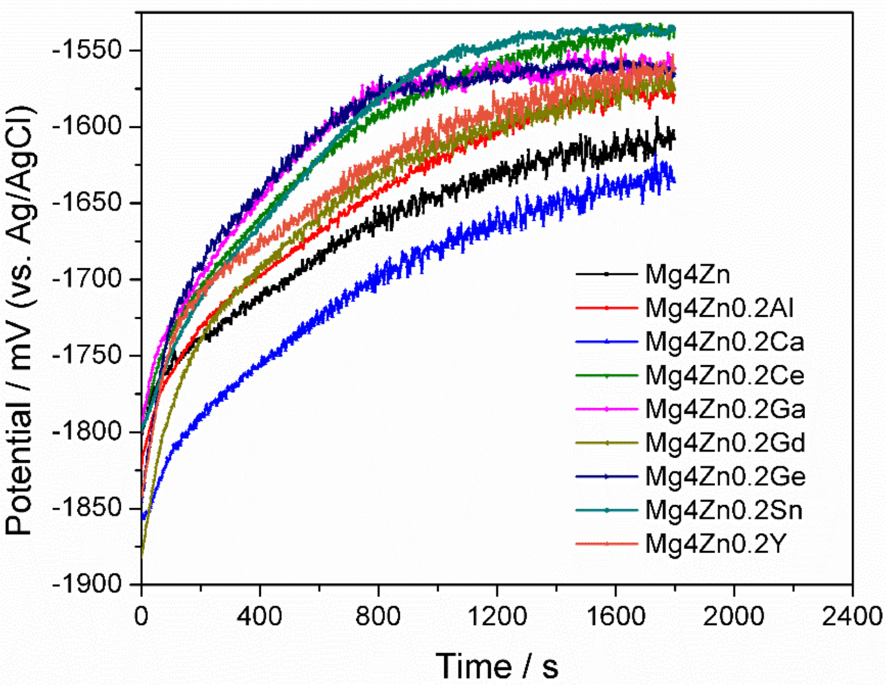

Figure 5.12 Open circuit potential (OCP) curves of as-cast Mg4Zn0.2X alloys after immersion in 0.9 *wt.*% NaCl solution for 30 min at room temperature.

Potentiodynamic polarization measurements

Figure 5.13 presents the potentiodynamic polarization curves of Mg4Zn0.2X alloys after conditioning at OCP for 30 min and 48 h in 0.9 *wt.*% NaCl solution, respectively. Addition of the ternary alloying elements enhance the corrosion potential of Mg4Zn alloy except Ca after conditioning for 30 min. After longer conditioning time, all corrosion potentials positively shift. In addition, some alloys show a bit more negative potential than Mg4Zn alloy besides Mg4Zn0.2Ca alloy, such as Mg4Zn0.2Gd and Mg4Zn0.2Y alloys, which should be caused by the formation of corrosion products due to the dissolution processes of the alloys in NaCl solution. For all anodic branches of the polarization curves, the current density increases steeply with increasing potential, showing no low-current plateau region nor obvious film breakdown potential, irrespective of how long the conditioning time was. This indicates that the corrosion product films formed on Mg4Zn0.2X alloy surfaces possess no protection or retardation to the dissolution of the alloys.

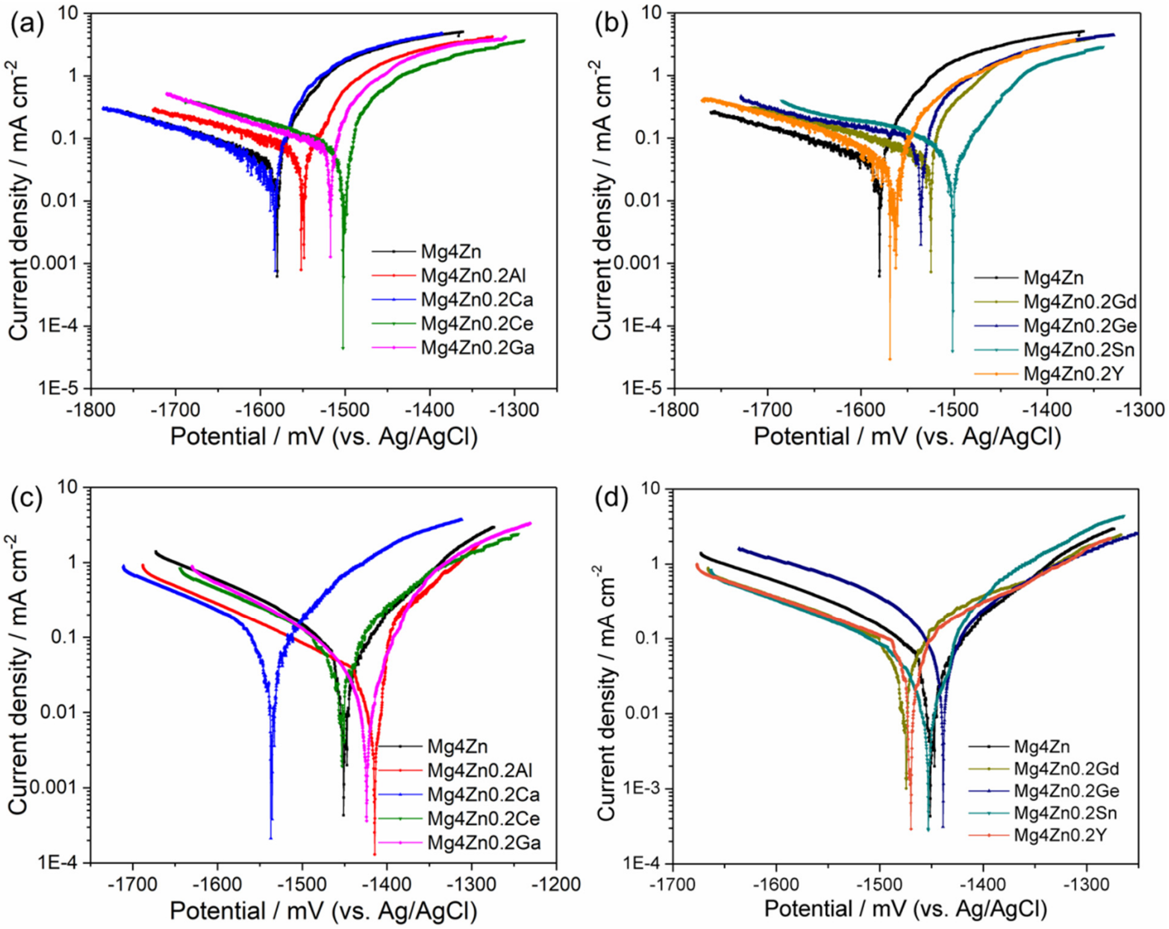

Figure 5.13 Potentiodynamic polarization curves of as-cast Mg4Zn0.2X alloys after OCP conditioning for (a, b) 30 min and (c, d) 48 h in 0.9 *wt.*% NaCl solution under ambient condition.

Table 5.6 Measured and calculated parameters for the potentiodynamic curves of as-cast Mg4Zn0.2X alloys.

Conditioning time	As-cast alloy	CR / mm year^{-1}	i_{corr} / mA cm^{-2}	E_{corr} / mV	E_{bd} / mV
30 min	Mg4Zn	0.98 ± 0.07	0.043 ± 0.003	-1582 ± 15	-
	Mg4Zn0.2Al	1.51 ± 0.10	0.066 ± 0.004	-1543 ± 16	-
	Mg4Zn0.2Ca	0.74 ± 0.11	0.032 ± 0.005	-1588 ± 9	-
	MgZn0.2Ce	1.23 ± 0.36	0.054 ± 0.016	-1502 ± 3	-
	Mg4Zn0.2Ga	1.73 ± 0.32	0.076 ± 0.014	-1525 ± 9	-
	Mg4Zn0.2Gd	1.02 ± 0.19	0.045 ± 0.08	-1532 ± 9	-
	Mg4Zn0.2Ge	2.41 ± 0.33	0.11 ± 0.01	-1520 ± 13	-
	Mg4Zn0.2Sn	1.56 ± 0.24	0.068 ± 0.11	-1501 ± 5	-
	Mg4Zn0.2Y	1.05 ± 0.17	0.046 ± 0.008	-1560 ± 10	-
48 h	Mg4Zn	1.13 ± 0.23	0.050 ± 0.010	-1450 ± 2	-
	Mg4Zn0.2Al	0.60 ± 0.07	0.026 ± 0.003	-1418 ± 12	-
	Mg4Zn0.2Ca	2.11 ± 0.50	0.092 ± 0.022	-1529 ± 7	-
	MgZn0.2Ce	1.19 ± 0.40	0.051 ± 0.018	-1462 ± 9	-
	Mg4Zn0.2Ga	0.61 ± 0.18	0.027 ± 0.08	-1421 ± 7	-
	Mg4Zn0.2Gd	1.45 ± 0.22	0.063 ± 0.010	-1464 ± 14	-
	Mg4Zn0.2Ge	2.58 ± 0.55	0.11 ± 0.02	-1439 ± 6	-
	Mg4Zn0.2Sn	1.08 ± 0.32	0.047 ± 0.014	-1464 ± 6	-
	Mg4Zn0.2Y	1.82 ± 0.07	0.080 ± 0.003	-1469 ± 11	-

The measured and calculated parameters derived from the polarization curves in Figure 5.13 are listed in Table 5.6. The corrosion rates are compared as a function of alloying elements, shown in Figure 5.14. When conditioned for 30 min, only Mg4Zn0.2Ca alloy (0.74 ± 0.11 mm/year) shows a lower corrosion rate than Mg4Zn alloy (0.98 ± 0.07 mm/year). With extended conditioning time, the corrosion rates of Mg4Zn0.2Al, Mg4Zn0.2Ga and Mg4Zn0.2Sn alloys decrease and are lower than that of Mg4Zn alloy while the other alloys show the inversed trend. Moreover, the corrosion rate of Mg4Zn0.2Ge alloy is the highest one irrespective of the conditioning time.

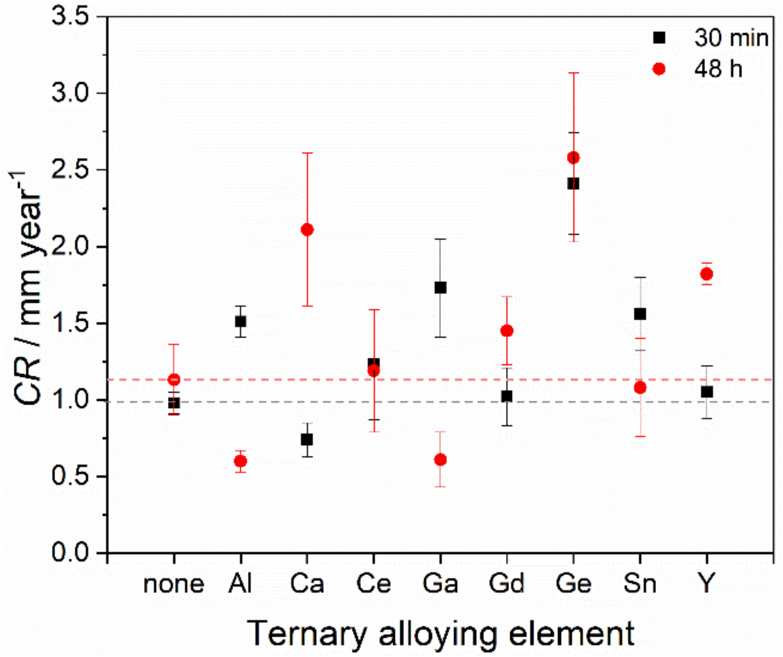

Figure 5.14 Comparison of the corrosion rates of as-cast Mg4Zn0.2X alloys calculated from the potentiodynamic polarization curves after conditioning at OCP for 30 min and 48 h in 0.9 *wt.*% NaCl solution.

Figure 5.15 presents the impedance spectra of Mg4Zn0.2X alloys immersed in 0.9 *wt.*% NaCl solution for up to 48 h. All spectra reveal a similar trend irrespective of the alloy. The spectra after immersion for 5 min show two clear capacitive loops. However, the data points are scattered at low frequencies. With further immersion for 1 h, the loop in the low frequency area becomes much less defined, even though the impedance value increases to some extent for several alloys. Extended immersion results in lower impedance values and almost invisible loop in the lower frequency region. This behavior suggests that active dissolution of the substrates dominates already as soon as the immersion started and the surface films formed on Mg4Zn0.2X alloys are not protective. This is in accordance with the potentiodynamic polarization results. For the development of the spectra after 3 h, Mg4Zn, Mg4Zn0.2Al, Mg4Zn0.2Ca and Mg4Zn0.2Ce alloys exhibit gradually decreased corrosion resistance. The impedance values decline to be only about 200 Ω cm^2 after 48 h. In comparison, the impedance values of Mg4Zn0.2Ga, Mg4Zn0.2Gd, Mg4Zn0.2Ge, Mg4Zn0.2Sn and Mg4Zn0.2Y alloys fluctuate with immersion time. Especially for Mg4Zn0.2Sn alloy, a relative stable impedance fluctuation at around 400 Ω cm^2 is revealed. The poorest corrosion resistance is observed for Mg4Zn0.2Ge alloy.

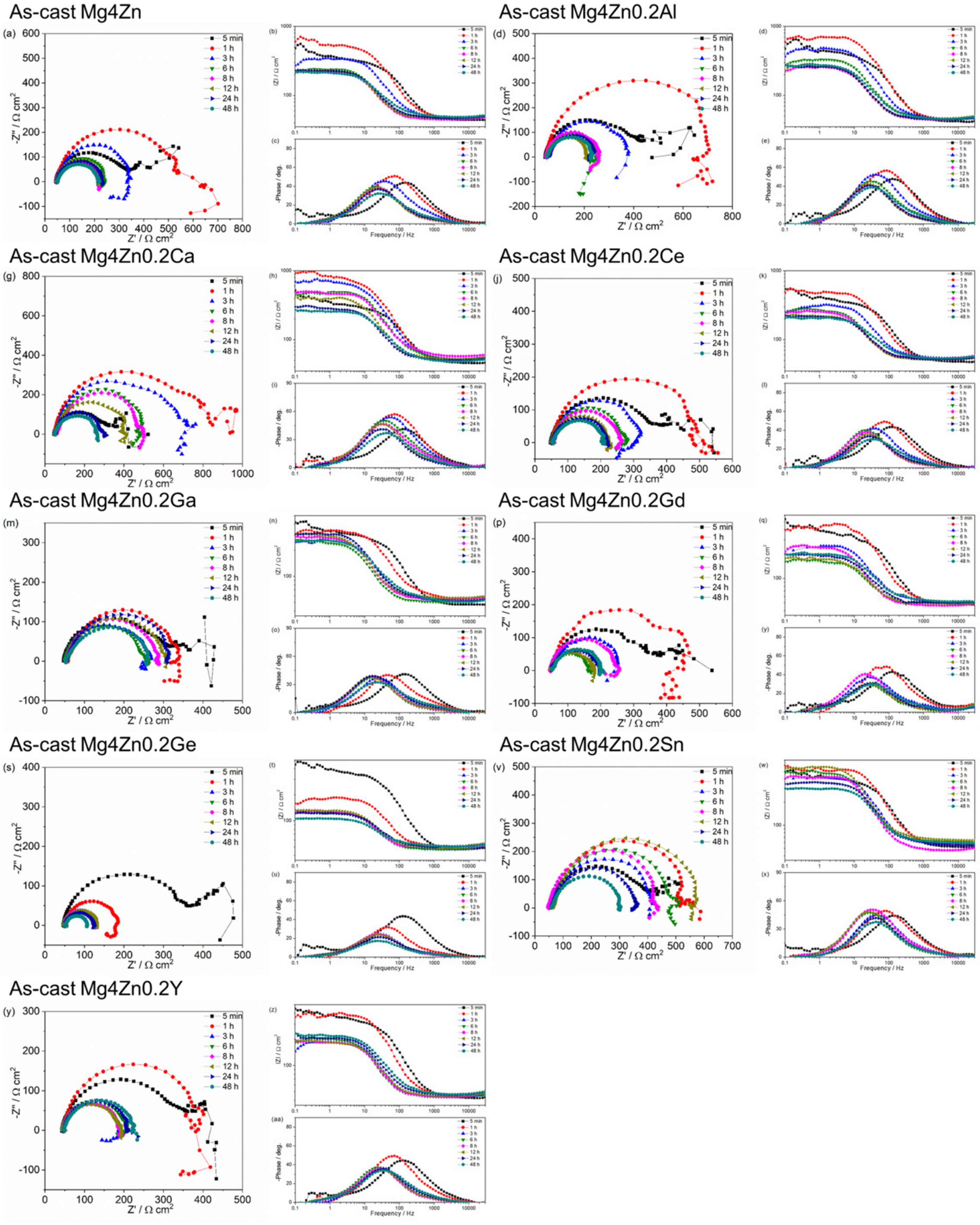

Figure 5.15 EIS spectra of as-cast Mg4Zn0.2X alloys tested in 0.9 *wt.*% NaCl solution for up to 48 h.

The decreased corrosion rate after prolonged OCP conditioning time and the fluctuation of impedance value at around 400 Ω cm^2 of Mg4Zn0.2Sn alloy demonstrate that the surface film formed on this alloy imparts potential protection to the material compared with the other Mg4Zn0.2X alloys. Therefore, hydrogen evolution tests were carried out for Mg4Zn0.2Sn alloy in 0.9 *wt.*% NaCl solution for up to 168 h to confirm the corrosion property of this alloy, in comparison with those of Mg0.5Zn and Mg4Zn alloys, shown in Figure 5.16. Apparent difference can be noted between the hydrogen evolution curves of Mg4Zn and Mg4Zn0.2Sn alloys. The curve develops more and more steep for Mg4Zn alloy while it is more gradual (almost linear) for Mg4Zn0.2Sn alloy. The latter evolved even less hydrogen volume than Mg0.5Zn alloy before 168 h. The corrosion rate calculated according to the evolved volume of hydrogen after 168 h is 6.03 ± 0.37 mm/year for Mg4Zn alloy and 1.73 ± 0.09 mm/year for Mg4Zn0.2Sn alloy (close to that of Mg0.5Zn alloy), respectively, revealing the significant improvement of corrosion resistance by the micro-addition of Sn for Mg4Zn system. Consequently, Mg4Zn0.2Sn alloy was selected as the promising Mg4Zn0.2X alloy for the following detailed study.

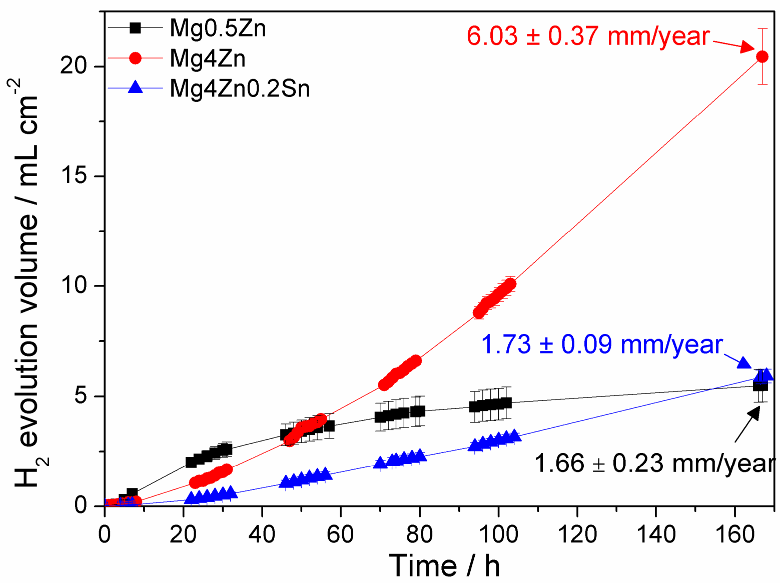

Figure 5.16 Hydrogen evolution results of as-cast Mg4Zn and Mg4Zn0.2Sn alloys after immersion in 0.9 *wt.*% NaCl solution for 168 h at room temperature.

By comparing the electrochemical results of Mg0.5Zn0.2X and Mg4Zn0.2X systems, it can be concluded that the corrosion behavior of Mg4Zn0.2X alloy is normally poorer than that of Mg0.5Zn0.2X alloy with the same ternary alloying element. This can be a result of the increased volume fraction of second phases.

5.3 Wrought processing of selected alloy

According to the above screening investigation, Mg0.5Zn0.2Ca, Mg0.5Zn0.2Ge and Mg4Zn0.2Sn alloys were selected as the most promising alloys regarding to corrosion performance compared with the other studied Mg0.5Zn0.2X and Mg4Zn0.2X alloys. Consequently, these three alloys were prepared by indirect chill casting in larger volume and subsequently wrought processed (hot extrusion), aiming at further improving the corrosion and mechanical properties of the alloys. Extrusion speed, temperature and ratio can affect the microstructures and properties of Mg alloys. In this study, only the influence of extrusion speed was investigated.

5.3.1 Microstructure

Mg0.5Zn0.2Ca alloy

Figure 5.17a-c depicts the recalculated inverse pole figures parallel to the extrusion direction of Mg0.5Zn0.2Ca alloys extruded at 0.6, 2.2 and 4.4 mm/s, respectively. It is noted that the extrusion speed does not obviously influence the texture of Mg0.5Zn0.2Ca alloy. The textures formed at different extrusion speeds show similar characteristics. The strongest intensity of the texture is only about 2.2 and it exhibits the preferred orientation of basal planes parallel to the extrusion direction. Such texture is typical for extruded Mg alloys [66, 67].

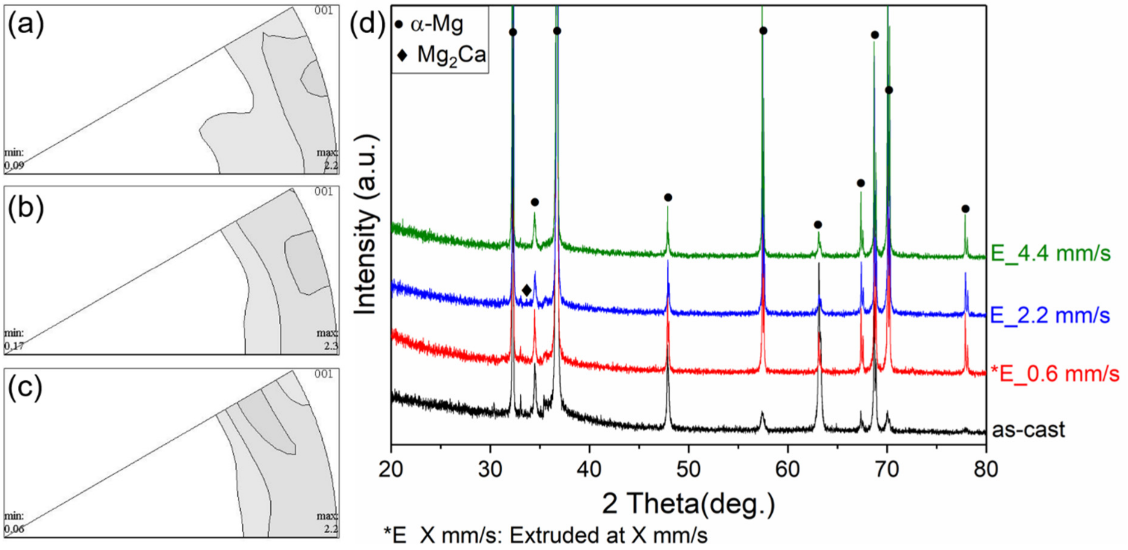

Figure 5.17 Inverse pole figures parallel to the extrusion direction of Mg0.5Zn0.2Ca alloys extruded at (a) 0.6 mm/s,(b) 2.2 mm/s and (c) 4.4 mm/s (left: <0001>, upper right: <11-20>, lower right: <10-10>). (d) Phase compositions of Mg0.5Zn0.2Ca alloys determined by XRD.

The X-ray diffraction patterns of Mg0.5Zn0.2Ca alloy extruded at different speed is shown in Figure 5.17d, with comparison to that of as-cast alloy. Similar to the as-cast alloy, a weak peak of Mg_2Ca phase is also detected in the alloy extruded at 2.2 mm/s. While for the alloys extruded at 0.6 and 4.4 mm/s, only α-Mg phase is detected. Two small peaks can be observed at about 33° and 35.5°. They cannot match with any possible peaks for studied alloys as well as hereafter corrosion products and always appear at the same position, which may be caused by the instrument.

Figure 5.18 presents the optical microstructures and micrographs imaged by SEM in BSE mode of Mg0.5Zn0.2Ca alloy in as-cast and extruded conditions. Apparently, the as-cast Mg0.5Zn0.2Ca alloy reveals a coarse dendritic microstructure, while the extruded alloy exhibits significantly refined globular grains. However, some elongated grains remain embedded in the microstructure of Mg0.5Zn0.2Ca alloy extruded at 0.6 mm/s, indicating that the grain structure is only partly recrystallized. In comparison, the microstructures of Mg0.5Zn0.2Ca alloys extruded at 2.2 and 4.4 mm/s are almost fully recrystallized. In addition, the size of the recrystallized grains visually increases with the extrusion rate.

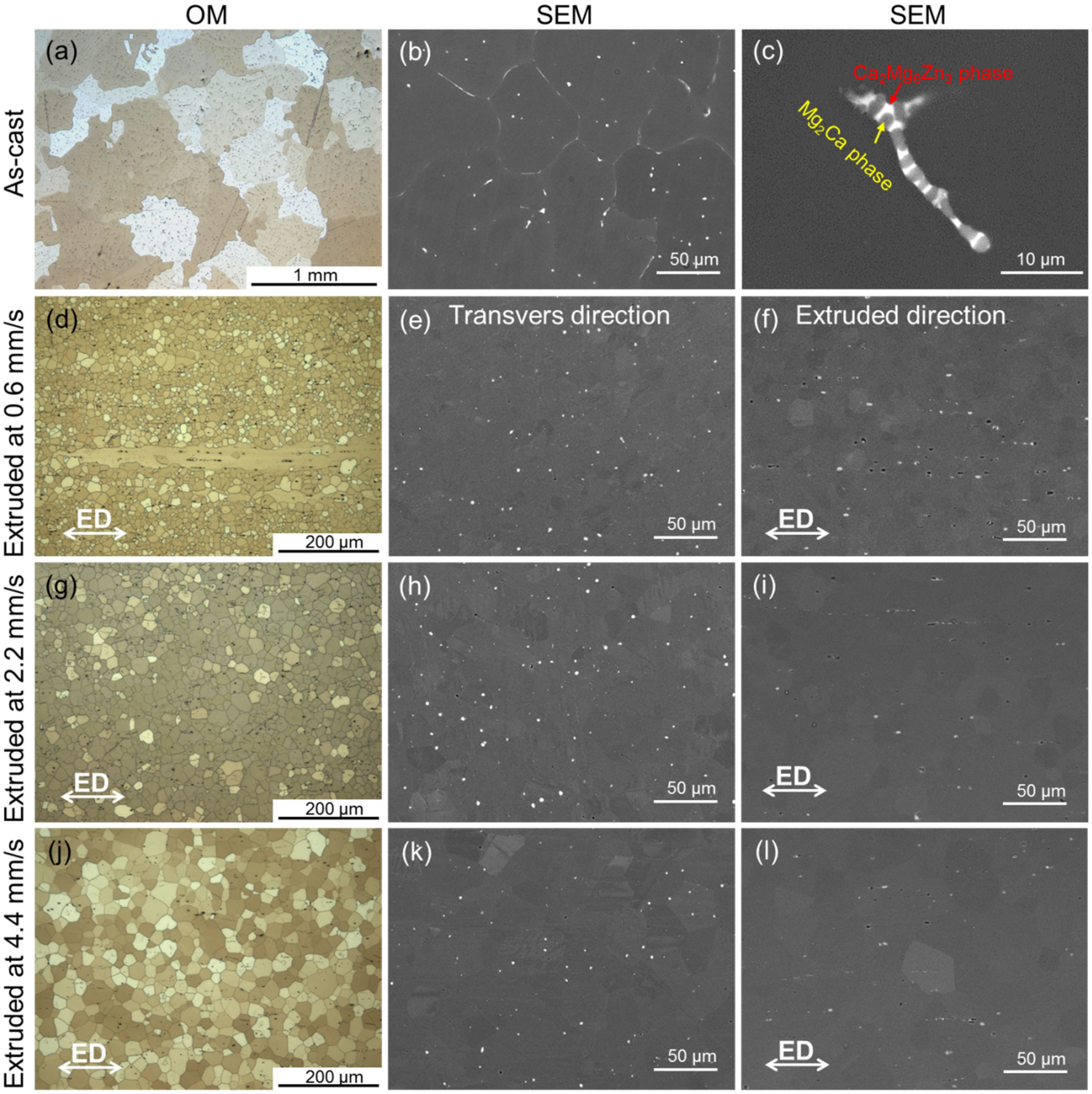

Figure 5.18 Microstructures of as-cast and extruded Mg0.5Zn0.2Ca alloys imaged by OM and SEM in BSE mode (ED: extrusion direction).

Compared with the microstructure of Mg0.5Zn0.2Ca alloy prepared by gravity casting in Figure 5.2c, more precipitates were formed on the grain boundaries and interdendrites interstices when the alloy was fabricated by indirect chill casting, as shown in Figure 5.18b, especially for those located at grain boundary triple junctions. However, similar eutectic phase (Figure 5.18c) is observed, which is composed of bright $Ca_2Mg_6Zn_3$ and grey Mg_2Ca phases according to the previous analysis. After extrusion, only circular phases are uniformly distributed along the extrusion direction. Note that some holes are observed in the micrographs (Figure 5.18f, i and l), which can be a result of the dissolution of these phases and will be explained later.

Table 5.7 Chemical compositions of different constituents in the microstructure of Mg0.5Zn0.2Ca alloy extruded at 2.2 mm/s determined by EDS.

Element	**Precipitates**		**α-Mg matrix**	
	at.%	***wt.%***	***at.%***	***wt.%***
Mg	84.1 ± 2.4	75.9 ± 3.2	99.6 ± 0.0	99.1 ± 0.1
Zn	0.5 ± 0.0	1.2 ± 0.1	0.3 ± 0.0	0.7 ± 0.0
Ca	15.4 ± 2.4	22.9 ± 3.2	0.1 ± 0.0	0.2 ± 0.1

EDS analysis demonstrates that the compositions of the particles in Mg0.5Zn0.2Ca alloys extruded at different speed are similar. Table 5.7 lists the analysis result of Mg0.5Zn0.2Ca alloy extruded at 2.2 mm/s as representative. The circular particles contain about 84.1 *at.*% of Mg, 0.5 *at.*% of Zn and 15.4 *at.*% of Ca. The content of Zn in the particles is only slightly higher than that in the α-Mg matrix (0.3 *at.*%). Thus, these second phases are considered to be Mg_2Ca phases, which corresponds well with the XRD result of Mg0.5Zn0.2Ca alloy extruded at 2.2 mm/s. This indicates that the $Ca_2Mg_6Zn_3$ phases dissolved during the homogenization or extrusion process. The absent peaks of Mg_2Ca phases in the X-ray diffraction patterns of Mg0.5Zn0.2Ca alloys extruded at 0.6 and 4.4 mm/s may be due to the detection limitation of the instrument, which can be influenced by the detected position of the sample considering such low volume fraction of the second phases.

The average grain size of as-cast and extruded Mg0.5Zn0.2Ca alloys is compared in Figure 5.19. For extruded alloys, only recrystallized grains are considered. Obviously, the grains are considerably refined after extrusion and the grain size gradually increases with increasing extrusion speed, which is in good agreement with the optical microstructures demonstrated in Figure 5.18a, d, g and j.

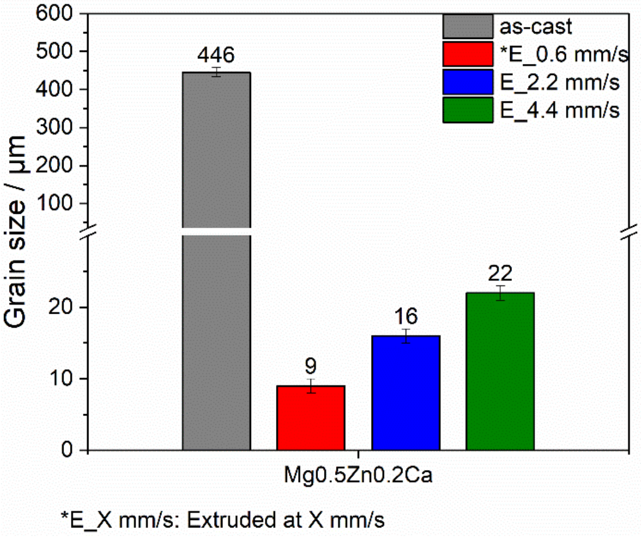

Figure 5.19 Influence of extrusion process on the grain size of Mg0.5Zn0.2Ca alloy

Mg0.5Zn0.2Ge alloy

Figure 5.20 displays the inverse pole figures and X-ray diffraction patterns of Mg0.5Zn0.2Ge alloys extruded at different speed. A distinct alignment of basal planes along the extrusion direction (Figure 5.20a, b and c) is exhibited irrespective of the extrusion speed. The highest intensities of the textures for extruded Mg0.5Zn0.2Ge alloys are similar at a value of about 5. Additionally, a strong prismatic component (the <11-20> pole at the upper right corner in the inverse pole figure) is also found. For the phase composition (Figure 5.20d), all extruded Mg0.5Zn0.2Ge alloys reveal obvious peaks of Mg_2Ge phases, which is similar to that of as-cast Mg0.5Zn0.2Ge alloy.

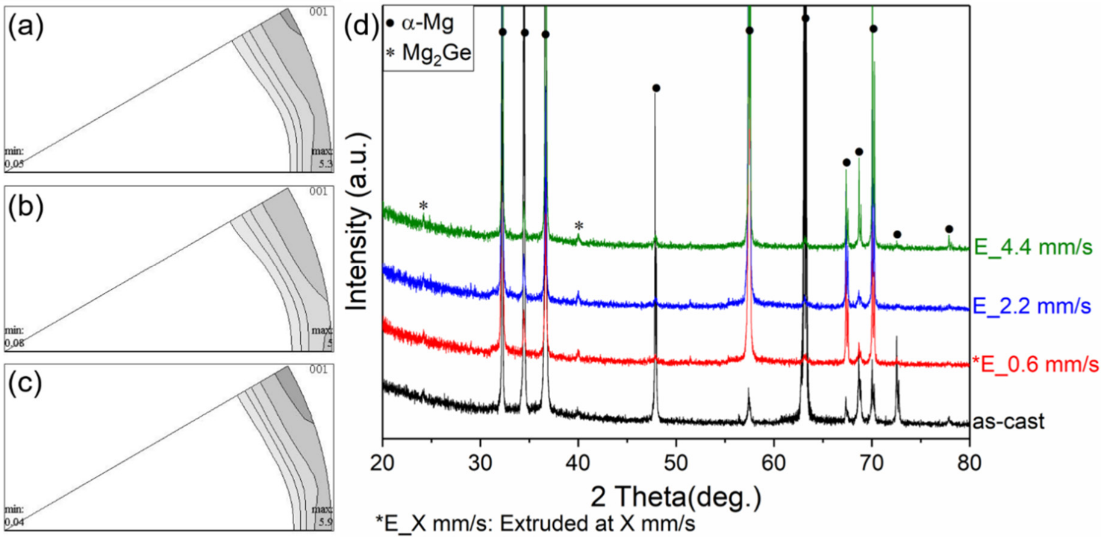

Figure 5.20 Inverse pole figures parallel to the extrusion direction of Mg0.5Zn0.2Ge alloys extruded at (a) 0.6 mm/s,(b) 2.2 mm/s and (c) 4.4 mm/s (left: <0001>, upper right: <11-20>, lower right: <10-10>). (d) Phase compositions of Mg0.5Zn0.2Ge alloys determined by XRD.

The optical micrographs in Figure 5.21a presents a dendritic microstructure of as-cast Mg0.5Zn0.2Ge alloy. After extrusion (Figure 5.21d, g and j), the coarse microstructure is evidently refined. However, some elongated grains parallel to the extrusion direction are embedded into the grain structure, which should be the non-recrystallized remains of deformed grains [68]. This indicates that the microstructure of Mg0.5Zn0.2Ge alloy is only partly recrystallized after extrusion irrespective of the extrusion speed. Nevertheless, smaller and a higher fraction of recrystallized globular grains are observed in the microstructure of the alloy extruded at higher extrusion speed.

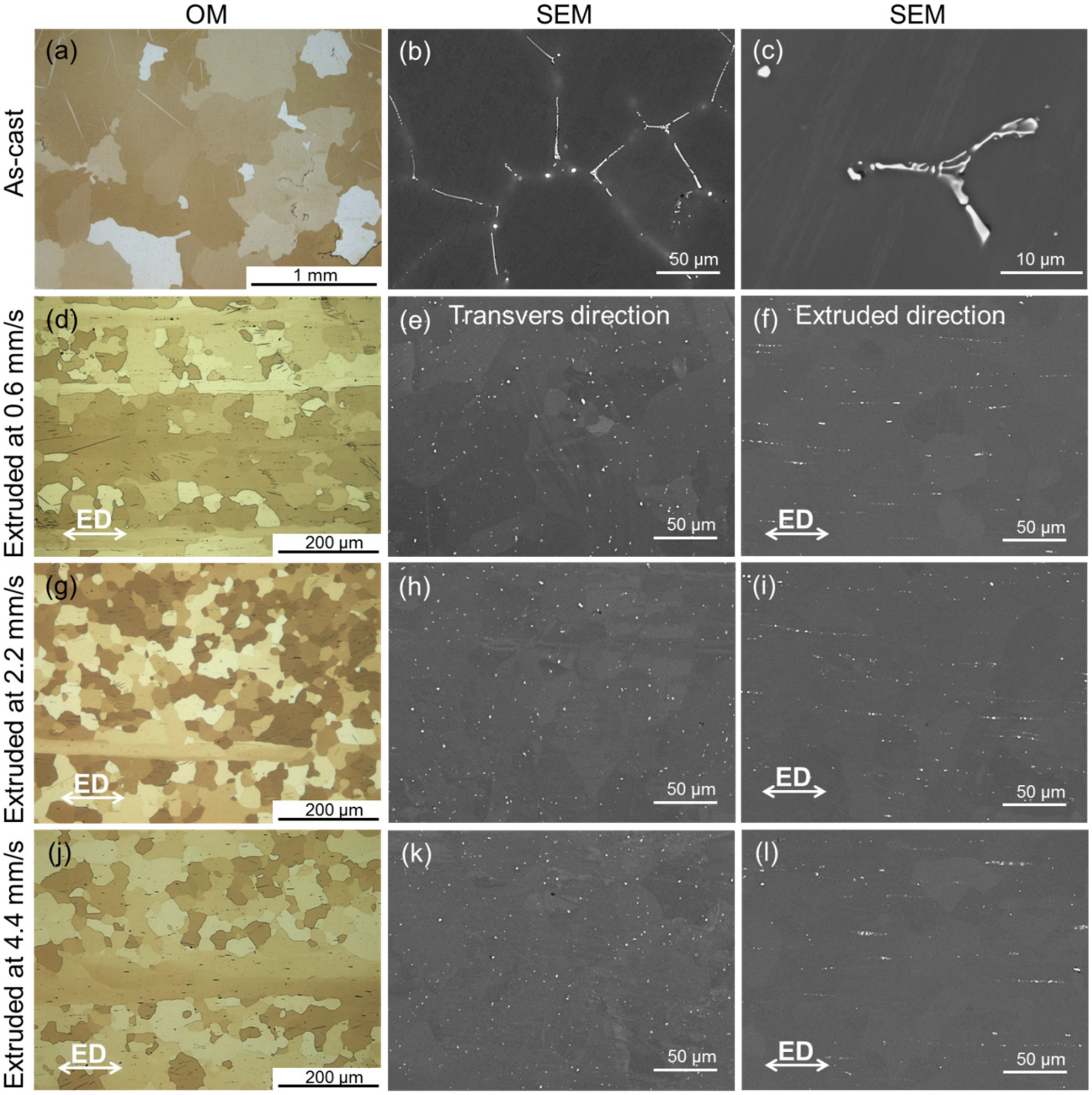

Figure 5.21 Microstructures of as-cast and extruded Mg0.5Zn0.2Ge alloys imaged by OM and SEM in BSE mode (ED: extrusion direction).

The SEM micrographs demonstrate that granular and rod-like/Chinese script-shaped second phases precipitated in the microstructure of as-cast Mg0.5Zn0.2Ge alloy (Figure 5.21b and c), which is in agreement with the gravity casted Mg0.5Zn0.2Ge alloys. After extrusion, those rod-like/Chinese script-shaped precipitates are deformed and broke into fine pieces and homogeneously distributed along the extrusion direction.

Table 5.8 Chemical compositions of different constituents in the microstructure of Mg0.5Zn0.2Ge alloy extruded at 2.2 mm/s determined by EDS.

Element	**Precipitates**		**α-Mg matrix**	
	at.%	***wt.%***	***at.%***	***wt.%***
Mg	92.7 ± 0.7	82.3 ± 1.5	99.6 ± 0.0	99.0 ± 0.1
Zn	0.1 ± 0.0	0.3 ± 0.0	0.2 ± 0.0	0.6 ± 0.0
Ge	6.3 ± 0.6	16.6 ± 1.5	0.1 ± 0.0	0.3 ± 0.0
Si	0.8 ± 0.1	0.8 ± 0.1	0.1 ± 0.0	0.1 ± 0.0

The phase compositions of Mg0.5Zn0.2Ge alloys extruded at different speed are also analyzed by EDS, shown in Table 5.8 with the alloy extruded at 2.2 mm/s as representative. Those fine particles are made up of 92.7 *at.*% Mg, 6.3 *at.*% Ge and 0.1 *at.*% Zn, among which the content of Zn is even slightly lower than that in the matrix. Accordingly, the second phases are Mg_2Ge phases, which is consistent with the XRD results. The detected low content of Si should result from the raw material, the casting procedure or the polishing process.

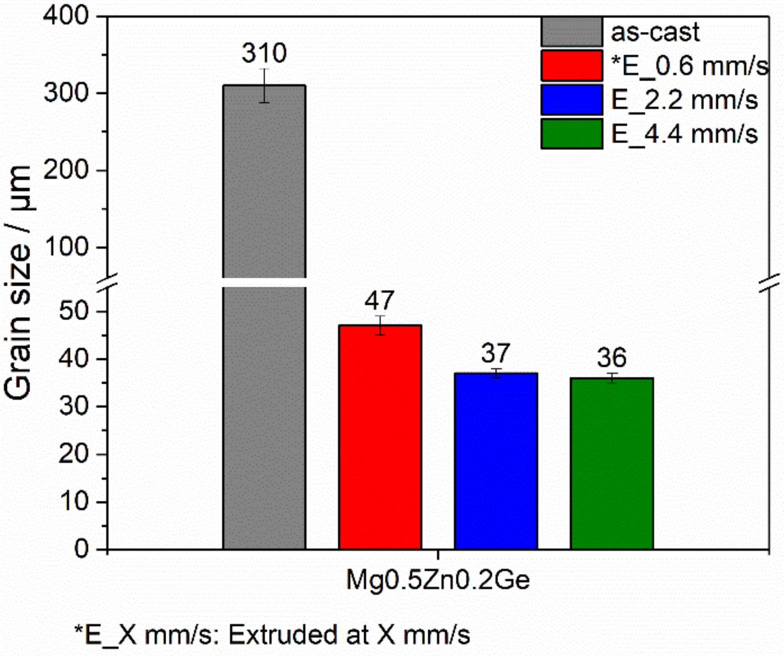

Figure 5.22 Influence of extrusion process on the grain size of Mg0.5Zn0.2Ge alloy

The effect of extrusion process on the grain size of Mg0.5Zn0.2Ge alloy is depicted in Figure 5.22. The average grain size of as-cast alloy prepared by indirect chill casting is about 310 µm, which is significantly refined to be 47 µm after extrusion at 0.6 mm/s. Different from the case of Mg0.5Zn0.2Ca alloy, faster extrusion speed leads to smaller recrystallized grains. However, no significant change happened when the extrusion speed was increased from 2.2 mm/s to 4.4 mm/s.

Mg4Zn0.2Sn alloy

The textures of extruded Mg4Zn0.2Sn alloys (Figure 5.23a, b and c) are similar to those of extruded Mg0.5Zn0.2Ge alloys. Different extrusion speed did not result in large difference in the microstructure. A distinct alignment of basal planes along the extrusion direction and a high intensity at the <11-20> pole of more than 4 are revealed. For the phase composition, only α-Mg phase is detected irrespective of as-cast or extruded conditions.

The microstructures of as-cast and extruded Mg4Zn0.2Sn alloys are presented in Figure 5.24. The obviously coarse dendritic microstructure of as-cast alloy is significantly refined by the extrusion process, replaced by fine globular grains. Moreover, the size of those globular grains visually are coarsened with increased extrusion speed. Different from the cases of Mg0.5Zn0.2Ca and Mg0.5Zn0.2Ge alloys, almost fully recrystallized microstructure is obtained irrespective of the extrusion speed for Mg4Zn0.2Sn alloys.

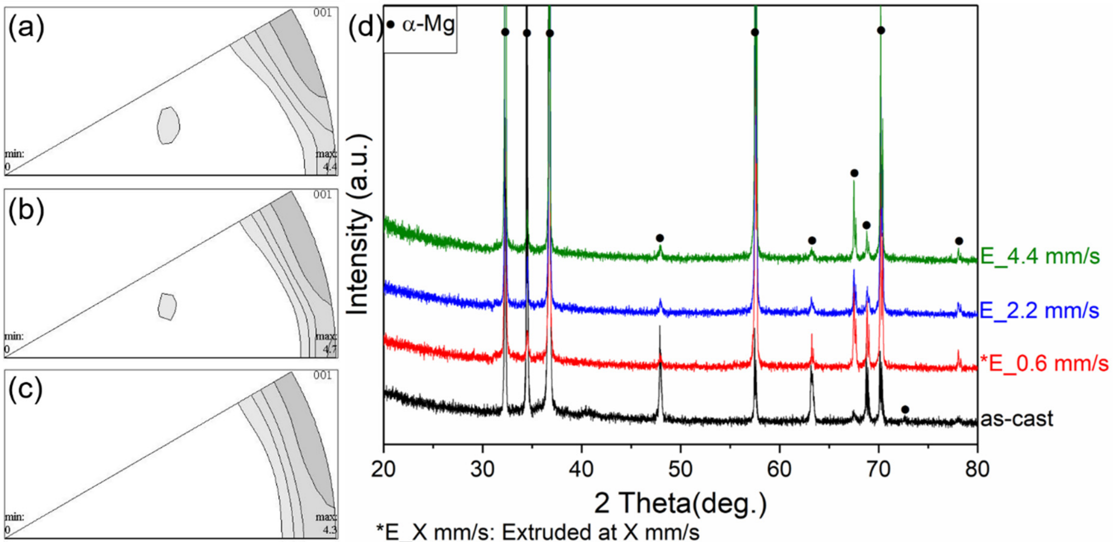

*E_X mm/s: Extruded at X mm/s

Figure 5.23 Inverse pole figures parallel to the extrusion direction of Mg4Zn0.2Sn alloys extruded at (a) 0.6 mm/s,(b) 2.2 mm/s and (c) 4.4 mm/s (left: <0001>, upper right: <11-20>, lower right: <10-10>). (d) Phase compositions of Mg4Zn0.2Sn alloys determined by XRD.

The microstructure of as-cast Mg4Zn0.2Sn alloy (Figure 5.24b and c) consists of divorced eutectic compounds in irregular and circular shapes at the interdendritic areas, Zn-segregated particle-free interdendritic regions and α-Mg matrix dendrites. This is in accordance with the microstructure of Mg4Zn0.2Sn alloy prepared by gravity casting. For extruded Mg4Zn0.2Sn alloys, those large particles disappear after extrusion and sub-micron-scale precipitates are visible instead, which are mainly distributed on the grain boundaries. However, a few larger particles (shown in the inserted image in Figure 5.24h,) in polygonal shapes are also observed. Bright globular particles exist inside some of those polygonal particles. It is noticed that there are alternating bright and dark regions or bands in the microstructures of extruded Mg4Zn0.2Sn alloys, which are especially obvious in the transverse direction (Figure 5.24e, h and k).

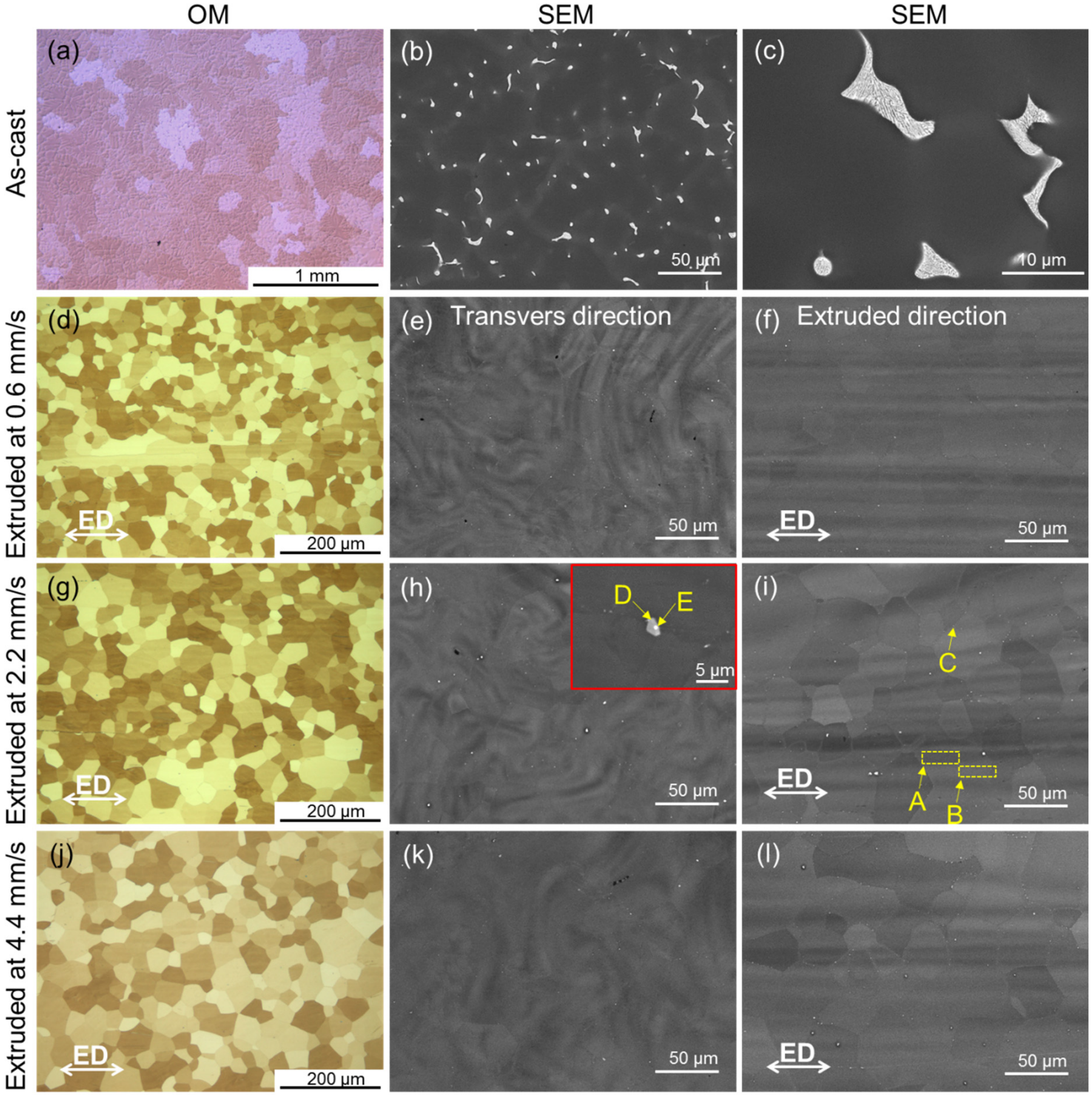

Figure 5.24 Microstructures of as-cast and extruded Mg4Zn0.2Sn alloys imaged by OM and SEM in BSE mode (ED: extrusion direction).

Since no second phases were detected for extruded Mg4Zn0.2Sn alloys by XRD except α-Mg phase, EDS analysis was conducted for the chemical compositions of different constituents, shown in Table 5.9. As marked in Figure 5.24h and i, letters A - E refer to the darker matrix region, brighter matrix region, tiny particles, bright globular part and grey polygonal part (or single grey polygonal particles) of the larger particles in extruded alloy, respectively. In spite of the different contrast in BSE images, the difference of Zn content between the darker and brighter matrix regions is not so significant but the Zn content is still slightly higher in the brighter regions. For the tiny particles, considering such a small size, it is difficult to define their exact or even approximate composition by EDS. However, compared to Sn, the relatively higher amount of Zn may suggest that they are Mg-Zn phases (more evidence is found in the element distribution of the cross sections after immersion tests). Compared with the grey polygonal particles, those bright globular particles inside the grey polygonal particles contain a similar amount of Zn, Sn and Si. However, the content of iron (Fe) and manganese (Mn) is much higher, suggesting that they are Fe-Mn impurities. The grey polygonal particles with higher amount of Si can be Mg_2Si phases. Furthermore, element mapping was performed to confirm the element distribution in the microstructures of Mg4Zn0.2Sn alloys under both conditions. This is especially important considering the different element compositions of the darker and brighter matrix regions of the extruded alloy, as shown in Figure 5.25. The EDS mapping results correlate well with the EDS point analysis. As expected, those impurity elements (Si, Fe and Mn) enrich inside the second phases in the as-cast Mg4Zn0.2Sn alloy. For the extruded alloy, an obviously alternating distribution of Mg and Zn in the corresponding darker and brighter regions is observed, indicating that segregation of Zn still exists in the alloy after extrusion. Moreover, the existence of those Mg_2Si phases and Fe-Mn/Mg_2Si co-existing precipitates are also confirmed.

Table 5.9 Chemical compositions of different constituents in the microstructure of Mg4Zn0.2Sn alloy extruded at 2.2 mm/s determined by EDS.

Element	**Matrix**				**C-Tiny particle**		**Larger particle**			
	A-Darker region		**B-Brighter region**				**D-Bright globular part**		**E-Grey polygonal part/particle**	
	at.%	***wt.%***	***at.%***	***wt.%***	***at.%***	***wt.%***	***at.%***	***wt.%***	***at.%***	***wt.%***
Mg	98.8 ± 0.3	96.9 ± 0.7	98.3 ± 0.1	95.6 ± 0.2	98.0 ± 0.1	94.6 ± 0.1	82.3 ± 1.6	72.9 ± 2.0	86.9 ± 2.3	80.4 ± 2.4
Zn	1.1 ± 0.3	2.9 ± 0.7	1.6 ± 0.1	4.2 ± 0.2	2.0 ± 0.0	5.2 ± 0.1	1.2 ± 0.1	2.9 ± 0.3	1.2 ± 0.2	3.1 ± 0.5
Sn	0.1 ± 0.0	0.2 ± 0.0	0.1 ± 0.0	0.2 ± 0.0	0.0 ± 0.0	0.2 ± 0.0	0.7 ± 0.1	2.8 ± 0.6	0.9 ± 0.1	4.1 ± 0.5
Si	-	-	-	-	-	-	10.6 ± 1.4	10.9 ± 1.4	10.4 ± 2.4	11.1 ± 2.5
Mn	-	-	-	-	-	-	1.2 ± 0.1	2.5 ± 0.2	0.2 ± 0.0	0.4 ± 0.1
Fe	-	-	-	-	-	-	4.0 ± 0.2	8.0 ± 0.5	0.4 ± 0.1	0.9 ±0.2

Figure 5.26 reveals a similar influence of extrusion process on the microstructure of Mg4Zn0.2Sn alloy compared to that of Mg0.5Zn0.2Ca alloy. The coarse grain size (about 232 µm) of as-cast Mg4Zn0.2Sn alloy is greatly refined by extrusion at 0.6 mm/s to 22 µm. Faster extrusion process coarsens the size of the recrystallized grains a bit but no big difference is observed when the extrusion speed is increased from 2.2 mm/s to 4.4 mm/s.

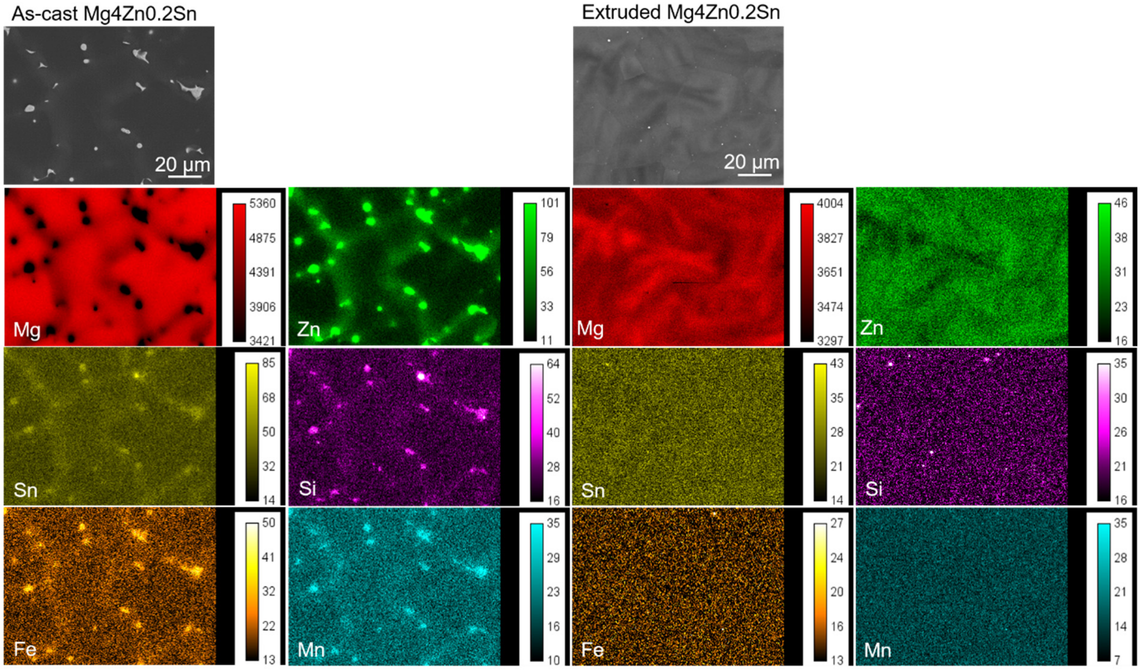

Figure 5.25 Element distributions for the microstructures of as-cast and extruded (at 2.2 mm/s in transverse direction) Mg4Zn0.2Sn alloys determined by EDS mapping.

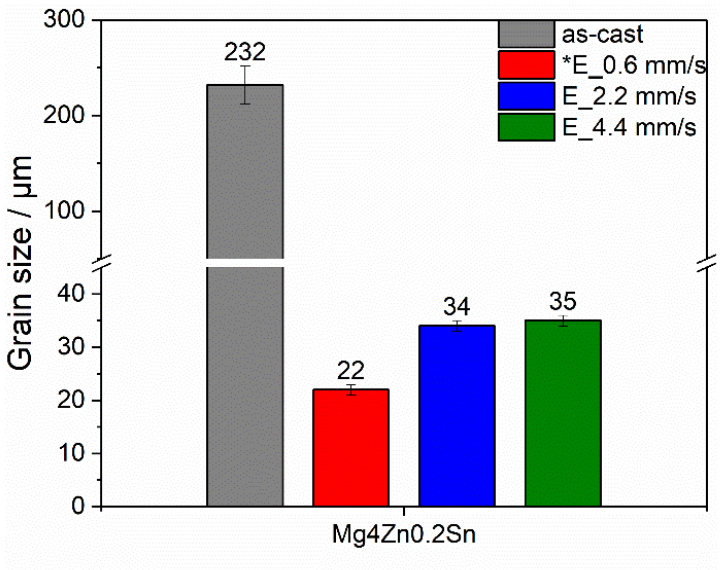

*E_X mm/s: Extruded at X mm/s

Figure 5.26 Influence of extrusion process on the grain size of Mg4Zn0.Sn alloy.

5.3.2 Corrosion performance

The corrosion performance of as-cast and extruded Mg0.5Zn0.2Ca, Mg0.5Zn0.2Ge and Mg4Zn0.2Sn alloys were investigated by EIS, potentiodynamic polarization and hydrogen evolution measurements to illustrate the effect of extrusion process and extrusion speed on the corrosion properties of these three alloys.

Mg0.5Zn0.2Ca alloy

Figure 5.27 depicts the impedance spectra of as-cast and extruded Mg0.5Zn0.2Ca alloys after immersion in 0.9 *wt.*% NaCl solution for 48 h. Well-defined two capacitive loops are observed in all cases. The diameters of the loops fluctuate with immersion time irrespective of the conditions of the alloy. Additionally, no big difference is noticed between the impedance values of as-cast and extruded Mg0.5Zn0.2Ca alloys or alloys extruded at different speed. These results suggest that the extrusion process and the different extrusion speed do not apparently affect the corrosion performance of Mg0.5Zn0.2Ca alloy.

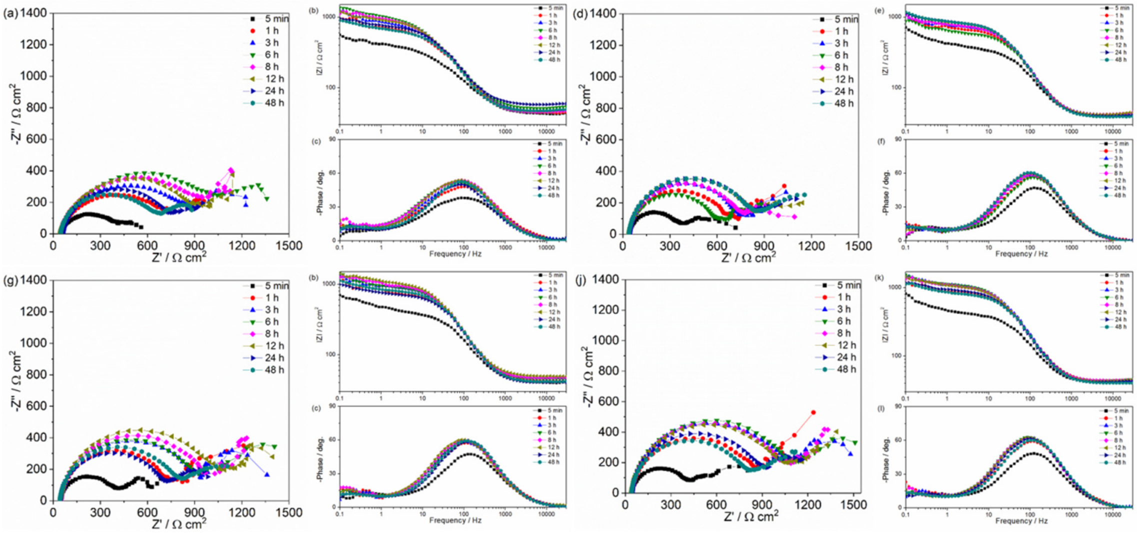

Figure 5.27 Impedance spectra of (a, b, c) as-cast Mg0.5Zn0.2Ca alloy and the alloy extruded at (d, e, f) 0.6 mm/s, (g, h, i) 2.2 mm/s and (j, k, l) 4.4 mm/s tested in 0.9 *wt.*% NaCl solution at room temperature.

The potentiodynamic polarization curves of Mg0.5Zn0.2Ca alloys after immersion in 0.9 *wt.*% NaCl solution for 48 h are displayed in Figure 5.28. Apparently, the low-current plateau region on the anodic branch significantly extends after the alloy was extruded and a much nobler film breakdown is obtained. This phenomenon indicates a better retardation of the anodic dissolution of the substrate by the surface films formed on the surfaces of extruded Mg0.5Zn0.2Ca alloys. In addition, compared with the as-cast alloy, lower cathodic current densities can be noted for the cathodic branches of the extruded alloys. Thus, the over-potential of the cathodic hydrogen evolution reaction is higher for extruded Mg0.5Zn0.2Ca alloys compared to the as-cast alloy. This reveals that the cathodic reaction is kinetically retarded on the extruded Mg0.5Zn0.2Ca alloys. Unlike the apparent difference between the polarization curves of as-cast and extruded Mg0.5Zn0.2Ca alloys, little difference is observed between the curves of Mg0.5Zn0.2Ca alloys extruded at different speed.

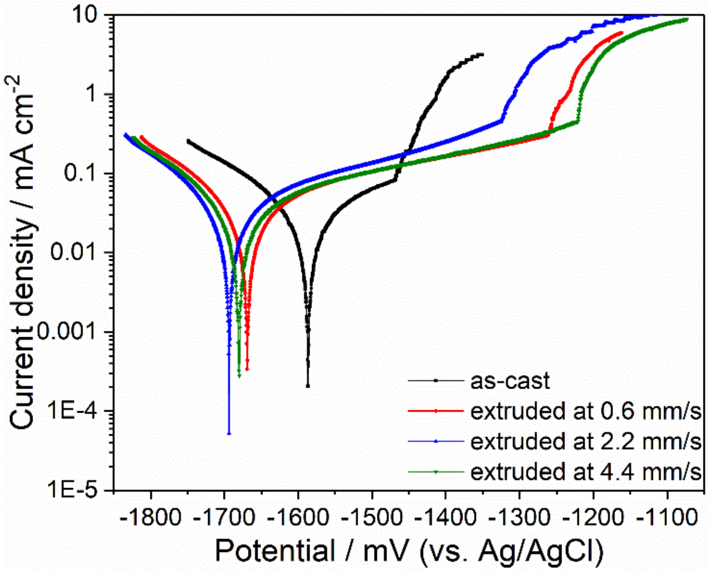

Figure 5.28 Potentiodynamic polarization curves of as-cast and extruded Mg0.5Zn0.2Ca alloys after immersion in 0.9 *wt.*% NaCl solution at room temperature for 48 h.

The measured and calculated parameters derived from the polarization curves in Figure 5.28 are presented in Table 5.10. The corrosion rate of Mg0.5Zn0.2Ca alloy is comparable under as-cast and extruded conditions, while the low-current plateau region is extended from 125 mV to about 360 mV after extrusion.

Table 5.10 Corrosion parameters derived from the potentiodynamic polarization curves and hydrogen evolution results of as-cast and extruded Mg0.5Zn0.2Ca alloys.

Condition	**Potentiodynamic polarization**				**Hydrogen evolution**
	CR	i_{corr}	E_{corr}	E_{bd}	***CR***
	mm year^{-1}	**mA cm^{-2}**	**mV**	**mV**	**mm year^{-1}**
As-cast	0.44 ± 0.11	0.019 ± 0.005	-1582 ± 8	-1457 ± 29	0.13 ± 0.04
*E_0.6 mm/s	0.41 ± 0.07	0.018 ± 0.003	-1683 ± 13	-1317 ± 114	0.12 ± 0.06
E_2.2 mm/s	0.41 ± 0.08	0.018 ± 0.004	-1694 ± 1	-1327 ± 118	0.12 ± 0.06
E_4.4 mm/s	0.43 ± 0.04	0.019 ± 0.002	-1684 ± 12	-1323 ± 74	0.13 ± 0.03

Notes: *E_X mm/s: Extruded at X mm/s

The hydrogen evolution curves in Figure 5.29 illustrate that the corrosion properties of as-cast and extruded Mg0.5Zn0.2Ca alloys are comparable and the extrusion speed does not influence the corrosion performance. After 168 h, the corrosion rate of Mg0.5Zn0.2Ca alloy calculated according to the evolved hydrogen volume is about 0.12 mm/year. The trend provided by EIS, potentiodynamic polarization and hydrogen evolution measurements coincide well with each other, demonstrating that neither the extrusion process nor the extrusion speed did not change the corrosion resistance of Mg0.5Zn0.2Ca alloy.

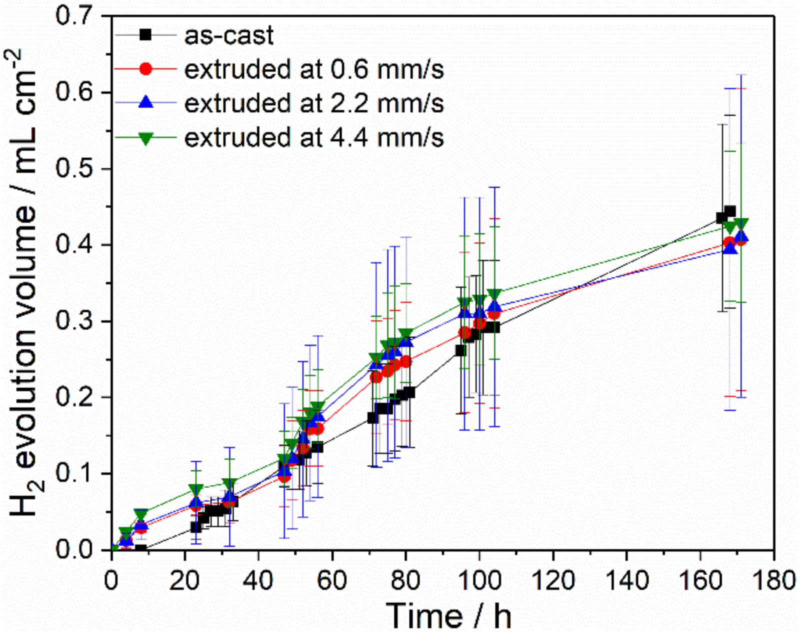

Figure 5.29 Hydrogen evolution curves of Mg0.5Zn0.2Ca alloys after immersion in 0.9 *wt.*% NaCl solution at room temperature for 168 h.

Mg0.5Zn0.2Ge alloy

The impedance spectra of Mg0.5Zn0.2Ge alloys are shown in Figure 5.30. Obvious difference can be observed between the as-cast and extruded alloys. For as-cast Mg0.5Zn0.2Ge alloy, within the initial 3 h of immersion, the Nyquist plots (Figure 5.30a) exhibit two well-defined capacitive loops at the high and middle frequency regions respectively. However, with continued exposure in the electrolyte, local active dissolution occurs on the alloy surface, indicated by a less visible capacitive loop in the middle frequency range and some scattered data points at lower frequencies. This is inconsistent with the EIS result of Mg0.5Zn0.2Ge alloy prepared by gravity casting (see Figure 5.6s, t and u, two well-defined loops are exhibited over the testing period with gradually increased diameters). The possible reasons can be the slower cooling rate, less uniform microstructure and more porosity of the alloy prepared by indirect chill casting due to the controlled cooling rate and larger steel mould used for the solidification process. In contrast, the EIS spectra of the extruded Mg0.5Zn0.2Ge alloys are characterized by two well-defined relaxation processes throughout the testing period. For alloys extruded at 0.6 and 2.2 mm/s, the diameters of the loops gradually increase as the immersion time prolonged. While those of the alloy extruded at 4.4 mm/s show slight fluctuation. The different development of the impedance spectra of as-cast and extruded Mg0.5Zn0.2Ge alloys indicates different corrosion mechanisms.

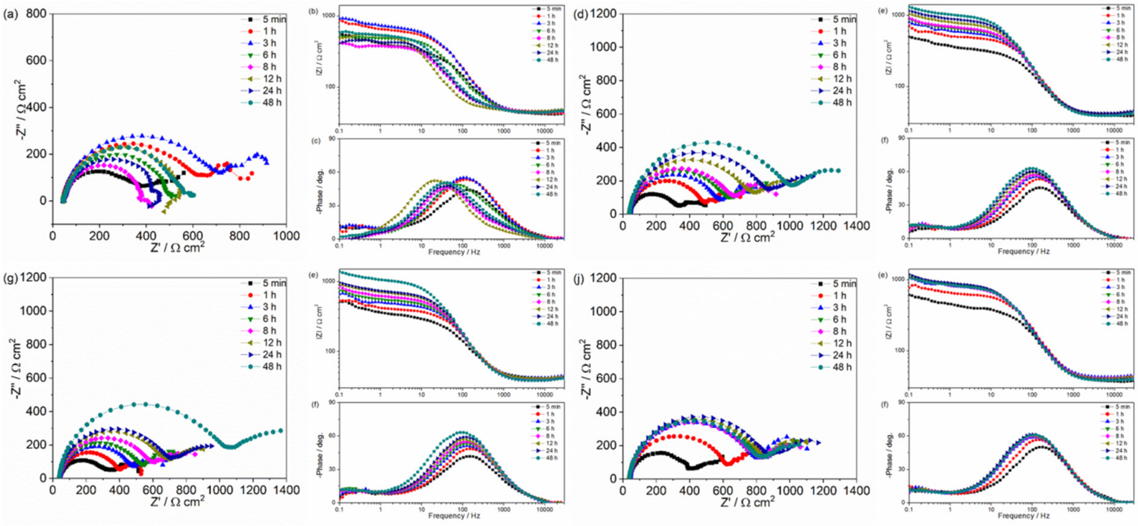

Figure 5.30 Impedance spectra of (a, b, c) as-cast Mg0.5Zn0.2Ge alloy and the alloy extruded at (d, e, f) 0.6 mm/s, (g, h, i) 2.2 mm/s and (j, k, l) 4.4 mm/s tested in 0.9 *wt.*% NaCl solution at room temperature.

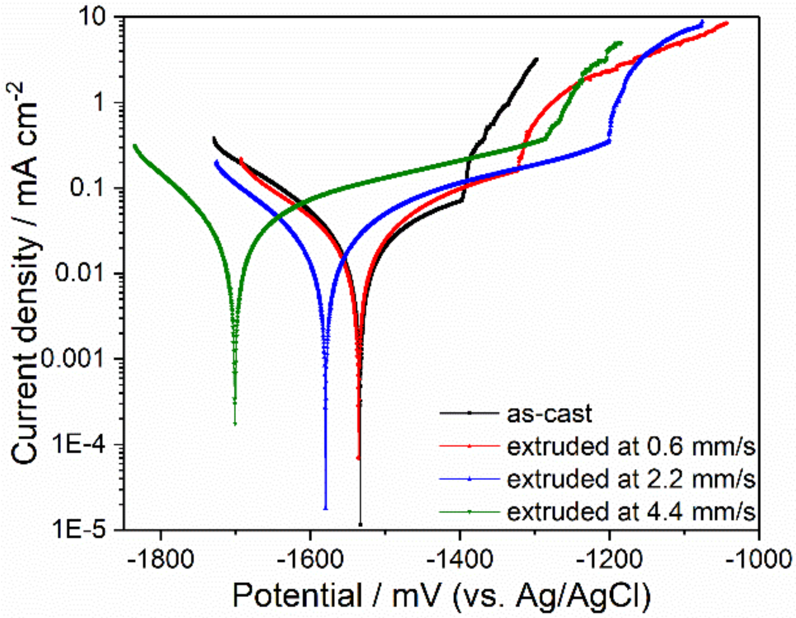

Figure 5.31 Potentiodynamic polarization curves of as-cast and extruded Mg0.5Zn0.2Ge alloys after immersion in 0.9 *wt.*% NaCl solution at room temperature for 48 h.

Despite the less-defined EIS spectra of as-cast Mg0.5Zn0.2Ge alloy, a short low-current plateau region is still noticed on the anodic part of the potentiodynamic polarization curve (Figure 5.31) with a film breakdown potential. This discloses that the surface film formed on the surface of as-cast Mg0.5Zn0.2Ge alloy provided a kinetic barrier to the anodic dissolution partial reaction of the substrate to some extent. In comparison, a more extended low-current plateau region is observed after the alloy was extruded, especially for those extruded at 2.2 and 4.4 mm/s. Moreover, for the cathodic parts of the polarization curves, lower current densities are reached for the extruded alloys compared to the as-cast one, indicating retarded cathodic hydrogen evolution reaction.

Table 5.11 Corrosion parameters derived from the potentiodynamic polarization curves and hydrogen evolution results of as-cast and extruded Mg0.5Zn0.2Ge alloys.

Condition	**Potentiodynamic polarization**				**Hydrogen evolution**
	CR mm year^{-1}	i_{corr} mA cm^{-2}	E_{corr} mV	E_{bd} mV	***CR*** mm year^{-1}
As-cast	0.30 ± 0.02	0.013 ± 0.001	-1528 ± 14	-1402 ± 5	0.31 ± 0.01
*E_0.6 mm/s	0.29 ± 0.02	0.013 ± 0.001	-1592 ± 35	-1208 ± 83	0.13 ± 0.04
E_2.2 mm/s	0.26 ± 0.05	0.011 ± 0.002	-1606 ± 27	-1218 ± 40	0.10 ± 0.03
E_4.4 mm/s	0.30 ± 0.02	0.013 ± 0.001	-1646 ± 6	-1216 ± 66	0.10 ± 0.02

Notes: *E_X mm/s: Extruded at X mm/s

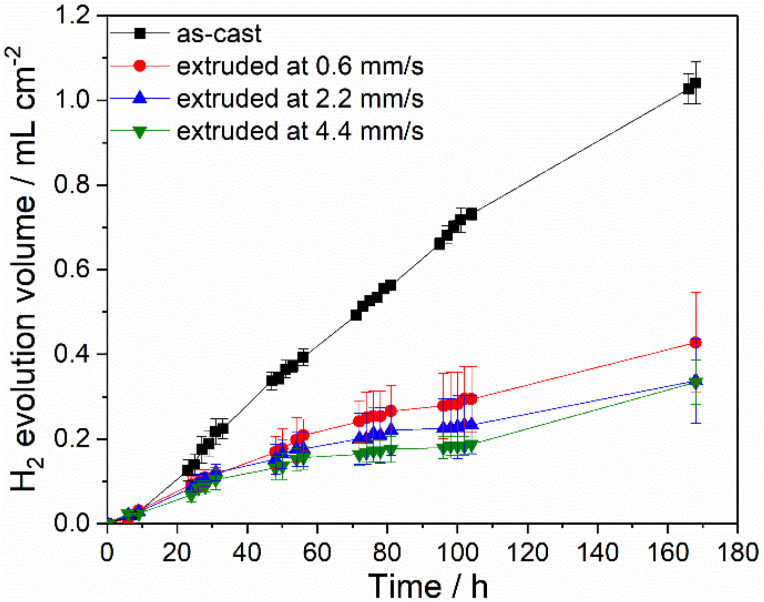

Figure 5.32 Hydrogen evolution curves of Mg0.5Zn0.2Ge alloys after immersion in 0.9 *wt.*% NaCl solution at room temperature for 168 h.

Table 5.11 shows the calculated and measured parameters of the polarization curves for Mg0.5Zn0.2Ge alloys. It reveals that the corrosion resistance of Mg0.5Zn0.2Ge alloy extruded at 2.2 mm/s is slightly enhanced compared to the as-cast alloy, while those of the alloys extruded at 0.6 and 4.4 mm/s are comparable in comparison to the as-cast alloy. The low-current plateau region on the anodic branch extends from about 126 mV to more than 380 mV for the alloy after extrusion.

Similar to the EIS results, hydrogen evolution curves in Figure 5.32 also disclose that the corrosion property of Mg0.5Zn0.2Ge alloy is improved by the extrusion process. Moreover, after 56 h, the difference between the alloys extruded at different speed becomes a bit more notable. The corrosion resistance of extruded Mg0.5Zn0.2Ge alloy is slightly enhanced with accelerated extrusion speed. After 168 h, the corrosion rates of Mg0.5Zn0.2Ge alloys extruded at 2.2 and 4.4 mm/s are comparable and slightly lower than that of the alloy extruded at 0.6 mm/s. In general, the extrusion process can obviously improve the corrosion performance of Mg0.5Zn0.2Ge alloy but different extrusion speed did not make a big difference.

Mg4Zn0.2Sn alloy

The impedance spectra of Mg4Zn0.2Sn alloys are shown in Figure 5.33. All spectra present poorly-defined characteristics with almost only one capacitive loop as soon as the tests started, despite the indistinct two capacitive loops after 5 min. This suggests a poor corrosion resistance of this alloy even under extruded condition and anodic dissolution of the alloys occurred as soon as the measurements started. However, some difference still exists between the as-cast and extruded alloys. For as-cast Mg4Zn0.2Sn alloy, the impedance value increases a bit after immersion for 1 h but subsequently declines with prolonged exposure in 0.9 *wt.*% NaCl solution. After a short stabilization from 3 h to 12 h, the impedance value continues to decrease to less than 250 Ω cm^2. For the alloys extruded at different speed, similar development of the impedance spectra is revealed. The impedance value decreases immediately after 1 h. However, with continued immersion, the impedance fluctuates at around 500 Ω cm^2, higher than that of as-cast Mg4Zn0.2Sn alloy.

The potentiodynamic polarization curves in Figure 5.34 disclose that the anodic branches are similar for both as-cast and extruded Mg4Zn0.2Sn alloys. The anodic current densities steeply increase with increasing potential. Neither a film breakdown potential nor a low-current plateau is observed. For the cathodic parts, lower cathodic current densities are noticed for the extruded alloys compared to the as-cast Mg4Zn0.2Sn alloy, suggesting slower cathodic hydrogen evolution reaction. Moreover, no evident difference exists between the polarization curves of Mg4Zn0.2Sn alloys extruded at different speed.

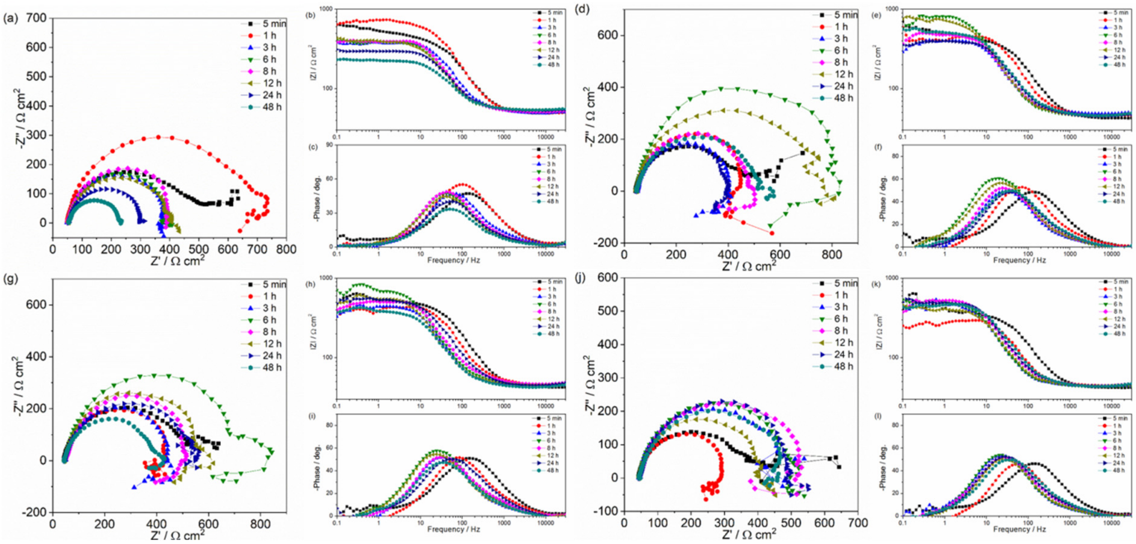

Figure 5.33 Impedance spectra of (a, b, c) as-cast Mg4Zn0.2Sn alloy and the alloy extruded at (d, e, f) 0.6 mm/s, (g, h, i) 2.2 mm/s and (j, k, l) 4.4 mm/s tested in 0.9 *wt.*% NaCl solution at room temperature.

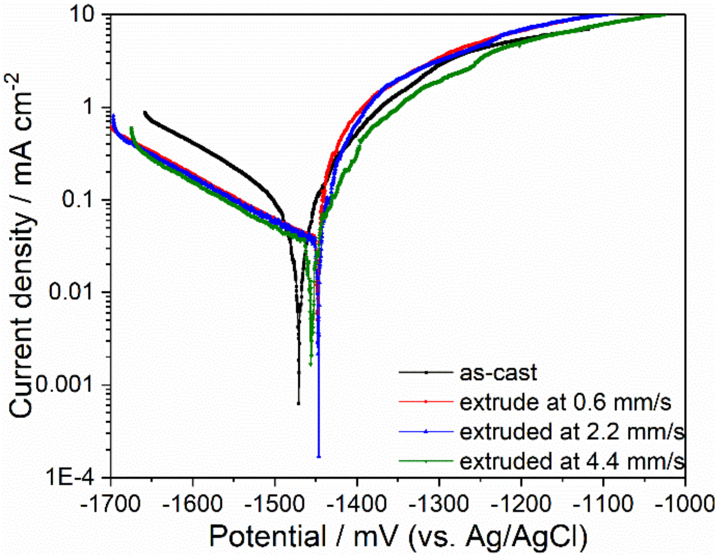

Figure 5.34 Potentiodynamic polarization curves of as-cast and extruded Mg4Zn0.2Sn alloys after immersion in 0.9 *wt.*% NaCl solution at room temperature for 48 h.

The calculated corrosion rates in Table 5.12 derived from the polarization curves demonstrate that the extruded Mg4Zn0.2Sn alloys show enhanced corrosion resistance compared with the as-cast alloy. Additionally, the different extrusion speed had little influence on the corrosion property of the alloy.

Table 5.12 Corrosion parameters derived from the potentiodynamic polarization curves and hydrogen evolution results of as-cast and extruded Mg4Zn0.2Sn alloys.

Condition	**Potentiodynamic polarization**				**Hydrogen evolution**
	CR **mm year^{-1}**	**i_{corr} mA cm^{-2}**	**E_{corr} mV**	**E_{bd} mV**	***CR*** **mm year^{-1}**
As-cast	1.41 ± 0.25	0.062 ± 0.011	-1463 ± 15	-	2.16 ± 0.06
*E_0.6 mm/s	0.83 ± 0.09	0.036 ± 0.004	-1453 ± 13	-	0.42 ± 0.12
E_2.2 mm/s	0.81 ± 0.13	0.036 ± 0.006	-1449 ± 28	-	0.44 ± 0.07
E_4.4 mm/s	0.85 ± 0.10	0.037 ± 0.004	-1448 ± 21	-	0.45 ± 0.08

Notes: *E_X mm/s: Extruded at X mm/s

The hydrogen evolution curves of as-cast and extruded Mg4Zn0.2Sn alloys are displayed in Figure 5.35. Notably, the extruded Mg4Zn0.2Sn alloys evolve much less hydrogen compared to the as-cast alloy, revealing that the extrusion process greatly improved the holistic corrosion property of Mg4Zn0.2Sn alloy. Furthermore, the evolution curves of Mg4Zn0.2Sn alloys extruded at 0.6, 2.2 and 4.4 mm/s are almost identical, demonstrating the weak influence of extrusion speed on the corrosion performance of the alloy. Obviously, the EIS, potentiodynamic polarization and hydrogen evolution results of Mg4Zn0.2Sn alloys agree well with each other. It can be concluded that the wrought processing improved the corrosion property of Mg4Zn0.2Sn alloy while the different extrusion speed had no influence on the corrosion performance.

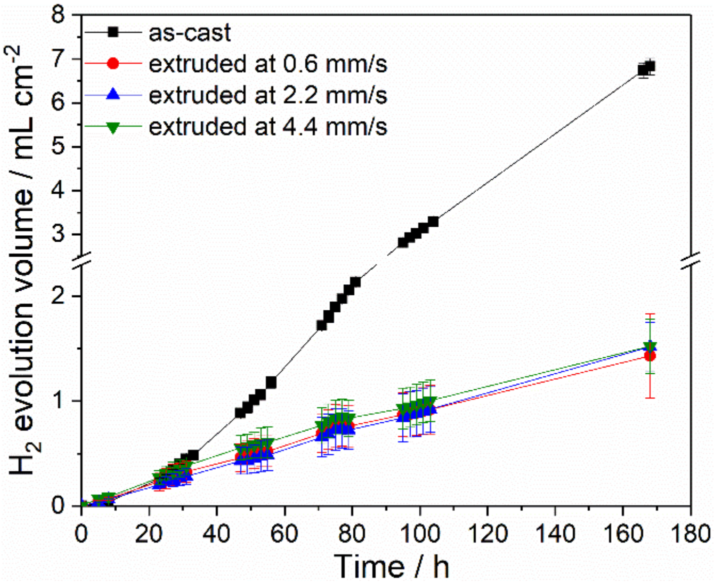

Figure 5.35 Hydrogen evolution curves of Mg4Zn0.2Sn alloys after immersion in 0.9 *wt.*% NaCl solution at room temperature for 168 h.

According to the above study about the influence of extrusion process and speed on the microstructures and corrosion performance of Mg0.5Zn0.2Ca, Mg0.5Zn0.2Ge and Mg4Zn0.2Sn alloys, some general summaries can be made:

(1) the extrusion process can significantly refine the coarse dendritic cast microstructures of these three alloys,
(2) almost fully recrystallized microstructure can be achieved for extruded Mg0.5Zn0.2Ca and Mg4Zn0.2Sn alloys and the grain size increased with increasing extrusion speed. While the microstructure was only partially recrystallized for extruded Mg0.5Zn0.2Ge alloy even at the highest speed of 4.4 mm/s in this study and the extrusion speed showed inverse effect on the grain size of this alloy,
(3) the extruded Mg0.5Zn0.2Ca alloy exhibited pretty low texture while extruded Mg0.5Zn0.2Ge and Mg4Zn0.2Sn alloys showed stronger alignment of basal planes parallel to the extrusion direction with a strong prismatic component,
(4) the extrusion process enhanced the corrosion properties of Mg0.5Zn0.2Ge and Mg4Zn0.2Sn alloys but showed little effect on that of Mg0.5Zn0.2Ca alloy,
(5) different extrusion speed did not obviously altered the texture and corrosion performance of extruded Mg0.5Zn0.2Ca, Mg0.5Zn0.2Ge and Mg4Zn0.2Sn alloys.

Therefore, an extrusion speed of 2.2 mm/s was chosen for further studies. In the following studies, Mg0.5Zn0.2Ca, Mg0.5Zn0.2Ge and Mg4Zn0.2Sn alloys extruded at 2.2 mm/s were referred as the optimized alloys for the comprehensive studies and comparison of corrosion performance, corrosion mechanisms, mechanical properties and integrity, fatigue and corrosion fatigue behavior and the susceptibility to stress corrosion cracking.

5.4 Properties of optimized alloys

5.4.1 Evaluation of corrosion properties

As disclosed above, the corrosion rates of optimized Mg0.5Zn0.2Ca and Mg0.5Zn0.2Ge alloys measured by hydrogen evolution tests after 168 h are only about 0.1 mm/year. This indicates that the optimized Mg0.5Zn0.2Ca and Mg0.5Zn0.2Ge alloys possess pretty good corrosion resistance, which shows potential application in both biomedical and industrial applications. Thus, the corrosion behavior of optimized Mg0.5Zn0.2Ca, Mg0.5Zn0.2Ge and Mg4Zn0.2Sn alloys were further studied in 0.5 *wt.*% NaCl prepared by DIW and ATW, respectively. The former one was frequently used to mimic a moderate industrial service environment. While the latter was utilized to present a closer condition to the actual service atmosphere of the materials because of the complicated compositions of water in practical applications.

The EIS, potentiodynamic polarization and hydrogen evolution results of optimized Mg0.5Zn0.2Ca, Mg0.5Zn0.2Ge and Mg4Zn0.2Sn alloys (extruded at 2.2 mm/s) tested in 0.9 *wt.*% solution was extracted out to give a clear comparison between the corrosion performance of different alloys and between the corrosion behavior of the alloys in different corrosive electrolytes.

Hydrogen evolution results

Figure 5.36 compares the hydrogen evolution results of Mg0.5Zn0.2Ca, Mg0.5Zn0.2Ge and Mg4Zn0.2Sn alloys after immersion in DIW based 0.9 *wt.*% and 0.5 *wt.*% NaCl solutions for up to 168 h. The corrosion rates derived from the evolved hydrogen volume can be found in Table 5.13. Apparently, the corrosion properties of these three alloys increase in the order of Mg4Zn0.2Sn, Mg0.5Zn0.2Ca, Mg0.5Zn0.2Ge in both solutions. The corrosion rates of the three alloys decrease in the DIW based NaCl solution with lower concentration, especially for Mg0.5Zn0.2Ge and Mg4Zn0.2Sn alloys. The hydrogen evolution results reveal very obvious difference of the corrosion resistance of the alloys in these two NaCl solutions.

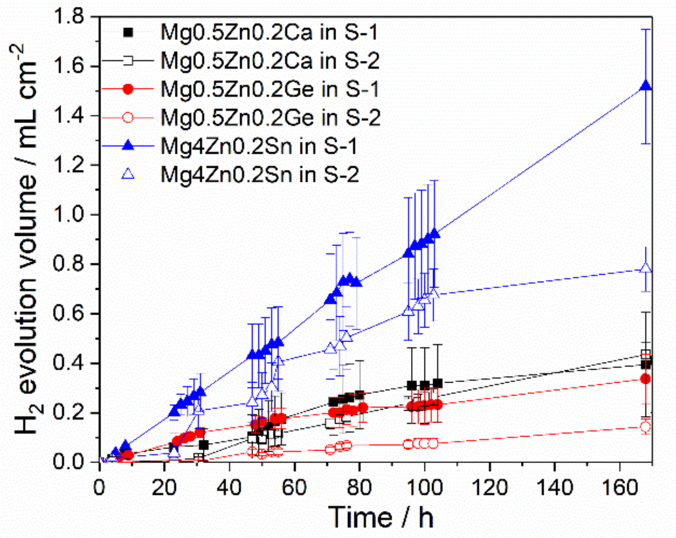

Figure 5.36 Hydrogen evolution curves of extruded Mg0.5Zn0.2Ca, Mg0.5Zn0.2Ge and Mg4Zn0.2Sn alloys after immersion in DIW based 0.9 *wt.*% NaCl (S-1) and DIW based 0.5 *wt.*% NaCl (S-2) solutions for 168 h at room temperature.

EIS in DIW based 0.9 wt.% NaCl solution

Figure 5.37 presents the EIS spectra of optimized Mg0.5Zn0.2Ca, Mg0.5Zn0.2Ge and Mg4Zn0.2Sn alloys tested in 0.9 *wt.*% NaCl solution at room temperature for 48 h. Obviously, two well-defined capacitive loops are observed for both Mg0.5Zn0.2Ca and Mg0.5Zn0.2Ge alloys, while that of Mg4Zn0.2Sn alloy is poorly-defined. The impedance values at 48 h of Mg0.5Zn0.2Ca and Mg0.5Zn0.2Ge alloys (more than 1000 Ω cm^2) are much higher than that of Mg4Zn0.2Sn alloy (about 400 Ω cm^2). Moreover, the diameters of the capacitive loops gradually increase for Mg0.5Zn0.2Ge alloy, while those of Mg0.5Zn0.2Ca alloy fluctuate with immersion time. Therefore, the EIS results indicate that Mg0.5Zn0.2Ca and Mg0.5Zn0.2Ge alloys are corrosion-resistant in 0.9 *wt.*% NaCl solution and the corrosion resistance of Mg0.5Zn0.2Ge alloy continually enhances with exposure time. In contrast, active dissolution occurs to Mg4Zn0.2Sn alloy as soon as the measurement started. This may be a combined result of the different microstructures and corrosion protection abilities of the surface films of the alloys.

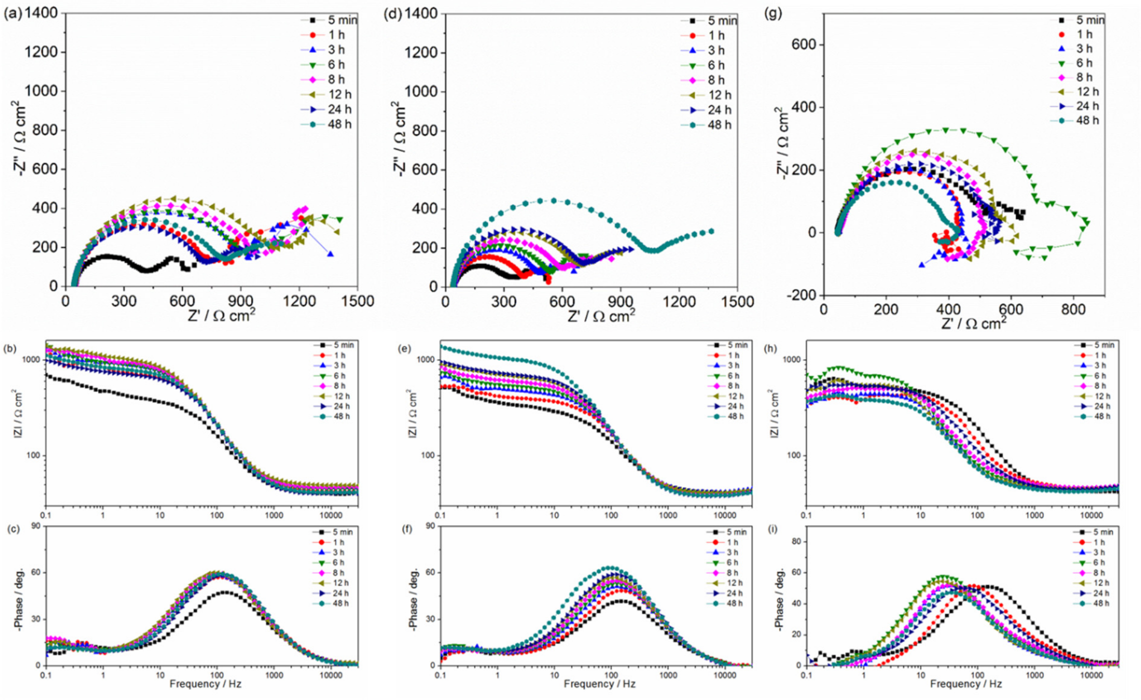

Figure 5.37 Impedance spectra of extruded (a, b, c) Mg0.5Zn0.2Ca, (d, e, f) Mg0.5Zn0.2Ge and (g, h, i) Mg4Zn0.2Sn alloys tested in DIW based 0.9 *wt.*% NaCl solution at room temperature.

EIS in DIW based 0.5 wt.% NaCl solution

Figure 5.38 depicts the EIS spectra of extruded Mg0.5Zn0.2Ca, Mg0.5Zn0.2Ge and Mg4Zn0.2Sn alloys immersed in DIW based 0.5 *wt.*% NaCl solution. Compared with the results of the corresponding alloys in 0.9 *wt.*% NaCl solution, no evident difference is observed except for the slightly increased impedance values for Mg0.5Zn0.2Ge and Mg4Zn0.2Sn alloys. The characteristics of the impedance spectra for the same alloy are similar. This demonstrates that the corrosion behavior of extruded Mg0.5Zn0.2Ca, Mg0.5Zn0.2Ge and Mg4Zn0.2Sn alloys in 0.5 *wt.*% NaCl solution is similar to that in 0.9 *wt.*% NaCl solution despite the slightly lower concentration of aggressive chloride ions (Cl$^-$) in the solution.

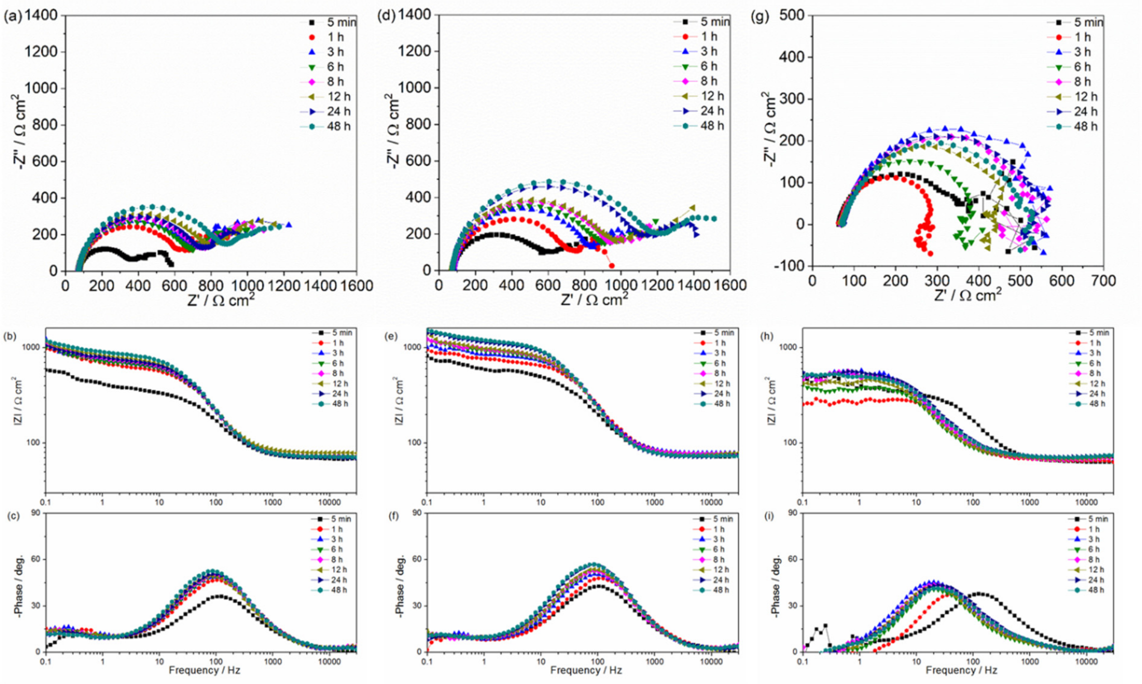

Figure 5.38 Impedance spectra of extruded (a, b, c) Mg0.5Zn0.2Ca, (d, e, f) Mg0.5Zn0.2Ge and (g, h, i) Mg4Zn0.2Sn alloys tested in DIW based 0.5 *wt.*% NaCl solution at room temperature.

EIS in ATW based 0.5 wt.% NaCl solution

Interestingly, in ATW based 0.5 *wt.*% NaCl solution (Figure 5.39), well-defined capacitive loops are present in all cases. The impedance values of the three alloys continually increase with prolonged exposure. After immersion for 24 h, the values become much higher than those in the solution prepared with DIW irrespective of the NaCl concentration. Furthermore, a new time constant is noticed in the high frequency region after 24 h, which becomes much clearer after 48 h of exposure for Mg0.5Zn0.2Ca and Mg0.5Zn0.2Ge alloys. This phenomenon indicates that a new barrier layer of corrosion products may have been formed on the alloy surfaces and imparts high corrosion resistance to the alloys. In addition, the obtained results disclose that, in ATW based electrolyte, the composition of the electrolyte dominates over the composition of the alloy in terms of controlling the corrosion rate during the respective period. Nevertheless, the impedance values of Mg4Zn0.2Sn alloy are still lower than those of Mg0.5Zn0.2Ca and Mg0.5Zn0.2Ge alloys at the same time point.

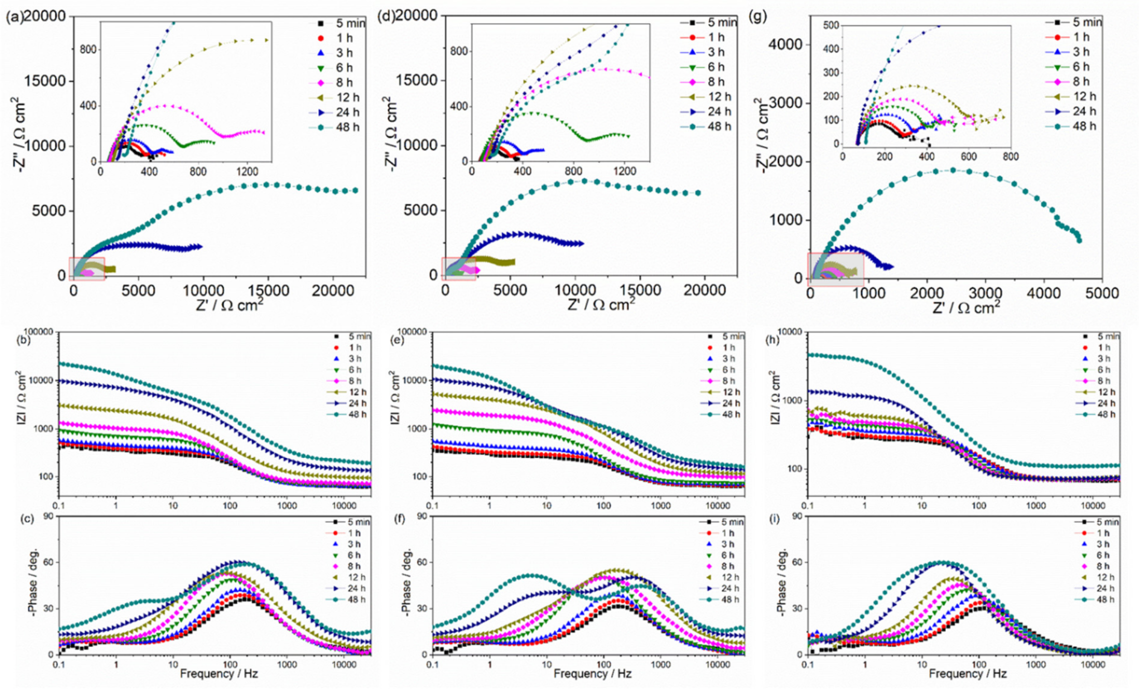

Figure 5.39 Impedance spectra of extruded (a, b, c) Mg0.5Zn0.2Ca, (d, e, f) Mg0.5Zn0.2Ge and (g, h, i) Mg4Zn0.2Sn alloys tested in ATW based 0.5 *wt.*% NaCl solution at room temperature.

To further understand the evolution of the corrosion resistance of the three alloys in different corrosive media, the impedance spectra were fitted with two different equivalent circuits (Figure 5.40) according to the characteristics of the spectra and the fitted data are plotted in Figure 5.41. It can be clearly observed from the Bode plots in Figure 5.39c, f and i, in 0.5 *wt.*% NaCl solution prepared with ATW, the charge transfer process is almost undistinguishable after 24 h. This is because of the gradually increased resistance resulting from the thicker and more compact corrosion product layers with extended immersion time, which are hiding the response of the double electric layer. Consequently, the accurate fitting for the double layer capacitance would not be possible. To avoid possible controversy, the detailed fitted parameters are not presented. In the equivalent circuits, R_s is the solution resistance between the reference electrode and the working electrode. R_{ct} accounts for the charge transfer resistance parallel to the double electric layer at the interface of the alloy and the electrolyte, CPE_{dl}, R_{f1} and CPE_{f1} represent the corrosion resistance and capacity of the primary corrosion product film. R_{f2} and CPE_{f2} are introduced to account for the secondary corrosion product layer in the case of ATW based 0.5 *wt.*% NaCl solution. The second equivalent circuit with three time constants was only used when the third relaxation process was evidenced at the spectra at high frequencies. In all other cases, the first equivalent consisting of two time constants was applied. For comparison, the sum (R_{sum}) of R_{ct}, R_{f1} and R_{f2} is displayed.

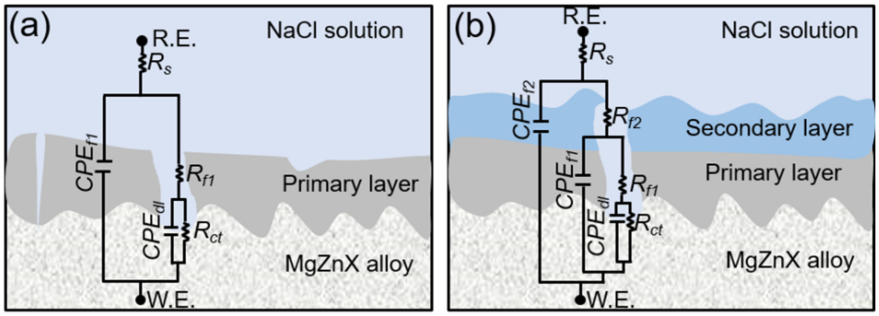

Figure 5.40 Equivalent circuits used to fit the impedance spectra of (a) Mg0.5Zn0.2Ca, Mg0.5Zn0.2Ge and Mg4Zn0.2Sn alloys after immersion in DIW based 0.9 *wt.*% NaCl, DIW based 0.5 *wt.*% NaCl and ATW based 0.5 *wt.*% NaCl solutions (for the spectra of Mg0.5Zn0.2Ca and Mg0.5Zn0.2Ge alloys immersed for less than 24 h) and (b) Mg0.5Zn0.2Ca and Mg0.5Zn0.2Ge alloys after immersion in ATW based 0.5 *wt.*% NaCl solution for more than 24 h.

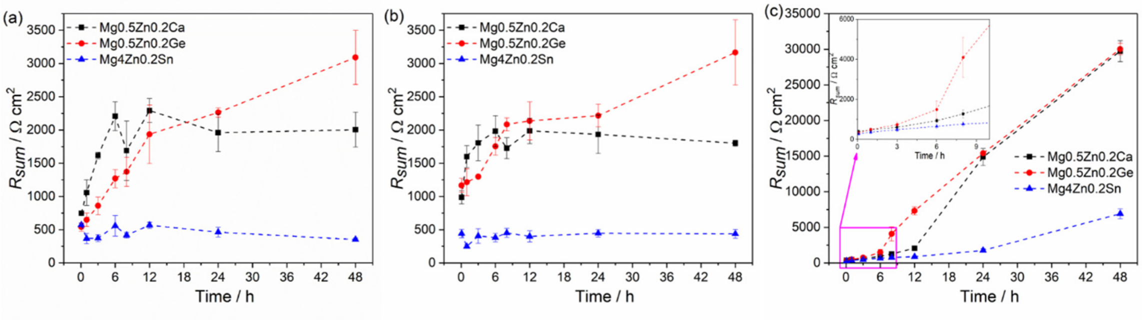

Figure 5.41 Plots of R_{sum} of Mg0.5Zn0.2Ca, Mg0.5Zn0.2Ge and Mg4Zn0.2Sn alloys as a function of immersion time in (a) DIW based 0.9 *wt.*% NaCl, (b) DIW based 0.5 *wt.*% NaCl and (c) ATW based 0.5 *wt.*% NaCl solutions.

It can be seen from Figure 5.41 that R_{sum} of Mg0.5Zn0.2Ca and Mg4Zn0.2Sn alloys fluctuates with prolonged immersion in both DIW based 0.9 *wt.*% (Figure 5.41a) and 0.5 *wt.*% NaCl (Figure 5.41b) solutions. In comparison, R_{sum} of Mg0.5Zn0.2Ge alloy gradually increases with immersion time in these two solutions. Moreover, the R_{sum} values are only marginally altered by the slight difference for the NaCl concentration for the specific alloy. Generally, the order of corrosion resistance of the three alloys in DIW based NaCl solutions is Mg0.5Zn0.2Ge > Mg0.5Zn0.2Ca > Mg4Zn0.2Sn. This is in good agreement with the hydrogen evolution results displayed in Figure 5.36. However, when the corrosive solution was prepared with ATW (concentration at 0.5 *wt.*%), R_{sum} values (Figure 5.41c) of all of the three alloys gradually increase with immersion time and are specifically higher than those measured in solutions prepared with DIW after 24 h. In addition, the corrosion resistance of Mg0.5Zn0.2Ca and

Mg0.5Zn0.2Ge alloys is similar and much higher than that of Mg4Zn0.2Sn alloy, especially after immersion for 12 h.

Potentiodynamic polarization curves

Potentiodynamic polarization curves were also collected after immersion for 48 h to investigate the corrosion protection abilities of the different corrosion product layers formed on the alloy surfaces under different conditions, as shown in Figure 5.42. In the figure, S-1, S-2 and S-3 refer to DIW based 0.9 *wt.*% NaCl solution, DIW based 0.5 *wt.*% NaCl solution and ATW based 0.5 *wt.*% NaCl solution, respectively.

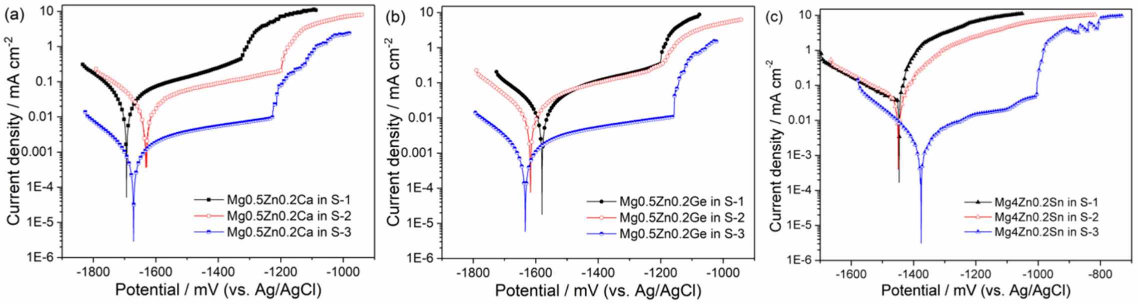

Figure 5.42 Potentiodynamic polarization curves of extruded (a) Mg0.5Zn0.2Ca, (b) Mg0.5Zn0.2Ge and (c) Mg4Zn0.2Sn alloys after immersion in DIW based 0.9 *wt.*% NaCl (S-1), DIW based 0.5 *wt.*% NaCl (S-2) and ATW based 0.5 *wt.*% NaCl solutions (S-3) for 48 h at room temperature.

In DIW based 0.9 *wt.*% and 0.5 *wt.*% NaCl solutions, the curves of the same alloy do not show significant difference, indicating that the corrosion mechanisms of the alloys are similar. Broad regions of low-current plateaus are observed for Mg0.5Zn0.2Ca and Mg0.5Zn0.2Ge alloys in both solutions, while the anodic current density of Mg4Zn0.2Sn alloy steeply increases with applied potential. Lower corrosion current densities of Mg0.5Zn0.2Ca and Mg0.5Zn0.2Ge alloys are detected compared to Mg4Zn0.2Sn alloy. These results demonstrate the higher corrosion resistance, existence of barrier surface films and their obstruction to the anodic dissolution of Mg0.5Zn0.2Ca and Mg0.5Zn0.2Ge alloys in DIW based 0.9 *wt.*% and 0.5 *wt.*% NaCl solutions in comparison with Mg4Zn0.2Sn alloy.

In ATW based 0.5 *wt.*% NaCl solution, the corrosion current densities of the three alloys are distinctly lower than those measured in DIW based solutions. However, Mg4Zn0.2Sn alloy still exhibits the highest current density. Meanwhile, all anodic curves exhibit an extended low-current plateau region, indicating that protective corrosion product films are formed on the alloy surfaces in this solution and effectively retard the anodic dissolution of the alloys.

Table 5.13 Corrosion parameters for extruded Mg0.5Zn0.2Ca, Mg0.5Zn0.2Ge and Mg4Zn0.2Sn alloys derived from the potentiodynmaic polarization curves and hydrogen evolution results after immersion in DIW based 0.9 *wt.*% NaCl, DIW based 0.5 *wt.*% NaCl and ATW based 0.5 *wt.*% NaCl solutions.

Solution	**Alloy**	**Potentiodynamic polarization**				**Hydrogen evolution**
		CR **mm year^{-1}**	**i_{corr}** **µA cm^{-2}**	**E_{corr}** **mV**	**E_{bd}** **mV**	***CR*** **mm year^{-1}**
0.9 *wt.*% NaCl_DIW	Mg0.5Zn0.2Ca	0.41 ± 0.08	18 ± 3.5	-1694 ± 1	-1327 ± 118	0.12 ± 0.06
	Mg0.5Zn0.2Ge	0.26 ± 0.05	11 ± 2.2	-1606 ± 27	-1218 ± 40	0.10 ± 0.03
	Mg4Zn0.2Sn	0.81 ± 0.13	36 ± 5.8	-1449 ± 28	-	0.45 ± 0.08
0.5 *wt.*% NaCl_DIW	Mg0.5Zn0.2Ca	0.22 ± 0.04	9.8 ± 1.8	-1655 ± 17	-1255 ± 51	0.13 ± 0.01
	Mg0.5Zn0.2Ge	0.21 ± 0.02	9.1 ± 0.6	-1616 ± 38	-1167 ± 78	0.04 ± 0.01
	Mg4Zn0.2Sn	0.76 ± 0.06	37 ± 2.1	-1443 ± 25	-	0.23 ± 0.03
0.5 *wt.*% NaCl_ATW	Mg0.5Zn0.2Ca	0.013 ± 0.001	0.6 ± 0.05	-1690 ± 11	-1280 ± 46	
	Mg0.5Zn0.2Ge	0.013 ± 0.001	0.6 ± 0.04	-1658 ± 28	-1195 ± 87	
	Mg4Zn0.2Sn	0.035 ± 0.006	1.5 ± 0.28	-1379 ± 23	-1045 ± 47	

The fitted corrosion parameters are listed in Table 5.13. In DIW based solutions at both concentrations, the results reveal that the corrosion resistance of alloys increase in the order of: Mg4Zn0.2Sn < Mg0.5Zn0.2Ca < Mg0.5Zn0.2Ge, which is consistent with the hydrogen evolution and impedance results. Furthermore, lower corrosion rates are reached for the three alloys in solution with lower Cl^- concentration, which was revealed also in refs. [69, 70] and widely accepted for Mg alloys. Meanwhile, in the case of ATW based 0.5 *wt.*% NaCl solution, *CR* and i_{corr} of Mg0.5Zn0.2Ca and Mg0.5Zn0.2Ge alloys are quite similar. In contrast, *CR* and i_{corr} of Mg4Zn0.2Sn alloy are higher. This is in good agreement with the EIS results and suggests that the corrosion behavior of Mg0.5Zn0.2Ca and Mg0.5Zn0.2Ge alloys is similar in ATW based 0.5 *wt.*% NaCl solution and the corrosion product films formed on the surfaces have similar properties. Notably, the *CR* and i_{corr}, irrespective of which alloy, decrease by more than one order of magnitude when the alloys are immersed in ATW based 0.5 *wt.*% NaCl solution compared to those tested in DIW based NaCl solutions. Thus, it can be concluded that the corrosion product films formed in ATW based 0.5 *wt.*% NaCl solution are much more protective to the alloys.

The evaluation of corrosion performance for optimized Mg0.5Zn0.2Ca, Mg0.5Zn0.2Ge and Mg4Zn0.2Sn alloys in three different corrosive electrolytes reveals that:

(1) the corrosion resistance of the alloys was a bit higher in DIW based 0.5 *wt.*% NaCl solution compared to that tested in DIW based 0.9 *wt.*% NaCl solution,
(2) the corrosion mechanisms of the alloys did not change in DIW based NaCl solution at different concentrations based on the electrochemical measurements,
(3) an additional layer of corrosion products was formed on the alloy surfaces in ATW based 0.5 *wt.*% NaCl solution, which imparted much higher corrosion resistance to the alloys.

5.4.2 Corrosion morphology and product analysis

To facilitate the understanding of the corrosion mechanisms of optimized Mg0.5Zn0.2Ca, Mg0.5Zn0.2Ge and Mg4Zn0.2Sn alloys in different corrosive electrolytes, the morphologies and compositions of the corrosion products were investigated after the corrosion tests, combined with the Volta potential measurements as well. The as-cast alloys were also studied to understand the influence of extrusion process on the corrosion mechanisms. Nevertheless, the SKPFM measurement for as-cast Mg0.5Zn0.2Ca alloy was limited by the resolution of the instrument due to the eutectic type ($Ca_2Mg_6Zn_3$ + Mg_2Ca) second phases in really small size in the microstructure. The extremely fine second phases (sub-micron-scale) in extruded Mg4Zn0.2Sn alloy and the low content and small size (about 3 µm) of those Fe-Mn/Mg_2Si impurity particles also pose great difficulty to the successful SKPFM measurement of a desired position (place with impurity particle). Thus, except the already presented SKPFM result of as-cast Mg4Zn0.2Sn alloy, only the Volta potential distribution map of as-cast and extruded Mg0.5Zn0.2Ge alloys are provided in this part.

Drop corrosion test

The respective role of each phase constituency of the alloys during the corrosion process can be revealed by local (electrolyte) drop corrosion test. However, the solubility of second phases in chromic acid or during the cleaning process can disturb the determination of the corrosion mechanism. Therefore, SEM images were taken for barely polished specimens before and after the cleaning process to check the solubility of the second phases, shown in Figure 5.43. The results reveal that the grey Mg_2Ca phases in Mg0.5Zn0.2Ca alloy dissolved after the cleaning process with chromic acid, while no changes are visible on the surfaces of Mg0.5Zn0.2Ge and Mg4Zn0.2Sn alloys. Accordingly, local drop corrosion test is not appropriate for the exact determination of the roles of second phases in Mg0.5Zn0.2Ca alloy during corrosion. This can also explain the holes observed in the micrographs of polished extruded Mg0.5Zn0.2Ca alloys in Figure 5.16. However, the test was still carried out for as-cast Mg0.5Zn0.2Ca alloy to semi-qualitatively judge the corrosion mechanism of the alloy, without consideration for the role of Mg_2Ca phase temporarily. Because $Ca_2Mg_6Zn_3$ phase behaved normally during the cleaning process. While the test was not performed for extruded Mg0.5Zn0.2Ca alloy concerning the disturbance of the dissolution of Mg_2Ca phase (the only second phase in extruded Mg0.5Zn0.2Ca alloy) during the cleaning process.

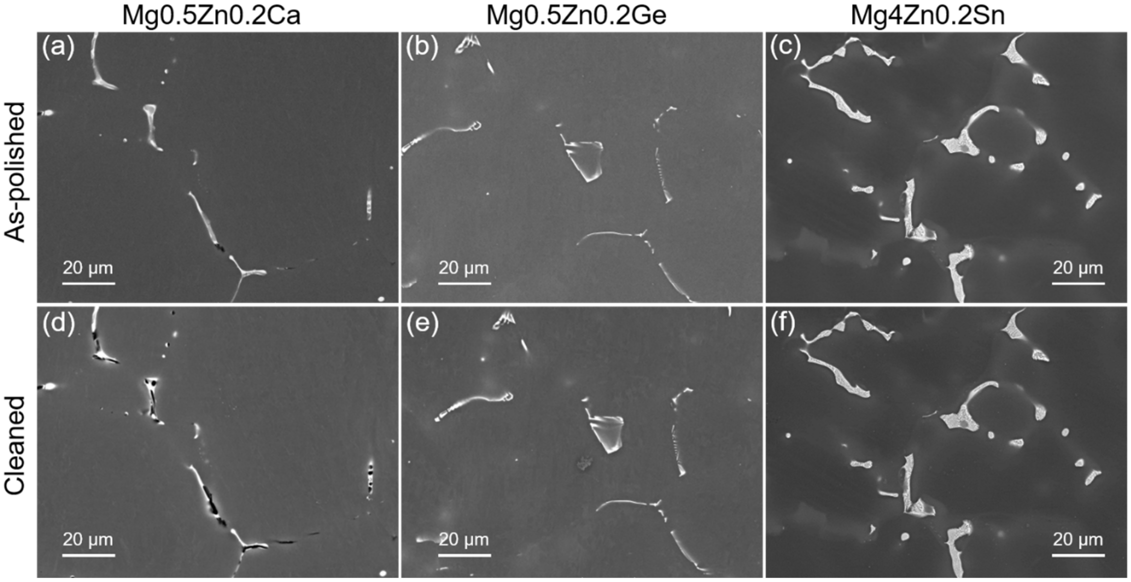

Figure 5.43 SEM images of typical microstructure of as-cast (a, d) Mg0.5Zn0.2Ca, (b, e) Mg0.5Zn0.2Ge and (c, f) Mg4Zn0.2Sn alloys before and after cleaning with chromic acid to check the solubility of second phases during the cleaning process.

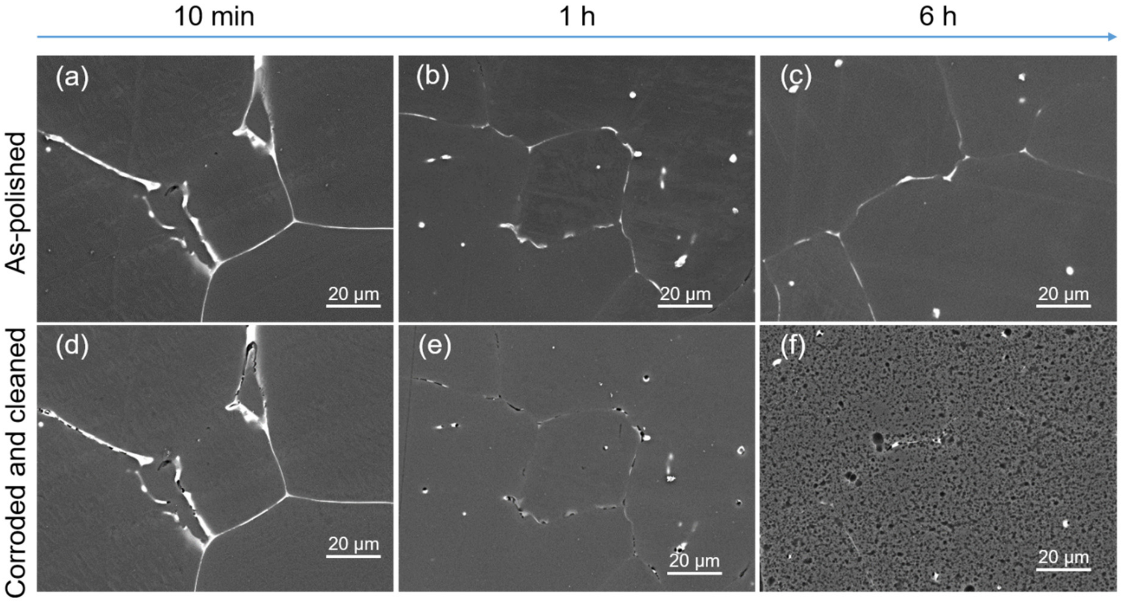

Figure 5.44 Typical SEM images of as-cast Mg0.5Zn0.2Ca alloy before (a, b, c) and after corrosion in 0.9 *wt.*% NaCl solution for (d) 10 min, (e) 1 h and (f) 6 h with removal of corrosion products.

Figure 5.44 discloses that the α-Mg matrix almost remains intact for as-cast Mg0.5Zn0.2Ca alloy after corrosion in 0.9 *wt.*% NaCl solution for up to 1 h, showing no obvious corrosion. When the immersion time extended to 6 h, the matrix is uniformly corroded. No clear galvanic corrosion is observed between the nobler $Ca_2Mg_6Zn_3$ phase and the surrounding matrix. This possibly indicates the uniform corrosion behavior of as-cast Mg0.5Zn0.2Ca alloy.

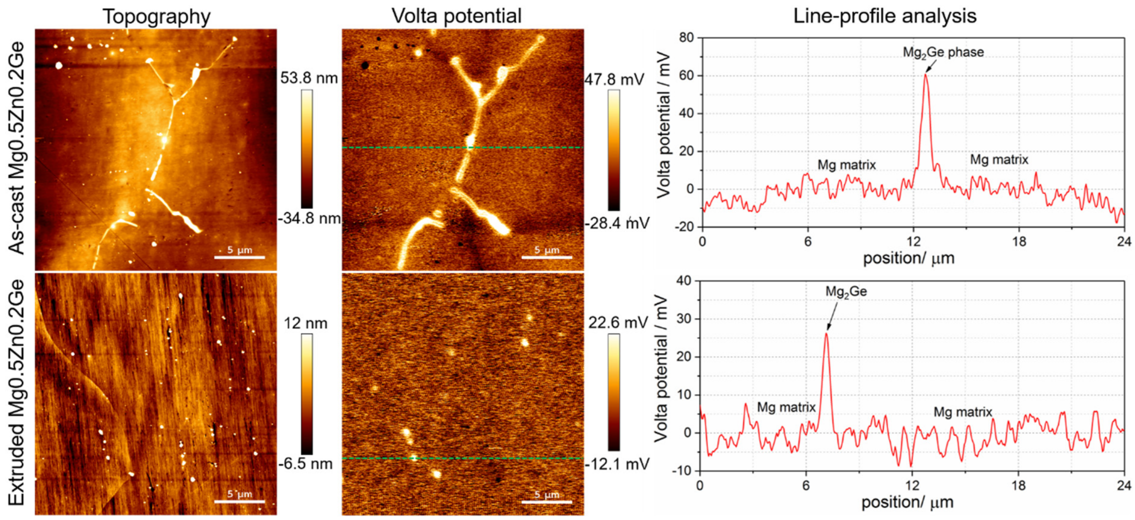

Figure 5.45 SKPFM study of as-cast and extruded Mg0.5Zn0.2Ge alloys including topography map, surface Volta potential map and line-profile analysis of relative Volta potential though second phases.

Figure 5.45 illustrates the Volta potential distribution of as-cast and extruded Mg0.5Zn0.2Ge alloys. The particles with negative or no Volta potential difference between the matrix should be contaminates on the sample surface or oxides in the alloys. It is revealed that the Volta potential difference between the Mg_2Ge phases and the Mg matrix is 52 ± 18 mV, close to that of Mg_2Ge phases in Mg4Zn0.2Ge alloy. A big difference can be found between the current result and the result from Liu et al. (about 400 mV) [51] most likely due to difference of bulk composition of alloy, SKPFM system and tip used. Similarly, the deformed tiny Mg_2Ge phase is nobler than the α-Mg matrix. However, the Volta potential difference between the Mg_2Ge phase and the matrix decreases to be 29 ± 9 mV, which can be a result of the dissolution of the Mg_xZn_y phases into the matrix during the homogenization or extrusion process.

The surface morphologies of as-cast Mg0.5Zn0.2Ge alloy before and after corrosion for different immersion time in DIW based 0.9 *wt.*% NaCl solution are presented in Figure 5.46. The results reveal that corrosion occurs preferentially at the α-Mg matrix, especially, at the matrix phases adjacent to the Mg_2Ge phases. Consequently, some Mg_2Ge phases are even detached and fall out from the matrix at later stages, indicating that the matrix close to the Mg_2Ge phase dissolves as an anode and the Mg_2Ge phase serves as a cathode in the micro-galvanic corrosion. This phenomenon is more obvious after relatively longer immersion time (6 h).

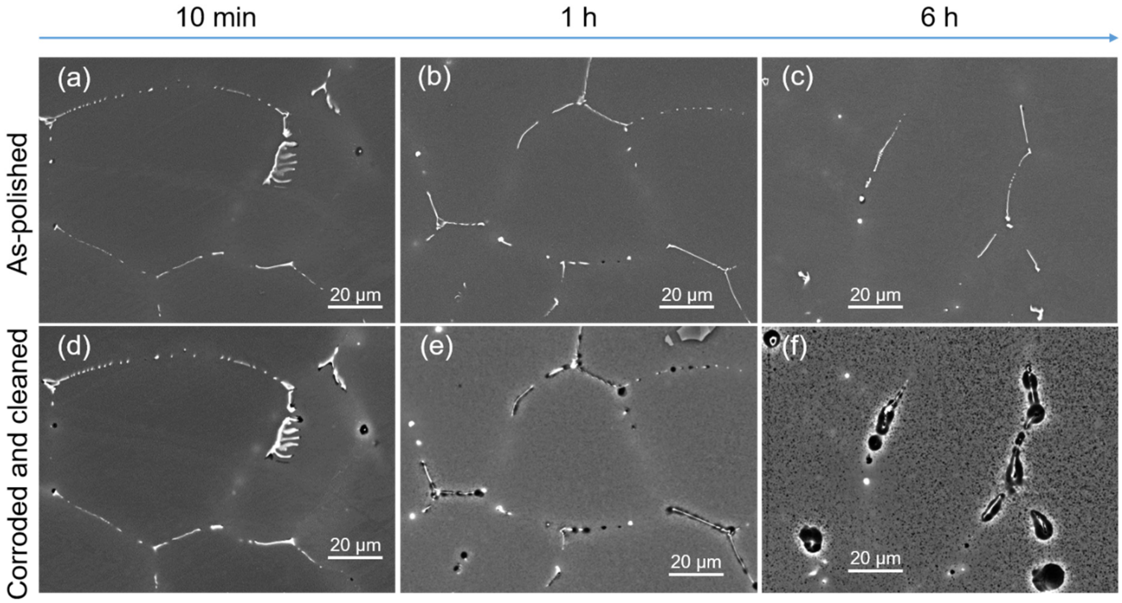

Figure 5.46 Typical SEM images of as-cast Mg0.5Zn0.2Ge alloy before (a, b, c) and after corrosion in 0.9 *wt.*% NaCl solution for (d) 10 min, (e) 1 h and (f) 6 h with removal of corrosion products.

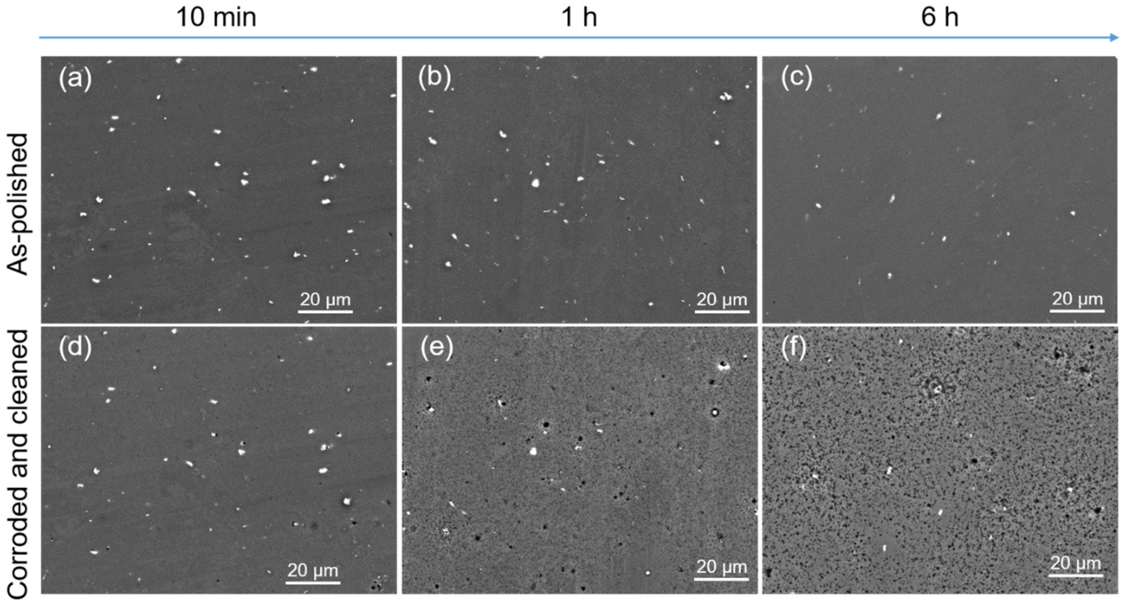

Figure 5.47 Typical SEM images of extruded Mg0.5Zn0.2Ge alloy before (a, b, c) and after corrosion in 0.9 *wt.*% NaCl solution for (d) 10 min, (e) 1 h and (f) 6 h with removal of corrosion products.

For extruded Mg0.5Zn0.2Ge alloy (Figure 5.47), in general, the case is similar to the as-cast Mg0.5Zn0.2Ge alloy. The α-Mg matrix dissolves preferentially during immersion and small Mg_2Ge phases are quickly detached due to the preferential dissolution of the adjacent α-Mg matrix with extended immersion time. Nevertheless, much milder micro-galvanic corrosion can be found for extruded Mg0.5Zn0.2Ge alloy compared with as-cast Mg0.5Zn0.2Ge alloy, which is in line with the measured corrosion rates. This might be a result of the lower Volta potential difference between Mg_2Ge phase and α-Mg matrix and the fast falling out of small Mg_2Ge phases of extruded Mg0.5Zn0.2Ge alloy. Combining with the decreased volume fraction and the more homogenous distribution of cathodic second phases after extrusion, more uniform corrosion of extruded Mg0.5Zn0.2Ge alloy is visible.

The SKPFM result of as-cast Mg4Zn0.2Sn alloy has been presented in Figure 5.10 and Table 5.5, which reveals that both the MgZn phase and Zn-rich interdendritic region exhibit higher Volta potential compared with the α-Mg matrix. Despite the missed SKPFM result of extruded Mg4Zn0.2Sn alloy, it has been widely accepted that Fe-containing impurity particles play a critical role in the corrosion performance of Mg alloys when exposed to corrosive environment [71]. Moreover, Fe impurity particles possess much higher standard electrode potential than Mg and the high Volta potential difference between an Fe impurity particle and α-Mg matrix has also been determined in pure Mg in [72-74]. Thus, it can be speculated that galvanic coupling may be formed between the Fe-Mn/Mg_2Si co-existing particle and the surrounding α-Mg matrix besides the Mg_xZn_y phases when the extruded Mg4Zn0.2Sn alloy is exposed to corrosive electrolyte. Actually, it has been reported that < 2 *wt.*% Si has no significant influence on the corrosion of Mg, but it (even at ppm level) can facilitate the formation of Fe-rich particles (Fe-Si particles). Consequently, the corrosion tolerance limit of Fe in Mg is significantly decreased even when the content of Fe is far below the widely accepted tolerance limit and the Fe-Si particles can lead to a high corrosion rate of Mg [75, 76]. However, the presence of Mn can suppress the detrimental effect of Fe on the corrosion behavior of Mg alloys. Therefore, the relative galvanic activity of the couple between the Fe-Mn/Mg_2Si particle and the matrix and that between the tiny second phase and the matrix remains to be considered, which will be clearly revealed by the below corrosion tests.

DIW based 0.5 *wt.*% NaCl solution was used for the observation of the corrosion process of Mg4Zn0.2Sn alloys due to the poorer corrosion resistance of this system. Figure 5.48 reveals that, after immersion for 6 h, the α-Mg dendrites and the α-Mg inside the eutectic phase dissolve preferentially, while the MgZn phases and the surrounding Zn-rich interdendritic regions seem to remain intact. This suggests that galvanic corrosion occurs between the components of the eutectic phase and between the α-Mg dendrites and the interdendritic area (second phase + Zn-rich interdendritic region). It is worth mentioning that many small particles are visible mainly along the boundaries between the α-Mg dendrites and the interdendritic regions after immersion. The EDS analysis (Table 5.14) demonstrated that those particles are considerably rich in Zn, even much higher than the original Zn-rich interdendritic regions (shown in Table 5.4).

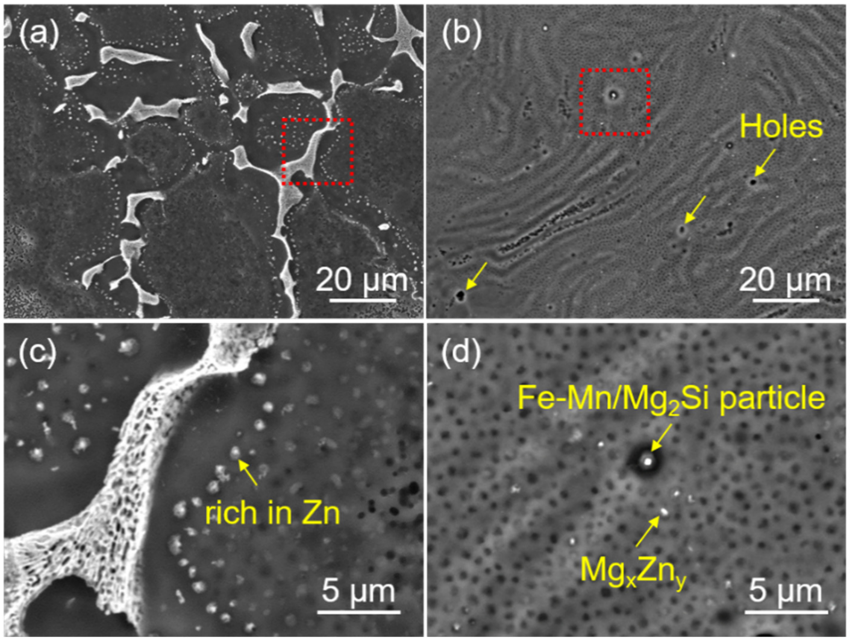

Figure 5.48 Surface morphologies of (a) as-cast and (b) extruded Mg4Zn0.2Sn alloys after immersion in 0.5 *wt.*% NaCl solution for 6 h at room temperature with removal of corrosion products.

Table 5.14 EDS analysis of the constituents in as-cast Mg4Zn0.2Sn alloy after immersion in 0.5 *wt.*% NaCl solution for 6 h with the removal of corrosion products.

Element	**Matrix**		**Second phase**		**Small particles**	
	at.%	***wt.%***	***at.%***	***wt.%***	***at.%***	***wt.%***
O	1.6	1.0	5.4	2.4	10.5	6.6
Mg	97.4	96.4	63.7	42.3	83.7	79.2
Cr	0.1	0.1	0.4	0.6	0.9	1.8
Zn	0.9	2.3	30.4	54.3	4.8	12.1
Sn	0.0	0.2	0.1	0.4	0.1	0.3

In the case of extruded Mg4Zn0.2Sn alloy, the brighter Zn-rich matrix seems to be less corroded than the darker matrix. Moreover, a dark circle was formed around the Fe-Mn/Mg$_2$Si particle, revealing the occurrence of micro-galvanic corrosion between the impurity containing particle and the surrounding matrix. In comparison, much milder galvanic corrosion can be noticed between the nearby Mg_xZn_y phases and the matrix, indicating the weaker galvanic effect. Some small holes are noticed on the corroded surface, which may be explained by the detachment of those particles or tiny second phases as a result of galvanic corrosion.

Surface and cross-section morphologies after immersion test

The surface and cross-section morphologies of as-cast Mg0.5Zn0.2Ca, Mg0.5Zn0.2Ge and Mg4Zn0.2Sn alloys fabricated by indirect chill casting were only studied in DIW based 0.9 *wt.*% NaCl solution as comparison, shown in Figure 5.49. Obviously different corroded surface morphologies are revealed, indicating the different corrosion behavior and properties of these three as-cast alloys. A corrosion product film with fine cracks covers the surface of as-cast Mg0.5Zn0.2Ca alloy (Figure 5.49a). In addition, a few aggregations of corrosion products are formed and randomly distributed on the cracked product layer (as indicated by the yellow arrows). The corrosion products on as-cast Mg0.5Zn0.2Ge alloy (Figure 5.49b) surface are more severely cracked due to the evolution of hydrogen bubbles or higher stress during drying process. Precipitates are formed on the surface. The deeper and more severe cracks indicate that the film formed on the surface of Mg0.5Zn0.2Ge alloy is more hydrated [77] or has a higher thickness. In comparison, apparently localized corrosion occurred to as-cast Mg4Zn0.2Sn alloy (Figure 5.49c). The corrosion product layer is much less intact, showing seriously localized attack morphology.

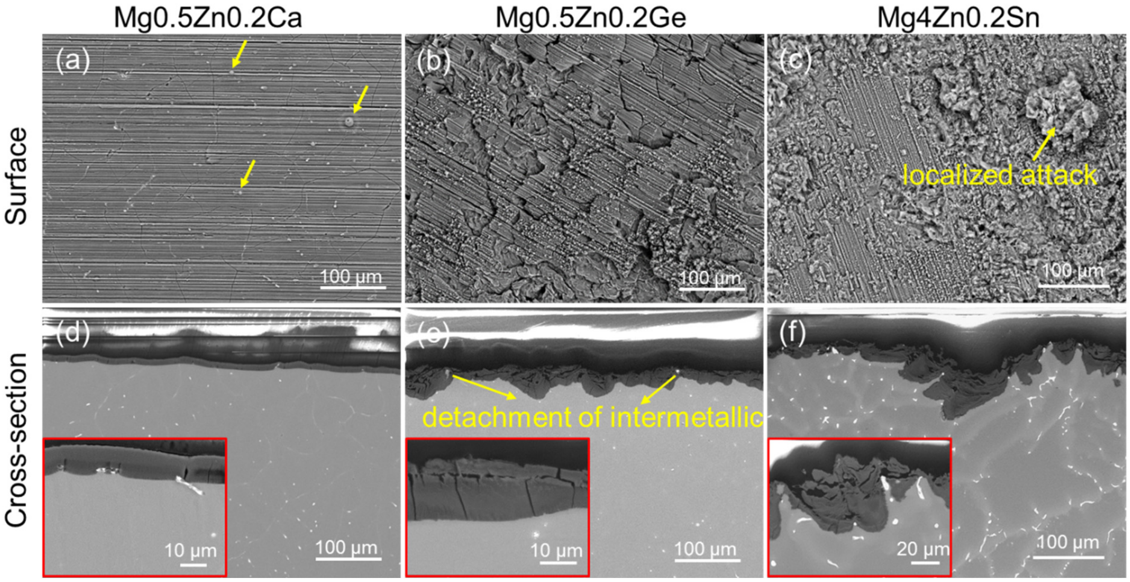

Figure 5.49 Surface and cross-section morphologies of as-cast Mg0.5Zn0.2Ca, Mg0.5Zn0.2Ge and Mg4Zn0.2Sn alloys after immersion in DIW based 0.9 *wt.*% NaCl solution for 48 h.

As revealed by Figure 5.49d, e and f, the corrosion product/metal interface is pretty flat for as-cast Mg0.5Zn0.2Ca alloy but really rough for Mg0.5Zn0.2Ge and Mg4Zn0.2Sn alloys. The thickness of the corrosion product layers of as-cast Mg0.5Zn0.2Ge and Mg4Zn0.2Sn alloys are visually thicker than that of as-cast Mg0.5Zn0.2Ca alloy. Furthermore, the layers are seriously broken and corrosion cavities are observed, especially for as-cast Mg4Zn0.2Sn alloy. This indicates more serious corrosion of as-cast Mg0.5Zn0.2Ge and Mg4Zn0.2Sn alloys, which is consistent with the EIS, polarization and hydrogen evolution results. Additionally, second phases are detached (for Mg0.5Zn0.2Ge and Mg4Zn0.2Sn alloys) or partially protruded (for Mg0.5Zn0.2Ca and Mg4Zn0.2Sn alloys) in the corrosion product layers, indicating the preferentially dissolution of the surrounding α-Mg matrix. As revealed above, the microstructure of as-cast Mg4Zn0.2Sn alloy consists of MgZn phase, Zn-rich interdendritic region and α-Mg matrix and these constituents exhibit Volta potential in a decreasing order. The partially protruded second phases in the corrosion product layer indicate that the surrounding Zn-rich interdendritic region also dissolves to some extent besides the α-Mg matrix, coinciding well with the SKPFM and local drop corrosion tests results. Besides, it also shows that the Zn-rich region acts as barrier for corrosion retarding dissolution when the normal α-Mg matrix is gone. Interestingly, the corrosion product layer of as-cast Mg0.5Zn0.2Ca alloy shows different contrast for the outer and inner parts in BSE image: brighter outer part and darker inner part. It is known that the backscattered electrons are useful to image the atomic number contrast of specimen and reveal the compositional microstructure by contrast [78]. Thus, this phenomenon indicates a preferred distribution of specific elements in the corrosion product layer of as-cast Mg0.5Zn0.2Ca alloy.

Figure 5.50 shows the surface morphologies of extruded Mg0.5Zn0.2Ca, Mg0.5Zn0.2Ge and Mg4Zn0.2Sn alloys after immersion in DIW based 0.9 *wt.*% NaCl, DIW based 0.5 *wt.*% NaCl and ATW based 0.5 *wt.*% NaCl solutions for 48 h. In DIW based 0.9 *wt.*% NaCl solution, both the surfaces of Mg0.5Zn0.2Ca and Mg0.5Zn0.2Ge alloys are covered by cracked corrosion product films because of the shrinkage in volume due to the dehydration of the film. For Mg4Zn0.2Sn alloy, localized attack of the surface occurred. In comparison with the corrosion morphologies of as-cast alloys in DIW based 0.9 *wt.*% NaCl solution, the corrosion behavior of Mg0.5Zn0.2Ca and Mg4Zn0.2Sn alloys do not show a big difference while that of Mg0.5Zn0.2Ge alloy seems to be improved after extrusion.

In DIW based 0.5 *wt.*% NaCl solution, the corrosion morphologies of the three alloys are similar to those tested in DIW based 0.9 *wt.*% NaCl solution, especially for Mg0.5Zn0.2Ca alloy. This indicates similar corrosion mechanisms for all three alloys in DIW based 0.9 *wt.*% and 0.5 *wt.*% NaCl solutions, as already revealed by the electrochemical and hydrogen evolution measurements. However, the corrosion product layers of Mg0.5Zn0.2Ge and

Mg4Zn0.2Sn alloys become more compact. Shallower and less serious cracks are noticed for Mg0.5Zn0.2Ge alloy and a milder corrosion situation is found for Mg4Zn0.2Sn alloy, indicating the corrosion resistance of Mg0.5Zn0.2Ge and Mg4Zn0.2Sn alloys in DIW based 0.5 *wt.*% NaCl solution is higher than in the solution with slightly higher NaCl concentration.

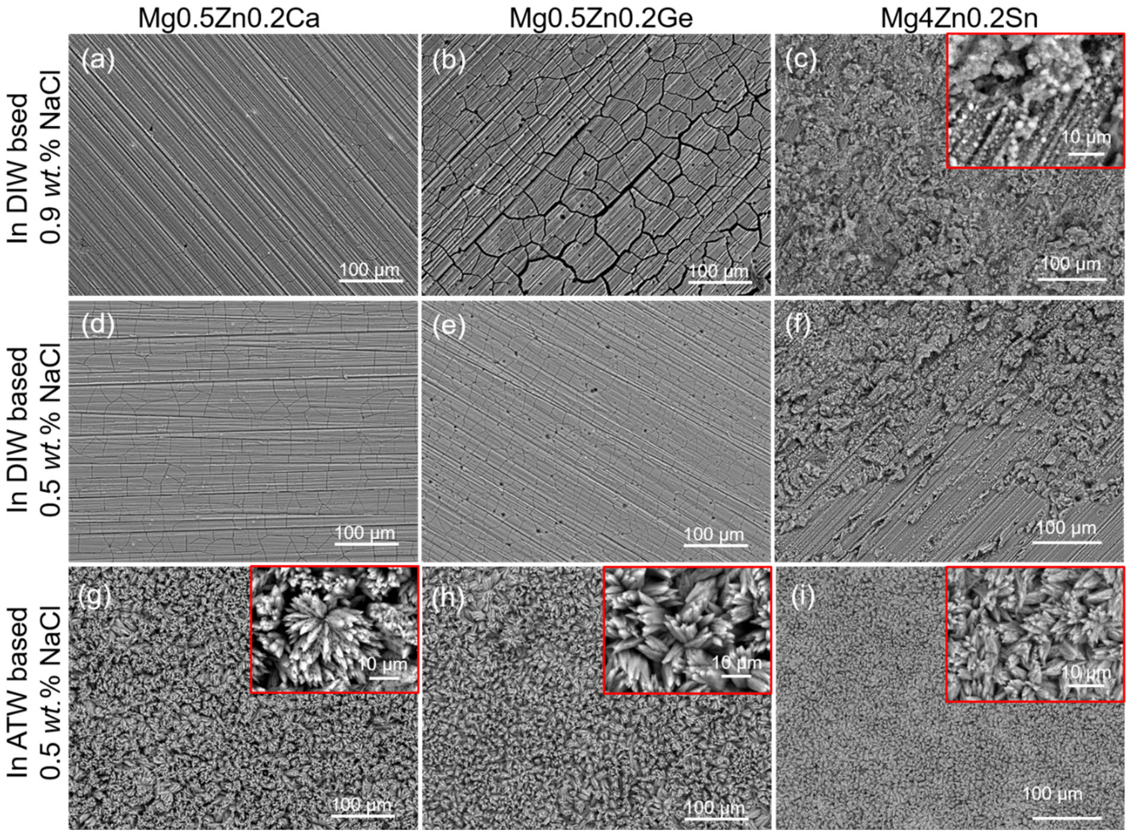

Figure 5.50 Surface morphologies of extruded Mg0.5Zn0.2Ca, Mg0.5Zn0.2Ge and Mg4Zn0.2Sn alloys after immersion in DIW based 0.9 *wt.*% NaCl, DIW based 0.5 *wt.*% NaCl and ATW based 0.5 *wt.*% NaCl solutions for 48 h.

When the alloys were immersed in ATW based 0.5 *wt.*% NaCl solution, totally different surface morphologies were formed compared to the cases in DIW based solutions, but they were identical for the three alloys. As shown in Figure 5.50g, h and i, flower-like products are closely arranged on the surfaces of the alloys. This explains not only the different impedance and polarization responses of the alloys in ATW and DIW based solutions, but also the similar electrochemical responses of the three alloys in ATW based NaCl solution.

Figure 5.51 displays the cross-section morphologies of the extruded alloys after immersion in the three electrolytes for 48 h. The white lines on the resin were from charging effects during imaging due to the poor conductivity of the resin.

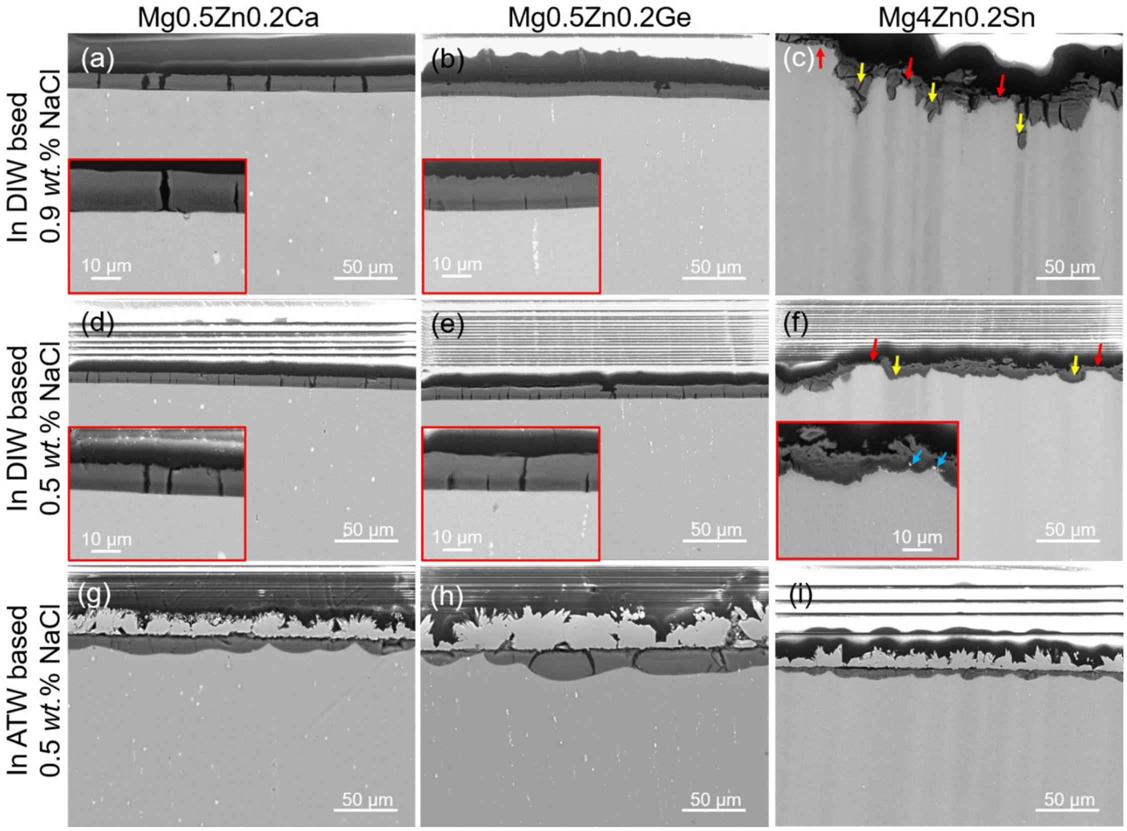

Figure 5.51 Cross-section morphologies of extruded Mg0.5Zn0.2Ca, Mg0.5Zn0.2Ge and Mg4Zn0.2Sn alloys after immersion in DIW based 0.9 *wt.*% NaCl, DIW based 0.5 *wt.*% NaCl and ATW based 0.5 *wt.*% NaCl solutions for 48 h.

The cases in the two DIW based NaCl solutions are similar. Only one layer of corrosion products is observed for the three alloys. Mg0.5Zn0.2Ca and Mg0.5Zn0.2Ge alloys show uniform and flat corrosion products and respective interfaces towards the substrates, while Mg4Zn0.2Sn alloy reveals a rough interface with strong and deep corrosion cavities. This suggests uniform corrosion of Mg0.5Zn0.2Ca and Mg0.5Zn0.2Ge alloys and localized corrosion for Mg4Zn0.2Sn alloy, agreeing well the electrochemical tests results. However, compared with the cross-section morphologies of as-cast alloys, the morphologies of extruded alloys reveal milder corrosion situations, suggesting an improvement of corrosion performance by the extrusion process. Interestingly, for extruded Mg4Zn0.2Sn alloy, generally, deeper corrosion cavities appear at those dark matrix regions (denoted by yellow arrows in Figure 5.51c) while the brighter matrices (denoted by red arrows in Figure 5.51f) remain as stilts. Small particles (denoted by blue arrows in Figure 5.51f) are embedded in the corrosion product layer or aggregate at the interface between the bulk alloy and the corrosion products. Moreover, obviously different gray level in BSE images (darker inner layer and brighter outer layer) for the product films of extruded Mg0.5Zn0.2Ca and Mg0.5Zn0.2Ge alloys are observed in both DIW based NaCl solutions.

In contrast, in ATW based 0.5 *wt.*% NaCl solution (Figure 5.51g, h and i), apparently, a new layer of corrosion products is formed besides the inner cracked layer. The outer layer composed of flower-like corrosion products completely covers the inner layer for all three alloys.

To validate the chemical compositions of the corrosion products formed in the different corrosive electrolytes, EDS element mappings (Figure 5.52) were performed for the cross sections. Both the electrochemical investigations and SEM studies demonstrated that the corrosion behavior of extruded Mg0.5Zn0.2Ca, Mg0.5Zn0.2Ge and Mg4Zn0.2Sn alloys in DIW based 0.9 *wt.*% NaCl solution was similar to that in DIW based 0.5 *wt.*% NaCl solution. Therefore, only the mapping results of these three alloys after immersion in DIW based 0.5 *wt.*% NaCl solution were provided as representative and to compare with the results in ATW based 0.5 *wt.*% NaCl solution.

It has been widely accepted that the corrosion products formed on Mg alloy surfaces is mainly composed of $MgO/Mg(OH)_2$ [2, 79, 80] in NaCl solution. As expected, in DIW based NaCl solutions, the corrosion product films are rich in Oxygen (O) and Mg for both as-cast and extruded Mg0.5Zn0.2Ca, Mg0.5Zn0.2Ge and Mg4Zn0.2Sn alloys. Interestingly, obvious enrichment of Zn is observed in the outer parts of the corrosion product layers for as-cast Mg0.5Zn0.2Ca, extruded Mg0.5Zn0.2Ca and extruded Mg0.5Zn0.2Ge alloys but not for the other conditions/materials. Moreover, for extruded Mg0.5Zn0.2Ge alloy, Ge also segregates in the same locations. In comparison, the distribution of other elements is quite uniform. This phenomenon explains the brighter contrast of the outer parts of the corrosion product layers of these alloys and indicates the participation of the alloying elements (Zn and Ge) in the formation of the corrosion products. For extruded Mg4Zn0.2Sn alloy, the small particles in the corrosion product layer or at the alloy/corrosion products interface are also rich in Zn, which may be the remaining tiny second phases after corrosion. In addition, enrichment of Zn is noticed at the interface of the bulk material and the corrosion product layer. The incorporation of alloying elements in the corrosion products or the enrichment of alloying elements at the film/Mg alloy interfaces have been reported for several Mg alloys and is related to the improvement of the corrosion resistance of the alloys [81-83].

In ATW based NaCl solution, element distribution in the inner layers of the corrosion product films is similar to the case of DIW based solutions for extruded alloys, rich in O and Mg. In comparison, the outer layers are extremely rich in Ca with some carbon (C) and O. In addition, Zn and Sn can also be found in the outer layers.

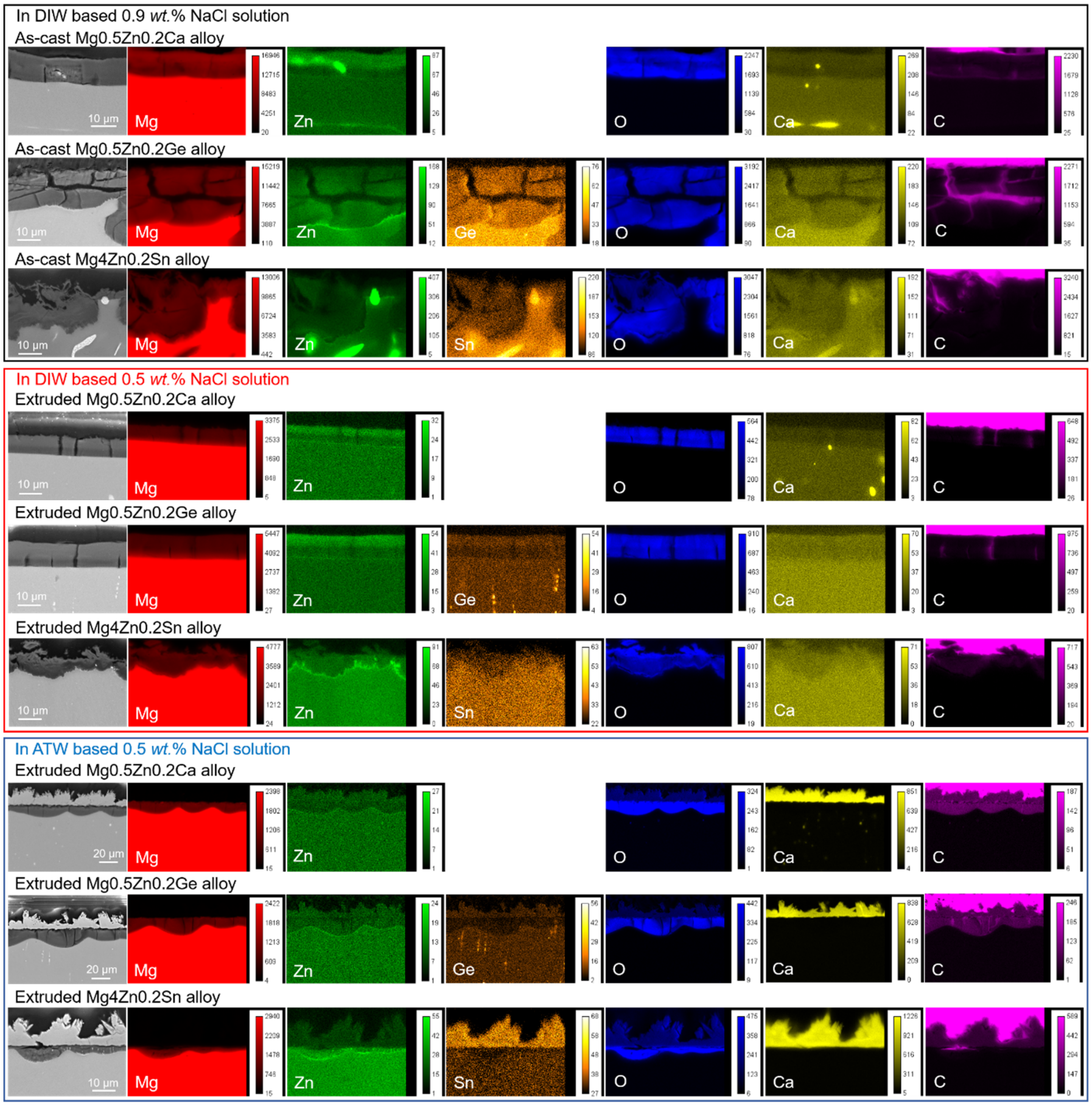

Figure 5.52 SEM images and chemical element mappings of the cross sections of as-cast and extruded Mg0.5Zn0.2Ca, Mg0.5Zn0.2Ge and Mg4Zn0.2Sn alloys after immersion in different corrosive electrolytes for 48 h.

According to the elemental mapping results, it can be speculated that the corrosion product films formed in NaCl solutions prepared with DIW and the inner layers of the films formed in NaCl solution prepared with ATW most likely is composed of MgO/Mg$(OH)_2$, while the outer layer of the corrosion products formed in solution prepared with ATW may be $CaCO_3$ based irrespective of the alloys.

As revealed by SEM and EDS mapping analysis, different corrosion products were formed in DIW and ATW based NaCl solutions for extruded Mg0.5Zn0.2Ca, Mg0.5Zn0.2Ge and Mg4Zn0.2Sn alloys. Therefore, XRD analysis was performed for the corroded surfaces of extruded alloys to determine the detailed compositions of the corrosion products formed in different corrosive electrolytes, with that of as-cast alloys after immersion in DIW based 0.9 *wt.*% NaCl solution as comparison. According to the XRD results shown in Figure 5.53, the corrosion products of alloys immersed in solution prepared with DIW (for both solutions with concentration of 0.9 *wt.*% and 0.5 *wt.*%) mainly consist of $Mg(OH)_2$ irrespective of the conditions of the alloys. Nevertheless, when the extruded alloys were immersed in solution prepared with ATW, the corrosion products become much more complex and calcium carbonate ($CaCO_3$) in crystalline polymorph of aragonite turns out to be the main corrosion products besides $Mg(OH)_2$. Combining SEM and EDS results (Figure 5.50, 5.51 and 5.52) with XRD analysis, we can conclude that the outer layers of flower-like corrosion products are aragonite. No evidence of magnesium carbonate components was found in this study. The small diffraction peak of Mg_2Ge should come from the second phases in Mg0.5Zn0.2Ge alloy. The compositions of the corrosion products determined by XRD, and element mapping results are in good agreement.

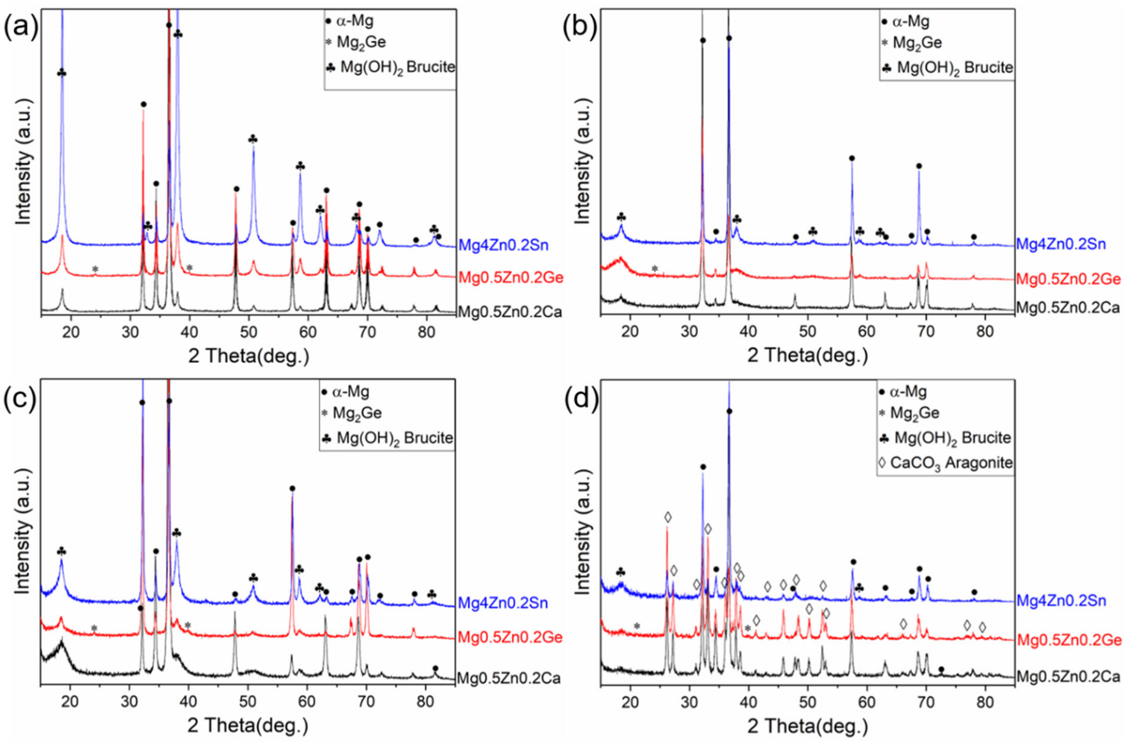

Figure 5.53 XRD patterns for (a) as-cast Mg0.5Zn0.2Ca, Mg0.5Zn0.2Ge and Mg4Zn0.2Sn alloys after immersion in DIW based 0.9 *wt.*% NaCl solution and extruded Mg0.5Zn0.2Ca, Mg0.5Zn0.2Ge and Mg4Zn0.2Sn alloys after immersion in (b) DIW based 0.9 *wt.*% NaCl, (c) DIW based 0.5 *wt.*% NaCl and (d) ATW based 0.5 *wt.*% NaCl solutions for 48 h.

5.4.3 Mechanical properties and integrity

Typical engineering tensile and compressive stress-strain curves of extruded Mg0.5Zn0.2Ca, Mg0.5Zn0.2Ge and Mg4Zn0.2Sn alloys at room temperature are displayed in Figure 5.54. The corresponding mechanical properties are presented in Table 5.15. Notably, Mg0.5Zn0.2Ge alloy exhibits higher tensile yield strength (TYS) and ultimate tensile strength (UTS) but much lower elongation to fracture and much higher mechanical anisotropy (TYS/CYS, CYS: compressive yield strength) (strength differential effect) than Mg0.5Zn0.2Ca and Mg4Zn0.2Sn alloys, especially compared with Mg0.5Zn0.2Ca alloy. Both the different microstructures (grain size, solid solution and precipitates) and textures can contribute to the difference between the mechanical properties of these two studied alloys. However, textures may influence stronger considering the clear difference in textures but much milder difference between the microstructures.

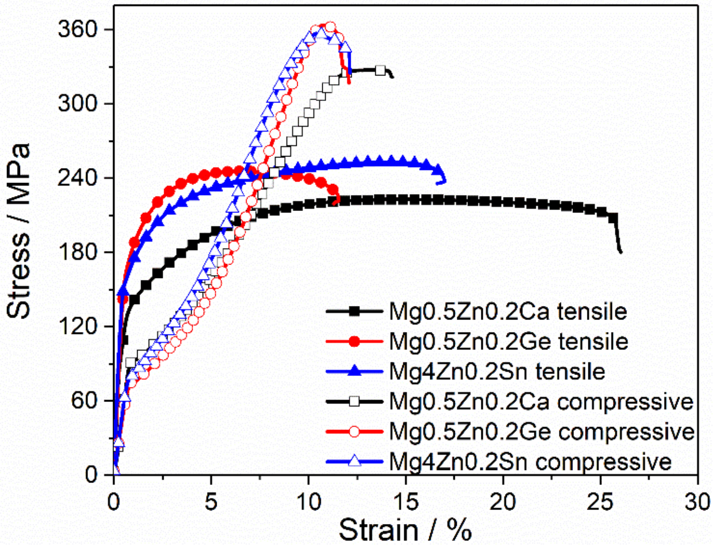

Figure 5.54 Tensile and compressive stress-strain curves of extruded Mg0.5Zn0.2Ca, Mg0.5Zn0.2Ge and Mg4Zn0.2Sn alloys at room temperature.

Table 5.15 Tensile and compressive mechanical properties of extruded Mg0.5Zn0.2Ca, Mg0.5Zn0.2Ge and Mg4Zn0.2Sn alloys at room temperature.

Alloy	**Tensile properties**			**Compressive properties**		**TYS/CYS**
	0.2% TYS MPa	**UTS MPa**	**E %**	**0.2% CYS MPa**	**UCS MPa**	
Mg0.5Zn0.2Ca	119 ± 2	224 ± 1	25 ± 2	93 ± 1	331 ± 3	1.3
Mg0.5Zn0.2Ge	171 ± 2	249 ± 2	10 ± 1	75 ± 1	367 ± 6	2.3
Mg4Zn0.2Sn	157 ± 1	254 ± 1	16 ± 1	81 ± 0	357 ± 2	1.9

Pre-corrosion in neutral salt spray for different durations was performed on samples to investigate the mechanical integrity of extruded Mg0.5Zn0.2Ca, Mg0.5Zn0.2Ge and Mg4Zn0.2Sn alloys. Figure 5.55a, b and c shows the tensile stress-strain curves of the three studied alloys after exposure in salt spray chamber for different time intervals. The variation of TYS, UTS and elongation to failure with exposure time is depicted in Figure 5.55d, e and f and summarized in Table 5.16 as well. For the convenience of comparison, data of the uncorroded sample is also presented. The data for Mg4Zn0.2Sn alloy after pre-corrosion in salt spray for 42 days is missing because the corrosion of the samples was so severe that the bee wax has lost its protective function and thus the corroded screw thread did not allow a tensile test anymore.

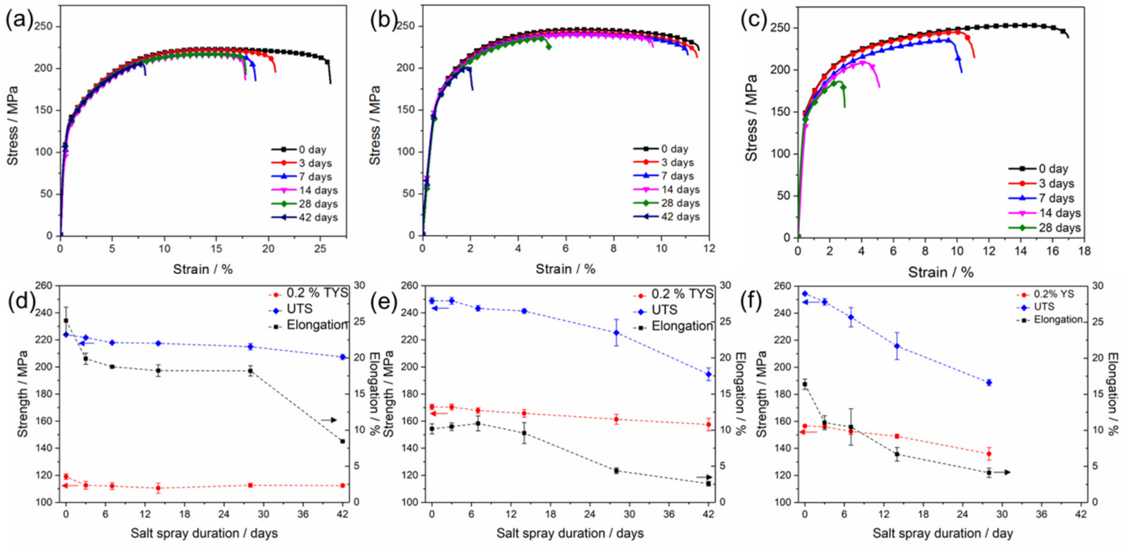

Figure 5.55 Tensile stress-strain curves of (a) Mg0.5Zn0.2Ca, (b) Mg0.5Zn0.2Ge and (c) Mg4Zn0.2Sn alloys tested at room temperature after pre-corrosion in salt spray for different durations and the variation of 0.2 % TYS, UTS and elongation to failure with pre-corrosion durations for (d) Mg0.5Zn0.2Ca, (e) Mg0.5Zn0.2Ge and (f) Mg4Zn0.2Sn alloys.

Generally, the TYS, UTS and elongation to fracture decrease with extended exposure time for all three alloys. The decrease in tensile strength may be related to the actual cross section area reduction due to corrosion while the original cross section area is still used to convert load values to stress values. However, much more reduction is observed for the elongation to fracture, especially after relatively long pre-corrosion time.

Moreover, the variation of tensile properties for the three alloys after salt spray exposure is different. In particular, the elongation to fracture of Mg0.5Zn0.2Ca alloy quickly drops from 25 % to 20 % while the TYS and UTS only slightly change after exposure in salt spray for 3 days. Afterwards, the TYS, UTS and elongation to fracture slightly decrease with prolongation of exposure until 28 days. Further exposure (up to 42 days) causes significant deterioration of elongation to fracture but still no obvious reduction is observed for the TYS and UTS. After pre-corrosion for 42 days, the TYS, UTS and elongation to fracture of Mg0.5Zn0.2Ca alloy decline to be 112 MPa, 207 MPa and 8 %, reduced by 6 %, 8 % and 68 %, respectively.

As for Mg0.5Zn0.2Ge alloy, the TYS, UTS and elongation to fracture almost keeps the same after exposure within 7 days. Nevertheless, with further extension of exposure, the properties gradually decrease, especially for the UTS and elongation to fracture. After 42 days, the TYS, UTS and elongation to fracture of Mg0.5Zn0.2Ge alloy decrease to be 157 MPa, 194 MPa and 3 %, declined by 8 %, 22 % and 70 %, respectively.

Table 5.16 Mechanical integrity of pre-corroded Mg0.5Zn0.2Ca, Mg0.5Zn0.2Ge and Mg4Zn0.2Sn alloys determined by tensile test at room temperature.

Alloy	**Mg0.5Zn0.2Ca**			**Mg0.5Zn0.2Ge**			**Mg4Zn0.2Sn**		
Time day	**0.2% TYS MPa**	**UTS MPa**	**E %**	**0.2% TYS MPa**	**UTS MPa**	**E %**	**0.2% TYS MPa**	**UTS MPa**	**E %**
0	119 ± 2	224 ± 1	25 ± 2	171 ± 2	249 ± 2	10 ± 1	157 ± 0	254 ± 1	16 ± 1
3	113 ± 3	222 ± 0	20 ± 1	170 ± 2	249 ± 3	10 ± 1	156 ± 1	248 ± 2	11 ± 1
7	112 ± 3	218 ± 0	19 ± 0	168 ± 2	243 ± 2	11± 1	153 ± 2	237 ± 7	10 ± 3
14	111 ± 4	217 ± 1	18 ± 1	166 ± 3	241 ± 2	10 ± 1	149 ± 2	216 ± 10	7 ± 1
28	113 ± 1	215 ± 2	18 ± 1	161 ± 4	225 ± 10	4 ± 0	136 ± 5	189 ± 2	4 ± 1
42	112 ± 1	207 ± 2	8 ± 0	157 ± 5	195 ± 5	3 ± 0	-	-	-

In the case of Mg4Zn0.2Sn alloy, the tensile properties already gradually decline with the extension of pre-corrosion time after 3 days. After 28 days, the TYS, UTS and elongation to fracture decrease to be 136 MPa, 189 MPa and 4 %, showing a reduction of 13 %, 26 % and 75 %, respectively. Apparently, the elongation to fracture suffers the greatest reduction.

In general, after exposure to salt spray (42 days for Mg0.5Zn0.2Ca and Mg0.5Zn0.2Ge alloys and only 28 days for Mg4Zn0.2Sn alloy), the decrease of TYS, UTS and elongation to fracture of Mg4Zn0.2Sn alloy is the highest, followed by Mg0.5Zn0.2Ge alloy. Whereas, that of Mg0.5Zn0.2Ca alloy is the least. This owes to a stronger effect of pre-corrosion which will be explained in the following.

In order to correlate the influence of exposure time in salt spray with the mechanical integrity for extruded Mg0.5Zn0.2Ca, Mg0.5Zn0.2Ge and Mg4zn0.2Sn alloys, the macroscopic surface appearance after pre-corrosion in salt spray for different durations was studied by OM, as shown in Figure 5.56. Pre-corrosion for 3 days, 28 days and 42 days for Mg0.5Zn0.2Ca and

Mg0.5Zn0.2Ge alloys and pre-corrosion for 3 days, 14 days and 28 days for Mg4Zn0.2Sn alloy are selected representatively according to the variation of mechanical properties for these three alloys.

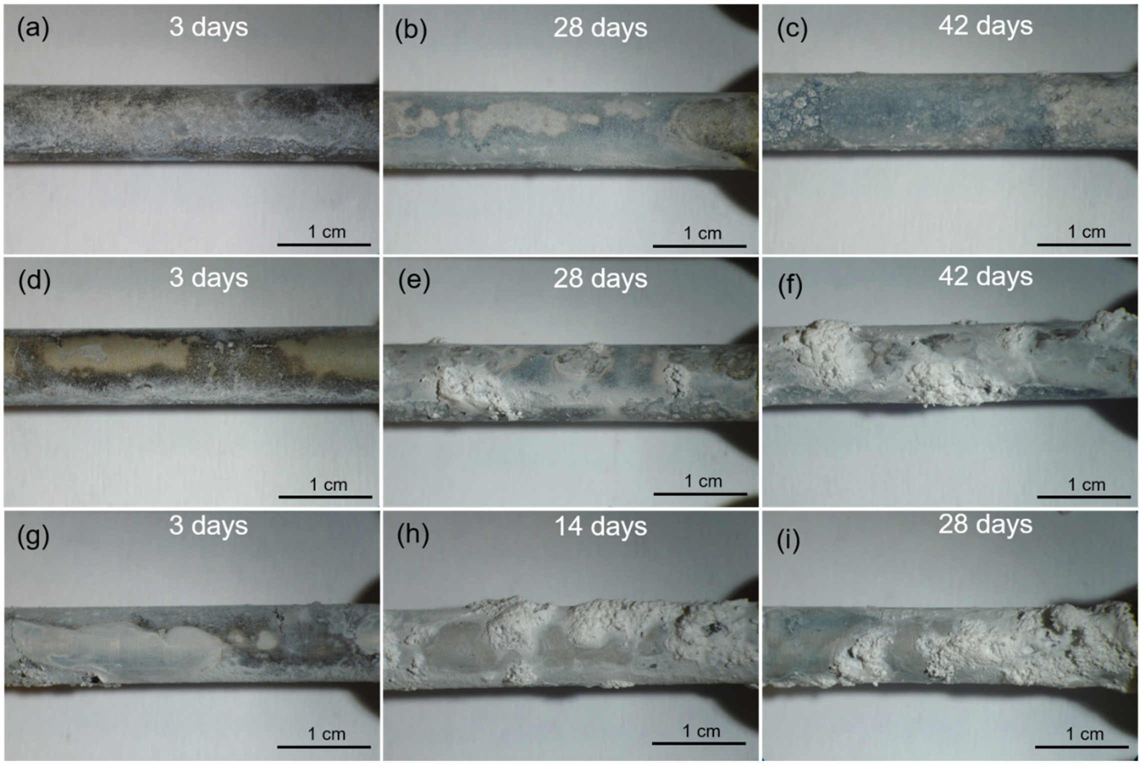

Figure 5.56 Macroscopic surface morphologies of (a, b, c) Mg0.5Zn0.2Ca, (d, e, f) Mg0.5Zn0.2Ge and (g, h, i) Mg4Zn0.2Sn alloys determined by OM after salt spray for different durations respectively.

Mg0.5Zn0.2Ca alloy (Figure 5.56a, b and c) reveals visually relatively uniform corrosion morphologies over the whole testing duration. The surface becomes whiter with exposure time, which may indicate the thickening of the corrosion products. In comparison, a darker surface is observed for Mg0.5Zn0.2Ge alloy after pre-corrosion for 3 days, suggesting a milder corrosion situation. Nevertheless, after 28 days of exposure, local aggregation of corrosion products appears, which implies the occurrence of serious localized corrosion. Moreover, the localized attack becomes more severe for Mg0.5Zn0.2Ge alloy after 42 days of exposure to salt spray. In comparison, notably localized attack already occurs to Mg4Zn0.2Sn alloy after only 3 days, which becomes increasingly intense with further exposure in salt spray, indicated by the formation of more and more white corrosion product aggregates.

The corresponding fracture surfaces after tensile tests were examined by SEM (Figure 5.57, 5.58 and 5.59) as well to get an insight into the development of mechanical properties under the influence of salt fog exposure. The overall and enlarged views of fracture morphologies (the first and third columns in Figure 5.57, 5.58 and 5.59) were taken using BSE mode to facilitate the observations of corrosion products and second phases, respectively.

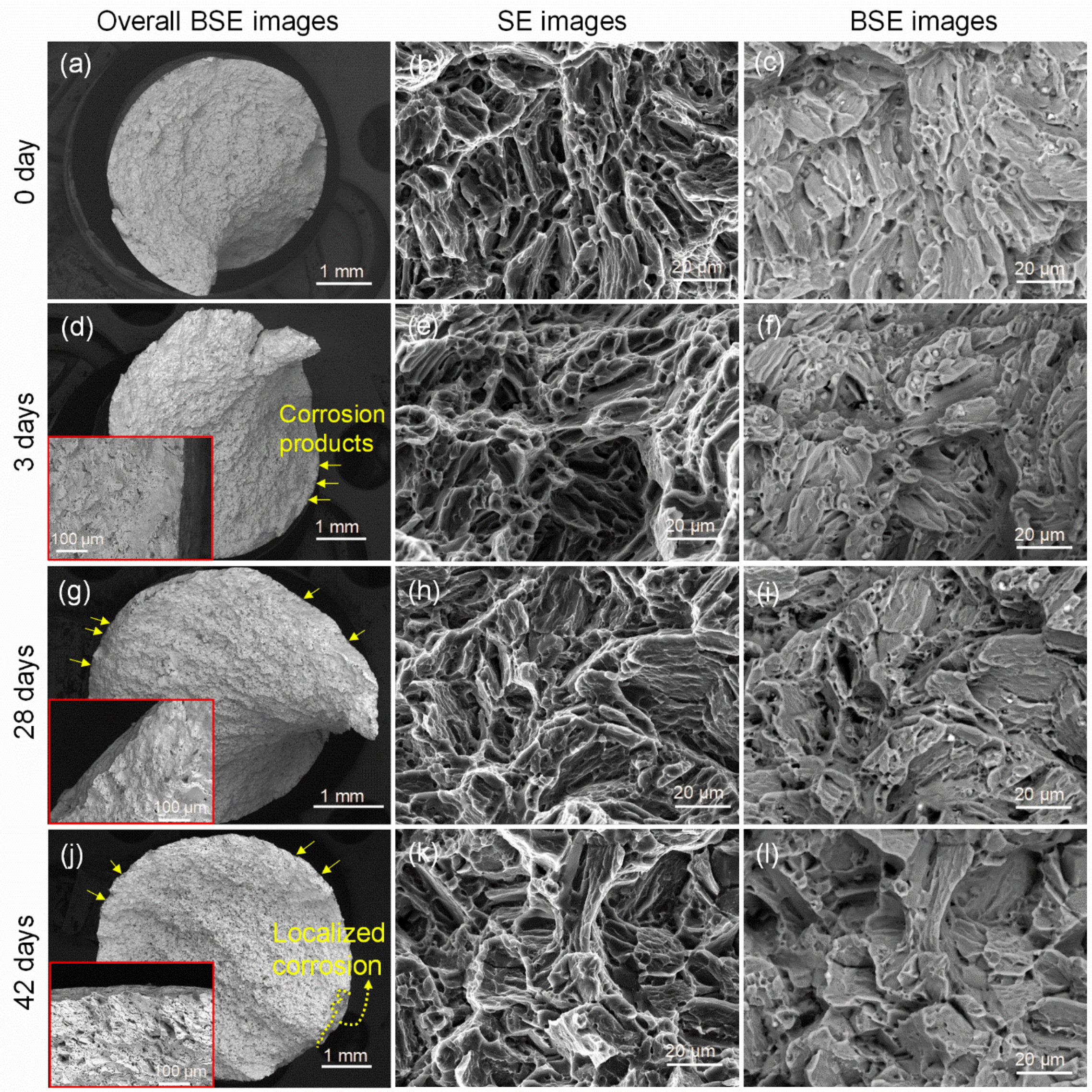

Figure 5.57 SEM observations of fractures for Mg0.5Zn0.2Ca alloy after tensile tests at room temperature (a, b, c) without pre-corrosion and with pre-corrosion for (d, e, f) 3 days, (g, h, i) 28 days and (j, k, l) 42 days.

In the case of Mg0.5Zn0.2Ca alloy, according to the overall view of fracture surfaces (the first column in Figure 5.57), thicker corrosion products exist on the sample surfaces with the extension of pre-corrosion exposure time. However, localized corrosion is observed on the fracture surface after pre-corrosion for 42 days, which was not clearly visually observed in the macroscopic images taken by OM (Figure 5.56c). For the enlarged details of the fracture (the second columns in Figure 5.57), amounts of dimples and some tearing ridges are present on the fracture surface of bare sample (without pre-corrosion), revealing the more ductile fracture feature of Mg0.5Zn0.2Ca alloy. After 3 days, the fracture characteristic is still similar to that of uncorroded sample. Nevertheless, less dimples, more tearing ridges and some cleavage surfaces are visible on the facture surfaces with further extended exposure time, indicating that the fracture type becomes less ductile and more brittle. In the BSE images of fracture surfaces (the third column in Figure 5.57), some bright particles can be noted. EDS analysis (not shown here) suggests that they are Mg_2Ca phases.

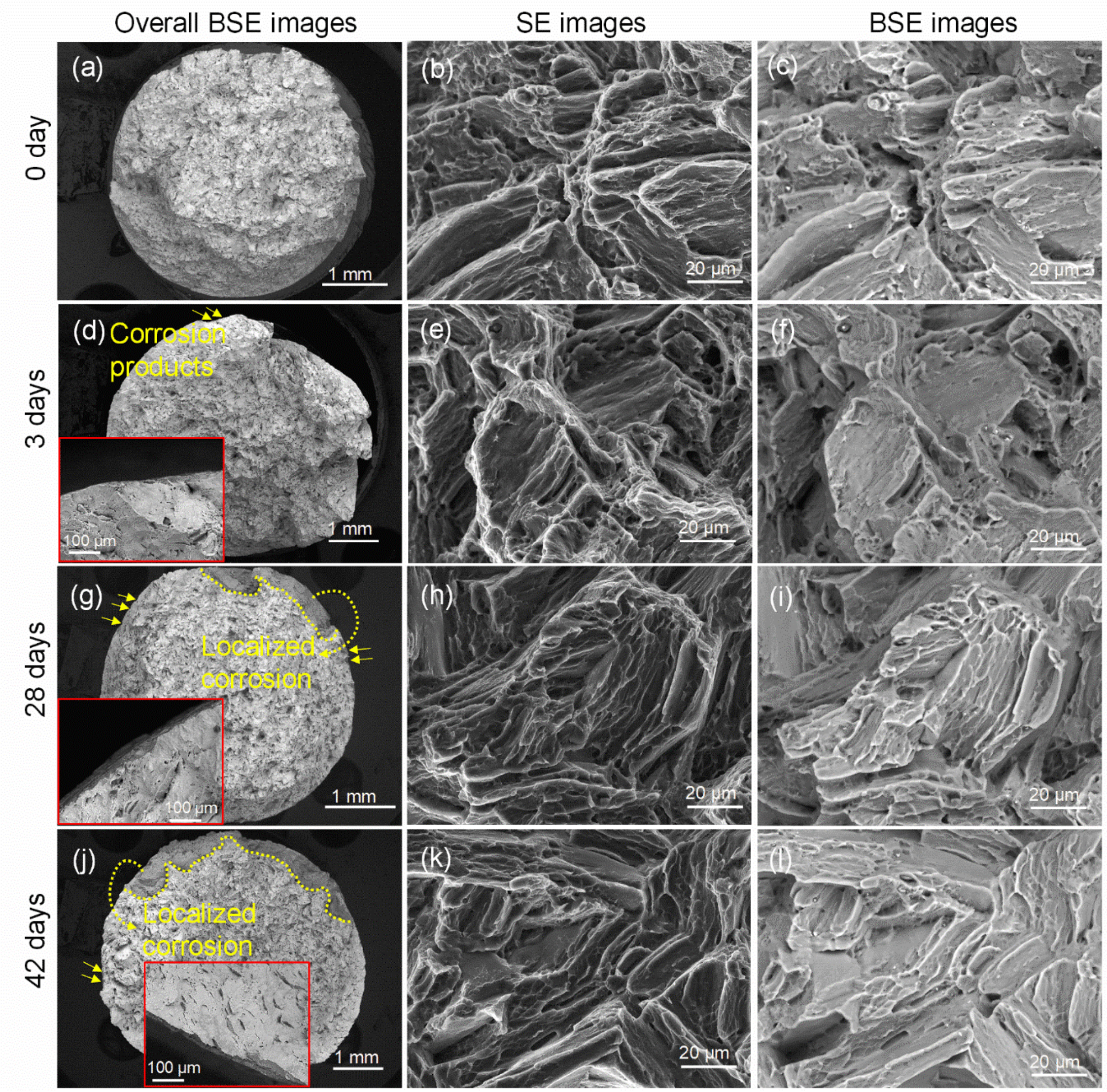

Figure 5.58 SEM observations of fractures for Mg0.5Zn0.2Ge alloy after tensile tests at room temperature (a, b, c) without pre-corrosion and with pre-corrosion for (d, e, f) 3 days, (g, h, i) 28 days and (j, k, l) 42 days.

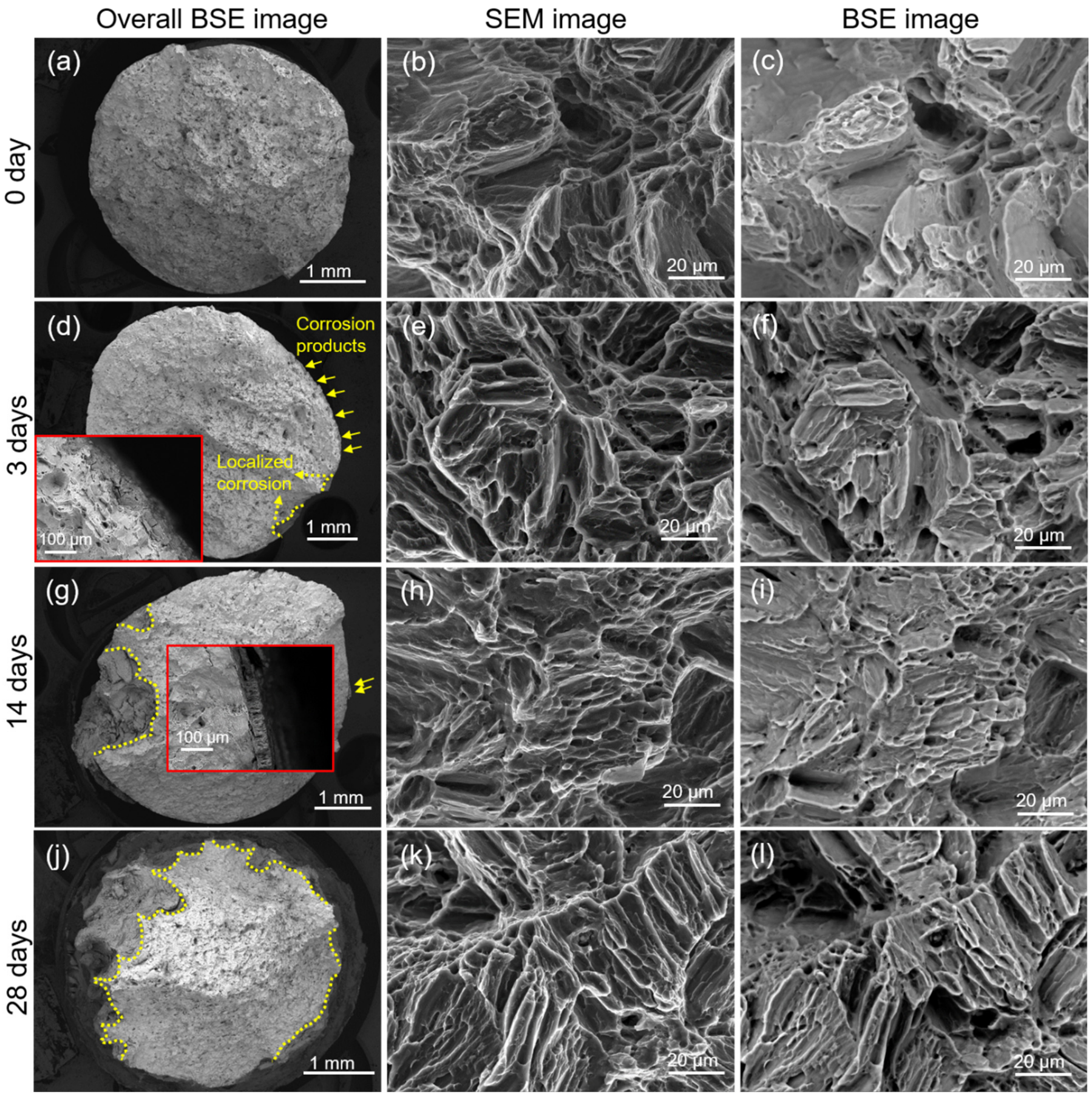

Figure 5.59 SEM observations of fractures of Mg4Zn0.2Sn alloy after tensile tests at room temperature (a, b, c) without exposure to salt spray and with exposure to salt spray for (d, e, f) 3 days, (g, h, i) 14 days and (j, k, l) 28 days.

For Mg0.5Zn0.2Ge alloy (the first column in Figure 5.58), a thin corrosion product layer forms on the sample surface after pre-corrosion for 3 days. However, serious localized corrosion is found on the facture surfaces after pre-corrosion for 28 days, which develops more severe when the salt spray duration is prolonged to 42 days. This is in a good agreement with the macroscopic observations of the surface appearance after salt spray. Different from the quite ductile fracture of the bare Mg0.5Zn0.2Ca alloy, the bare Mg0.5Zn0.2Ge alloy (Figure 5.58b) exhibits already more brittle fracture feature. Only a few dimples can be seen on the fracture surface besides tearing ridges and cleavages. For samples corroded for 3 days (Figure 5.58e), the fracture characteristic is similar to that of bare Mg0.5Zn0.2Ge alloy. When localized corrosion occurred (pre-corrosion for 28 days or 42 days) (Figure 5.58h and 5.58k), dimples can be hardly observed and fractures present typical brittle features. More bright tiny particles are observed on the fracture surfaces (the third column in Figure 5.58), which are Mg_2Ge phases according to EDS analysis.

In accordance with the macroscopic morphologies of Mg4Zn0.2Sn alloy in Figure 5.56, the overall images of the fractures (the first column in Figure 5.59) show that thicker corrosion product layers form on the sample surfaces as the pre-corrosion time prolongs. Meanwhile, localized corrosion cavities increase, expand and/or grow deeper inside the material. For the bare alloy (Figure 5.59b), the fracture surface also discloses a mixed characteristic, dominated by tearing ridges with some dimples and cleavages. Similar fracture feature is also observed for the fracture surfaces of pre-corroded Mg4Zn0.2Sn alloy (Figure 5.59e, h and k) despite the corrosion attack by salt fog. However, more tearing ridges and less dimples are noticed, especially after pre-corrosion for 28 days, indicating that the fracture becomes less ductile but more brittle. This is the effect of corrosion and the formation of localized corrosion pits. In accordance with the microstructure revealed in Figure 5.24, a few bright particles are observed in the fracture surfaces when imaged by BSE mode (the third column in Figure 5.59).

5.4.4 Fatigue and corrosion fatigue behavior

Figure 5.60 exhibits the stress-life cycle (S-N) curves of Mg0.5Zn0.2Ca, Mg0.5Zn0.2Ge and Mg4Zn0.2Sn alloys tested in air and 0.5 *wt.*% NaCl solutions prepared with either DIW or ATW. Apparently, the S-N curves of the three alloys in air deviate from the near-linear trend between loading and cycles to failure and a clear horizontal part is present in the range of 10^5 - 10^7 cycles, exhibiting a ‘knee’. At the stress level of the fatigue limit in air, the fatigue lives in NaCl solutions are remarkably reduced for all alloys. However, the fatigue lives in solution prepared with ATW are longer than those in solution prepared with DIW when tested at the same stress amplitude for Mg0.5Zn0.2Ca and Mg0.5Zn0.2Ge alloys. For Mg4Zn0.2Sn alloy, the S-N curve in DIW based solution is highly scattered, while it is not the case in ATW based solution. This may be related to the different corrosion performance of the alloy in these two solutions as revealed above. With decreasing stress level, the fatigue lives of Mg0.5Zn0.2Ca and Mg0.5Zn0.2Ge alloys in NaCl solutions extended and reached the fatigue limit (10^7 cycles) eventually. In contrast, even under a much lower stress amplitude compared to the fatigue limit in air (as low as 120 MPa), no fatigue limits are detected for Mg4Zn0.2Sn alloy in the corrosive solutions.

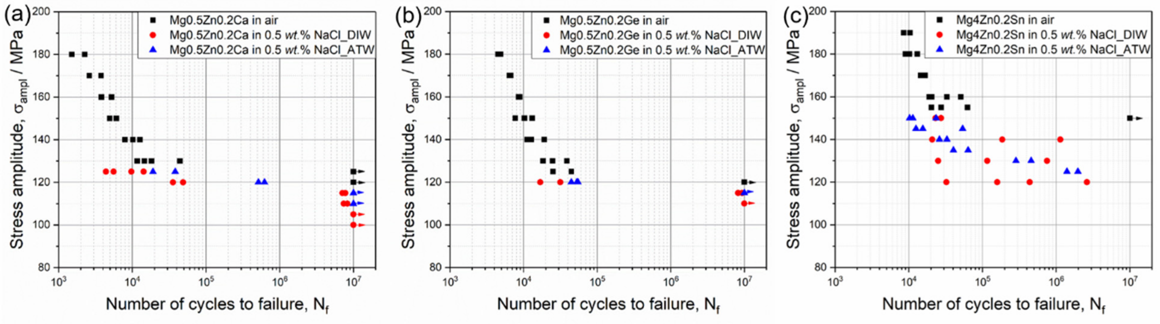

Figure 5.60 Stress-life cycle (S-N) curves of (a) Mg0.5Zn0.2Ca (b) Mg0.5Zn0.2Ge and (c) Mg4Zn0.2Sn alloys measured in air and 0.5 *wt.*% NaCl solution prepared with either DIW or ATW.

Table 5.17 Comparison of the fatigue limit (FL) of extruded Mg0.5Zn0.2Ca, Mg0.5Zn0.2Ge and Mg4Zn0.2Sn alloys under different conditions.

Condition	**Mg0.5Zn0.2Ca**		**Mg0.5Zn0.2Ge**		**Mg4Zn0.2Sn**	
	FL / MPa	**Reduction of fatigue limit**	**FL / MPa**	**Reduction of fatigue limit**	**FL / MPa**	**Reduction of fatigue limit**
air	125	-	120	-	150	-
0.5 *wt.*% NaCl_DIW	105	16 %	110	8.3 %	-	-
0.5 *wt.*% NaCl_ATW	115	8 %	115	4.2 %	-	-

The fatigue limits under different conditions are compared in Table 5.17. No distinct difference is observed between Mg0.5Zn0.2Ca and Mg0.5Zn0.2Ge alloys or between the limits of these two alloys tested in air and in NaCl solution prepared with ATW. A much higher fatigue limit of 150 MPa was detected for Mg4Zn0.2Sn alloy. The fatigue limits in air and in ATW based 0.5 *wt.*% NaCl solution are 125 MPa and 115 MPa for Mg0.5Zn0.2Ca alloy and 120 MPa and 115 MPa for Mg0.5Zn0.2Ge alloy, respectively. Nevertheless, the fatigue limits decrease to 105 MPa for Mg0.5Zn0.2Ca alloy and 110 MPa for Mg0.5Zn0.2Ge alloy in DIW based 0.5 *wt.*% NaCl solution. Obviously, compared to the fatigue limit in air, the fatigue limit of Mg0.5Zn0.2Ge alloy decreases less than those of Mg0.5Zn0.2Ca and Mg4Zn0.2Sn alloys in corrosive electrolyte. In addition, the reduction of the fatigue limit is higher in the DIW based NaCl solution than in the ATW based solution for Mg0.5Zn0.2Ca and Mg0.5Zn0.2Ge alloys. This difference may arise from the different corrosion performance of the alloys under these two corrosive conditions.

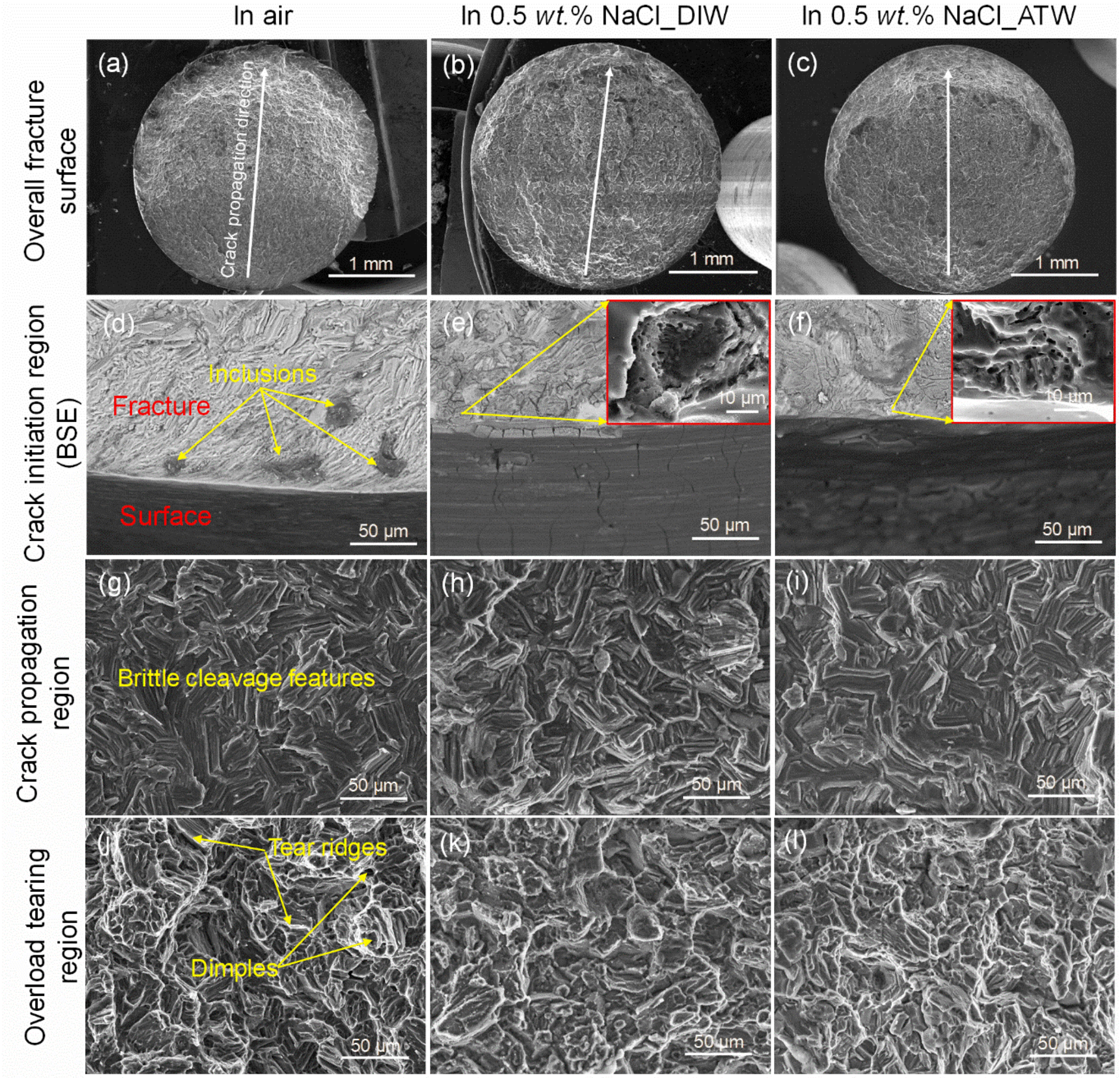

Figure 5.61 Fatigue fractography of Mg0.5Zn0.2Ca alloy after fatigue tests under stress amplitude of (a, d, g, j) 130 MPa (failure at 44441.5 cycles) in air, (b, e, h, k) 110 MPa (failure at 7379802 cycles) in 0.5 *wt.*% NaCl solution prepared with DIW and (c, f, i, l) 120 MPa (failure at 513478.5 cycles) in 0.5 *wt.*% NaCl solution prepared with ATW.

The typical fatigue fracture morphologies of Mg0.5Zn0.2Ca alloy failed in air and in DIW and ATW based 0.5 *wt.*% NaCl solutions (at stress level below the fatigue limit in air) are shown in Figure 5.61. The fracture surfaces of Mg0.5Zn0.2Ca alloy failed in NaCl solutions at stress amplitude of the fatigue limit in air will be described in the following paragraph. The first row in Figure 5.61 displays the overall fracture surfaces of specimens failed under different testing conditions. Three distinct regions, i.e. fatigue crack initiation, steady crack propagation and overload tearing regions, can be clearly observed on the fracture surfaces in all cases. The crack propagation direction is indicated by the white arrows in Figure 5.61a, b, and c. Enlarged details of these three regions are correspondingly displayed in the remaining rows. For a better identification of the crack initiation sites in NaCl solutions, the fracture surfaces after removal of the corrosion products were also examined. They are indicated by the inserted images in Figure 5.61e and f. According to the crack initiation regions shown in Figure 5.61d, e and f, the fatigue cracks initiated from inclusions in air, but from corroded sites in NaCl solution prepared with DIW or ATW (at stress level below the fatigue limit in air). Those inclusions in the microstructures are rich in C, O and Mg with a small amount of Cl, Si, sulphur (S) and potassium (K) (the typical EDS analysis is shown in Figure 5.62), which may result from the casting process or the raw materials used for alloying. The crack propagation regions (Figure 5.61g, h and i) reveal brittle cleavage features with fine steps for all these three conditions. However, in the overload region of Mg0.5Zn0.2Ca alloy tested in air (Figure 5.61j), the presence of tear ridges and dimples indicates quasi-cleavage features. In the cases of NaCl solutions prepared with DIW (Figure 5.61k) and ATW (Figure 5.61l), the fracture surfaces seem to be similar to that in air but less defined because of the existence of corrosion products.

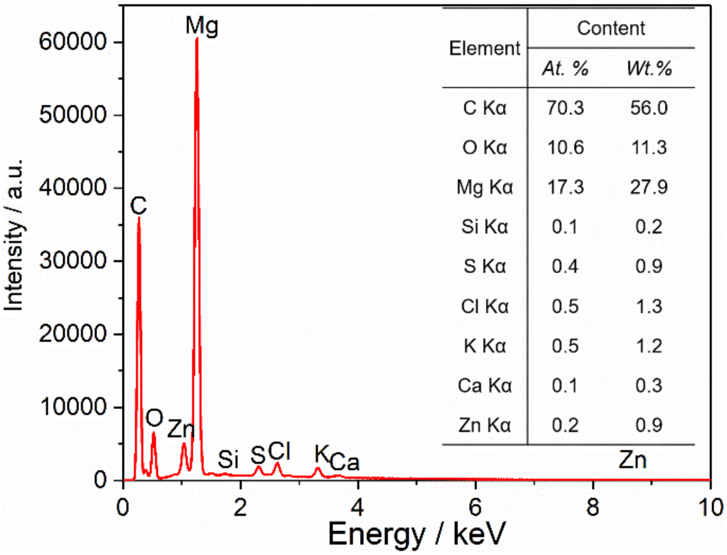

Element	Content	
	At. %	*Wt.%*
C Kα	70.3	56.0
O Kα	10.6	11.3
Mg Kα	17.3	27.9
Si Kα	0.1	0.2
S Kα	0.4	0.9
Cl Kα	0.5	1.3
K Kα	0.5	1.2
Ca Kα	0.1	0.3
Zn Kα	0.2	0.9

Figure 5.62 Typical EDS analysis result of the inclusions in the fractured surface of Mg0.5Zn0.2Ca, Mg0.5Zn0.2Ge and Mg4Zn0.2Sn alloys after fatigue tests in air.

The general case of Mg0.5Zn0.2Ge alloy is similar to that of Mg0.5Zn0.2Ca alloy. However, the overall fracture surfaces of Mg0.5Zn0.2Ge alloy (Figure 5.63a, b and c) turn out to be much rougher than those of Mg0.5Zn0.2Ca alloy. Similarly, fatigue crack initiated from inclusions in air (Figure 5.63d). However, when the stress level was below the fatigue limit in air, corroded sites trigger the fatigue crack in NaCl solution prepared with DIW (Figure 5.63e). Interestingly, when the specimens failed at stress level of the fatigue limit in air, the crack also initiated from inclusions in solution prepared with ATW (Figure 5.63f). In fact, when tested at the stress amplitude of the fatigue limit in air, a similar phenomenon is also observed for Mg0.5Zn0.2Ca alloy failed in NaCl solutions (either prepared by DIW or by ATW) and for

Mg0.5Zn0.2Ge alloy failed in DIW based NaCl solution. The crack propagation regions (Figure 5.63g, h and i) are characterized by brittle cleavage facets while the overload regions reveal quasi-cleavage fracture modes. Meanwhile, more tearing ridges and much less dimples are found on the overload regions of Mg0.5Zn0.2Ge alloy under all testing conditions compared to those of Mg0.5Zn0.2Ca alloys, suggesting that the alloy is less ductile, which is in accordance with the tensile test results.

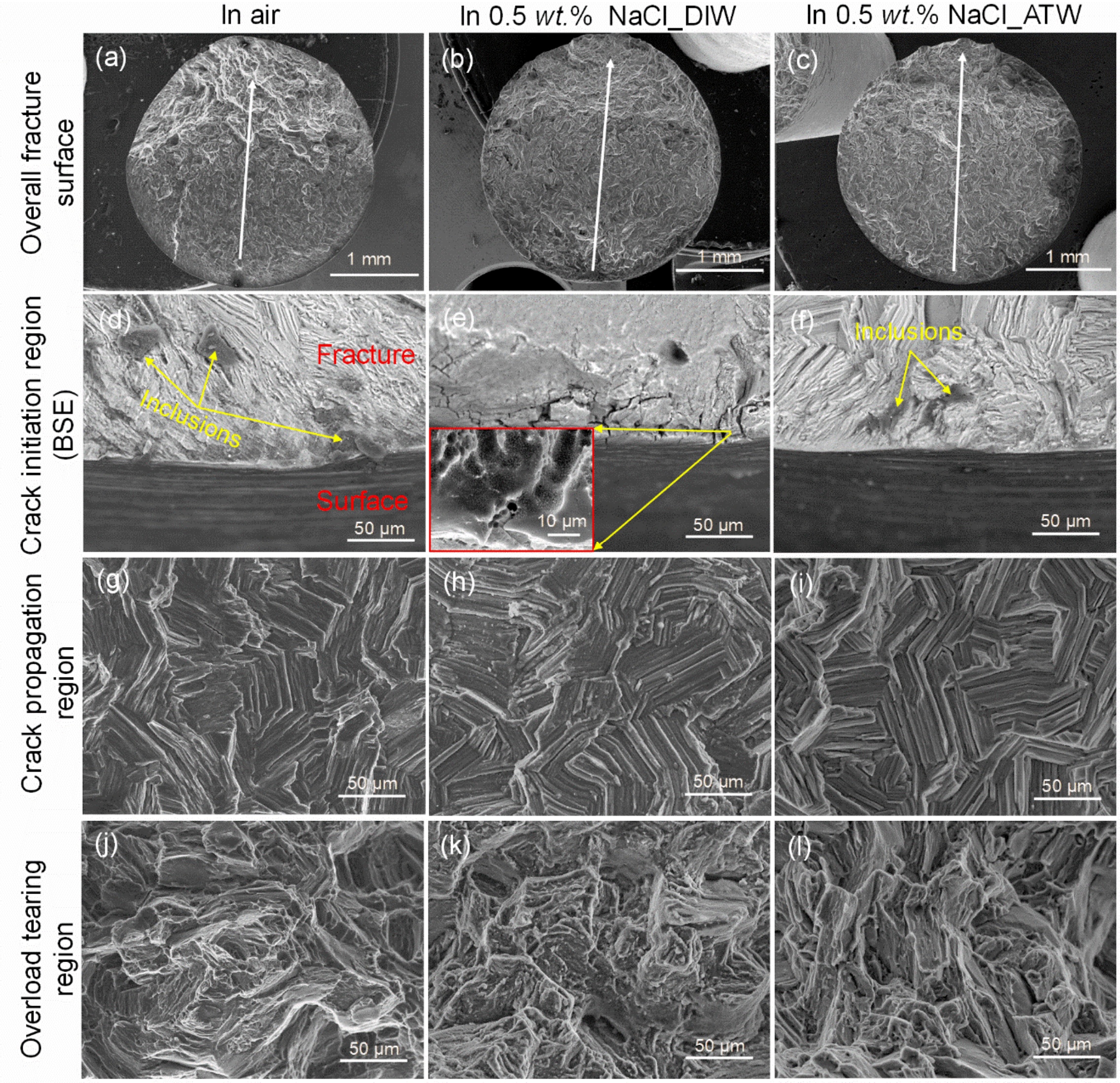

Figure 5.63 Fatigue fractography of Mg0.5Zn0.2Ge alloy after fatigue tests under stress amplitude of (a, d, g, j) 130 MPa (failure at 18404 cycles) in air, (b, e, h, k) 115 MPa (failure at 8237379 cycles) in 0.5 *wt.*% NaCl solution prepared with DIW and (c, f, i, l) 120 MPa (failure at 52962 cycles) in 0.5 *wt.*% NaCl solution prepared with ATW.

For Mg4Zn0.2Sn alloy, inclusions also triggered the fatigue crack in air and in both NaCl solutions when tested at the stress amplitude of the fatigue limit in air (results not shown here).

The inserted pictures in Figure 5.64e and f reveal the fracture when tested in NaCl solutions at stress level below the fatigue limit in air after removal of corrosion products. Obvious corrosion pits turn out to be the initiators of the cracks, especially in DIW based NaCl solution when the specimen failed after a relatively long life cycle (about 24 h). The crack propagation regions (Figure 5.64g, h and i) show similar characteristics under different testing conditions, featured by brittle cleavages composed of fine steps. For the overload tearing regions, the fracture surfaces formed in air and in DIW based 0.5 *wt.*% NaCl solution are similar to the fracture surfaces after tensile tests, showing many tearing ridges with a few dimples. In the case of ATW based 0.5 *wt.*% NaCl solution, the corrosion products result in a less-defined surface morphology due to a delayed disassembly of the sample after fatigue failure.

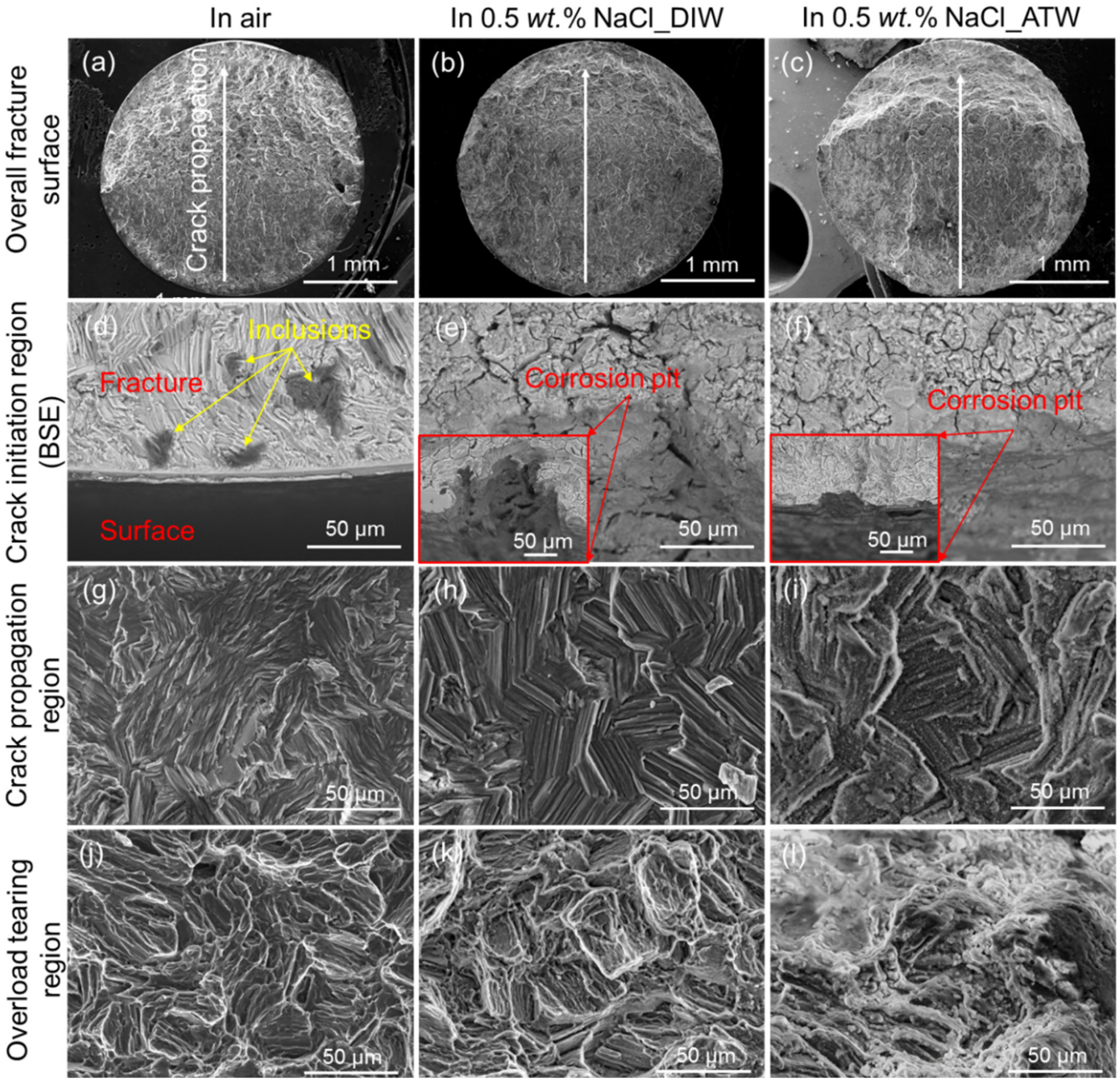

Figure 5.64 Fatigue fractography of Mg4Zn0.2Sn alloy after fatigue tests under stress amplitude of (a, d, g, j) 155 MPa (27476.5 cycles) in air, (b, e, h, k) 120 MPa (2620869 cycles) in DIW based 0.5 *wt.*% NaCl solution and (c, f, i, l) 125 MPa (1976289 cycles) in ATW based 0.5 *wt.*% NaCl solution.

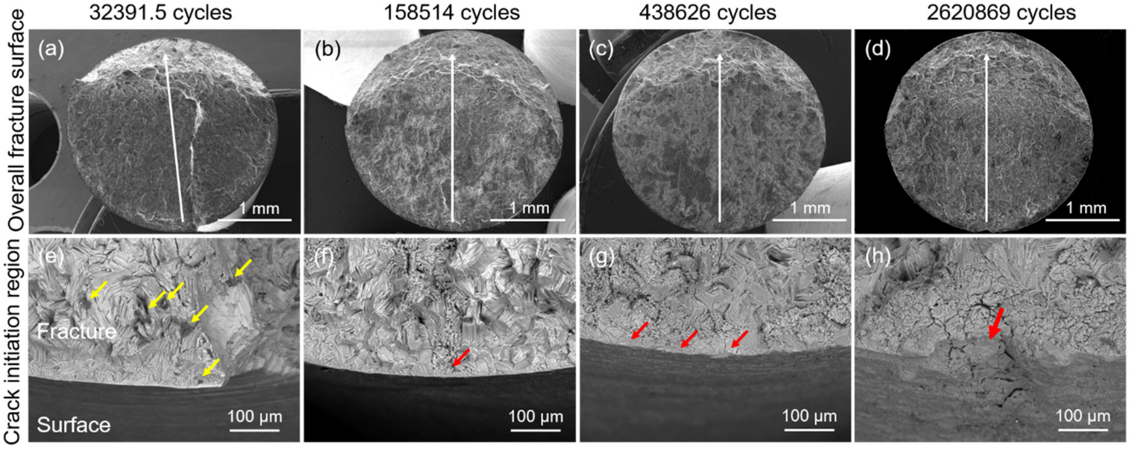

Figure 5.65 Fracture surfaces of extruded Mg4Zn0.2Sn alloy after corrosion fatigue tests in DIW based 0.5 *wt.*% NaCl solution under stress amplitude of 120 MPa (failed after different cycles).

To understand the substantially scattered behavior of the S-N curve of Mg4Zn0.2Sn alloy in DIW based 0.5 *wt.*% NaCl solution, the fracture surfaces formed after different fatigue life cycles at 120 MPa were examined by SEM, as shown in Figure 5.65. It is revealed that inclusions (indicated by yellow arrows) seem to trigger the cracks, resulting in a fast fatigue failure of the sample due to the relatively high amount of those inclusions. While in the other cases, corrosion pits (indicated by red arrows) are the sources of fatigue cracks. More, larger or deeper pits are formed when the sample failed after higher life cycles.

5.4.5 Sensitivity to stress corrosion cracking

The sensitivity to stress corrosion cracking (SCC) of extruded Mg0.5Zn0.2Ca, Mg0.5Zn0.2Ge and Mg4Zn0.2Sn alloys was evaluated by constant load tests at about 70 % of the yield strength of the alloys for 30 days in four different corrosive electrolytes. Table 5.18 lists the status of the alloys after the tests. As revealed, all alloys survived the full testing period in the tested solutions except in the case of Mg0.5Zn0.2Ge alloy in DIW (the specimen broke after 669 ± 33 h).

Table 5.18 Status of Mg0.5Zn0.2Ca, Mg0.5Zn0.2Ge and Mg4Zn0.2Sn alloys after constant load tests in different corrosive electrolytes for 30 days.

Alloy	**DIW**	**ATW**	**0.5 *wt.*% NaCl_DIW**	**0.5 *wt.*% NaCl_ATW**
Mg0.5Zn0.2Ca	Survived	Survived	Survived	Survived
Mg0.5Zn0.2Ge	Failed after 669 ± 33 h	Survived	Survived	Survived
Mg4Zn0.2Sn	Survived	Survived	Survived	Survived

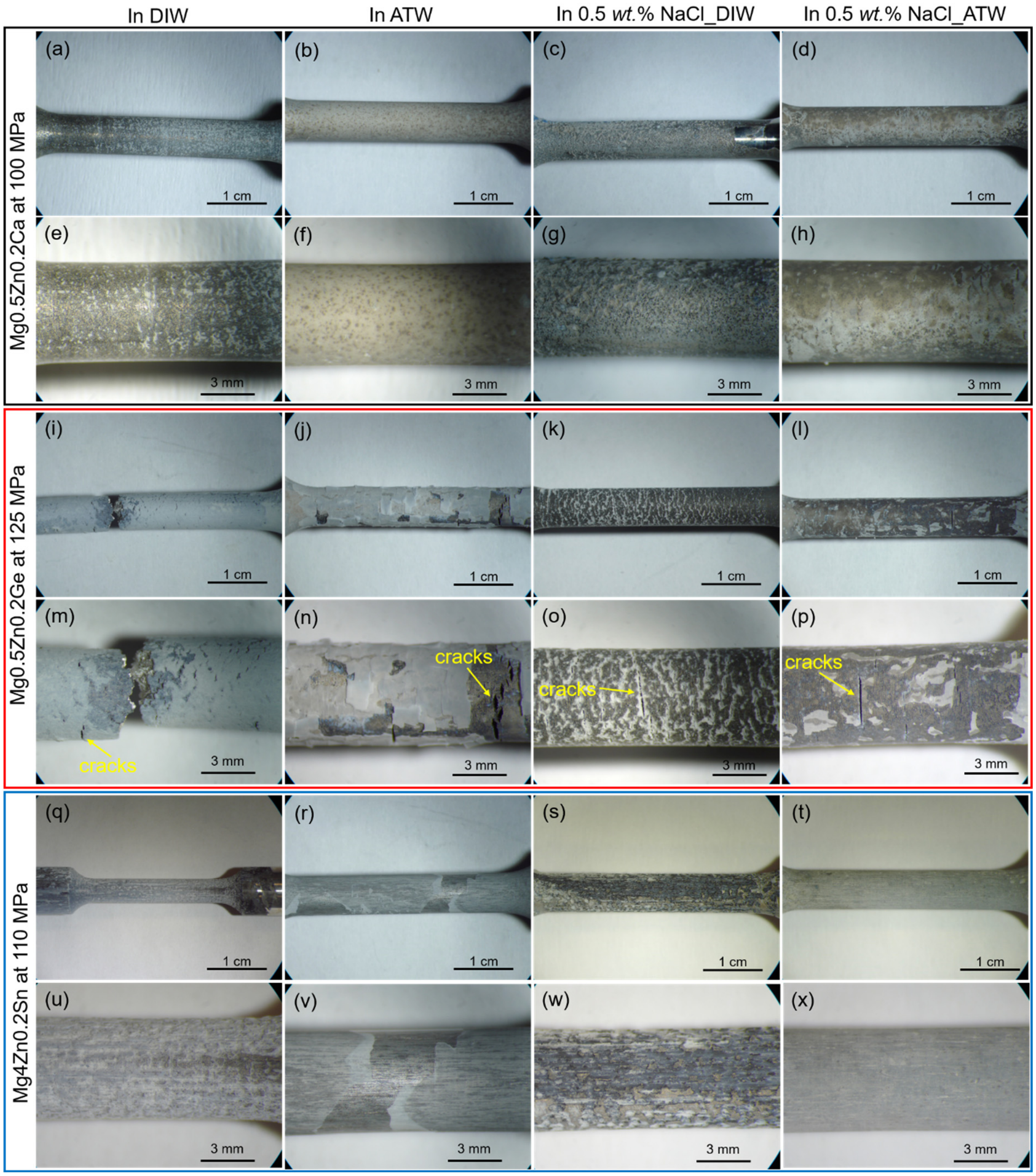

Figure 5.66 Macroscopic surface morphologies of (a, b, c) Mg0.5Zn0.2Ca, (d, e, f) Mg0.5Zn0.2Ge and (g, h, i) Mg4Zn0.2Sn alloys determined by OM after constant load tests.

Although the three studied alloys survived in most tested conditions, the surface appearance was also recorded by optical microscope to investigate the corrosion situations and formation of cracks, shown in Figure 5.66. Firstly, the corrosion is visually most severe in DIW based 0.5 *wt.*% NaCl solution for all three alloys, indicated by the rough surface appearance due to the harsh environment. In ATW and ATW based NaCl solution, an additional layer of white corrosion products is formed on the surfaces, which peeled off to some extent, especially for extruded Mg0.5Zn0.2Ge alloy. This is in accordance with the study of the formation of corrosion products formed in different electrolytes (see chapter 5.4.2). No cracks are observed for extruded Mg0.5Zn0.2Ca and Mg4Zn0.2Sn alloys irrespective of the testing solutions. In contrast, obvious and fine cracks are noticed on the surfaces of Mg0.5Zn0.2Ge alloys in all four testing solutions and on the specimen which broke in DIW in additional locations. Therefore, it reveals that extruded Mg0.5Zn0.2Ca and Mg4Zn0.2Sn alloys show no tendency for SCC in DIW, ATW, DIW and ATW based 0.5 *wt.*% NaCl solutions. In comparison, despite the survival of the samples in ATW and NaCl solutions prepared with both DIW and ATW, extruded Mg0.5Zn0.2Ge alloy is susceptible to SCC in these four electrolytes, especially in DIW.

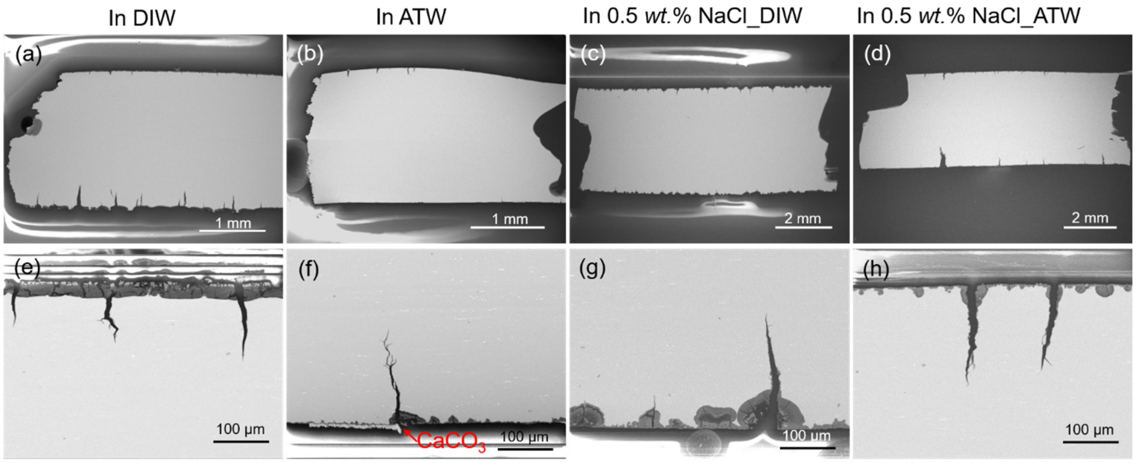

Figure 5.67 Cross-section morphologies of Mg0.5Zn0.2Ge alloys after constant load tests in different corrosive electrolytes.

It has been reported that Mg alloys are susceptible to stress corrosion cracking in corrosive electrolytes, even in distilled/deionized water [9, 84]. For the studied Mg0.5Zn0.2Ge alloy, susceptibility to SCC was revealed in all tested electrolytes. Cracks were formed in all testing solutions but the specimen only failed in DIW, indicating the highest sensitivity of the alloy to SCC in DIW despite the much higher concentration of Cl^- in NaCl solutions. Thus, cross sections of specimens after constant load tests were examined by SEM to reveal the possible reasons. As revealed in Figure 5.67, much more cracks are formed on the specimen surface in DIW compared to the other three solutions. Above all, sharp cracks directly develops from the relatively flat corrosion product layer or corroded interface in DIW (Figure 5.67e), while the cracks starts from the corrosion cavities (especially in DIW based NaCl solution) formed in solutions containing aggressive ions (Figure 5.67f, g and h). This may explain the lowest resistance to SCC of extruded Mg0.5Zn0.2Ge alloy in DIW.

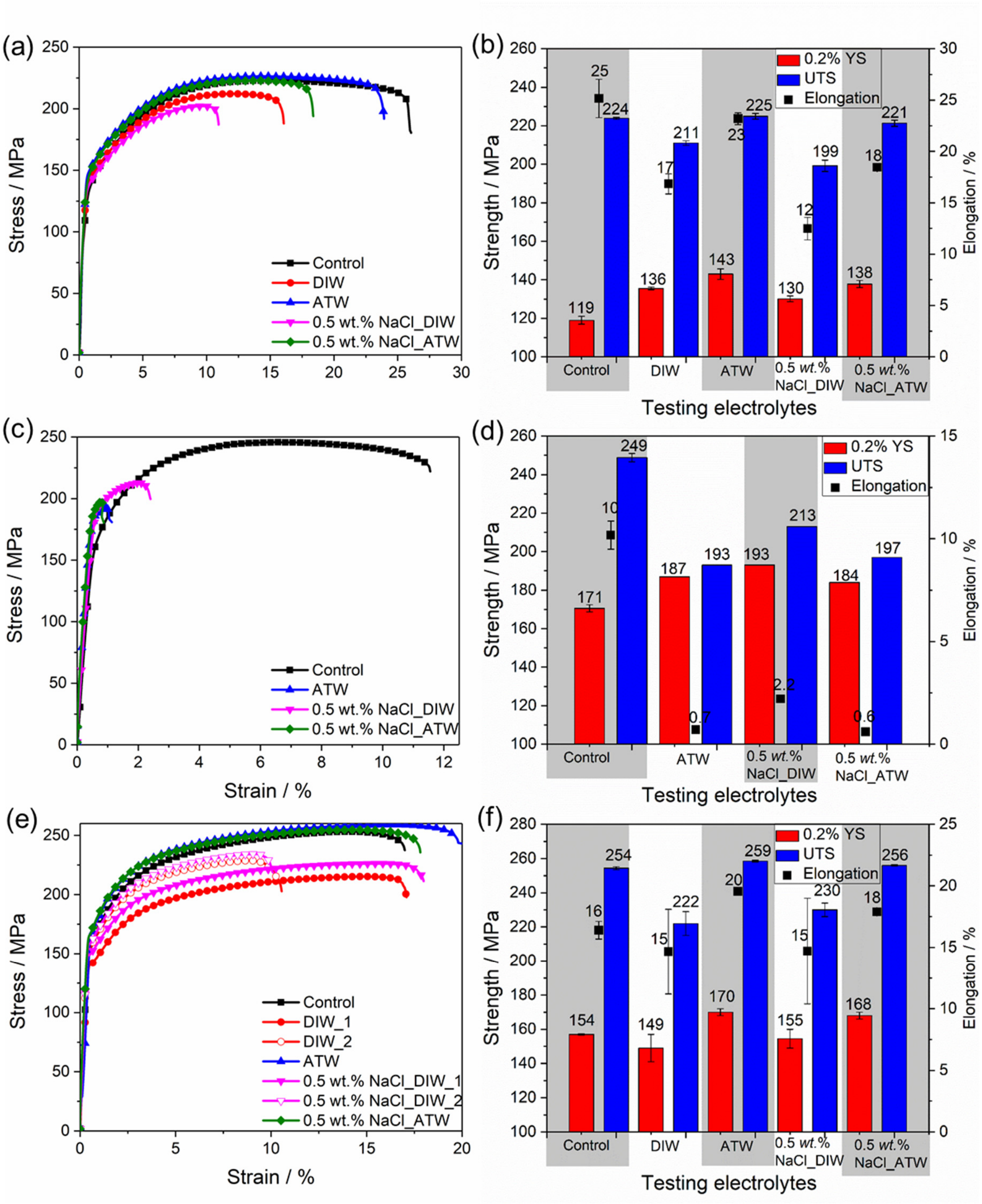

Figure 5.68 Engineering tensile stress-strain curves and tensile properties for (a, d) Mg0.5Zn0.2Ca, (b, e) Mg0.5Zn0.2Ge and (c, f) Mg4Zn0.2Sn alloys after constant load tests in different corrosive electrolytes compared with the bare alloys.

Tensile tests were also carried out for the specimens surviving the constant load tests and compared with those of the bare alloys (without corrosion and load), shown in Figure 5.68. Interestingly, for extruded Mg0.5Zn0.2Ca alloy, the YS slightly increases after the constant load tests, especially in ATW based solutions. UTS almost keeps the same in ATW based solutions but decreases in DIW based solution. In contrast, the elongation to fracture decreases in all case. Nevertheless, less reduction was noticed for the specimens tested in ATW based solutions. Extruded Mg4Zn0.2Sn alloy also shows no sign of stress corrosion cracking in the tested solutions. The tensile properties of samples after constant load tests in ATW solutions exhibit similar characteristics to those of Mg0.5Zn0.2Ca alloy: YS inclines while UTS almost keeps the same as the bare alloy. However, the elongation to fracture also almost keeps the same or even increases a bit. In comparison, YS, UTS and elongation to fracture of Mg4Zn0.2Sn alloy generally decrease after constant load test in DIW based solutions. Moreover, a bigger variation can be observed between the replicates tested in DIW based solutions as indicated by the curves in Figure 5.68e, which is similar to the scattered characteristic of the S-N curve of Mg4Zn0.2Sn alloy in DIW based solution. The difference between the results tested in DIW and ATW based solutions may come from the different corrosion behavior of the alloys in these solutions. Despite the decreased actual cross section area after constant load tests, the increase in YS is really interesting, which may be attributed to the diffusion of H_2 into the material (up-take of H), the compressive stress induced by the mismatch between the lattice constants of the surface layer and the substrate and the tensile twins developed during the tests. For extruded Mg0.5Zn0.2Ge alloy, only one specimen was tested because another one was used for the cross-section investigation. YS slightly increased while UTS and elongation to fracture deteriorated after the constant load tests, especially for the elongation to fracture, due to the formation of cracks. As revealed in Figure 5.66, some bigger cracks were formed in ATW based solutions compared to in DIW based solution. Thus, the tensile properties of the samples tested in ATW based solutions were worse.

6. Discussion

6.1 Influence of ternary alloying elements

During the casting process of Mg-Zn system, the solidification sequence starts with nucleation of primary magnesium (α-Mg) and then is followed by the formation of α-Mg + Mg_7Zn_3 eutectic phases at 341 °C. When the solidification temperature decreases due to fast cooling, Mg_7Zn_3 may conduct eutectic reaction at 325 °C, decomposing into MgZn phase and α-Mg [61, 85]. As a result, a microstructure composed of α-Mg dendrites and eutectic phases located in the interdendritic region is formed. Although the formation of eutectic phase is expected when the Zn content reaches 6.4 *wt.*% according to the Mg-Zn binary phase diagram [85], it already appears in the as-cat Mg4Zn alloy due to the non-equilibrium casting conditions. This is also the reason for the formation of Mg_xZn_y second phases in as-cast Mg0.5Zn alloy even when the added amount (0.5 *wt.*% Zn) is below the solid solubility of Zn in Mg at room temperature (1.6 *wt.*%). With increased Zn content (from 0.5 *wt.*% to 4 *wt.*%), more second phases are formed between the α-Mg dendrite arms.

The effects of Zn on the corrosion resistance of as-cast Mg-Zn alloys have been investigated previously. However, controversial results were presented. Cai et al. [61] and Koç et al. [21] revealed that increased Zn content enhanced the corrosion resistance of the alloys when Zn addition was below 5 *wt.*%. They attributed this to the improved passivity of the alloys with higher Zn content (in simulated body fluid). In contrast, Kubásek et al. [86] demonstrated that the increased Zn content was detrimental to the corrosion resistance of Mg-Zn alloys when the amount was increased from 1 *wt.*% to 6 *wt.*%. This was because of the accelerating effect of micro-galvanic couples between the nobler Mg-Zn binary phases and the α-Mg matrix, which was enhanced when the Zn addition was increased. The results revealed in this thesis are consistent with the latter. The clearly increased volume fraction and size of second phases is revealed by the microstructures (Figure 5.2a and Figure 5.9a) when Zn addition increased from 0.5 *wt.*% to 4 *wt.*%. No passivity is observed for both alloys according to the potentiodynamic polarization curves (Figure 5.4 and Figure 5.13) in NaCl solution, especially for Mg4Zn alloy. Moreover, the SKPFM result of Mg4Zn alloy (Figure 5.10) demonstrates that the Volta potential of MgZn phase is much higher than that of the surrounding α-Mg matrix. Therefore, according to the results in this thesis, higher level of Zn would result in lower corrosion resistance of Mg-Zn alloys due to the enhanced micro-galvanic effect.

The micro-addition of ternary alloying elements can influence the microstructures and corrosion rates of Mg0.5Zn and Mg4Zn alloys to different extent due to different solid solubility of the alloying elements in Mg or Mg-Zn system and the electrochemical properties of second phases that possibly can be formed.

6.1.1 Microstructure of as-cast Mg0.5Zn0.2X alloys

In the presence of ternary alloying elements, the solubility of Zn and the ternary alloying elements in Mg may be decreased due to the possible interaction between the two alloying elements. As a result, new ternary phases (for Mg0.5Zn0.2Al, Mg0.5Zn0.2Ca, Mg0.5Zn0.2Ga and Mg0.5Zn0.2Y alloys) or Mg-X binary (for Mg0.5Zn0.2Ca, Mg0.5Zn0.2Ce, Mg0.5Zn0.2Gd and Mg0.5Zn0.2Ge alloys) phases could be formed despite the micro-addition amount of the ternary alloying elements into the Mg0.5Zn system. In principle, the exact compositions of the second phases could be characterized by transmission electron microscopy but this analysis was not conducted since it is beyond the scope of this study.

6.1.2 Corrosion behavior of as-cast Mg0.5Zn0.2X alloys

Micro-addition of the ternary alloying elements changes the corrosion behavior of Mg0.5Zn alloy to different extent. Given the low added amounts of these elements, it is considered that the inherent electrochemical properties of the second phases are mainly responsible for the corrosion performance of Mg0.5Zn0.2X alloys instead of the volume or morphology. The potentiodynamic polarization (Figure 5.4) and EIS (Figure 5.6) results generally reveal that addition of Al, Ca and Ge enhances the corrosion resistance of Mg0.5Zn system while the other elements decrease the corrosion rate. It has been widely studied and accepted that the Mg-Al-Zn series alloys exhibit relatively good corrosion resistance [87-90]. For the studied Mg0.5Zn0.2Al alloy, active localized corrosion also occurs after immersion for 1 h but the continued formation of corrosion products suppresses the local activity of corrosion with extended exposure (after 24 h) (Figure 5.6d) and imparts limited retardation to the anodic dissolution of the substrate (Figure 5.4c). Interestingly, compared with the counterpart Mg0.5Zn0.2Al alloy, Mg0.5Zn0.2Ca and Mg0.5Zn0.2Ge alloys showed much better corrosion performance. The impedance spectra (Figure 5.6g and s) suggest a uniform corrosion process of the two alloys in NaCl solution and the polarization curves (Figure 5.4c and d) after 48 h indicate that the corrosion product films formed on these two alloy surfaces are highly protective compared with those formed on the other alloy surfaces. Thus, the protective surface films prevent the substrates from corrosion in corrosive electrolytes. Moreover, the cathodic current densities of Mg0.5Zn0.2Ca and Mg0.5Zn0.2Ge alloys (Figure 5.4c and d) are the lowest after 48 h, implying the retarded cathodic hydrogen evolution action on these two alloys. The holistic evaluation of corrosion rate by hydrogen evolution (Figure 5.7) also demonstrates the enhanced corrosion resistance of Mg0.5Zn0.2Ca and Mg0.5Zn0.2Ge alloys compared with that of Mg0.5Zn alloy. The detailed corrosion mechanisms of these two alloys will be discussed in more detail in the following parts considering short and extended immersion tests. The other Mg0.5Zn0.2X alloys behave similarly as Mg0.5Zn alloy. Local active dissolution happens on the alloy surfaces after immersion for 1 h and the surface layers exhibit no apparent protection to the substrate during polarization. This may be attributed to the micro-galvanic couples formed between the second phases and the matrix. The SKPFM measurements were not performed for Mg0.5Zn0.2X alloy due to the low volume fraction and small size of second phases but can be referred to those of Mg4Zn0.2X alloys.

6.1.3 Microstructure of as-cast Mg4Zn0.2X alloys

With the increased Zn content, higher amount of intermetallic particles are formed. However, several ternary phases (for Mg4Zn0.2Al, Mg4Zn0.2Ca, Mg4Zn0.2Ce and Mg4Zn0.2Gd alloys) are still precipitated despite the micro-addition of these ternary alloying elements, demonstrating the interaction between Zn and the ternary alloying elements. For Mg4Zn0.2Ga and Mg4Zn0.2Y alloys, MgZn phases are formed because the system is almost close to Mg-Zn binary system at this composition. Given the low content of Sn and the fact that no ternary phase can be formed in Mg-Zn-Sn system, only MgZn phases are found in Mg4Zn0.2Sn alloy.

6.1.4 Corrosion behavior of as-cast Mg4Zn0.2X alloys

Generally, the corrosion resistance of Mg4Zn0.2X alloys is lower than that of the corresponding Mg0.5Zn0.2X alloys in NaCl solution. This suggests that the increased volume fraction of second phases obviously affects the corrosion behavior of Mg4Zn0.2X alloys and both the volume fraction and the inherent electrochemical properties of the second phases will influence the corrosion performance of Mg4Zn0.2X alloys under this circumstance. The SKPFM results (Table 5.5) reveal that all precipitated second phases in Mg4Zn0.2X alloys are nobler than the α-Mg matrix. Consequently, the existence of higher amounts of second phases will result in higher micro-galvanic intensity of the alloys. Therefore, local active dissolution occurs for all Mg4Zn0.2X alloys as soon as immersion tests started. The relatively better corrosion behavior of Mg4Zn0.2Sn alloy may be attributed to the fully dissolved Sn in the matrix, the formation of only one kind of second phase (MgZn phase) in the microstructure and the almost unchanged Volta potential difference between the second phase and the α-Mg matrix. In comparison, two kinds of second phases are formed in Mg4Zn0.2Gd and Mg4Zn0.2Ge alloys, which normally is detrimental to the corrosion resistance of the alloys. Meanwhile, for the other alloys, the Volta potential difference between the second phases and the α-Mg matrix is much higher because of the formation of new ternary phases or due to the effects of small amount of dissolved ternary alloying elements in the MgZn phases.

6.2 Influence of extrusion on selected alloys

In the process of hot extrusion, dynamic recrystallization, dynamic precipitation and plastic deformation occur concurrently. As a result, the microstructure of Mg alloy is greatly affected and redistribution of alloying elements can happen, with an attendant influence on the corrosion properties of Mg alloys [1].

6.2.1 Microstructure

The coarse grains in as-cast ingot/billet are replaced by finely recrystallized grains due to dynamic recrystallization during hot extrusion. In this study, the large grains of more than 200 µm in diameter in as-cast Mg0.5Zn0.2Ca, Mg0.5Zn0.2Ge and Mg4Zn0.2Sn alloys are significantly refined to less than 50 µm after extrusion. Moreover, the solute Ca can also retard the grain growth during recrystallization [91, 92], causing the finest grain microstructure of extruded Mg0.5Zn0.2Ca alloy. While in the case of Mg0.5Zn0.2Ge alloy, the solute effect of Ge is restricted by the extremely low solubility of Ge in Mg, which consequently gives rise to a comparably coarse-grained microstructure of the alloy. Extrusion also leads to the fragmentation of relatively large-sized second phases distributing along the grain boundaries or interdendrite interstices, which is apparently revealed by the replacement of rod-like/Chinese script-shaped Mg_2Ge phases by fine Mg_2Ge pieces after extrusion of Mg0.5Zn0.2Ge alloy.

Generally, a higher extrusion speed leads to a larger average grain size, larger fraction of recrystallized grains, weaker basal texture and more precipitates [1]. The effective extrusion temperature is increased with increase in extrusion speed because both friction and adiabatic heating on the die walls contribute to the rise of local temperature of the billet in the die. Therefore, the growth of recrystallized grains is accelerated and the fraction of recrystallized grains is increased [93]. Moreover, elevated (effective) extrusion temperature facilitates the diffusion of solute atoms, leading to the formation of precipitates [94, 95]. During recrystallization, the deformed parent grains are replaced by the recrystallized grains, with the orientation of recrystallized grains deviating from that of the parent grains and dominated by the preferential growth of deformation twins with strong basal texture. Since a higher extrusion speed accelerates the recrystallization kinetics, the basal texture intensity is weakened. The general effect of extrusion speed on the fraction of recrystallization grains is also found in the studied Mg0.5Zn0.2Ca, Mg0.5Zn0.2Ge and Mg4Zn0.2Sn alloys. However, the texture intensity of these three alloys is marginally affected by the extrusion speed. In addition, the grain size increases with accelerating extrusion speed for extruded Mg0.5Zn0.2Ca and Mg4Zn0.2Sn alloys but shows an inverse trend for extruded Mg0.5Zn0.2Ge alloy, which might be influenced by the highly stable Mg_2Ge phases in the alloy.

6.2.2 Corrosion resistance

Normally, the corrosion mechanism of Mg alloys is not fundamentally changed by the extrusion process. Nevertheless, the alternations of local microstructure, such as refined grain and precipitates size and redistribution of alloying elements, can influence the corrosion properties of Mg alloys. With respect to intermetallic-free Mg alloys, the refined grain size enhances the corrosion resistance of Mg alloys. This is usually related to the formation of more coherent oxide/hydroxide corrosion product layers formed on the fine-grained Mg alloys [96]. In the presence of second phases, the type, distribution and amount of intermetallic particles predominately affect the corrosion resistance of Mg alloys. For as-cast Mg alloys, large-sized second phases cause localized corrosion in the alloys, leading to increased surface roughness and large mass loss. When the intermetallic particles are refined and uniformly distributed in the alloy after extrusion, the so-called micro-galvanic corrosion intensity can be decreased such that corrosion resistance can be improved, resulting in more shallow and homogeneous corrosion morphology. However, the effect of microstructural refinement by extrusion on corrosion rate of Mg alloy is still confined by the original alloy. Thus, the alloy chemistry dictates the corrosion resistance more than the refinement of microstructure. Consequently, different Mg alloys with different bulk compositions (chemistry) present a different window of corrosion resistance alternation by microstructural refinement.

The corrosion behavior of Mg0.5Zn0.2Ca alloy is not obviously changed by the extrusion process. A small fraction of eutectic $Ca_2Mg_6Zn_3$ + Mg_2Ca phases exists in the microstructure of the as-cast alloy. These two phases present opposite electrochemistry: $Ca_2Mg_6Zn_3$ phase is cathodic while Mg_2Ca phase is anodic relative to the α-Mg matrix [97, 98]. Nevertheless, as revealed by the drop corrosion test of as-cast Mg0.5Zn0.2Ca alloy (Figure 5.44), the α-Mg matrix was uniformly corroded and no obvious galvanic corrosion was detected after 6 h. The electrochemical tests (Figure 5.27) and the surface (Figure 5.49a) and cross-section morphologies after immersion (Figure 5.49d) also demonstrate the uniform corrosion process of the as-cast alloy in NaCl solution. A homogeneous and protective corrosion product layer is formed on the alloy surface and the corroded alloy/layer interface is pretty flat. No corrosion cavities are present. After extrusion, the $Ca_2Mg_6Zn_3$ phase dissolves during the homogenization or hot extrusion process, leaving Mg_2Ca phase uniformly distributed behind. Considering the small size, active electrochemistry and homogeneous distribution of Mg_2Ca phase, uniform corrosion is also observed for the extruded Mg0.5Zn0.2Ca alloy. Homogeneous microstructure composed of only α-Mg matrix is formed once the Mg_2Ca phase dissolves. Moreover, Zn participates in the formation of the corrosion product layer for both as-cast and extruded Mg0.5Zn0.2Ca alloys, imparting enhanced corrosion protection ability to the surface layer. Consequently, a very small window of corrosion rate alternation through microstructural refinement by extrusion is provided by Mg0.5Zn0.2Ca alloy. No evident change of corrosion behavior and resistance is observed for Mg0.5Zn0.2Ca alloy after extrusion.

For Mg0.5Zn0.2Ge alloy, hot extrusion enhances the corrosion resistance and the corrosion behavior is changed from localized corrosion to uniform corrosion. Obvious micro-galvanic corrosion exists in the microstructure of as-cast Mg0.5Zn0.2Ge alloy, indicated by the preferential corrosion occurring at the α-Mg matrix, especially at the matrix adjacent to the nobler rod-like Mg_2Ge phases (Figure 5.46e and f). As a result, some Mg_2Ge phases are even detached and fall out from the matrix after longer immersion (Figure 5.46f and Figure 5.49e). The galvanic coupling, attack of aggressive Cl^- ions and poor protection ability of the surface film result in the active dissolution (localized corrosion) of the substrate. After extrusion, the rod-like Mg_2Ge phases are broken into small pieces, more uniformly distributed in the microstructure. Moreover, the Volta potential difference between the Mg_2Ge phase and the α-Mg matrix decreases from 52 ± 18 mV to 29 ± 9 mV most likely due to the dissolution of the small volume fraction of Mg_xZn_y phases into the matrix. The small Mg_2Ge particles quickly fall out with extended immersion time. As a result, much milder galvanic corrosion occurs to the extruded Mg0.5Zn0.2Ge alloy. In addition, Zn and Ge obviously enrich in the outer part of the corrosion product layer of extruded Mg0.5Zn0.2Ge alloy which is not that evident for the as-cast alloy (Figure 5.52), imparting higher and even gradually increased corrosion resistance to the extruded alloy. This may also be because of the increased Zn in solid solution due to the dissolution of Mg_xZn_y phases during the homogenization or extrusion process. Therefore, a uniform protective surface layer and a flat corroded interface are found for the extruded Mg0.5Zn0.2Ge alloy. The refined microstructure and redistribution of precipitates and alloying elements after extrusion contribute to the improvement of corrosion performance of Mg0.5Zn0.2Ge alloy.

Significant improvement of corrosion rate is achieved by extrusion of Mg4Zn0.2Sn alloy. Nevertheless, the corrosion mechanism is not changed and localized corrosion occurs for both as-cast and extruded Mg4Zn0.2Sn alloys. A large volume fraction of large-sized MgZn phase induces strong galvanic corrosion, leading to severe localized corrosion of as-cast Mg4Zn0.2Sn alloy (Figure 5.48a and Figure 5.49f). Although dynamically precipitated fine particles replace those large MgZn phases after extrusion, the dissolution of MgZn phases leaves behind the high melting Mg_2Si and Fe-Mn particles which were embedded in MgZn phases in the as-cast alloy. The short immersion tests (Figure 5.48b and d) and literature review [99, 100] demonstrate that the Fe-Mn/Mg_2Si and single Mg_2Si particles are nobler than α-Mg matrix and can also form micro-galvanic couples with the matrix, thereby triggering localized corrosion. Moreover, galvanic effect also still exists between the Zn segregated matrix and the normal α-Mg matrix (Figure 5.51c and f) due to the heterogeneous distribution of elements after extrusion, resulting in rough corroded alloy/corrosion products interface. Nevertheless, the intensity of galvanic coupling is greatly reduced for extruded Mg4Zn0.2Sn alloy compared to the as-cast one owing to the altered microstructure by extrusion. More importantly, the presence of Mn favors the formation of Fe-Mn solid solution (Mn encapsulates Fe) instead of pure Fe particles as revealed. Since the galvanic activity between Mn and Mg is less than that between Fe and Mg, the Fe-Mn particles would exhibit significantly lower electrocatalytic activity towards hydrogen reduction reaction compared with pure Fe impurities [101-104]. Accordingly, the re-deposition process observed in the case of pure Fe impurities [105] can also be affected due to the altered self-corrosion behavior of Fe-Mn particles after detachment. Consequently, the corrosion rate of the alloy greatly decreases in spite of the micro-galvanic effect between the impurity particles and the α-Mg matrix. In addition, for the extruded alloy, Zn uniformly enriches at the surface film/substrate interface, as revealed by the cross-section element mapping results (Figure 5.52). Similar enrichment of alloying elements at the film/Mg alloy interfaces have been reported for E717 alloy (Unocic et al.) [106, 107], AZ31 alloy (Cristóbal et al.) [108] and Mg5Sn3Zn alloy (Yang et al.) [109]. Moreover, according to the investigations carried out in refs. [106, 108, 110], it is speculated that the uniform enrichment of Zn at the entire film/alloy interface is related to the enhanced corrosion resistance of Mg alloys possibly by suppressing the outward migration of Mg. According to these literatures, the segregation of Zn is mainly attributed two reasons. On the one hand, as corrosion proceeds in a relatively aggressive electrolyte, the active Mg atoms are selectively dissolved, leaving behind the inert Zn atoms [109]. Sn segregation can also occur for Mg5Sn3Zn alloy. However, given the much lower content of Sn in Mg4Zn0.2Sn alloy studied herein, only Zn segregation was detected at the surface film/substrate interface. On the other hand, in comparison with MgO, the lower thermodynamic stability of ZnO favors the enrichment of unreacted Zn at the corroding interface as corrosion proceeds [106]. Unocic et al. and Cristóbal et al. considered that the enriched Zn existed in metallic form based on EDS line profile (the peaks of O and Zn did not correlate with each other) and XPS analysis. While Yang et al. identified the XPS region spectra of Zn $2p_{3/2}$ to be the mixture of ZnO and metallic Zn, which might be ambiguous because of the strong overlap between the binding energy of Zn^{2+} and Zn^0. This was also mentioned by Cristóbal et al. and they determined the chemical state of Zn more effectively by measuring both FWHM value and the splitting value ($2p_{1/2}$-$2p_{3/2}$).

In general, increasing extrusion speed can give rise to finer and more uniform distribution of second phases, thereby enhancing the corrosion resistance of Mg alloys. For the studied Mg0.5Zn0.2Ca, Mg0.5Zn0.2Ge and Mg4Zn0.2Sn alloys, no big difference is observed between the microstructures (distribution, size and volume fraction of intermetallic particles) formed at different extrusion speed besides the small or slight variation of grain size. Consequently, the corrosion resistance of the three alloys extruded at different speed is almost comparable as revealed by the electrochemical and hydrogen evolution results (Figure 5.27 – Figure 5.35). In other words, the extrusion speed (0.6, 2.2 and 4.4 mm/s) do not pose notable effect to the corrosion properties of Mg0.5Zn0.2Ca, Mg0.5Zn0.2Ge and Mg4Zn0.2Sn alloys.

6.3 Influence of corrosive electrolyte on the corrosion behavior

Mg and its alloys are intrinsically susceptible to corrosion due to two reasons. On the one hand, the electrical potential of Mg is highly negative, which allows the proceeding of corrosion process even at the absence of oxygen. As a result, the water reduction predominates as the cathodic reaction. On the other hand, the protective property of the surface film formed on Mg surface is poor. Additionally, the oxide/hydroxide surface layer is relatively soluble in the presence of water [2, 60, 111].

In dry air, magnesium oxide (MgO) is instantaneously formed on Mg alloy surface at room temperature:

$$2\text{Mg (s)} + \text{O}_2\text{ (g)} \rightarrow 2\text{MgO (s)} \tag{6.1}$$

Such surface film is only a few nanometers in thickness but imparts good corrosion resistance to Mg alloys in dry air. In the presence of humidity or in aqueous solution, MgO reacts with water, generating magnesium hydroxide ($Mg(OH)_2$, brucite):

$$\text{MgO (s)} + \text{H}_2\text{O (l)} \leftrightarrow \text{Mg(OH)}_2\text{ (s)} \tag{6.2}$$

Nevertheless, more corrosion products can be formed on Mg alloy surface when the composition of the soaking environment is more complicated, which can govern the corrosion behavior of Mg alloy depending on their protective properties.

6.3.1 Sodium chloride solution at different concentrations

When Mg alloy is exposed to NaCl solution, corrosion initiates as:

$$\text{Mg (s)} \rightarrow \text{Mg}^{2+}\text{ (aq)} + 2\text{e}^- \tag{6.3}$$

Simultaneously, the dominant cathodic water reduction reaction occurs:

$$2\text{H}_2\text{O (l)} + 2\text{e}^- \rightarrow 2\text{OH}^-\text{ (aq)} + \text{H}_2\text{ (g)} \tag{6.4}$$

Cathodic oxygen reduction can also occur:

$$\text{O}_2 + 2\text{H}_2\text{O} + 4\text{e}^- \rightarrow 4\text{OH}^- \tag{6.5}$$

Following that, the metallic cations react with the hydroxyl ions forming insoluble $Mg(OH)_2$ precipitates:

$$Mg^{2+} (aq) + 2OH^- (aq) \rightarrow Mg(OH)_2 (s) \qquad (6.6)$$

The cathodic processes of Mg result in an increase of pH near the substrate surface. Subsequently, $Mg(OH)_2$ quickly precipitates on the alloy surface forming the primary corrosion product layer besides the pre-formed very thin oxide layer in air. Formation of magnesium carbonate components is possible in the presence of CO_2 [112-114]. However, in this study, no clear evidence of magnesium carbonate components is found according to the EDS mapping (Figure 5.52) and XRD (Figure 5.53) analysis for the composition of corrosion products, which is in accordance with the results reported by Pardo et al. and Xin et al. [115, 116]. In the presence of Cl^- ions, local breakdown of the corrosion products layer can occur, resulting in the exposure of the underneath substrate to the corrosive electrolyte and triggering localized corrosion. This may be achieved by the formation of metal-hydroxyl-chloride complex compounds [117]. Furthermore, those uncovered noble second phases, impurities and inclusions due to the defective surface layer can also be locally polarized and initiates localized corrosion. Increasing Cl^- concentration can lead to more fraction of film-free surface of the alloy (uncovered or defective areas of the surface film) where corrosion predominately occurs. Therefore, normally, the corrosion resistance of Mg alloys decreases with increasing Cl^- concentration, which has been broadly revealed and widely accepted for Mg alloys [69, 70].

Since the corrosion mechanism of Mg alloy is not altered by the Cl^- concentration, similar corrosion morphologies and corrosion products are formed on the extruded alloys investigated in this study despite the slight difference of Cl^- concentration. The well-formed surface films impart good corrosion resistance to extruded Mg0.5Zn0.2Ca and Mg0.5Zn0.2Ge alloys in both DIW based NaCl solutions, while broken surface layers cannot effectively protect extruded Mg4Zn0.2Sn alloy from corrosion. However, as revealed by electrochemical and hydrogen evolution results (Figures 5.36, 5.37, 5.38, and 5.42), the corrosion resistance of extruded Mg0.5Zn0.2Ge and Mg4Zn0.2Sn alloys are generally higher in NaCl solution prepared with DIW at lower concentration (0.5 *wt.*%), especially for Mg4Zn0.2Sn alloy. This is consistent with the above analysis about the influence of Cl^- concentration on the corrosion behavior of Mg alloys. In comparison, no evident difference is revealed for the corrosion rate of extruded Mg0.5Zn0.2Ca alloy by the different Cl^- concentration. This may be attributed to the different bulk compositions and microstructures of these three alloys. Another possible reason may be the different amount of galvanic active intermetallics.

6.3.2 Deionized water and artificial tap water based sodium chloride solution

The mechanisms of the formation of different corrosion products in the two different corrosive media are schematically depicted in Figure 6.1.

As discussed above, partially protective $MgO/Mg(OH)_2$ surface films are formed on Mg alloy surface in simple NaCl solution, which is demonstrated by the analysis for the compositions of the corrosion products by EDS mapping and XRD measurements of extruded alloys. Big difference can be observed for the corrosion performance of different Mg alloys owing to the different bulk compositions of the materials. Under this circumstance, the electrochemical nature of the alloy dominates the corrosion behavior.

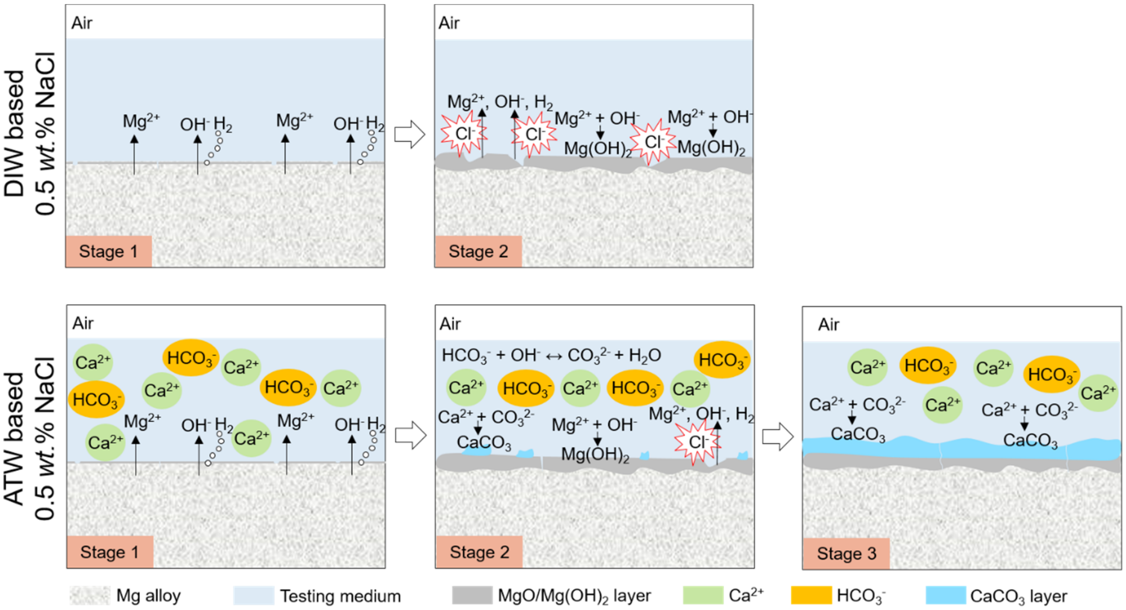

Figure 6.1 Schematic presentation of the corrosion processes of the studied alloys in 0.5 *wt.*% NaCl solutions prepared with DIW and ATW.

In NaCl solution prepared with ATW, cases are different due to the presence of abundant calcium ions (Ca^{2+}) and bicarbonate ions (HCO_3^-). As mentioned above, when Mg alloy is immersed in corrosive electrolyte and corrosion occurs, the concentration of Mg^{2+} and pH at the alloy/solution interface increase because of the corrosion process. The alkalization of the solution near the sample surface resulting from Mg dissolution encourages the conversion of HCO_3^- ions to carbonate (CO_3^{2-}) ions. Consequently, the precipitation of calcium carbonate ($CaCO_3$) is facilitated as following:

$$HCO_3^- \text{ (aq)} + OH^- \text{ (aq)} \leftrightarrow CO_3^{2-} \text{ (aq)} + H_2O \text{ (l)} \qquad (6.7)$$

$$Ca^{2+} \text{ (aq)} + CO_3^{2-} \text{ (aq)} \rightarrow CaCO_3 \text{ (s)} \qquad (6.8)$$

Therefore, insoluble $CaCO_3$ crystallizes as a new corrosion product layer covering the top of the inner $MgO/Mg(OH)_2$ layer. $CaCO_3$ can exist in three anhydrous crystalline phases: calcite, aragonite and vaterite. Among them, aragonite is the secondly thermodynamically stable crystalline form of $CaCO_3$. However, Mg^{2+} has been proven to promote the aragonite form of

$CaCO_3$ [118, 119] and the dissolution of the alloys in the present study can provide sufficient Mg^{2+} at the alloy/solution interface, which may account for the presence of aragonite flowers. Formation of aragonite flowers on Mg alloy surface has been reported when pure Mg and ZM21 alloy are immersed in Ringer's solution (containing $CaCl_2$ and $NaHCO_3$) [77]. The corroded cavities and stilts of non-corroded bulk materials in Figure 5.51 indicate that the primary $MgO/Mg(OH)_2$ layer grew predominately adjacent to the bulk material, i.e., from the initial surface (external surface) towards the internal bulk material. This phenomenon has been reported in the work of Kalb et al. [120] by observing the temporal evolution of bulk erosion and corrosion layer formation. In comparison, Ca^{2+} and HCO_3^-/CO_3^{2-} diffuses from the electrolyte towards the material surface and deposits on the primary $MgO/Mg(OH)_2$ layer surface, in which process the $Mg(OH)_2$ serves as a nucleus for the deposition of $CaCO_3$. The increased pH resulting from the dissolution of Mg can drive the equilibrium between HCO_3^- and CO_3^{2-} shifting strongly towards carbonates near the alloy surface, which in turn favors the precipitation of $CaCO_3$. Additionally, the gradual compactness of $CaCO_3$ layer can block the ions diffusion (Mg^{2+} from interior towards exterior and Ca^{2+} from exterior towards interior). As a result, an apparent two-layer cross section morphology is formed. Small amount of other ions (sulfate, nitrate etc.) also exist in ATW and may affect the formation of corrosion products. For example, sulfate has been demonstrated to favor the transformation from calcite to aragonite [118] but the effects of other trace ions on the crystalline of $CaCO_3$ remain to be considered but seem to be not very effective. According to the elemental mapping results (Figure 5.52), the existence of Zn, Ge and Sn in the $CaCO_3$ layer can be a result of the incorporation of those metallic ions into the precipitation of $CaCO_3$ [121, 122].

With extended exposure of the alloys in ATW based NaCl solution, the $CaCO_3$ layer gradually grows to be more intact and thicker, which imparts good corrosion protection to the underlying substrate, giving rise to a continuously increasing and higher impedance values. As a result, the corrosion resistance of the three extruded alloys is significantly improved in NaCl solution prepared by ATW compared to solution prepared by DIW, despite the higher Cl^- concentration in ATW based NaCl solution. Especially for extruded Mg4Zn0.2Sn alloy, the active localized dissolution of the substrate is suppressed and replaced by gradually increased corrosion resistance. The minor difference between the corrosion behavior of extruded Mg0.5Zn0.2Ca and Mg0.5Zn0.2Ge alloys that comes from the bulk materials is concealed by the pronounced effect of the water. In contrast, the corrosion rate of extruded Mg4Zn0.2Sn alloy is still higher than that of the other two alloys, which may result from the substantially lower corrosion resistance of the bulk material.

6.4 Comprehensive comparison of the overall properties

6.4.1 Corrosion properties

As revealed, the corrosion mechanisms of extruded Mg0.5Zn0.2Ca, Mg0.5Zn0.2Ge and Mg4Zn0.2Sn alloys in DIW based 0.9 *wt.*% and 0.5 *wt.*% NaCl solutions are similar. The corrosion behavior of the three alloys in ATW based 0.5 *wt.*% NaCl solution is dominated by the formation of the additional $CaCO_3$ layer due to the composition of ATW instead of the electrochemical nature of the bulk material. Therefore, hereafter the comparison of the corrosion properties of extruded Mg0.5Zn0.2Ca, Mg0.5Zn0.2Ge and Mg4Zn0.2Sn alloys mainly considers the corrosion behavior in DIW based 0.5 *wt.*% NaCl solution and in salt spray tests. Figure 6.2 compares the corrosion properties of the three alloys according to the R_{sum} plots fitted from impedance spectra, potentiodynamic polarization curves and hydrogen evolution results obtained in DIW based 0.5 *wt.*% NaCl solution.

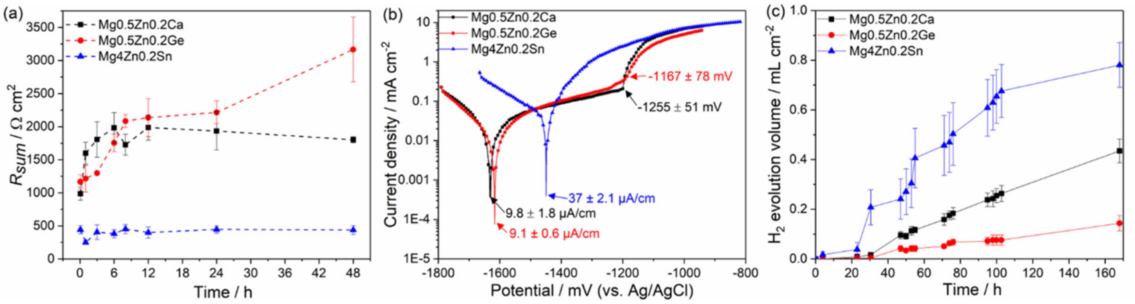

Figure 6.2 Comparison of the corrosion properties of extruded Mg0.5Zn0.2Ca, Mg0.5Zn0.2Ge and Mg4Zn0.2Sn alloys illustrated by (a) R_{sum} plots fitted from the impedance spectra, (b) potentiodynamic polarization curves and (c) hydrogen evolution results tested in DIW based 0.5 *wt.*% NaCl solution.

Micro additions of Ca and Ge into Mg-Zn system have been reported to enhance the corrosion resistance of Mg-Zn alloys while studies about the corrosion properties of Mg-Zn-Sn system are still limited. The improvement of corrosion properties by Ca micro-alloying is mainly attributed to the purification of melts, while the enhancement by Ge addition is mainly ascribed to the suppressed cathodic kinetics for hydrogen evolution [98, 123, 124]. Due to the different bulk compositions and microstructures of extruded Mg0.5Zn0.2Ca, Mg0.5Zn0.2Ge and Mg4Zn0.2Sn alloys, the corrosion behavior of the three alloys exhibits some difference in NaCl solution. Extruded Mg0.5Zn0.2Ca and Mg0.5Zn0.2Ge alloys are corrosion-resistant in NaCl solution due to the partially Zn segregated surface films, which leads to well-defined capacitive loops in EIS measurements (Figure 5.38a and d). However, the dissolution of the film happens simultaneously, competing with its formation process. The relative speed of the formation and dissolution processes affects the protection abilities of the corrosion product films. Thus, the different development of impedance values with immersion time for these two alloys (fluctuated for Mg0.5Zn0.2Ca alloy and gradually increased for Mg0.5Zn0.2Ge alloy as indicated by Figure 6.2a) suggests that the corrosion product layer formed on the surface of Mg0.5Zn0.2Ge alloy is more protective than that of Mg0.5Zn0.2Ca alloy. This is also confirmed by potentiodynamic polarization results (Figure 6.2b). A lower current density and a nobler breakdown potential are revealed for the Mg0.5Zn0.2Ge alloy. More evident difference between the corrosion properties of extruded Mg0.5Zn0.2Ca and Mg0.5Zn0.2Ge alloys is revealed by the holistic corrosion rate evaluated by hydrogen evolution curves (Figure 6.2c). In comparison, the Mg4Zn0.2Sn alloy is much less corrosion-resistant in NaCl solution. The existence of nobler Fe-Mn impurities and heterogeneous micro-chemistry (segregation of Zn in the matrix) is unfavorable for a uniform corrosion of the alloy and the formation of homogeneous or protective surface layers. Moreover, local breakdown of the corrosion products layer happens due to the presence of aggressive Cl^- ions. Thus, active dissolution of the alloy happens through the defects of the corrosion product film as soon as the immersion starts, which is revealed by the poorly defined capacitive loop in the impedance spectra (Figure 5.38g). With prolonged immersion, the formation of corrosion products marginally suppresses the activity of localized dissolution of the alloy and thus the impedance values do not obviously change even with extended immersion. Herein, it is disclosed that the corrosion resistance of the three extruded alloys decreases in an order of Mg0.5Zn0.2Ge > Mg0.5Zn0.2Ca > Mg4Zn0.2Sn after a relatively short immersion (up to 7 days) in DIW based 0.5 *wt.*% NaCl solution.

Furthermore, the macroscopic surface morphologies after salt spray tests (Figure 5.56) also disclose the different corrosion properties of extruded Mg0.5Zn0.2Ca, Mg0.5Zn0.2Ge and Mg4Zn0.2Sn alloys. Similarly, Mg4Zn0.2Sn alloy exhibits the worst corrosion property over the whole salt spray measurement. Interestingly, Figure 5.56 indicates better corrosion performance for Mg0.5Zn0.2Ge alloy during the initial days, which is in agreement with the electrochemical and hydrogen evolution results. Whereas, after long-term test (28 days), higher corrosion resistance can be observed for Mg0.5Zn0.2Ca alloy and severe localized corrosion is visible for Mg0.5Zn0.2Ge alloy, which was not found from electrochemical and hydrogen evolution results. This difference may come from the higher content of nobler second phases in Mg0.5Zn0.2Ge alloy compared with Mg0.5Zn0.2Ca alloy [123, 125], which can induce more intensive micro-galvanic corrosion between α-Mg matrix and the second phases. On the other hand, compared with electrochemical test condition, the salt spray condition gives a harsher atmosphere for the corrosion of the alloys, which was used to accelerate the corrosion process of the alloys. The salt fog was generated from 5 *wt.*% NaCl, leading to a higher concentration of Cl^-, which will promote the corrosion of the alloys and can induce more severe localized corrosion of the alloy [60]. Moreover, during the tests, salts, for example, NaCl, can nucleate and grow on the alloy surface, which can further enhance the invasion of Cl^- to corrosion product layer and accelerate the corrosion of the alloy, especially causing localized corrosion. Therefore, the different corrosion behavior of these two alloys during salt spray tests can be a result of the harsher corrosive environment and the different microstructure (second phase) of the alloys. Furthermore, the surface morphologies after constant load test (Figure 5.66) indicate that the oxide layer grows faster on the surface of Mg0.5Zn0.2Ge alloy. After certain thickness is reached, the oxide layer flakes off (Figure 5.66), which can also be responsible for the poorer long-term corrosion resistance of Mg0.5Zn0.2Ge alloy compared with that of Mg0.5Zn0.2Ca alloy.

6.4.2 Mechanical properties and integrity

The typical basal planes-preferred texture for extruded Mg0.5Zn0.2Ca, Mg0.5Zn0.2Ge and Mg4Zn0.2Sn alloys is a result of the recrystallization and unidirectional deformation during the extrusion processing [126]. A strong basal plane is beneficial for the tensile strength but detrimental to the ductility of alloys [127]. With the strong basal texture, a high tensile strength can be reached when extruded Mg alloys are tensile tested parallel to the extrusion direction because of the low Schmid factor for extension twinning and basal slip. In contrast, deformation twinning is readily operative due to the compression along the basal plane when the alloy is compressively tested along the extrusion direction, giving rise to low compressive strength [1]. The hexagonal close-packed (HCP) structure of Mg inherently lacks sufficient number of activated slip systems, predominating by basal slip, which results in the poor ductility of Mg at room temperature [128]. Moreover, the well-established Hall-Petch relation reveals that fine grain size can contribute to an improvement of mechanical properties [129, 130]. The average size of recrystallized grains is 16 ± 1 μm for Mg0.5Zn0.2Ca alloy, 37 ± 1 μm for Mg0.5Zn0.2Ge alloy and 34 ± 1 μm for Mg4Zn0.2Sn alloy. Meanwhile, the highest texture intensity is 2.3 for Mg0.5Zn0.2Ca alloy, 5 for Mg0.5Zn0.2Ge alloy and 4.7 for Mg4Zn0.2Sn alloy, respectively. As such, the stronger alignment of basal planes parallel to the extrusion direction leads to higher tensile strength for Mg0.5Zn0.2Ge and Mg4Zn0.2Sn alloys (Table 5.15). However, an enhanced activity of twinning promoted by the preferential orientation and the large grains result in lower CYS of Mg0.5Zn0.2Ge and Mg4Zn0.2Sn alloys, exhibiting a significant mechanical anisotropy (TYS/CYS). In comparison, the weaker texture and the smaller grain size of Mg0.5Zn0.2Ca alloy decrease this difference in the activity of deformation mechanisms, reducing the strength differential effect. Also, the elongation to fracture is therefore higher. The fracture surfaces after tensile test and elongation to fracture corroborate each other for the three alloys. Actually, the tensile properties of the present Mg0.5Zn0.2Ge (TYS: 171 MPa, UTS: 249 MPa, elongation to fracture: 10 %) and

Mg4Zn0.2Sn (TYS: 157 MPa, UTS: 254 MPa, elongation to fracture: 16 %) alloys are comparable to those of commercial AZ series alloys [131]. Moreover, compared with the extruded Mg4ZnxSn (x= 1.0; 1.5; 2.0, in *wt.*%) alloys studied by Jiang et al. [132], currently extruded Mg4Zn0.2Sn possesses higher strength despite the much lower concentration of Sn, higher extrusion temperature (extrusion speed was not provided in the reference) and the missing possible strengthening effect of precipitated Mg_2Sn phases in this study. What still needs to be mentioned here is the possible strengthening effect of the dispersed Mg_2Ge phase in Mg0.5Zn0.2Ge alloy, which is also referred by Liu et al. [124]. More investigations are needed in the future to reveal its strengthening role.

Generally, along with the propagation of corrosion, the actual cross section area of the samples for tensile tests decreases, leading to a significantly reduced load capacity of the samples. As a result, the mechanical properties deteriorate with the extension of pre-corrosion time. Additionally, when localized corrosion pits are formed, serious stress concentration can happen at those sites during tensile test, thereby initiating and promoting cracks. Moreover, in the presence of localized corrosion pits, the unidirectional stress for uncorroded sample during tensile test can be transformed to be multidirectional, which can also cause the occurrence of stress concentration and embrittlement [19]. The different trends in tensile property variations of Mg0.5Zn0.2Ca, Mg0.5Zn0.2Ge and Mg4Zn0.2Sn alloys are closely related to the different corrosion behavior of these three alloys under salt spray. As indicated by the macroscopic surface appearance (Figure 5.56g) and the overall fracture surfaces after tensile tests (the first column in Figure 5.59), localized corrosion already occurred for Mg4Zn0.2Sn alloy after 3 days and became more and more serious with prolonged exposure in salt spray. As a result, the tensile properties of Mg4Zn0.2Sn alloy obviously decreased after exposure for 3 days and gradually deteriorated with extended exposure time. In comparison, situation is a bit more complicated for Mg0.5Zn0.2Ca and Mg0.5Zn0.2Ge alloys. More visible corrosion occurred for Mg0.5Zn0.2Ca alloy already after exposure for 3 days (Figure 5.56a and the first column in Figure 5.57) but was apparent for Mg0.5Zn0.2Ge alloy only after 7 days (Figure 5.56g and the first column in Figure 5.58). This gives rise to the reduction of elongation to fracture for Mg0.5Zn0.2Ca alloy after pre-corrosion for 3 days and only after 7 days for Mg0.5Zn0.2Ge alloy. Localized corrosion pits were firstly observed in the case of Mg0.5Zn0.2Ge alloy after 28 days at which time the tensile properties of the alloy remarkably deteriorated. While the appearance and adverse effect of localized corrosion pits were notable until 42 days for Mg0.5Zn0.2Ca alloy. The sudden deterioration of tensile properties for Mg0.5Zn0.2Ca and Mg0.5Zn0.2Ge alloys due to the existence of corrosion pits indicates the critical influence of localized corrosion on the mechanical integrity of the alloys. Owing to the effect of corrosion and the formation of localized corrosion pits, the fracture characteristic of these three alloys became more and more brittle, as shown in Figure 5.57, Figure 5.58 and Figure 5.59.

6.4.3 Fatigue and corrosion fatigue behavior

When samples are tested under axial alternating tension in air, defects in microstructures, such as micro-pores, shrinkage voids and inclusions resulting from manufacturing etc., or the interfaces between the matrix and intermetallics can enhance stress intensity and trigger the fatigue crack initiation [133, 134]. Twin boundaries and slip bands can act as crack initiators when the alloys are defect-free. Moreover, those defects can further accelerate crack propagation [134-138]. With the progress of crack growth, each single cycle of loading contributes to the formation of a radial cleavage striation on the fracture surface [139], finally leading to a mechanical overload failure of specimens.

In chloride-containing corrosive solutions, local breakdown of the surface film on Mg alloy surface can occur, resulting in localized corrosion, and corrosion pits are the most common triggers for corrosion fatigue [134, 140]. Therefore, both the pre-existing microstructural defects and formation of corrosion pits need to be taken into consideration under this circumstance.

Under a stress level greater than or at the fatigue limit in air (high stress amplitude), those pre-existing defects in microstructures can trigger the formation and accelerate the growth of fatigue cracks before the formation of corrosion pits and their growth into the critical size within relatively short testing period [136]. Thus, inclusions instead of corrosion pits are recognized as crack initiation sites on the fracture surfaces of Mg0.5Zn0.2Ca, Mg0.5Zn0.2Ge and Mg4Zn0.2Sn alloys failing in both NaCl solutions at the stress amplitude of the fatigue limits in air. In this regime, the role of mechanical parameter predominates over the role of corrosion [139, 141]. However, it can still be speculated that the fatigue cracking of the alloy was accelerated or the crack initiator roles of microstructural defects were magnified in corrosive solutions.

At stress levels below the fatigue limit in air, the testing period is longer. The corrosive electrolyte gets more time to erode the specimen surface. Besides, in the presence of cyclic loading, the persistent slip bands can result in cumulative plastic deformation and formation of intrusions and extrusions, which consequently breaks the corrosion products layer [142, 143]. Subsequently, corrosive electrolyte penetrates into the underlying material and corrosion preferentially occurs at these film-free sites, which leads to the formation of corrosion pit. The growth of the corrosion pit is then favored by the stress concentration occurring at the root of the pit. Once the pit grows into the critical size for fatigue cracking, failure of the sample can eventually happen. In such circumstance, the pre-existing defects may also trigger the formation of cracks and facilitate their growth. However, the propagation rate of the cracks is much slower compared with that accelerated by the corrosion pits. As a result, the corrosion processes dominate under stress levels lower than the fatigue limit in air due to fatigue-environmental interaction.

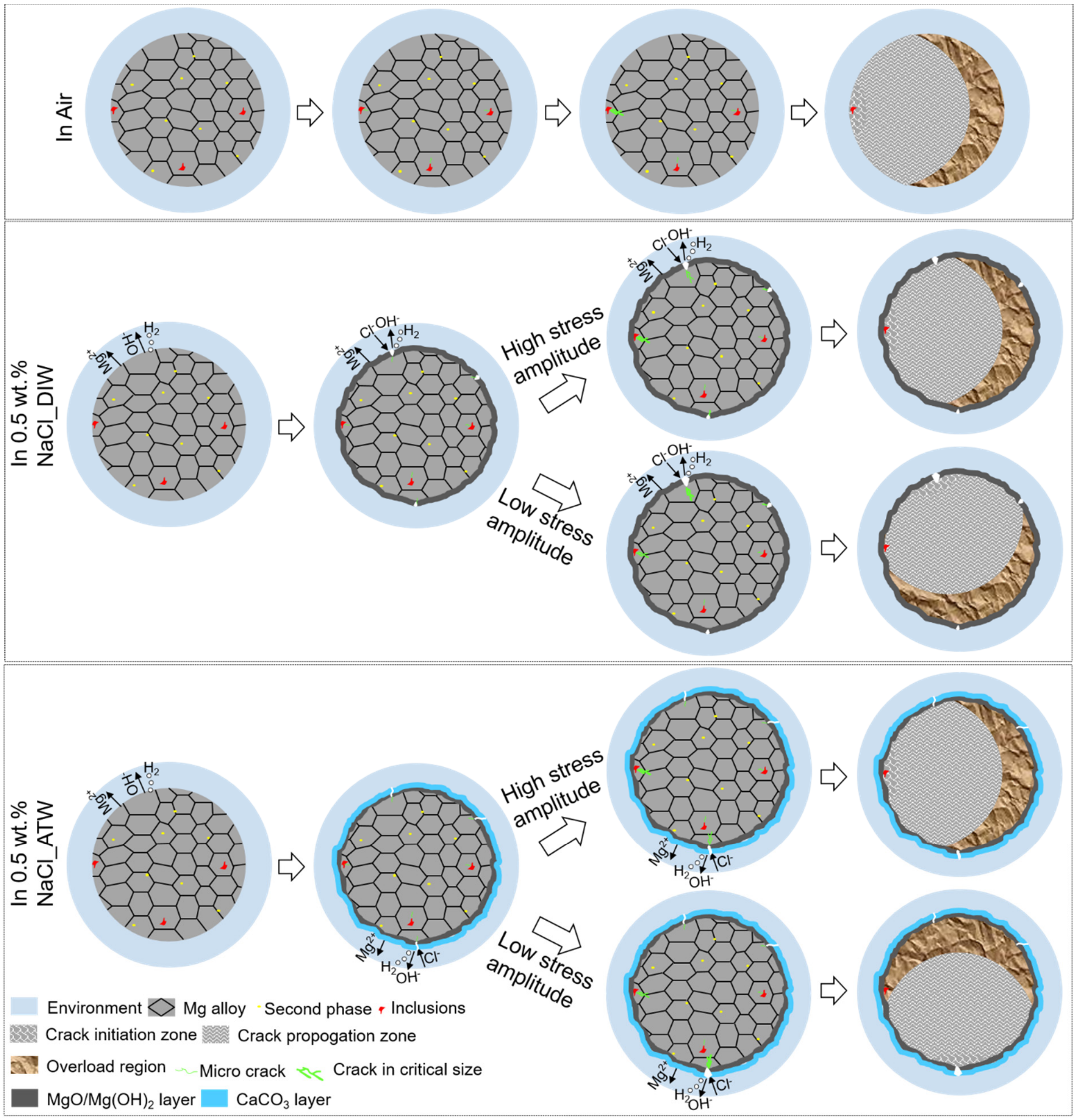

Figure 6.3 Schematic presentation for the process of fatigue in air and corrosion fatigue in different corrosive electrolytes of the studied alloys.

Generally, it is believed that hydrogen embrittlement is the primary factor and anodic dissolution is the secondary one for the fatigue crack growth in corrosive electrolytes [134, 144]. Hydrogen is the byproduct of the corrosion of Mg. During corrosion fatigue tests, the cyclic loading and/or the localized development of less resistant surface layer can result in the disruption of the surface layer, facilitating the ingress of hydrogen into the material. Consequently, localized hydrogen build-up will occur and lead to crack propagation. On the other hand, less protective surface layer means more dissolution of the underneath alloy and thus reducing the fatigue resistance of the material. Therefore, as discussed above, the enhanced resistance to dissolution should be the reason for the better fatigue resistance of extruded Mg0.5Zn0.2Ca, Mg0.5Zn0.2Ge and Mg4Zn0.2Sn alloys in ATW based NaCl solution compared to that in DIW based solution. This also stresses the effects of testing solutions on the corrosion performance of the substrates and thus on the corrosion fatigue crack propagation of these three alloys. In addition, according to the electrochemical tests and salt spray tests in DIW based NaCl solution/fog, higher short-term corrosion rate and less protective surface layers are revealed for Mg0.5Zn0.2Ca alloy. Therefore, the fatigue limit decreased more for Mg0.5Zn0.2Ca alloy in both NaCl solutions, revealing that Mg0.5Zn0.2Ca alloy is more sensitive to corrosive environment compared with Mg0.5Zn0.2Ge alloy in the short-term duration of the fatigue tests (longest one was about 92 h for 10^7 cycles). For Mg4Zn0.2Sn alloy, considering the poor chemical inhomogeneity of the microstructure (especially the segregation of Zn in the matrix), the non-protective surface film and the consequent poor corrosion property, the fatigue resistance of Mg4Zn0.2Sn alloy is the most sensitive in DIW based NaCl solution due to the active dissolution of the material. All these accumulated impacts give rise to the quite scattered behavior of the S-N curve of Mg4Zn0.2Sn alloy in DIW based NaCl solution even when the load is low. In comparison, in ATW based NaCl solution, the dissolution of the alloy is sufficiently retarded owing to the formation of an additional protective $CaCO_3$ layer. Accordingly, the fatigue life of the alloy is much less scattered and longer compared to that in DIW based NaCl solution. However, no fatigue limit was detected in both corrosive electrolytes even when the applied stress amplitude was 20 % lower than that of the fatigue limit in air due to the active electrochemical nature of the bulk material. This is similar to the critical role of the nature of bulk material in the corrosion behavior of Mg4Zn0.2Sn alloy in ATW based NaCl solution. Although the protective $CaCO_3$ layer conferred significantly improved corrosion resistance on the three alloys, the corrosion rate of Mg4Zn0.2Sn alloy was still higher than that of Mg0.5Zn0.2Ca and Mg0.5Zn0.2Ge alloys. The mechanisms for the different fatigue behavior of these three alloys under different conditions are schematically presented in Figure 6.3.

6.4.4 Susceptibility to stress corrosion cracking

Stress corrosion cracking (SCC) is another particular form of environment-assisted cracking besides corrosion fatigue. It is well known that Mg alloys are susceptible to SCC in common service environments such as distilled/deionized water and dilute chloride solution [84]. Especially, it has been well established that alloying addition of Al and Zn can promote SCC of Mg alloys [145]. However, SCC does not initiate from pitting but from the cracking of the surface film [146]. Accordingly, the initiation and propagation of SCC are strongly affected by the nature and stability of the surface films formed on the alloy surfaces in aqueous solutions [147]. Since the load intensity governs the mechanical stability of the surface film, the susceptibility of Mg alloys to SCC also depends on the applied stress [148]. Moreover, large second phase particles tend to increase the susceptibility to SCC of Mg alloys [145]. Generally, two propagation mechanisms are considered for SCC of Mg alloys: continuous crack propagation induced by anodic dissolution and hydrogen-assisted embrittlement (discontinuous crack propagation) [9, 84, 149]. The latter is believed to be more common for SCC in Mg alloys in aqueous environments [84, 150].

In this study, the evaluation of susceptibility to SCC by constant load tests (less intensive straining compared to the popular slow strain rate test) for extruded Mg0.5Zn0.2Ca, Mg0.5Zn0.2Ge and Mg4Zn0.2Sn alloys allows the maintenance of the surface films formed in different electrolytes. Thus, the difference mainly comes from the mechanical stability of the different surface films for a specific alloy formed in different solutions. However, direct comparison between different alloys tested in the same solution may not be reasonable enough. This is because the intensity of load is varied for different alloys, which was chosen at about 70 % of the yield strength of the alloys. Nevertheless, according to Figure 5.66, one can still tell that Mg0.5Zn0.2Ca and Mg4Zn0.2Sn alloys are not susceptible to SCC in the four solutions, while Mg0.5Zn0.2Ge alloy shows apparent susceptibility, especially in deionized water. In other words, the threshold stress for SCC of Mg0.5Zn0.2Ca and Mg4Zn0.2Sn alloys is higher than (or maybe equal to) 70 % of the specific yield strength of the alloys, while that of Mg0.5Zn0.2Ge alloy is below 70 % of the yield strength of the alloy. This may be due to the different microstructures of the three alloys since only partly recrystallized microstructure and more and larger second phases were revealed for the extruded Mg0.5Zn0.2Ge alloy. The H_2 resulting from the galvanic corrosion between the nobler Mg_2Ge phase and the matrix can lead to embrittlement. Furthermore, according to Figure 5.66, it seems that the surface film formed on the surface of Mg0.5Zn0.2Ge alloy after relatively long time is less adhesive and even flakes off.

The highest susceptibility of Mg0.5Zn0.2Ge alloy to SCC was found in deionized water that principally is free of aggressive Cl^- ions instead of the other solutions containing Cl^- ions. According to part 6.3, $MgO/Mg(OH)_2$ layer was formed on the surfaces of the alloys in DIW and DIW based 0.5 *wt.*% NaCl solution. While in ATW based NaCl solution, an additional $CaCO_3$ layer was formed on the top of the primary $MgO/Mg(OH)_2$ layer, which conferred much higher corrosion resistance to the three alloys despite the higher concentration of Cl^- in the solution compared to DIW based NaCl solution. Actually, the additional flower-like $CaCO_3$

layer was also formed in ATW, as indicated by the partially peeled off white corrosion products in Figure 5.66n and 5.66v and by the cross section morphology of Mg0.5Zn0.2Ge alloy in Figure 5.67f. These corrosion products formed on the alloy surface can protect the substrate from corrosion to some extent and block hydrogen transport. However, as indicated by Figure 5.67, uniform corrosion occurred to Mg0.5Zn0.2Ge alloy due to the relatively mild electrolyte (deionized water) and the good corrosion resistance of the alloy. The cracks directly developed from the relatively flat corrosion product layer of corroded alloy/film interface in DIW. While in the other three solutions containing aggressive ions, cracks were found at the bottom of the round corrosion pits that may be formed due to the existence of the aggressive ions. Since SCC initiates from cracking of the surface film instead of pitting, it indicates that cracks is formed more easily in the flat surface layer and the propagation of the cracks developed underneath the corrosion cavities may be slower than those near the uniformly corroded interface. As a result, Mg0.5Zn0.2Ge alloy is the least resistant to SCC in deionized water.

Normally, the tensile properties should decrease after the constant load tests if the specimens survived the full testing period owing to the decreased actual cross section area resulting from corrosion. Nevertheless, increased YS are observed in some cases. This may be attributed to three reasons. Firstly, the contribution may come from the mismatch between the lattice constants of the corrosion product layers formed on the alloy surfaces and the substrates. The different corrosion products formed in different electrolytes also make some difference. The more enhancements of YS detected for specimens tested in ATW or ATW based NaCl solution may be because of the formation of the additional $CaCO_3$ layer. Secondly, during the constant load process, tensile twins can be formed, which could resist the deformation process during tensile test and thus enhance the YS. Additionally, H_2 generated by the dissolution of the substrate can diffuse into the substrate, especially at the positions of dislocation, which can pin the dislocations and then more force is needed to start the deformation during tension test and consequently give rise to increased YS. Similar to the scattered behavior of the S-N curve of Mg4Zn0.2Sn alloy in DIW based NaCl solution, the big variation between the replicates tested in DIW or DIW based NaCl solution for constant load tests may also come from the active dissolution of the alloy in these two electrolytes. While the formation of protective $CaCO_3$ layer in ATW or ATW based NaCl solution suppressed the local active dissolution of the alloy and contributed to the good repeatability of the results. This, again, confirmed the significantly beneficial effect of ATW upon the corrosion resistance of the alloy, and also indicates that Ca^{2+} can be considered as a corrosion inhibitor.

7. Summary and conclusions

In the present study, micro-alloyed Mg-Zn based ternary alloys were developed. After screening for promising alloys with improved corrosion performance, wrought processing (hot extrusion) was applied to further improve the properties of the alloys. At the same time, the influence of extrusion speed on the microstructure and corrosion resistance of the alloys was investigated. Finally, the properties of the optimized alloys were comprehensively studied in terms of corrosion performance in different corrosive electrolytes, mechanical properties and integrity, fatigue and corrosion fatigue behavior and susceptibility to stress corrosion cracking.

For as-cast Mg0.5Zn0.2X system, addition of Ca and Ge improved the corrosion resistance of the alloy while alloying with other elements (Al, Ce, Gd, Ga, Sn and Y) did not show significant enhancement. When the addition amount of Zn increased to 4 *wt.*%, more intermetallic particles were formed, leading to an overall decreased corrosion resistance of the alloys in NaCl solution. However, Mg4Zn0.2Sn alloy showed slightly higher corrosion resistance. The different solid solubility of different ternary alloying elements gave rise to different microstructures. The different Volta potential difference between the second phases and the α-Mg matrix resulted in the different micro-galvanic corrosion intensity. Consequently, different corrosion resistance of the alloys was presented.

Extrusion significantly refined the microstructures of as-cast Mg0.5Zn0.2Ca, Mg0.5Zn0.2Ge and Mg4Zn0.2Sn alloys due to dynamic recrystallization. Higher extrusion speed resulted in increased fraction of recrystallization grains but showed little effect on the texture intensity of the three alloys. However, almost fully recrystallized microstructure can be obtained for Mg0.5Zn0.2Ca and Mg4Zn0.2Sn alloys when the extrusion speed increased to 2.2 mm/s, while the microstructure of Mg0.5Zn0.2Ge alloy was still partially recrystallized even extruded at 4.4 mm/s. The grain sizes of Mg0.5Zn0.2Ca and Mg4Zn0.2Sn alloys generally increased with accelerated extrusion speed, while that of Mg0.5Zn0.2Ge alloy showed an inverse trend. The unique behavior of Mg0.5Zn0.2Ge alloy upon extrusion speed was affected by the extremely low solid solubility of Ge in Mg and the existence of highly stable Mg_2Ge phases in the alloy.

The different bulk compositions of the three alloys presented different windows of alternation of corrosion resistance by microstructural refinement due to extrusion process. The corrosion resistance of Mg0.5Zn0.2Ge and Mg4Zn0.2Sn alloys was obviously improved by extrusion while that of Mg0.5Zn0.2Ca alloys did not change compared to that of the as-cast condition. Since no big changes of the microstructures (distribution, size and volume fraction of intermetallic particles) are introduced by different extrusion speeds, the corrosion resistance of the three alloys was independent from the extrusion speed.

After extrusion, the corrosion performance of Mg0.5Zn0.2Ca alloy did not change, showing always uniform corrosion. In comparison, the active localized dissolution of as-cast Mg0.5Zn0.2Ge alloy was altered to uniform corrosion after extrusion due to the refined microstructure and the increased participation of Zn and Ge in the outer part of the corrosion product layer. For Mg4Zn0.2Sn alloy, both extruded and as-cast alloys suffered from localized corrosion induced by micro-galvanic effect, despite the greatly decreased micro-galvanic corrosion intensity owing to the substantially refined second phases after extrusion.

The corrosion resistance of the optimized alloys decreased in an order of Mg0.5Zn0.2Ge > Mg0.5Zn0.2Ca > Mg4Zn0.2Sn after short-term exposure to corrosive environment. The homogeneous microstructure and Zn-participated protective corrosion product layer contributed to the good corrosion resistance of extruded Mg0.5Zn0.2Ca and Mg0.5Zn0.2Ge alloys. While a heterogeneous microstructure, obvious existence of Fe-Mn/Mg_2Si impurity particles and poor protective ability of the surface film were responsible for the poor corrosion resistance of extruded Mg4Zn0.2Sn alloy. However, Mg0.5Zn0.2Ge alloy exhibited lower long-term corrosion resistance than Mg0.5Zn0.2Ca alloy, resulting from the higher content of nobler second phase in the alloy.

NaCl solutions at concentration of 0.9 *wt.*% and 0.5 *wt.*% did not affect the corrosion mechanism of the optimized alloys. Similar corrosion morphologies and corrosion products ($MgO/Mg(OH)_2$) were formed. However, extruded Mg0.5Zn0.2Ge and Mg4Zn0.2Sn alloys showed slightly lower corrosion rates in 0.5 *wt.*% NaCl solution due to the lower concentration of aggressive Cl^- ions. In comparison, no clear difference was detected for the corrosion performance of extruded Mg0.5Zn0.2Ca alloy in NaCl solutions with different concentration. When the 0.5 *wt.*% NaCl solution was prepared with artificial tap water, an additional layer of flower-like $CaCO_3$ was formed on the top of the primary $MgO/Mg(OH)_2$ layer due to the existence of Ca^{2+} and HCO_3^-, which considerably enhanced the corrosion resistance of the optimized alloys. Especially, Mg4Zn0.2Sn alloy changed from active localized corrosion to uniform corrosion when the solution was prepared with artificial tap water instead of deionized water. This indicates the possible overestimation of the corrosion rates of Mg alloys with the typical lab practice of using deionized water for corrosive electrolyte in comparison to the actual service conditions where different ions including Ca^{2+} and HCO_3^- are present.

The different microstructures, especially the texture, results in the higher tensile strength, lower elongation to fracture and higher mechanical anisotropy of extruded Mg0.5Zn0.2Ge and Mg4Zn0.2Sn alloys compared to those of Mg0.5Zn0.2Ca alloy. The tensile properties of these three alloys deteriorated with prolonged exposure in salt spray but showed different variation tendency, which was closely related to the corrosion resistance of the alloys.

Compared with the fatigue behavior in air, the fatigue lives and fatigue limits of the optimized alloys decreased in corrosive electrolytes. However, less reduction was noticed in artificial tap water based NaCl solution. The fatigue resistance of Mg0.5Zn0.2Ge alloy showed the lowest sensitivity to corrosive electrolyte, while that of Mg4Zn0.2Sn alloy displayed the highest one. Moreover, the S-N curve of Mg4Zn0.2Sn alloy exhibited obviously scattered characteristic. The different corrosion fatigue behavior of the three alloys was also closely related to the corrosion behavior of the alloys.

With a load of 70 % that of the yield strength, Mg0.5Zn0.2Ca and Mg4Zn0.2Sn alloys were resistant to stress corrosion cracking in deionized water, artificial tap water and NaCl solutions prepared with these two kinds of water. In contrast, Mg0.5Zn0.2Ge alloy showed obvious susceptibility to stress corrosion cracking in all corrosive electrolytes. Especially, the alloy completely failed in deionized water. The difference may come from the different mechanical stability of the surface films at different applied stress and the different microstructures of the alloys.

In conclusion, the most promising alloy is the Mg0.5Zn0.2Ca alloy, which is almost independent from the processing, possesses good long-term stability in various surroundings and exhibits relatively uniform degradation of mechanical integrity and good resistance to corrosion fatigue and stress corrosion cracking.

The results clearly revealed the alloying-processing-microstructure-properties relationship. More importantly, the corrosion performance-mechanical integrity, corrosion performance-corrosion fatigue and corrosion performance-susceptibility to stress corrosion cracking interactions can be noted. It highlights the importance of balancing the overall properties of Mg alloys when optimizing alloy compositions and the significance of selecting proper alloys by combining the overall properties with the actual service environment in practical applications instead of only focusing on an individual property of the alloy.

References

[1] Z. Zeng, N. Stanford, C.H.J. Davies, et al., Magnesium extrusion alloys: a review of developments and prospects, *International Materials Reviews,* 64 **(2019)** 27-62.

[2] K. Gusieva, C. Davies, J. Scully, et al., Corrosion of magnesium alloys: the role of alloying, *International Materials Reviews,* 60 **(2015)** 169-194.

[3] Y. Zhang, P. Gore, W. Rong, et al., Quasi-in-situ STEM-EDS insight into the role of Ag in the corrosion behaviour of Mg-Gd-Zr alloys, *Corrosion Science,* 136 **(2018)** 106-118.

[4] X. Gu, Y. Zheng, S. Zhong, et al., Corrosion of, and cellular responses to Mg–Zn–Ca bulk metallic glasses, *Biomaterials,* 31 **(2010)** 1093-1103.

[5] K. Yu, L. Chen, J. Zhao, et al., In vitro corrosion behavior and in vivo biodegradation of biomedical β-Ca3 (PO4) 2/Mg–Zn composites, *Acta biomaterialia,* 8 **(2012)** 2845-2855.

[6] X. Gu, N. Li, Y. Zheng, et al., In vitro degradation performance and biological response of a Mg–Zn–Zr alloy, *Materials Science and Engineering: B,* 176 **(2011)** 1778-1784.

[7] T. Itoi, T. Suzuki, Y. Kawamura, et al., Microstructure and mechanical properties of Mg-Zn-Y rolled sheet with a Mg12ZnY phase, *Materials Transactions,* **(2010)** 1008091140-1008091140.

[8] Y. Sun, B. Zhang, Y. Wang, et al., Preparation and characterization of a new biomedical Mg–Zn–Ca alloy, *Materials & design,* 34 **(2012)** 58-64.

[9] S. Jafari, S.E. Harandi, R.S. Raman, A review of stress-corrosion cracking and corrosion fatigue of magnesium alloys for biodegradable implant applications, *JOM,* 67 **(2015)** 1143-1153.

[10] X. Gao, J.F. Nie, Characterization of strengthening precipitate phases in a Mg–Zn alloy, *Scripta Materialia,* 56 **(2007)** 645-648.

[11] L. Wei, G. Dunlop, H. Westengen, Precipitation hardening of Mg-Zn and Mg-Zn-RE alloys, *Metallurgical and Materials Transactions A,* 26 **(1995)** 1705-1716.

[12] M.C. Zhao, M. Liu, G.-L. Song, et al., Influence of Microstructure on Corrosion of As‐cast ZE41, *Advanced Engineering Materials,* 10 **(2008)** 104-111.

[13] G. Ben-Hamu, D. Eliezer, K. Shin, The role of Mg2Si on the corrosion behavior of wrought Mg–Zn–Mn alloy, *Intermetallics,* 16 **(2008)** 860-867.

[14] F. Rosalbino, S. De Negri, A. Saccone, et al., Bio-corrosion characterization of Mg–Zn–X (X= Ca, Mn, Si) alloys for biomedical applications, *Journal of Materials Science: Materials in Medicine,* 21 **(2010)** 1091-1098.

[15] P. Yin, N.F. Li, T. Lei, et al., Effects of Ca on microstructure, mechanical and corrosion properties and biocompatibility of Mg–Zn–Ca alloys, *Journal of Materials Science: Materials in Medicine,* 24 **(2013)** 1365-1373.

[16] J.Y. Lee, D.H. Kim, H.K. Lim, et al., Effects of Zn/Y ratio on microstructure and mechanical properties of Mg-Zn-Y alloys, *Materials Letters,* 59 **(2005)** 3801-3805.

[17] C. Li, D. Xu, Z. Zeng, et al., Effect of volume fraction of LPSO phases on corrosion and mechanical properties of Mg-Zn-Y alloys, *Materials & design,* 121 **(2017)** 430-441.

[18] Y. Kawamura, K. Hayashi, A. Inoue, et al., Rapidly solidified powder metallurgy Mg97Zn1Y2Alloys with excellent tensile yield strength above 600 MPa, *Materials Transactions,* 42 **(2001)** 1172-1176.

[19] R. Song, D.-B. Liu, Y.-C. Liu, et al., Effect of corrosion on mechanical behaviors of Mg-Zn-Zr alloy in simulated body fluid, *Frontiers of Materials Science,* 8 **(2014)** 264-270.

[20] B. Zhang, Y. Wang, L. Geng, Research on Mg-Zn-Ca alloy as degradable biomaterial, *Biomaterials-Physics and Chemistry,* **(2011)** 183-204.

[21] E. Koç, M.B. Kannan, M. Ünal, et al., Influence of zinc on the microstructure, mechanical properties and in vitro corrosion behavior of magnesium–zinc binary alloys, *Journal of Alloys and Compounds,* 648 **(2015)** 291-296.

[22] J. Hofstetter, M. Becker, E. Martinelli, et al., High-strength low-alloy (HSLA) Mg–Zn–Ca alloys with excellent biodegradation performance, *JOM,* 66 **(2014)** 566-572.

[23] J. Hofstetter, S. Rüedi, I. Baumgartner, et al., Processing and microstructure–property relations of high-strength low-alloy (HSLA) Mg–Zn–Ca alloys, *Acta Materialia,* 98 **(2015)** 423-432.

[24] P. Jiang, C. Blawert, M.L. Zheludkevich, The Corrosion Performance and Mechanical Properties of Mg-Zn Based Alloys—A Review, *Corrosion and Materials Degradation,* 1 **(2020)** 7.

[25] R. Buzolin, M. Mohedano, C. Mendis, et al., As cast microstructures on the mechanical and corrosion behaviour of ZK40 modified with Gd and Nd additions, *Materials Science and Engineering: A,* 682 **(2017)** 238-247.

[26] Stadtwerke Geesthacht, 2018 (Accessed 23 April 2018). https://www.stadtwerke-geesthacht.de/wasser.

[27] B. Zhang, Y. Hou, X. Wang, et al., Mechanical properties, degradation performance and cytotoxicity of Mg–Zn–Ca biomedical alloys with different compositions, *Materials Science and Engineering: C,* 31 **(2011)** 1667-1673.

[28] H. Okamoto, Comment on Mg-Zn (magnesium-zinc), *Journal of phase equilibria,* 15 **(1994)** 129-130.

[29] F. Witte, N. Hort, C. Vogt, et al., Degradable biomaterials based on magnesium corrosion, *Current opinion in solid state and materials science,* 12 **(2008)** 63-72.

[30] H. Somekawa, Y. Osawa, T. Mukai, Effect of solid-solution strengthening on fracture toughness in extruded Mg–Zn alloys, *Scripta Materialia,* 55 **(2006)** 593-596.

[31] J. Zhang, Z. Guo, F. Pan, et al., Effect of composition on the microstructure and mechanical properties of Mg–Zn–Al alloys, *Materials Science and Engineering: A,* 456 **(2007)** 43-51.

[32] L. Wei, G. Dunlop, The solidification behaviour of Mg-Al-rare earth alloys, *Journal of Alloys and Compounds,* 232 **(1996)** 264-268.

[33] S. Wasiur-Rahman, M. Medraj, Critical assessment and thermodynamic modeling of the binary Mg–Zn, Ca–Zn and ternary Mg–Ca–Zn systems, *Intermetallics,* 17 **(2009)** 847-864.

[34] M. Aljarrah, M. Medraj, Thermodynamic modelling of the Mg–Ca, Mg–Sr, Ca–Sr and Mg–Ca–Sr systems using the modified quasichemical model, *Calphad,* 32 **(2008)** 240-251.

[35] Z. Li, X. Gu, S. Lou, et al., The development of binary Mg–Ca alloys for use as biodegradable materials within bone, *Biomaterials,* 29 **(2008)** 1329-1344.

[36] Y. Chino, X. Huang, K. Suzuki, et al., Influence of Zn concentration on stretch formability at room temperature of Mg–Zn–Ce alloy, *Materials Science and Engineering: A,* 528 **(2010)** 566-572.

[37] C.-n. Chiu, J. Gröbner, A. Kozlov, et al., Experimental study and thermodynamic assessment of ternary Mg–Zn–Ce phase relations focused on Mg-rich alloys, *Intermetallics,* 18 **(2010)** 399-405.

[38] L. Jiang, J. Jonas, R. Mishra, Effect of dynamic strain aging on the appearance of the rare earth texture component in magnesium alloys, *Materials Science and Engineering: A,* 528 **(2011)** 6596-6605.

[39] H. Liu, G. Qi, Y. Ma, et al., Microstructure and mechanical property of Mg–2.0 Ga alloys, *Materials Science and Engineering: A,* 526 **(2009)** 7-10.

[40] J. Kubásek, D. Vojtěch, J. Lipov, et al., Structure, mechanical properties, corrosion behavior and cytotoxicity of biodegradable Mg–X (X= Sn, Ga, In) alloys, *Materials Science and Engineering: C,* 33 **(2013)** 2421-2432.

[41] Y. Feng, R. Wang, H. Liu, et al., Thermodynamic reassessment of the magnesium–gallium system, *Journal of Alloys and Compounds,* 486 **(2009)** 581-585.

[42] D. Wu, L. Ouyang, C. Wu, et al., Phase transition and hydrogen storage properties of Mg–Ga alloy, *Journal of Alloys and Compounds,* 642 **(2015)** 180-184.

[43] A. Srinivasan, Y. Huang, C. Mendis, et al., Investigations on microstructures, mechanical and corrosion properties of Mg–Gd–Zn alloys, *Materials Science and Engineering: A,* 595 **(2014)** 224-234.

[44] A. Nayeb-Hashemi, J. Clark, R. Olesinski, et al., The Ge-Mg (Germanium-Magnesium) System, *Journal of phase equilibria,* 5 **(1984)** 359-365.

[45] F. Elsayed, T. Sasaki, C. Mendis, et al., Compositional optimization of Mg–Sn–Al alloys for higher age hardening response, *Materials Science and Engineering: A,* 566 **(2013)** 22-29.

[46] H. Liu, Y. Chen, Y. Tang, et al., The microstructure, tensile properties, and creep behavior of as-cast Mg–(1–10)% Sn alloys, *Journal of Alloys and Compounds,* 440 **(2007)** 122-126.

[47] E. Zhang, W. He, H. Du, et al., Microstructure, mechanical properties and corrosion properties of Mg–Zn–Y alloys with low Zn content, *Materials Science and Engineering: A,* 488 **(2008)** 102-111.

[48] R.H. de Tendler, M. Soriano, M. Pepe, et al., Calculation of metastable free-energy diagrams and glass formation in the Mg–Cu–Y alloy and its boundary binaries using the Miedema model, *Intermetallics,* 14 **(2006)** 297-307.

[49] P.-R. Cha, H.-S. Han, G.-F. Yang, et al., Biodegradability engineering of biodegradable Mg alloys: Tailoring the electrochemical properties and microstructure of constituent phases, *Scientific reports,* 3 **(2013)** 2367.

[50] G. Levi, S. Avraham, A. Zilberov, et al., Solidification, solution treatment and age hardening of a Mg–1.6 wt.% Ca–3.2 wt.% Zn alloy, *Acta Materialia,* 54 **(2006)** 523-530.

[51] R. Liu, M. Hurley, A. Kvryan, et al., Controlling the corrosion and cathodic activation of magnesium via microalloying additions of Ge, *Scientific reports,* 6 **(2016)** 28747.

[52] B. Kim, K. Park, H. Kimura, et al., Influence of Addition of Ge on the Microstructure and Corrosion Properties of Magnesium, *Materials Transactions,* 53 **(2012)** 240-243.

[53] R. Liu, J. Scully, G. Williams, et al., Reducing the corrosion rate of magnesium via microalloying additions of group 14 and 15 elements, *Electrochimica Acta,* 260 **(2018)** 184-195.

[54] C.L. Mendis, C.J. Bettles, M. Gibson, et al., An enhanced age hardening response in Mg–Sn based alloys containing Zn, *Materials Science and Engineering: A,* 435 **(2006)** 163-171.

[55] F. Meng, J. Wang, L. Liu, et al., Thermodynamic modeling of the Mg–Sn–Zn ternary system, *Journal of Alloys and Compounds,* 508 **(2010)** 570-581.

[56] N. Mingolo, E. Nassif, B. Arcondo, et al., Two competitive effects in the glass-forming ability of Mg-based alloys, *Journal of non-crystalline solids,* 113 **(1989)** 161-166.

[57] G. Shao, V. Varsani, Z. Fan, Thermodynamic modelling of the Y–Zn and Mg–Zn–Y systems, *Calphad,* 30 **(2006)** 286-295.

[58] Z. Shi, A. Atrens, An innovative specimen configuration for the study of Mg corrosion, *Corrosion Science,* 53 **(2011)** 226-246.

[59] Z. Shi, M. Liu, A. Atrens, Measurement of the corrosion rate of magnesium alloys using Tafel extrapolation, *Corrosion Science,* 52 **(2010)** 579-588.

[60] M. Esmaily, J. Svensson, S. Fajardo, et al., Fundamentals and advances in magnesium alloy corrosion, *Progress in Materials Science,* 89 **(2017)** 92-193.

[61] S. Cai, T. Lei, N. Li, et al., Effects of Zn on microstructure, mechanical properties and corrosion behavior of Mg–Zn alloys, *Materials Science and Engineering: C,* 32 **(2012)** 2570-2577.

[62] X.-B. Liu, D.-Y. Shan, Y.-W. Song, et al., Effects of heat treatment on corrosion behaviors of Mg-3Zn magnesium alloy, *Transactions of Nonferrous Metals Society of China,* 20 **(2010)** 1345-1350.

[63] S. Zhang, X. Zhang, C. Zhao, et al., Research on an Mg–Zn alloy as a degradable biomaterial, *Acta biomaterialia,* 6 **(2010)** 626-640.

[64] M. Hurley, C. Efaw, P. Davis, et al., Volta potentials measured by scanning Kelvin probe force microscopy as relevant to corrosion of magnesium alloys, *Corrosion,* 71 **(2014)** 160-170.

[65] H. Asgharzadeh, E. Yoon, H. Chae, et al., Microstructure and mechanical properties of a Mg–Zn–Y alloy produced by a powder metallurgy route, *Journal of Alloys and Compounds,* 586 **(2014)** S95-S100.

[66] N. Stanford, D. Atwell, A. Beer, et al., Effect of microalloying with rare-earth elements on the texture of extruded magnesium-based alloys, *Scripta Materialia,* 59 **(2008)** 772-775.

[67] B. Zhang, Y. Wang, L. Geng, et al., Effects of calcium on texture and mechanical properties of hot-extruded Mg–Zn–Ca alloys, *Materials Science and Engineering: A,* 539 **(2012)** 56-60.

[68] J. Bohlen, S. Yi, D. Letzig, et al., Effect of rare earth elements on the microstructure and texture development in magnesium–manganese alloys during extrusion, *Materials Science and Engineering: A,* 527 **(2010)** 7092-7098.

[69] M.-C. Zhao, M. Liu, G.-L. Song, et al., Influence of pH and chloride ion concentration on the corrosion of Mg alloy ZE41, *Corrosion Science,* 50 **(2008)** 3168-3178.

[70] C. Taltavull, Z. Shi, B. Torres, et al., Influence of the chloride ion concentration on the corrosion of high-purity Mg, ZE41 and AZ91 in buffered Hank's solution, *Journal of Materials Science: Materials in Medicine,* 25 **(2014)** 329-345.

Reference

[71] A. Atrens, M. Liu, N.I.Z. Abidin, Corrosion mechanism applicable to biodegradable magnesium implants, *Materials Science and Engineering: B,* 176 **(2011)** 1609-1636.

[72] S. Pawar, X. Zhou, G. Thompson, et al., The role of intermetallics on the corrosion initiation of twin roll cast AZ31 Mg alloy, *Journal of The Electrochemical Society,* 162 **(2015)** C442-C448.

[73] R. Takei, H. Imai, J. Umeda, et al., Relationship between surface potential difference and galvanic corrosion of magnesium alloy using SKPFM, *Transactions of JWRI,* 39 **(2010)** 75-80.

[74] K.A. Yasakau, D. Höche, S.L. Lamaka, et al., Kelvin microprobe analytics on iron-enriched corroded magnesium surface, *Corrosion,* 73 **(2017)** 583-595.

[75] L. Yang, X. Zhou, S.-M. Liang, et al., Effect of traces of silicon on the formation of Fe-rich particles in pure magnesium and the corrosion susceptibility of magnesium, *Journal of Alloys and Compounds,* 619 **(2015)** 396-400.

[76] S. Cramer, B. Covino, ASM Handbook Vol. 13 A Corrosion: Fundamentals, Testing, and Protection, *Materials Park, OH: ASM International, 2003. 1135,* **(2003)**.

[77] M. Jamesh, S. Kumar, T.S. Narayanan, Corrosion behavior of commercially pure Mg and ZM21 Mg alloy in Ringer's solution–Long term evaluation by EIS, *Corrosion Science,* 53 **(2011)** 645-654.

[78] J.I. Goldstein, D.E. Newbury, J.R. Michael, et al., Scanning electron microscopy and X-ray microanalysis, Springer**(2017)**.

[79] C. Li, D. Xu, X.-B. Chen, et al., Composition and microstructure dependent corrosion behaviour of Mg-Li alloys, *Electrochimica Acta,* 260 **(2018)** 55-64.

[80] C. Ke, Y. Wu, Y. Qiu, et al., Influence of surface chemistry on the formation of crystalline hydroxide coatings on Mg alloys in liquid water and steam systems, *Corrosion Science,* 113 **(2016)** 145-159.

[81] J. Chang, X. Guo, S. He, et al., Investigation of the corrosion for Mg–xGd–3Y–0.4 Zr (x= 6, 8, 10, 12 wt%) alloys in a peak-aged condition, *Corrosion Science,* 50 **(2008)** 166-177.

[82] J.H. Nordlien, K. Nisancioglu, S. Ono, et al., Morphology and structure of water‐formed oxides on ternary MgAl alloys, *Journal of The Electrochemical Society,* 144 **(1997)** 461-466.

[83] H. Yao, Y. Li, A. Wee, et al., Correlation between the corrosion behavior and corrosion films formed on the surfaces of Mg82− xNi18Ndx (x= 0, 5, 15) amorphous alloys, *Applied surface science,* 173 **(2001)** 54-61.

[84] N. Winzer, A. Atrens, G. Song, et al., A critical review of the stress corrosion cracking (SCC) of magnesium alloys, *Advanced Engineering Materials,* 7 **(2005)** 659-693.

[85] T.B. Massalski, Binary alloy phase diagrams, *ASM international,* 3 **(1992)** 2874.

[86] J. Kubasek, D. Vojtech, I. Pospisilova, Structural and corrosion characterization of biodegradable Mg-Zn alloy castings, *Kovove Mater,* 50 **(2012)** 415-424.

[87] C. Liu, H. Yang, P. Wan, et al., Study on biodegradation of the second phase Mg17Al12 in Mg–Al–Zn Alloys: In vitro experiment and thermodynamic calculation, *Materials Science and Engineering: C,* 35 **(2014)** 1-7.

[88] T. Yan, L. Tan, D. Xiong, et al., Fluoride treatment and in vitro corrosion behavior of an AZ31B magnesium alloy, *Materials Science and Engineering: C,* 30 **(2010)** 740-748.

[89] Y. Song, D. Shan, R. Chen, et al., Biodegradable behaviors of AZ31 magnesium alloy in simulated body fluid, *Materials Science and Engineering: C,* 29 **(2009)** 1039-1045.

[90] N. Li, Y. Zheng, Novel magnesium alloys developed for biomedical application: a review, *Journal of Materials Science & Technology,* 29 **(2013)** 489-502.

[91] J.P. Hadorn, K. Hantzsche, S. Yi, et al., Role of solute in the texture modification during hot deformation of Mg-rare earth alloys, *Metallurgical and Materials Transactions A,* 43 **(2012)** 1347-1362.

[92] K. Hantzsche, J. Bohlen, J. Wendt, et al., Effect of rare earth additions on microstructure and texture development of magnesium alloy sheets, *Scripta Materialia,* 63 **(2010)** 725-730.

[93] M. Bauser, K. Siegert, Extrusion, ASM international**(2006)**.

[94] I. Kim, D. Bae, D.H. Kim, Precipitates in a Mg–Zn–Y alloy reinforced by an icosahedral quasicrystalline phase, *Materials Science and Engineering: A,* 359 **(2003)** 313-318.

[95] G. Yuan, Y. Liu, W. Ding, et al., Effects of extrusion on the microstructure and mechanical properties of Mg–Zn–Gd alloy reinforced with quasicrystalline particles, *Materials Science and Engineering: A,* 474 **(2008)** 348-354.

[96] K. Ralston, N. Birbilis, C. Davies, Revealing the relationship between grain size and corrosion rate of metals, *Scripta Materialia,* 63 **(2010)** 1201-1204.

[97] A. Südholz, N. Kirkland, R. Buchheit, et al., Electrochemical properties of intermetallic phases and common impurity elements in magnesium alloys, *Electrochemical and Solid-State Letters,* 14 **(2011)** C5-C7.

[98] D. Zander, N.A. Zumdick, Influence of Ca and Zn on the microstructure and corrosion of biodegradable Mg–Ca–Zn alloys, *Corrosion Science,* 93 **(2015)** 222-233.

[99] G. Ben-Hamu, D. Eliezer, K. Shin, The role of Si and Ca on new wrought Mg–Zn–Mn based alloy, *Materials Science and Engineering: A,* 447 **(2007)** 35-43.

[100] F. Andreatta, I. Apachitei, A.A. Kodentsov, et al., Volta potential of second phase particles in extruded AZ80 magnesium alloy, *Electrochimica Acta,* 51 **(2006)** 3551-3557.

[101] D.S. Gandel, M.A. Easton, M.A. Gibson, et al., CALPHAD simulation of the Mg–(Mn, Zr)–Fe system and experimental comparison with as-cast alloy microstructures as relevant to impurity driven corrosion of Mg-alloys, *Materials Chemistry and Physics,* 143 **(2014)** 1082-1091.

[102] G.L. Song, A. Atrens, Corrosion mechanisms of magnesium alloys, *Advanced Engineering Materials,* 1 **(1999)** 11-33.

[103] H. Robinson, P. George, Effect of alloying and impurity elements in magnesium alloy cast anodes, *Corrosion,* 10 **(1954)** 182-188.

[104] H. Matsubara, Y. Ichige, K. Fujita, et al., Effect of impurity Fe on corrosion behavior of AM50 and AM60 magnesium alloys, *Corrosion Science,* 66 **(2013)** 203-210.

[105] D. Höche, S.V. Lamaka, B. Vaghefinazari, et al., Performance boost for primary magnesium cells using iron complexing agents as electrolyte additives, *Scientific reports,* 8 **(2018)** 7578.

[106] K.A. Unocic, H.H. Elsentriecy, M.P. Brady, et al., Transmission electron microscopy study of aqueous film formation and evolution on magnesium alloys, *Journal of The Electrochemical Society,* 161 **(2014)** C302-C311.

[107] M. Brady, G. Rother, L. Anovitz, et al., Film breakdown and nano-porous Mg (OH) 2 formation from corrosion of magnesium alloys in salt solutions, *Journal of The Electrochemical Society,* 162 **(2015)** C140-C149.

[108] M. Cristóbal, D. Gesto, P. Minino, et al., An XPS analysis of the oxide surface layers formed on a friction stir processed magnesium alloy, *Surface and Interface Analysis,* 44 **(2012)** 1030-1034.

[109] J. Yang, C. Yim, B. You, Effects of solute Zn on corrosion film of Mg–Sn–Zn alloy formed in NaCl solution, *Journal of The Electrochemical Society,* 163 **(2016)** C839-C844.

[110] R. Phillips, J. Kish, Nature of surface film on matrix phase of Mg alloy AZ80 formed in water, *Corrosion,* 69 **(2013)** 813-820.

[111] G. Song, A. Atrens, Understanding magnesium corrosion—a framework for improved alloy performance, *Advanced Engineering Materials,* 5 **(2003)** 837-858.

[112] J. Liao, M. Hotta, S.-i. Motoda, et al., Atmospheric corrosion of two field-exposed AZ31B magnesium alloys with different grain size, *Corrosion Science,* 71 **(2013)** 53-61.

[113] L. Wang, T. Shinohara, B.-P. Zhang, Corrosion behavior of AZ31 magnesium alloy in dilute sodium chloride solutions, *Zairyo-to-Kankyo,* 58 **(2009)** 105-110.

[114] Q. Qu, J. Ma, L. Wang, et al., Corrosion behaviour of AZ31B magnesium alloy in NaCl solutions saturated with CO2, *Corrosion Science,* 53 **(2011)** 1186-1193.

[115] A. Pardo, M. Merino, A.E. Coy, et al., Corrosion behaviour of magnesium/aluminium alloys in 3.5 wt.% NaCl, *Corrosion Science,* 50 **(2008)** 823-834.

[116] R. Xin, B. Li, L. Li, et al., Influence of texture on corrosion rate of AZ31 Mg alloy in 3.5 wt.% NaCl, *Materials & design,* 32 **(2011)** 4548-4552.

[117] L. Wang, B.-P. Zhang, T. Shinohara, Corrosion behavior of AZ91 magnesium alloy in dilute NaCl solutions, *Materials & design,* 31 **(2010)** 857-863.

[118] J. Bischoff, W. Fyfe, Catalysis, inhibition, and the calcite-aragonite problem;[Part] 1, The aragonite-calcite transformation, *American Journal of Science,* 266 **(1968)** 65-79.

[119] F.C. Meldrum, S.T. Hyde, Morphological influence of magnesium and organic additives on the precipitation of calcite, *Journal of Crystal Growth,* 231 **(2001)** 544-558.

[120] H. Kalb, A. Rzany, B. Hensel, Impact of microgalvanic corrosion on the degradation morphology of WE43 and pure magnesium under exposure to simulated body fluid, *Corrosion Science,* 57 **(2012)** 122-130.

[121] A. Glasner, D. Weiss, The crystallization of calcite from aqueous solutions and the role of zinc and magnesium ions—I. Precipitation of calcite in the presence of Zn2+ ions, *Journal of Inorganic and Nuclear Chemistry,* 42 **(1980)** 655-663.

[122] E. Elzinga, R. Reeder, X-ray absorption spectroscopy study of Cu2+ and Zn2+ adsorption complexes at the calcite surface: Implications for site-specific metal incorporation preferences during calcite crystal growth, *Geochimica et Cosmochimica Acta,* 66 **(2002)** 3943-3954.

[123] P. Jiang, C. Blawert, R. Hou, et al., Microstructural influence on corrosion behavior of MgZnGe alloy in NaCl solution, *Journal of Alloys and Compounds,* 783 **(2019)** 179-192.

[124] R. Liu, Z. Zeng, J. Scully, et al., Simultaneously improving the corrosion resistance and strength of magnesium via low levels of Zn and Ge additions, *Corrosion Science,* 140 **(2018)** 18-29.

[125] M. Deng, D. Höche, S.V. Lamaka, et al., Revealing the impact of second phase morphology on discharge properties of binary Mg-Ca anodes for primary Mg-air batteries, *Corrosion Science,* 153 **(2019)** 225-235.

[126] S. Yi, H.-G. Brokmeier, J. Bohlen, et al., Neutron diffraction study on the texture development during extrusion of magnesium alloy AZ31, *Physica B: Condensed Matter,* 350 **(2004)** E507-E509.

[127] J. Bohlen, M.R. Nürnberg, J.W. Senn, et al., The texture and anisotropy of magnesium–zinc–rare earth alloy sheets, *Acta Materialia,* 55 **(2007)** 2101-2112.

[128] M. Barnett, Twinning and the ductility of magnesium alloys: Part I:"Tension" twins, *Materials Science and Engineering: A,* 464 **(2007)** 1-7.

[129] N. Petch, The cleavage strength of polycrystals, *Journal of the Iron and Steel Institute,* 174 **(1953)** 25-28.

[130] E. Hall, The deformation and ageing of mild steel: III discussion of results, *Proceedings of the Physical Society. Section B,* 64 **(1951)** 747.

[131] M.M. Avedesian, H. Baker, ASM specialty handbook: magnesium and magnesium alloys, ASM international**(1999)**.

[132] W. Jiang, J. Wang, W. Zhao, et al., Effect of Sn addition on the mechanical properties and bio-corrosion behavior of cytocompatible Mg–4Zn based alloys, *Journal of Magnesium and Alloys,* 7 **(2019)** 15-26.

[133] R.S. Raman, S. Jafari, S.E. Harandi, Corrosion fatigue fracture of magnesium alloys in bioimplant applications: A review, *Engineering fracture mechanics,* 137 **(2015)** 97-108.

[134] C. Potzies, K.U. Kainer, Fatigue of magnesium alloys, *Advanced Engineering Materials,* 6 **(2004)** 281-289.

[135] F. Yang, F. Lv, X. Yang, et al., Enhanced very high cycle fatigue performance of extruded Mg–12Gd–3Y–0.5 Zr magnesium alloy, *Materials Science and Engineering: A,* 528 **(2011)** 2231-2238.

[136] D. Bian, W. Zhou, Y. Liu, et al., Fatigue behaviors of HP-Mg, Mg–Ca and Mg–Zn–Ca biodegradable metals in air and simulated body fluid, *Acta biomaterialia,* 41 **(2016)** 351-360.

[137] S. Yin, F. Yang, X. Yang, et al., The role of twinning–detwinning on fatigue fracture morphology of Mg–3% Al–1% Zn alloy, *Materials Science and Engineering: A,* 494 **(2008)** 397-400.

[138] M. Horstemeyer, N. Yang, K. Gall, et al., High cycle fatigue mechanisms in a cast AM60B magnesium alloy, *Fatigue & Fracture of Engineering Materials & Structures,* 25 **(2002)** 1045-1056.

[139] S.E. Harandi, R.S. Raman, Corrosion fatigue of a magnesium alloy under appropriate human physiological conditions for bio-implant applications, *Engineering fracture mechanics,* 186 **(2017)** 134-142.

[140] D. Hoeppner, Model for prediction of fatigue lives based upon a pitting corrosion fatigue process, Fatigue Mechanisms, ASTM International**(1979)**.

[141] Y. Uematsu, K. Tokaji, T. Ohashi, Corrosion fatigue behavior of extruded AZ80, AZ61, and AM60 magnesium alloys in distilled water, *Strength of Materials,* 40 **(2008)** 130-133.

[142] Z. Nan, S. Ishihara, T. Goshima, Corrosion fatigue behavior of extruded magnesium alloy AZ31 in sodium chloride solution, *International Journal of Fatigue,* 30 **(2008)** 1181-1188.

[143] Z. Sajuri, Y. Miyashita, Y. Mutoh, Effects of humidity and temperature on the fatigue behaviour of an extruded AZ61 magnesium alloy, *Fatigue & Fracture of Engineering Materials & Structures,* 28 **(2005)** 373-379.

[144] R.C. Zeng, E.H. Han, W. Ke, Fatigue and corrosion fatigue of magnesium alloys, Materials Science Forum, Trans Tech Publ, **(2005)**, pp. 721-724.

[145] A. Atrens, N. Winzer, W. Dietzel, Stress corrosion cracking of magnesium alloys, *Advanced Engineering Materials,* 13 **(2011)** 11-18.

[146] P.B. Srinivasan, C. Blawert, W. Dietzel, Effect of plasma electrolytic oxidation treatment on the corrosion and stress corrosion cracking behaviour of AM50 magnesium alloy, *Materials Science and Engineering: A,* 494 **(2008)** 401-406.

[147] D.A. Jones, Principles and prevention of corrosion. 2, Prentice Hall**(1996)**.

[148] R.S. Raman, Evaluation of caustic embrittlement susceptibility of steels by slow strain rate testing, *Metallurgical and Materials Transactions A,* 36 **(2005)** 1817-1823.

[149] L. Choudhary, R.S. Raman, Magnesium alloys as body implants: fracture mechanism under dynamic and static loadings in a physiological environment, *Acta biomaterialia,* 8 **(2012)** 916-923.

[150] M.B. Kannan, W. Dietzel, C. Blawert, et al., Stress corrosion cracking of rare-earth containing magnesium alloys ZE41, QE22 and Elektron 21 (EV31A) compared with AZ80, *Materials Science and Engineering: A,* 480 **(2008)** 529-539.

Appendix

1. List of symbols and abbreviations

Ag	Silver
AgCl	Silver chloride
Al	Aluminum
ATW	Artificial tap water
at.%	Atomic percentage
BSE	Backscattering electron
C	Carbon
Ca	Calcium
$CaCl_2$	Calcium chloride
$CaCO_3$	Calcium Carbonate
C_{dl}	Capacitance of the double electrical layer
Ce	Cerium
C_f	Capacitance of the surface film
Cl	Chloride
CO_2	Carbon dioxide
CO_3^{2-}	Carbonate ion
CR	Corrosion rate
CrO_3	Chromium trioxide
Cu	Copper
CYS	Compressive yield strength
DIW	Deionized water
E_{bd}	Breakdown potential
E_{corr}	Corrosion potential
EDS	Energy dispersive X-ray spectroscopy
e.g.	*exempli gratia*
EIS	Electrochemical impedance spectroscopy
Fe	Iron
Ga	Gallium
Gd	Gadolinium
Ge	Germanium
H_2	Hydrogen
HCO_3^-	Bicarbonate ion
H_2O	Water
i_{corr}	Current density
K	Potassium
Mg	Magnesium
$MgCO_3$	Magnesium carbonate

MgO	Magnesium oxide
$Mg(OH)_2$	Magnesium hydroxide
$MgSO_4$	Magnesium sulfate
Mn	Manganese
NaCl	Sodium chloride
$NaHCO_3$	Sodium bicarbonate
$NaNO_3$	Sodium Nitrate
Ni	Nickel
O	Oxygen
O_2	Oxygen gas
OCP	Open circuit potential
OH^-	hydroxide ion
OM	Optical microscopy
OPS	Colloidal silica suspension
R_{ct}	Charge transfer resistance
RE	Rare-earth elements
R_f	Resistance of the surface film
R_s	Resistance of the solution
R_{sum}	Sum of surface film resistance and charge transfer resistance
S	Sulphur
SCC	Stress corrosion cracking
SE	Secondary electron
SEM	Scanning electron microscopy
Si	Silicon
SiC	Silicon carbide
SKPFM	Scanning kelvin probe force microscopy
Sn	Tin
S-N curves	Stress-life cycle curves
TYS	Tensile yield strength
UCS	Ultimate compressive strength
UTS	Ultimate tensile strength
***wt.*%**	Weight percentage
XRD	X-ray diffraction
Y	Yttrium
Zn	Zinc

2. Table (Cited reference numbers refer to the publication inserted in Chapter 2)

Table A1. Potentials or relative Volta potentials of some secondary phases in Mg-Zn based alloys summarized from published literature.

Secondary Phase	Alloy	Condition of Alloy	Testing Method	Potential or Relative Volta Potential	Condition of measurement	Details about the Instrument	Ref.
MgZn$_2$	Mg-Zn	Induction melting	Microcapillary electrochemical cell	-1.03 V (vs. SCE)	0.1 M NaCl	-	[77]
Mg$_{12}$ZnY	Mg3.1Zn7.6Y	As-cast	Scanning Kelvin probe force microscopy	250 mV	In air	Multimode 3D, Bruker Corporation	[88]
CaMgSi	Mg6Zn5Si0.8Ca	Extruded	Scanning Kelvin probe force microscopy	384.56 mV	In air	Nanoscope III Multimode AFM	[281]
Mg2Si				96.23 mV			
MgZn$_2$	Mg6Zn5Si0.8Ca	Extruded	Scanning Kelvin probe force microscopy	551.19 ± 77.85 mV	In air	Nanoscope III Multimode AFM	[282]
Mn$_5$Si$_3$				427.81 ± 147.88 mV			
CaMgSi				408.32 ± 26.35 mV			
Mg$_2$Si				96.23 ± 21.91 mV			
Grain boundary	ZE41	As-cast	Scanning Kelvin probe force microscopy	-80 ± 5 mV	In air	Nanoscope Dimension™ 3100 AFM	[123]
Mg$_7$Zn$_3$RE				100 ± 5 mV			
Zr-Zn-rich				180 ± 10 mV			
Mg$_7$Zn$_3$	Mg2Zn0.6Zr	As-cast	Scanning Kelvin probe force microscopy	120 mV	In air	Dimension Icon AFM	[283]
Mg(Zn, Zr)	Mg2Zn0.6Zr	Extrusion	Scanning Kelvin probe force microscopy	50mV	In air	Dimension Icon AFM	[283]
MgZn$_2$	Mg6Zn0.5Zr	Extrusion	Scanning Kelvin probe force microscopy	320 mV	In air	NT-MDT, Moscow	[284]
Zn$_2$Zr$_3$				230 mV			
CuMgZn	Mg6Zn0.5Zr1Cu	Extrusion	Scanning Kelvin probe force microscopy	680 mV	In air	NT-MDT, Moscow	[284]
MgZn$_2$				510 mV			
Zn$_2$Zr$_3$				370 mV			
Mg$_{75}$Zn$_{20}$Nd$_5$	Mg2Zn0.2MnxNd	As-cast	Scanning Kelvin probe force microscopy	250 mV	In air	MFP 3D Infinity AFM	[285]
Ca$_2$Mg$_6$Zn$_3$	Mg2Zn1Ca0.2Mn	As-cast	Scanning Kelvin probe force microscopy	60 mV	In air	MFP 3D Infinity AFM	[286]
Ca$_2$Mg$_6$Zn$_3$		T4		30 mV			
MgZn$_2$	Mg2Zn0.2MnxCa (x= 0.38; 0.76; 1.10)	As-cast	Scanning Kelvin probe force microscopy	96 mV*	In air	MFP 3D Infinity AFM	[287]

Mg-Zn	ZK40	As-cast	Scanning Kelvin probe force microscopy	50 mV	In air	Nanoscope IIIa Multimode microscope	[288]
Mg-Zn-Zr-Fe	Mg4Zn0.5Zr2Gd	As-cast	Scanning Kelvin probe force microscopy	430 mV	In air	Nanoscope IIIa Multimode microscope	[288]
$(MgZn)_3Gd_2$				170 mV			
Mg-Zn-Zr-Fe	Mg4Zn0.5Zr2Nd	As-cast	Scanning Kelvin probe force microscopy	140 mV	In air	Nanoscope IIIa Multimode microscope	
$Mg_{75}Zn_{20}Nd_5$				35 mV			

[*] The value was the highest potential compiled from the line-profile analysis of the secondary phase because no average value was afforded in the reference.

Table A2. Corrosion rates and mechanical properties (tested at room temperature) of Mg-Zn based alloys summarized from published researches.

Composition/wt.%	Condition	Electrolyte	Impurity Content / wt.%	Corrosion Rate / mm year^{-1}			Tensile Property			Ref.
				P_i	P_H	P_W	YS/MPa	UTS/MPa	Elongation/%	
Mg0.5Zn	As-cast	SBF, 37 ºC	0.003Fe; 0.0004Cu; 0.0005Ni; 0.004Mn; 0.002Al	3.1			75	112	18.4	[46]
Mg0.5Zn	As-cast	SBF, RT	0.004Fe; 0.004Cu; 0.001Ni	1.2	1		38	95	4.2	[50]
Mg0.5Zn	Backward-extrusion	SBF, RT		0.5	0.5		62	145	17.2	[50]
Mg0.8Zn	Extrusion						198	238	26.5	[26]
Mg1Zn	As-cast	SBF, 37 °C	0.004Fe; 0.0003Cu; 0.0004Ni; 0.003Mn; 0.003Al	2.8			80	128	16.1	[46]
Mg1Zn	As-cast	SBF, 37 °C	<0.00016Fe; <0.002Cu; <0.001Mn	0.5		2	61	188	13.8	[10]
Mg1Zn	As-cast	9 g/L NaCl	<0.004Fe; <0.004Cu; <0.004Ni; 0.03Mn; 0.02Al	0.9		1.3				[49]
Mg1Zn	As-cast		0.004Fe; 0.058Mn; 0.023Al; 0.031Si				20	102	1	[22]
Mg1Zn	As-cast	SBF, 37 °C	0.007Fe; 0.0295Cu; 0.013Mn; 0.023Al; 0.041Si			0.07				[42]
Mg1Zn	As-cast	SBF, RT	0.008Fe; 0.004Cu; 0.005Ni	4.1	1.1		43	99	6.1	[50]
Mg1Zn	As-cast	SBF, 37 °C		1.5	2					[45]
		Hank's, 37 °C		0.2	0.3					
Mg1Zn	T4	SBF, 37 °C				0.09				[42]

Mg1Zn	Backward-extrusion	SBF, RT		1.1	0.5		91	169	18.7	[50]
Mg1Zn	Extrusion	0.6 M NaCl				1.7				[61]
Mg1Zn	Hot-rolling	SBF, 37 °C		0.9	2.3					[45]
		Hank's, 37 °C		0.2	0.6					
Mg1Zn	Induction melting	In vivo				0.4				[157]
		EBSS, 37 °C				0.5				
		MEM, 37 °C				1				
		MEMp, 37 °C				1.7				
Mg1.25Zn	As-cast	SBF, 37 °C	0.008Fe; 0.043Mn; 0.022Al; 0.029Si	6.5		3.2				[41]
Mg1.5Zn	As-cast	SBF, RT	0.007Fe; 0.006Cu; 0.004Ni	8.5	1.4		51	109	5.9	[50]
Mg1.5Zn	Backward-extrusion	SBF, RT		1.3	0.5		101	190	17.2	[50]
Mg2Zn	As-cast	SBF, 37 °C	0.002Fe; 0.0005Cu; 0.0005Ni; 0.004Mn; 0.002Al	2.6			86	137	14.5	[46]
Mg2Zn	As-cast		0.007Fe; 0.03Mn; 0.033Al; 0.039Si				27	146	12.2	[22]
Mg2Zn	As-cast	SBF, RT	0.004Fe; 0.003Cu; 0.007Ni	9.7	1.3		65	121	5.3	[50]
Mg2Zn	Backward-extrusion	SBF, RT		1.4	0.6		111	198	15.7	[50]
Mg2Zn	Extrusion	0.6 M NaCl				3.4				[61]
Mg2Zn	Extrusion	3.5 wt.% NaCl		0.2						[40]
Mg2.5Zn	As-cast	SBF, 37 °C	0.010Fe; 0.032Mn; 0.018Al; 0.033Si	5.5		2.4				[41]
Mg2.6Zn	Extrusion						208	263	25.6	[26]
Mg2.65Zn	As-cast	0.9 wt.% NaCl				13.4	45	145	12	[289]
Mg2.9Zn	Powder metallurgy						84	219	4.7	[54]
Mg3Zn	As-cast	SBF, 37 °C	0.004Fe; 0.0005Cu; 0.0002Ni; 0.002Mn; 0.004Al	2.3			93	147	12.4	[46]
Mg3Zn	As-cast	9 g/L NaCl	<0.004Fe; 0.01Cu; <0.004Ni; 0.04Mn; <0.01Al	0.9		2.5				[49]
Mg3Zn	As-cast		0.007Fe; 0.022Mn; 0.029Al; 0.036Si				47	168	13.7	[22]

Mg3Zn	As-cast	MEM, 37 °C			0.5					[59]
Mg3Zn	As-cast	0.1 M NaCl		0.5	1.5					[58]
Mg3Zn	As-cast	SBF, 37 °C		5.2		2				[48]
Mg3Zn	T4	SBF, 37 °C		4.8		1.9				[48]
Mg3Zn	T4	0.1 M NaCl		0.4	1.4					[58]
Mg3Zn	T6	0.1 M NaCl		0.4	1.3					[58]
Mg3Zn	T6	SBF, 37 °C		2.1		1.2	28	140	9.7	[187]
Mg3Zn	T6 (aging for 10 h)	SBF, 37 °C	0.0045Fe; <0.0001Cu; 0.0006Ni; <0.0001Si		6.6					[43]
Mg3Zn	T6 (aging for 50 h)	SBF, 37 °C			7.3					[43]
Mg3Zn	T6 (aging for 144 h)	SBF, 37 °C			9.7					[43]
Mg3Zn	Extrusion	0.6 M NaCl				8.4				[61]
Mg3Zn	Extrusion	3.5 wt.% NaCl		0.3						[40]
Mg3Zn	Bi-direction rolling	SBF, 37 °C		2.6		2	49	183	12.6	[187]
Mg3.3Zn	Powder metallurgy						90	210	4.6	[54]
Mg4Zn	As-cast		0.008Fe; 0.021Mn; 0.019Al; 0.032Si				58	217	15.8	[22]
Mg4Zn	As-cast	SBF, 37 °C	0.009Fe; 0.028Mn; 0.024Al; 0.025Si	4.9		2.1				[41]
Mg4Zn	Powder metallurgy						95	216	4.1	[54]
Mg4Zn	As-cast	SBF, 37 °C	0.0072Fe; 0.0308Cu; 0.0101Mn; 0.0273Al; 0.0565Si			0.4				[42]
Mg4Zn	T4	SBF, 37 °C				0.1				[42]
Mg4Zn	Extrusion	0.6 M NaCl				10				[61]
Mg4Zn	Extrusion	3.5 wt.% NaCl		0.4						[40]
Mg4.2Zn	Extrusion						227	288	21	[26]
Mg4.4Zn	Powder metallurgy						68	155	8.4	[54]
Mg4.5Zn	T6						57	209	14.7	[138]
Mg5Zn	As-cast		0.009Fe; 0.031Mn; 0.027Al; 0.034Si				68	185	9.2	[22]

Mg5Zn	As-cast	SBF, 37 °C		0.3		1.3	76	195	8.5	[10]
Mg5Zn	As-cast	3.5 wt.% NaCl+$Mg(OH)_2$	0.0034Fe; 0.0028Cu; 0.0015Ni; 0.0545Mn; 0.0105Al; 0.0296Si	7.8	13.5	15.1				[57]
		Salt spray (5 wt.%)				12.4				
Mg5Zn	As-cast	3.5 wt.% NaCl		0.6		2.7				[47]
Mg5Zn	T4	3.5 wt.% NaCl		0.5		2.3				[47]
Mg5Zn	T6 (aging for 4 h)	3.5 wt.% NaCl		1.2		4				[47]
Mg5Zn	T6 (aging for 10 h)	3.5 wt.% NaCl		1.5		5.5				[47]
Mg5Zn	Solid solution treatment	3.5 wt.% NaCl+$Mg(OH)_2$		2.7	10	6.5				[57]
		Salt spray (5 wt.%)				9.1				
Mg5Zn	Extrusion	3.5 wt.% NaCl		0.5						[40]
Mg5Zn	Extrusion	3.5 wt.% NaCl+$Mg(OH)_2$	0.000017Fe; <0.00001Cu; <0.000001Ni; 0.000011Si		1.7	2.6				[168]
Mg6Zn	As-cast		0.012Fe; 0.019Mn; 0.024Al; 0.033Si				69	182	7.2	[22]
Mg6Zn	As-cast	SBF, 37 °C	0.0062Fe; 0.025Cu; 0.0077Mn; 0.0478Al; 0.0489Si			3				[42]
Mg6Zn	T4	SBF, 37 °C				0.8				[42]
Mg6Zn	As-cast	SBF, 37 °C		6.2		3.5				[48]
Mg6Zn	T4	SBF, 37 °C		4.4		1.4				[48]
Mg6Zn	Extrusion	SBF, 37 °C		5.4		12.6				[60]
Mg6Zn	Extrusion	SBF, 37 °C	0.0038Fe; 0.0005Cu; 0.0005Ni; 0.0085Al; 0.0004Mn; 0.0016Si	0.16		0.07	170	280	19	[160]
		In vivo				2.3				
Mg6Zn	Extrusion (PM)	Ringer's solution, 37 °C		0.4						[55]
Mg6Zn	Extrusion (PM)+T4	Ringer's solution, 37 °C		0.5						[55]
Mg6Zn	Extrusion (PM)+T6	Ringer's solution, 37 °C		0.4						[55]
Mg6Zn	Extrusion (PM)+T5	Ringer's solution, 37 °C		0.2						[55]
Mg6Zn1Ag	Extrusion (at 275 °C)	3.5 wt.% NaCl saturated with $Mg(OH)_2$				8.5				[144]
Mg6Zn1Ag	Extrusion (at 350 °C)	3.5 wt.% NaCl saturated with $Mg(OH)_2$				16.5				[144]

Mg6Zn1Ag	Extrusion (at 275 °C) + Aging	3.5 wt.% NaCl saturated with $Mg(OH)_2$				83				[144]
Mg6Zn1Ag	Extrusion (at 350 °C) + Aging	3.5 wt.% NaCl saturated with $Mg(OH)_2$				100.3				[144]
Mg7Zn	As-cast	SBF, 37 °C		1.2	3.2		67	136	6	[10]
Mg14.5Zn	Extrusion (PM)	Ringer's solution, 37 °C		1.2						[55]
Mg25.3Zn	Extrusion (PM)	Ringer's solution, 37 °C		1.8						[55]
Mg40.3Zn	Extrusion (PM)	Ringer's solution, 37 °C		3						[55]
Mg0.8Zn0.6Ca	As-cast	HBSS, 37 °C	0.0021Fe; 0.0021Cu; <0.0021Ni; 0.0231Mn; 0.02Al; 0.0343Si	0.08		0.1				[75]
		PBS, 37 °C		0.02		0.1				
Mg0.8Zn1.6Ca	As-cast	HBSS, 37 °C	<0.0006Fe; 0.0012Cu; <0.0021Ni; 0.011Mn; 0.036Al; 0.019Si	0.1		0.2				[75]
		PBS, 37 °C		0.04		0.2				
Mg1Zn0.5Ca	Extrusion						105	210	44	[72]
Mg1Zn1Ca	As-cast	Hank's, 37 °C	0.004Fe; 0.058Mn; 0.023Al; 0.031Si			2.1	45	125	5.7	[23]
Mg1.2Zn0.5Ca	As-cast	SBF, 37 °C		15.8		8.2	60	121	3.2	[176]
Mg1.2Zn0.5Ca	T6	SBF, 37 °C		9.6		4.8	84	151	4.9	[176]
Mg1.8Zn0.6Ca	As-cast	HBSS, 37 °C	<0.0006Fe; 0.001Cu; <0.0021Ni; 0.0079Mn; 0.0199Al; 0.024Si	0.03		0.1				[75]
		PBS, 37 °C		0.02		0.2				
Mg1.8Zn1.6Ca	As-cast	HBSS, 37 °C	<0.0006Fe; 0.0011Cu; <0.0021Ni; 0.0077Mn; 0.0358Al; 0.0225Si	0.04		0.2				[75]
		PBS, 37 °C		0.06		0.3				
Mg2Zn0.2Ca	As-cast	Ringer's solution, 37 °C		10.3						[51]
Mg2Zn0.2Ca	Extrusion						118	211	24.4	[167]
Mg2Zn0.24Ca	As-cast	SBF, 37 °C		12.1						[290]
Mg2Zn0.24Ca	High pressure torsion	SBF, 37 °C		0.08						[290]
Mg2Zn0.5Ca	Rapid solidification	SBF, 37 °C				9.6				[291]
Mg2Zn1Ca	As-cast	Hank's, 37 °C	0.007Fe; 0.03Mn; 0.033Al; 0.039Si			2.4	52	143	7.3	[23]

Mg3Zn0.2Ca	Extrusion	SBF, 37 °C	0.0096Fe; 0.1302Al			1.2	224	273	18.5	[7]
Mg3Zn0.3Ca	As-cast	SBF, 37 °C	0.004Fe; <0.0001Cu; <0.0001Ni; <0.0001Si		6.9					[70]
Mg3Zn0.3Ca	T4	SBF, 37 °C			3.4					[70]
Mg3Zn1Ca	As-cast	Hank's, 37 °C	0.007Fe; 0.022Mn; 0.029Al; 0.036Si			2.9	57	160	8.3	[23]
Mg3Zn1.34Ca	Induction melting	In vivo				0.8				[157]
		EBSS, 37 °C				1.6				
		MEM, 37 °C				4.7				
		MEMp, 37 °C				3.3				
Mg3Zn2Ca	Gravity casting						90*	101	0.4	[215]
Mg3Zn2Ca	Aging						88*	126	2	[215]
Mg3Zn2Ca	Squeeze casting						80*	135	0.9	[215]
Mg3Zn2Ca	Squeeze casting + Aging						74*	144	3.3	[215]
Mg3Zn2Ca	ECAP						166*	206	1.1	[215]
Mg3Zn2Ca	Aging + ECAP						174*	223	2.4	[215]
Mg3.3Zn3.2Ca0.5RE	Squeeze casting (surface)	3.5 wt.% NaCl, pH 11	0.02Fe;0.002Ni; 0.01Mn; 0.04Al; 0.02Si	7.2						[213]
	Squeeze casting (core)			6.1						
Mg3.6Zn3.5Ca0.7RE	Thixocasting (surface)	3.5 wt.% NaCl, pH 11	0.009Fe;0.002Ni; 0.01Mn; 0.06Al; 0.03Si	3						[213]
	Thixocasting (core)			3.6						
Mg4Zn0.2Ca	Extrusion	SBF, 37 °C	0.0095Fe; 0.1125Al			1.3	243	295	18	[7]
Mg4Zn0.5Ca	As-cast	Hank's, 37 °C	0.007Fe; 0.022Mn; 0.029Al; 0.036Si				70	180	12.3	[22]
Mg4Zn0.5Ca	As-cast							211	17	[16]
Mg4Zn0.5Ca	Extrusion							273	34	[16]
Mg4Zn1Ca	As-cast	Hank's, 37 °C	0.008Fe; 0.021Mn; 0.019Al; 0.032Si				83	175	8.7	[22]
Mg4Zn1.5Ca	As-cast	Hank's, 37 °C	0.009Fe; 0.031Mn; 0.027Al; 0.034Si				83	167	7.1	[22]
Mg4Zn2Ca	As-cast	Hank's, 37 °C	0.012Fe; 0.019Mn; 0.024Al; 0.033Si				90	143	2.1	[22]

Mg4Zn1Ca	As-cast	Hank's, 37 °C	0.008Fe; 0.021Mn; 0.019Al; 0.032Si			4.4	63	182	9.1	[23]
Mg5Zn1Ca	As-cast	Hank's, 37 °C	0.009Fe; 0.031Mn; 0.027Al; 0.034Si			6.2	65	173	8.2	[23]
Mg5Zn1Ca	As-cast	SBF, 37 °C	<0.0016Fe; <0.002Cu; <0.001Mn	0.28	1.36			87		[5]
Mg5Zn2Ca	As-cast	SBF, 37 °C		0.34	1.84			93		[5]
Mg5Zn3Ca	As-cast	SBF, 37 °C		0.44	3.23			83		[5]
Mg5.25Zn0.6Ca	Extrusion						178	276	25.9	[193]
Mg5.25Zn0.6Ca	Extrusion+ECAP-A						246	332	15.5	[193]
Mg5.25Zn0.6Ca	Extrusion+ECAP-B						180	287	21.9	[193]
Mg5.25Zn0.6Ca	Extrusion+ECAP-C						131	228	12.6	[193]
Mg5.25Zn0.6Ca	Extrusion						220		21.4	[292]
Mg5.25Zn0.6Ca0.3Mn	Extrusion						272		18.9	[292]
Mg6Zn1Ca	As-cast	Hank's, 37 °C	0.012Fe; 0.019Mn; 0.024Al; 0.033Si			9.2	67	145	4.5	[23]
Mg6Zn1Ca	Rapid solidification	PBS, RT		2.9						[230]
Mg6.6Zn0.19Ca	Extrusion						148	275	26	[293]
Mg5.7Zn0.17Ca0.84Zr	Extrusion						310	357	18	[293]
Mg10Zn1Ca	Rapid solidification	PBS, RT		3.1						[230]
Mg20Zn1Ca	Rapid solidification	PBS, RT		4.7						[230]
Mg46Zn10Ca	Induction melting	MEM, RT		0.4						[294]
Mg49Zn10Ca	Induction melting	MEM, RT		0.04						[294]
Mg51Zn10Ca	Induction melting	MEM, RT		0.04						[294]
Mg54Zn10Ca	Induction melting	MEM, RT		0.03						[294]
Mg56Zn10Ca	Induction melting	MEM, RT		0.4						[294]
Mg46Zn15Ca	Induction melting	MEM, RT		0.05						[294]
Mg49Zn15Ca	Induction melting	MEM, RT		0.2						[294]
Mg51Zn15Ca	Induction melting	MEM, RT		0.1						[294]
Mg54Zn15Ca	Induction melting	MEM, RT		0.1						[294]

Mg56Zn15Ca	Induction melting	MEM, RT		0.4						[294]
Mg51Zn10Ca	Induction melting	SBF, 37 °C		0.18						[295]
Mg50Zn10Ca2.6Y	Induction melting	SBF, 37 °C		0.19						[295]
Mg47Zn10Ca7.7Y	Induction melting	SBF, 37 °C		0.19						[295]
Mg50Zn10Ca	Induction melting	SBF, 37 °C		0.06	12.2					[296]
Mg50Zn10Ca2.6Y	Induction melting	SBF, 37 °C		0.2	28.3					[296]
Mg50Zn10Ca5.2Y	Induction melting	SBF, 37 °C		0.4	60.1					[296]
Mg51Zn12Ca	Rapid solidification	SBF, 37 °C		5.2	1.8					[297]
Mg51Zn12Ca	Rapid solidification +Annealing	SBF, 37 °C		9.2	10.4					[297]
Mg54Zn10Ca	Induction melting	SBF, 37 °C				0.2				[211]
Mg47Zn12Ca	Induction melting	SBF, 37 °C				0.4				[211]
Mg54Zn10Ca	Induction melting (22 mm)	SBF, 37 °C		35						[298]
Mg54Zn10Ca	Induction melting (8 mm)	SBF, 37 °C		0.2						[298]
Mg59Zn12Ca	Induction melting (22 mm)	SBF, 37 °C		5.1						[298]
Mg59Zn12Ca	Induction melting (8 mm)	SBF, 37 °C		0.1						[298]
Mg0.5Zn1Y	As-cast	3.5 wt.% NaCl		1.9	25.1	27.9				[87]
Mg0.9Zn1.6Y	As-cast	0.1 M NaCl		0.3	0.7	1.1	59	97	6.3	[88]
Mg1Zn2Y	As-cast	3.5 wt.% NaCl		0.2	1.9	2.4				[87]
Mg1.3Zn5Y	Rapid solidification	0.17 M NaCl			5.8					[299]
Mg1.5Zn0.2Y	Extrusion+Rolling		0.011Fe;0.0006Cu; 0.001Ni; 0.024Mn; 0.02Al; 0.0091Si				139	222	23	[94]
Mg1.5Zn0.2Y	Extrusion+Rolling		0.011Fe;0.006Cu; 0.001Ni; 0.024Mn; 0.019Al; 0.0073Si				178	225	18	[94]
Mg2Zn0.36Y	Extrusion	Hank’s, 37 °C		0.04		0.7	197	260	23	[53]
Mg2Zn0.82Y	Extrusion	Hank’s, 37 °C	<0.015Fe; <0.001Cu; <0.0005Ni	0.1		2	212	265	25	[53]
Mg2Zn1.54Y	Extrusion	Hank’s, 37 °C		0.05		0.8	214	265	27	[53]
Mg2Zn4Y	As-cast	3.5 wt.% NaCl		8.1	88.8	110.4				[87]

Mg2Zn5Y	Gravity casting	0.17 M NaCl		33.8					[300]
Mg2Zn5Y	Injection casting	0.17 M NaCl		12.5					[300]
Mg2Zn5Y	Rapid solidification (10 m s^{-1})	0.17 M NaCl		5.1					[300]
Mg2Zn5Y	Rapid solidification (20 m s^{-1})	0.17 M NaCl		1.4					[300]
Mg2Zn5Y	Rapid solidification (40 m s^{-1})	0.17 M NaCl		1.2					[300]
Mg2Zn5Y1.3Al	Rapid solidification	0.17 M NaCl		0.6					[299]
Mg2Zn5Y2.6Al	Rapid solidification	0.17 M NaCl		0.3					[299]
Mg2Zn5Y3.9Al	Rapid solidification	0.17 M NaCl		0.1					[299]
Mg2Zn5Y1.3Nd	Rapid solidification	0.17 M NaCl		1					[299]
Mg2Zn5Y1.3Si	Rapid solidification	0.17 M NaCl		0.8					[299]
Mg2.1Zn5.2Y	As-cast	0.1 M NaCl	1.5	5.4	4.5	95	141	5.2	[88]
Mg2.6Zn5Y	Rapid solidification	0.17 M NaCl		2.4					[299]
Mg2.6Zn5.2Y	As-cast	DMEM+FBS, 37 °C	0.2						[89]
Mg2.6Zn5.2Y0.5Zr	As-cast	DMEM+FBS, 37 °C	0.1						[89]
Mg2.6Zn5.2Y0.5Zr	Extruded	DMEM+FBS, 37 °C	0.2						[89]
Mg2.6Zn2.6Y	As-cast					102		16	[97]
Mg2.6Zn2.6Y	Rolling					261		12	[97]
Mg2.6Zn2.6Y	Rolling+Annealing					190		25	[97]
Mg3Zn0.6Y	Rolling					121	226	30.2	[108]
Mg3.1Zn5.2Y	As-cast	0.1 M NaCl	0.6	2.1	9.5	107	148	3	[88]
Mg3.3Zn5Y	Rapid solidification	0.17 M NaCl		13.5					[299]
Mg4Zn0.7Y	Rolling					209	258	17.4	[74]
Mg3.24Zn3.34Y0.67Zr	As-cast					127	185	3	[301]
Mg3.93Zn4.14Y0.69Zr	As-cast					168	226	2	[301]
Mg4.87Zn5.03Y0.73Zr	As-cast					150	195	1.9	[301]
Mg5.95Zn6.08Y0.64Zr	As-cast					121	165	1.4	[301]
Mg4Zn8Y	As-cast	3.5 wt.% NaCl	3.8	71.3	80.5				[87]

Mg5Zn0.5Y	Rolling						157	306	23.4	[93]
Mg5.2Zn5.2Y	As-cast						130		11	[97]
Mg5.2Zn5.2Y	Rolling						317		10	[97]
Mg5.2Zn5.2Y	Rolling+Annealing						217		22	[97]
Mg5.2Zn10Y	As-cast	DMEM+FBS, 37 °C		0.07						[89]
Mg4.4Zn2.4Y6.2RE	Extrusion	PBS	0.00246Fe; 0.1Mn	0.4	4.9					[302]
Mg5.7Zn1Y3.8RE	Extrusion	PBS	0.00139Fe; 0.1Mn	0.1	2.5					[302]
Mg6Zn1.2Y	Rolling						157	259	29.3	[108]
Mg6Zn1.5Y0.5Zr	Extrusion (at 300 ℃)						285	340	10.2	[180]
Mg6Zn1.5Y0.5Zr	Extrusion (at 300 ℃)+Peak-aging						289	336	15.5	[180]
Mg6Zn1.5Y0.5Zr	Extrusion (at 350 ℃)						278	336	108	[180]
Mg6Zn1.5Y0.5Zr	Extrusion (at 350 ℃)+Peak-aging						290	332	17.9	[180]
Mg6Zn1.5Y0.5Zr	Extrusion (at 400 ℃)						258	325	14.6	[180]
Mg6Zn1.5Y0.5Zr	Extrusion (at 400 ℃)+Peak-aging						277	326	16.9	[180]
Mg6Zn1.2Y0.4Zr	As-cast						157	237	3	[177]
Mg6Zn1.2Y0.4Zr	Extrusion						203	290	16.7	[177]
Mg6.7Zn1.3Y0.6Zr	As-forged	0.1 M NaCl		0.5		2.2	202	280	17	[303]
Mg6.7Zn1.3Y0.6Zr	As-forged+T4	0.1 M NaCl		0.3		1.3	183	262	22	[303]
Mg7.7Zn10.7Y	As-cast	DMEM+FBS, 37 °C		0.08						[89]
Mg7.7Zn7.7Y	As-cast						177		10	[97]
Mg5.2Zn5.2Y	Rolling						380		6	[97]
Mg5.2Zn5.2Y	Rolling+Annealing						293		15	[97]
Mg8Zn1.6Y	Rolling						173	270	26.9	[108]
Mg8Zn14Y	As-cast			0.9						[304]
Mg8Zn6Y6Gd	As-cast			1.1						[304]
Mg8Zn5Y8Gd	As-cast			1.5						[304]
Mg8Zn4Y12Gd	As-cast			1.5						[304]

Mg8.6Zn1.6Y	Rolling			1.1			210	355	23.4	[90]
Mg10Zn2Y	Rolling						181	276	21.9	[108]
Mg10.8Zn1.9Y	Rolling						220	370	19.7	[90]
Mg10.8Zn1.9Y0.5Zr	Rolling						180	325	23.5	[90]
Mg11Zn2Y	Rolling						220	370	17.2	[93]
Mg10.5Zn2.1Y	Extrusion (at 300 °C)						200	300		[92]
Mg10.5Zn2.1Y	Extrusion +Heat-treatment						197	297	18	[305]
Mg11Zn2Y	Extrusion (Ratio: 10)						232	258	4.5	[86]
Mg11Zn2Y	Extrusion (Ratio: 15)						236	312	13.2	[86]
Mg11Zn2Y	Extrusion (Ratio: 20)						240	336	15.6	[86]
Mg12Zn2.4Y	Rolling						189	285	21.3	[108]
Mg12Zn1.2Y0.4Zr	As-cast						172	216	0.8	[177]
Mg12Zn1.2Y0.4Zr	Extrusion						231	320	13	[177]
Mg15.5Zn2.6Y	Extrusion (at 300 °C)						210	320		[92]
Mg15.5Zn2.6Y	Extrusion +Heat-treatment						213	321		[305]
Mg2Zn5Y0.6Zr	Extrusion						233	290	17.2	[306]
Mg4Zn5Y0.6Zr	Extrusion						322	345	18.3	[306]
Mg6Zn5Y0.6Zr	Extrusion						244	283	20.2	[306]
ZE41	As-cast	1 N NaCl	0.006Fe; <0.002Cu; <0.001Ni; 0.02Mn; 0.004Al; <0.001Cr	2.1	13.5	12				[118]
ZE41	As-cast	Hank’s, 37 °C	0.0056Fe; 0.0014Cu; 0.0002Ni; 0.02Mn: 0.0101Al	0.24	1.6	2.3				[113]
ZE41	As-cast	0.2 M Na_2SO_4 + 0.1 M NaCl (30 °C)	0.006Fe; <0.002Cu; 0.02Mn; <0.001Ni; 0.004Al	5.4						[117]
		0.2 M Na_2SO_4 + 1.0 M NaCl (30 °C)		10						
		0.6 M Na_2SO_4 + 0.1 M NaCl (30 °C)		8.49						
		0.6 M Na_2SO_4 + 1.0 M NaCl(30 °C)		14.3						

		1.0 M Na_2SO_4 + 0.1 M NaCl(30 °C)			12.3			
		0.1 M Na_2SO_4 + 1.0 M NaCl (30 °C)			18.4			
ZE41	As-cast	0.1 M NaCl (pH3)		0.006Fe; <0.002Cu; 0.02Mn; <0.001Ni; 0.004Al	3.7	9.7		[119]
		0.1 M NaCl (pH7)			0.63	2.3		
		0.1 M NaCl (pH11)			0.22	1.5		
		1 M NaCl (pH3)			5	20		
		1 M NaCl (pH7)			1.6	14		
		1 M NaCl (pH11)			0.6	8		
ZE41	As-cast	Hank’s, 37 °C (pH6.6)		0.0056Fe; 0.0014Cu; 0.0002Ni; 0.02Mn: 0.0101Al		1.5	3.4	[148]
		Hank’s, 37 °C (pH6.9)				2.3	4.2	
		Hank’s, 37 °C (pH7.4)				2.9	1.5	
		Hank’s, 37 °C (pH8.2)				3.2	1.5	
ZE41	T5	0.5 wt.% NaCl		0.003Fe	0.1			[120]
ZE41	As-cast	0.001 M NaCl		0.1Cu; 0.01Ni; 0.15Mn	0.07			[122]
ZE41	T4	0.001 M NaCl			0.1			[122]
ZE41	As-cast	0.2 M Na_2SO_4	pH2	0.006Fe; <0.002Cu; <0.001Ni; 0.02Mn; 0.004Al	12			[150]
			pH5		5.4			
			pH7		2.8			
			pH9		2			
			pH12		1.3			
		0.6 M Na_2SO_4	pH2		15			
			pH5		9.3			
			pH7		6.2			
			pH9		4.7			
			pH12		3.9			
		1.0 M Na_2SO_4	pH2		20.1			
			pH5		14.2			
			pH7		11.1			

		pH9		8.1						
		pH12		7.1						
ZE41	As-cast	3 wt.% NaCl	0.006Fe; <0.002Cu; <0.001Ni; 0.02Mn; 0.004Al	1.1	46					[15]
		Interrupted 3 wt.% NaCl salt spray (1 min spray, 119 min humid)				47				
		Interrupted 3 wt.% NaCl salt spray (15 min spray, 105 min humid)				2.7				
Mg1Zn0.3Zr	Rolling						194	254	15.6	[74]
Mg2Zn0.6Zr	As-cast	Hank's, 37 °C	<0.01Fe; <0.01Cu; <0.01Ni	0.3			51	195	18.1	[283]
Mg2Zn0.6Zr	Extrusion	Hank's, 37 °C	<0.01Fe; <0.01Cu; <0.01Ni	0.1			194	258	17.6	[283]
Mg2Zn0.8Zr	Extrusion						221	271	24.5	[307]
Mg3Zn0.6Zr	As-cast						215	300	9	[125]
Mg3Zn0.8Zr	Extrusion+Aging	SBF, 37 °C		0.04				245	8.8	[206]
Mg3Zn0.8Zr0.5β-TCP	Extrusion+Aging	SBF, 37 °C		0.05				260	10.3	[206]
Mg3Zn0.8Zr1 β-TCP	Extrusion+Aging	SBF, 37 °C		0.03				280	10.5	[206]
Mg3Zn0.8Zr1.5 β-TCP	Extrusion+Aging	SBF, 37 °C		0.04				275	6.3	[206]
Mg4Zn0.5Zr	As-cast	DMEM+FBS, 37 °C	0.002Fe; 0.014Cu; 0.018Ni; 0.003Mn; 0.007Si	0.8		1.1				[308]
Mg4Zn0.5Zr	Heat-treatment	DMEM+FBS, 37 °C		0.9		0.5				[308]
Mg4Zn0.5Zr	Indirect chill casting	0.5 wt.% NaCl	0.00113Fe; 0.00141Cu; 0.00128Ni		2.9		102	225	12.8	[288]
Mg4Zn0.5Zr2Gd	Indirect chill casting	0.5 wt.% NaCl	0.00069Fe; 0.00292Cu; <0.003Ni		1.8		100	228	17.9	[288]
Mg4Zn0.5Zr2Nd	Indirect chill casting	0.5 wt.% NaCl	0.0011Fe; 0.00148Cu; 0.00282Ni		4.1		99	148	3.9	[288]
Mg4Zn0.7Zr	As-cast		0.03Cu; 0.01Ni; 0.2Si				108	216	16	[132]
Mg4Zn0.7Zr3Nd	As-cast						144	202	6	[132]
Mg6Zn0.6Zr	As-cast						235	315	8	[125]
Mg5Zn0.3Zr	Extrusion+Heat-treatment	5 wt.% NaCl				9.8				[129]

Mg5Zn0.3Zr1Nd	Extrusion+Heat-treatment	5 wt.% NaCl			9				[129]
Mg5Zn0.3Zr2Nd	Extrusion+Heat-treatment	5 wt.% NaCl			4.7				[129]
Mg5Zn0.3Zr0.5Y	Extrusion+Heat-treatment	5 wt.% NaCl			5.4				[129]
Mg5Zn0.3Zr1Y	Extrusion+Heat-treatment	5 wt.% NaCl			9				[129]
Mg5Zn0.6Zr	As-cast					88	236	18.2	[136]
Mg5Zn0.6Zr1Nd	As-cast					102	196	7.3	[136]
Mg5Zn0.6Zr2Nd	As-cast					89	133	2.9	[136]
Mg5Zn0.6Zr2Nd0.5Y	As-cast					94	203	9.1	[136]
Mg5Zn0.6Zr2Nd1Y	As-cast					102	219	12.1	[136]
Mg5.3Zn0.48Zr	Extrusion	PBS, 37 °C			5.6				[189]
Mg5.3Zn0.48Zr	Extrusion+ECAP	PBS, 37 °C			3.8				[189]
Mg5.3Zn0.48Zr	Extrusion	PBS, 37 °C	1.4			290	340	15.1	[191]
Mg5.3Zn0.48Zr	Extrusion+ECAP	PBS, 37 °C	1.3			219	285	32.4	[191]
Mg5.45Zn0.45Zr	As-cast	Hank’s, 37 °C	0.4	0.9					[126]
		DMEM, 37 °C	0.7						
		DMEM+FBS, 37 °C	1.3						
Mg5.45Zn0.45Zr	Extrusion	Hank’s, 37 °C	0.2	0.3					[126]
		DMEM, 37 °C	0.3						
		DMEM+FBS, 37 °C	0.5						
Mg5.54Zn0.56Zr	Extrusion					237	312	15.5	[309]
Mg5.54Zn0.56Zr	Extrusion +T5					273	329	16.5	[309]
Mg5.6Zn0.5Zr	Laser rapid solidification (420 J/mm^3)	Hank’s, 37 °C		1					[229]
Mg5.6Zn0.5Zr	Laser rapid solidification (500 J/mm^3)	Hank’s, 37 °C		0.8					[229]
Mg5.6Zn0.5Zr	Laser rapid solidification (600 J/mm^3)	Hank’s, 37 °C		0.2					[229]
Mg5.6Zn0.5Zr	Laser rapid solidification (750 J/mm^3)	Hank’s, 37 °C		0.7					[229]
Mg5.5Zn0.4Zr0.74Y	Extrusion (at 300 °C)					263	326	12.9	[310]

Mg5.5Zn0.4Zr0.74Y	Extrusion (at 350 °C)			268	331	14.6	[310]
Mg5.5Zn0.4Zr0.74Y	Extrusion (at 400 °C)			257	327	14.5	[310]
Mg5.5Zn0.4Zr1.35Y	Extrusion (at 300 °C)			285	341	10.2	[310]
Mg5.5Zn0.4Zr1.35Y	Extrusion (at 350 °C)			279	338	10.8	[310]
Mg5.5Zn0.4Zr1.35Y	Extrusion (at 400 °C)			258	327	14.6	[310]
Mg5.5Zn0.4Zr1.72Y	Extrusion (at 300 °C)			267	335	15.3	[310]
Mg5.5Zn0.4Zr1.72Y	Extrusion (at 350 °C)			263	330	12.8	[310]
Mg5.5Zn0.4Zr1.72Y	Extrusion (at 400 °C)			283	338	10.1	[310]
Mg5.5Zn0.6Zr	High strain-rate rolling			223	311	18.3	[133]
Mg5.5Zn0.6Zr0.2Gd	High strain-rate rolling			227	307	25.3	[133]
Mg5.5Zn0.6Zr0.5Gd	High strain-rate rolling			235	318	23.2	[133]
Mg5.5Zn0.6Zr0.8Gd	High strain-rate rolling			242	327	22	[133]
Mg5.79Zn0.35Zr	As-cast			108	233	9.6	[135]
Mg5.79Zn0.35Zr	T4			84	272	15.7	[135]
Mg5.79Zn0.35Zr	T6			165	281	10.9	[135]
Mg5.79Zn0.35Zr	Extrusion (at 300 °C) + T5			261	340	19.8	[135]
Mg5.79Zn0.35Zr	Extrusion (at350 °C) + T5			269	343	19.2	[135]
Mg5.79Zn0.35Zr	Extrusion (at 400 °C) + T5			273	341	18.3	[135]
Mg5.79Zn0.35Zr	Extrusion +T6			222	311	15.8	[135]
Mg5.79Zn0.35Zr1.3Gd	As-cast			99	212	7.7	[135]
Mg5.79Zn0.35Zr1.3Gd	T4			78	262	16.1	[135]
Mg5.79Zn0.35Zr1.3Gd	T6			146	276	13.2	[135]
Mg5.79Zn0.35Zr1.3Gd	Extrusion (at 300 °C) + T5			252	321	20	[135]
Mg5.79Zn0.35Zr1.3Gd	Extrusion (at 350 °C) + T5			258	324	19.8	[135]
Mg5.79Zn0.35Zr1.3Gd	Extrusion (at 400 °C) + T5			261	325	19.9	[135]
Mg5.79Zn0.35Zr1.3Gd	Extrusion + T6			239	306	18.8	[135]
Mg6Zn0.5Zr	As-cast	Ringer's solution, 37 °C	1.9				[124]
		SBF, 37 °C	9.6				
Mg6.01Zn0.49Zr	Extrusion			209	315	19.3	[134]

Mg5.94Zn0.37Zr0.96Y	Extrusion					246	325	22.3	[134]
Mg5.73Zn0.39Zr1.63Y	Extrusion					229	313	15.6	[134]
Mg5.50Zn0.43Zr2.2Y	Extrusion					261	313	17.6	[134]
Mg5.30Zn0.41Zr3.59Y	Extrusion					292	330	20.7	[134]
Mg5.88Zn0.48Zr	Extrusion					289	346	16.4	[311]
Mg5.57Zn0.52Zr0.45Yb	Extrusion					322	367	15.3	[311]
Mg5.64Zn0.47Zr0.93Yb	Extrusion					355	382	6.9	[311]
Mg6.03Zn0.56Zr1.78Yb	Extrusion					412	418	2.7	[311]
Mg5.88Zn0.48Zr	T5					315	352	14.3	[311]
Mg5.57Zn0.52Zr0.45Yb	T5					324	367	15.1	[311]
Mg5.64Zn0.47Zr0.93Yb	T5					323	371	14.8	[311]
Mg6.03Zn0.56Zr1.78Yb	T5					359	397	10.6	[311]
Mg5.88Zn0.48Zr	T6					266	332	14.3	[311]
Mg5.57Zn0.52Zr0.45Yb	T6					302	356	15.1	[311]
Mg5.64Zn0.47Zr0.93Yb	T6					314	368	14.9	[311]
Mg6.03Zn0.56Zr1.78Yb	T6					312	378	10.5	[311]
Mg9Zn0.6Zr	Extrusion					263	351	25	[175]
Mg9Zn0.6Zr	Aging					313	352	20	[175]
Mg9Zn0.6Zr0.5Er	Extrusion					313	366	22	[175]
Mg9Zn0.6Zr0.5Er	Aging					342	372	18	[175]
Mg1Zn3Gd	As-cast	9g/L NaCl	<0.004Fe; <0.004Cu; <0.004Ni; 0.3Al; 0.02Mn	1.2	0.83				[49]
Mg3Zn3Gd	As-cast		<0.004Fe; <0.004Cu; <0.004Ni; <0.01Al; 0.02Mn	1.9	5.29				[49]
Mg1Zn1Gd	Rolling					182	231	29.2	[185]
Mg2Zn1Gd	Rolling					189	233	27.2	[185]
Mg2.6Zn6.5Gd	Induction melting					288	335	9.2	[312]
Mg2.6Zn6.5Gd	Extrusion (Homogenized for 0.5 h)					303	352	8.3	[312]

Mg2.6Zn6.5Gd	Extrusion (Homogenized for 5 h)					336	391	7	[312]
Mg2.6Zn6.5Gd	Extrusion (Homogenized for 10 h)					345	380	6.9	[312]
Mg4.5Zn0.5Gd	T6					98	160	2.2	[138]
Mg4.5Zn1Gd	T6					110	189	4.1	[138]
Mg4.5Zn1.5Gd	T6					113	231	8.3	[138]
Mg4.5Zn2Gd	T6					121	215	6.4	[139]
Mg4.5Zn3Gd	T6					92	194	6.3	[139]
Mg4.5Zn5Gd	T6					80	154	5.6	[139]
Mg8.9Zn1.6Gd	Extrusion (at 300 °C)					214	311	16.5	[313]
Mg8.9Zn1.6Gd	Extrusion (at 400 °C)					199	302	14.6	[313]
Mg8.9Zn1.6Gd	Extrusion (at 300 °C) + T4					170	284	15.6	[313]
Mg8.9Zn1.6Gd	Extrusion (at 300 °C) + T6					188	285	15.3	[313]
Mg8.9Zn1.6Gd	Extrusion (at 400 °C) + T4					166	275	16.3	[313]
Mg8.9Zn1.6Gd	Extrusion (at 400 °C) + T6					190	274	15.7	[313]
Mg8.9Zn1.6Gd3.9Cu	Extrusion (at 300 °C)					222	297	10.4	[313]
Mg8.9Zn1.6Gd3.9Cu	Extrusion (at 400 °C)					223	299	11.4	[313]
Mg8.9Zn1.6Gd3.9Cu	Extrusion (at 300 °C) + T4					164	258	11.1	[313]
Mg8.9Zn1.6Gd3.9Cu	Extrusion (at 300 °C) + T6					161	248	10.6	[313]
Mg8.9Zn1.6Gd3.9Cu	Extrusion (at 400 °C) + T4					174	266	16.3	[313]
Mg8.9Zn1.6Gd3.9Cu	Extrusion (at 400 °C) + T6					172	257	12.3	[313]
Mg1Zn0.1Ce	Rolling					191	216	19.8	[74]
Mg1Zn0.3RE0.5Zr	Rolling					203	234	23.7	[74]
Mg4Zn1RE0.5Zr	Rolling					258	291	8.8	[74]
Mg1Zn0.5Mn	As-cast	Ringer’s solution, 37 °C		1.6					[112]
Mg1Zn1Mn	As-cast		<0.01Fe; <0.005Cu; <0.005Ni; <0.3Al			44	175	12.1	[314]
Mg1Zn1Mn	Extrusion	SBF, 37 °C	<0.01Fe; <0.005Cu; <0.005Ni; <0.3Al		0.06	247	280	21.8	[133]

Mg1.5Zn0.5Mn	As-cast	Ringer's solution, 37 °C		1.1						[112]
Mg1.5Zn1Mn	As-cast	Ringer's solution, 37 °C		0.9						[112]
Mg2Zn0.2Mn	As-cast	Hank's, 37 °C	0.003Fe; 0.002Mn; <0.001Ni; 0.1Al; 0.02Si	0.2	0.2	1.1				[113]
Mg2Zn0.2Mn	As-cast	Ringer's solution, 37 °C		3.4						[51]
Mg2Zn0.2Mn	As-cast	SBF, 37 °C				3.7				[109]
Mg2Zn0.2Mn	Extrusion Aging	SBF, 37 °C				3.1				[109]
Mg2Zn1Mn	As-cast						58	181	11.1	[314]
Mg2Zn1Mn	Extrusion	SBF, 37 °C	<0.01Fe; <0.005Cu; <0.005Ni; <0.3Al			0.2	249	284	20.9	[133]
Mg2Zn1Mn	Rolling						127	236	24.3	[74]
Mg2Zn1Mn0.3Ca	As-cast	Hank's, 37 °C		1.7			59	162	7.4	[52]
Mg2Zn1Mn0.5Ca	As-cast	Hank's, 37 °C		1.3			73	188	9.1	[52]
Mg2Zn1Mn1Ca	As-cast	Hank's, 37 °C		0.07			81	136	2.7	[52]
Mg2Zn0.2Mn	As-cast	SBF, 37 °C	<0.01Fe; <0.01Cu; <0.01Ni	8.4		20.4				[287]
Mg2Zn0.2Mn0.38Ca	As-cast	SBF, 37 °C	<0.01Fe; <0.01Cu; <0.01Ni	7		15.4				[287]
Mg2Zn0.2Mn0.76Ca	As-cast	SBF, 37 °C	<0.01Fe; <0.01Cu; <0.01Ni	10.1		23.5				[287]
Mg2Zn0.2Mn1.1Ca	As-cast	SBF, 37 °C	<0.01Fe; <0.01Cu; <0.01Ni	13.1		27.8				[287]
Mg2Zn0.2Mn	Solid solution treatment	Kokubo solution, 37 °C		6.6		14.6				[315]
Mg2Zn0.2Mn0.38Ca	Solid solution treatment	Kokubo solution, 37 °C		6.3		11.8				[315]
Mg2Zn0.2Mn0.76Ca	Solid solution treatment	Kokubo solution, 37 °C		8.1		18.6				[315]
Mg2Zn0.2Mn1.1Ca	Solid solution treatment	Kokubo solution, 37 °C		9.2		23.5				[315]
Mg2Zn0.2Mn1.1Ca	As-cast	SBF, 37 °C		13.1				129	1.5	[286]
Mg2Zn0.2Mn1.1Ca	Solid solution treatment (at 300 °C)	SBF, 37 °C		11.1				148	3	[286]
Mg2Zn0.2Mn1.1Ca	Solid solution treatment (at 360 °C)	SBF, 37 °C		10.6						[286]
Mg2Zn0.2Mn1.1Ca	Solid solution treatment (at 420 °C)	SBF, 37 °C		5.9				198		[286]
Mg2Zn0.2Mn1.1Ca	Solid solution treatment (at 460 °C)	SBF, 37 °C		8.1				220		[286]

Mg2Zn0.2Mn1.1Ca	Solid solution treatment (at 500 °C)	SBF, 37 °C		8.8					[286]
Mg2Zn0.2Mn	As-cast	Kokubo solution, 37 °C	<0.01Fe; <0.01Cu; <0.01Ni	8.4			102		[285]
Mg2Zn0.2Mn0.6Nd	As-cast	Kokubo solution, 37 °C	<0.01Fe; <0.01Cu; <0.01Ni	1.2			178		[285]
Mg2Zn0.2Mn1.2Nd	As-cast	Kokubo solution, 37 °C	<0.01Fe; <0.01Cu; <0.01Ni	2.2			208		[285]
Mg2Zn0.2Mn1.8Nd	As-cast	Kokubo solution, 37 °C	<0.01Fe; <0.01Cu; <0.01Ni	3.8			215		[285]
Mg2Zn0.2Mn	Solid solution treatment	Kokubo solution, 37 °C	<0.01Fe; <0.01Cu; <0.01Ni	6.6			158		[316]
Mg2Zn0.2Mn0.6Nd	Solid solution treatment	Kokubo solution, 37 °C	<0.01Fe; <0.01Cu; <0.01Ni	0.8			224		[316]
Mg2Zn0.2Mn1.2Nd	Solid solution treatment	Kokubo solution, 37 °C	<0.01Fe; <0.01Cu; <0.01Ni	1.8			228		[316]
Mg2Zn0.2Mn1.8Nd	Solid solution treatment	Kokubo solution, 37 °C	<0.01Fe; <0.01Cu; <0.01Ni	3.1			235		[316]
Mg3Zn1Mn	As-cast					66	217	15.5	[314]
Mg3Zn1Mn	Extrusion	SBF, 37 °C	<0.01Fe; <0.005Cu; <0.005Ni; <0.3Al		0.4	276	316	10.5	[133]
Mg6Zn0.5Mn	Extrusion	3.5 wt.% NaCl saturated with $Mg(OH)_2$	0.04Fe(max); 0.005Ni(max); 0.05Cu(max)	0.46	8.3				[114]
Mg6Zn0.5Mn0.5Si	Extrusion	3.5 wt.% NaCl saturated with $Mg(OH)_2$	0.04Fe(max); 0.005Ni(max); 0.05Cu(max)	1.25	26.7				[114]
Mg6Zn0.5Mn1Si	Extrusion	3.5 wt.% NaCl saturated with $Mg(OH)_2$	0.04Fe(max); 0.005Ni(max); 0.05Cu(max)	0.54	13.5				[114]
Mg6Zn0.5Mn2Si	Extrusion	3.5 wt.% NaCl saturated with $Mg(OH)_2$	0.04Fe(max); 0.005Ni(max); 0.05Cu(max)	0.47	9.5				[114]
Mg6Zn1Mn	Induction melting	3.5 wt.% NaCl		0.1		108	335	20.3	[111]
Mg6Zn1Mn	Rapid solidification	3.5 wt.% NaCl		0.01		154	460	20.5	[111]
Mg6Zn1Mn	Extrusion	Hank's		0.2	1				[317]
Mg6Zn1Mn	Extrusion + Aging	Hank's		0.3	1.3				[317]
Mg6Zn1Mn	Twin roll casting + T4					170	284	17.1	[217]
Mg6Zn1Mn	Twin roll casting + T6					256	310	16.2	[217]
Mg6Zn1Mn1Al	Twin roll casting + T4					216	308	17.3	[217]
Mg6Zn1Mn1Al	Twin roll casting + T6					307	330	16.2	[217]
Mg6Zn1Mn3Al	Twin roll casting + T4					227	327	7.8	[217]
Mg6Zn1Mn1Al	Twin roll casting + T6					319	360	6.3	[217]

Mg6Zn0.5Mn	Extrusion	3.5 wt.% NaCl saturated with $Mg(OH)_2$	5.9	3.1	[115]
		0.01M NaOH	7.3	0.27	[116]
Mg6Zn0.5Mn0.5Si	Extrusion	3.5 wt.% NaCl saturated with $Mg(OH)_2$	28.3	16.9	[115]
		0.01M NaOH	4.1	0.36	[116]
Mg6Zn0.5Mn0.5Si0.2Ca	Extrusion	3.5 wt.% NaCl saturated with $Mg(OH)_2$	25.5	9.1	[115]
		0.01M NaOH	5.4	0.42	[116]
Mg6Zn0.5Mn0.5Si0.4Ca	Extrusion	3.5 wt.% NaCl saturated with $Mg(OH)_2$	21.1	7.1	[115]
		0.01M NaOH	4.5	0.42	[116]
Mg6Zn0.5Mn1Si	Extrusion	3.5 wt.% NaCl saturated with $Mg(OH)_2$	15.6	12.3	[115]
		0.01M NaOH	3.2	0.36	[116]
Mg6Zn0.5Mn1Si0.2Ca	Extrusion	3.5 wt.% NaCl saturated with $Mg(OH)_2$	22.3	10.3	[115]
		0.01M NaOH	2.7	0.38	[116]
Mg6Zn0.5Mn1Si0.4Ca	Extrusion	3.5 wt.% NaCl saturated with $Mg(OH)_2$	25.9	12.1	[115]
		0.01M NaOH	3.8	0.49	[116]
Mg6Zn0.5Mn2Si	Extrusion	3.5 wt.% NaCl saturated with $Mg(OH)_2$	18.9	12.6	[115]
		0.01M NaOH	2.7	0.52	[116]
Mg6Zn0.5Mn2Si0.2Ca	Extrusion	3.5 wt.% NaCl saturated with $Mg(OH)_2$	16.9	12.2	[115]
		0.01M NaOH	2.6	0.59	[116]
Mg6Zn0.5Mn2Si0.4Ca	Extrusion	3.5 wt.% NaCl saturated with $Mg(OH)_2$	21.9	14.3	[115]
		0.01M NaOH	3.6	0.78	[116]
Mg2Zn0.2Si	As-cast	Ringer’s solution, 37 °C	12.3		[51]]

Mg6Zn1Si	As-cast					135	183	5.8	[318]
Mg6Zn1Si0.1Ca	As-cast					149	213	5.1	[318]
Mg6Zn1Si0.25Ca	As-cast					161	220	5.2	[318]
Mg6Zn1Si0.5Ca	As-cast					146	197	4.7	[318]
Mg6Zn4Si	As-cast	3.5 wt.% NaCl		4.2	2.8				[319]
Mg6Zn4Si0.1Sr	As-cast	3.5 wt.% NaCl		4.1	2.5				[319]
Mg6Zn4Si0.5Sr	As-cast	3.5 wt.% NaCl		0.003	1.5				[319]
Mg6Zn4Si1Sr	As-cast	3.5 wt.% NaCl		0.1	1.6				[319]
Mg6Zn4Si1.5Sr	As-cast	3.5 wt.% NaCl		5	1				[319]
Mg6Zn3Si1Mn0.4Ca	Extrusion	3.5 wt.% NaCl saturated with $Mg(OH)_2$	0.04Fe(max); 0.005Ni(max); 0.05Cu(max)	0.73					[282]
Mg6Zn5Si1Mn0.4Ca	Extrusion	3.5 wt.% NaCl saturated with $Mg(OH)_2$	0.04Fe(max); 0.005Ni(max); 0.05Cu(max)	0.42					[282]
Mg6Zn5Si1Mn0.6Ca	Extrusion	3.5 wt.% NaCl saturated with $Mg(OH)_2$	0.04Fe(max); 0.005Ni(max); 0.05Cu(max)	0.44					[282]
Mg6Zn5Si1Mn0.8Ca	Extrusion	3.5 wt.% NaCl saturated with $Mg(OH)_2$	0.04Fe(max); 0.005Ni(max); 0.05Cu(max)	0.49					[282]
Mg6Zn10Si1Mn0.4Ca	Extrusion	3.5 wt.% NaCl saturated with $Mg(OH)_2$	0.04Fe(max); 0.005Ni(max); 0.05Cu(max)	0.39					[282]
Mg6Zn2Al0.2Mn	As-cast	1 M NaCl		7.3		101	190	8.5	[320]
Mg6Zn2Al0.2Mn0.5Sn	As-cast	1 M NaCl		8.6		118	225	8.9	[320]
Mg6Zn2Al0.2Mn1Sn	As-cast	1 M NaCl		7		122	215	7.8	[320]
Mg6Zn2Al0.2Mn2Sn	As-cast	1 M NaCl		6.8		127	206	7	[320]
Mg6Zn2Al0.2Mn3Sn	As-cast	1 M NaCl		6.4		137	203	6.5	[320]
Mg6Zn2Al0.2Mn0.5Sn0.2Ca	As-cast	1 M NaCl		5.3		115	220	8	[320]
Mg6Zn2Al0.2Mn3Sn0.2Ca	As-cast	1 M NaCl		3.8		135	255	9	[320]
Mg8Zn5Al0.2Mn	As-cast	1 M NaCl		11.9		106	142	3.5	[320]
Mg6Zn5Al4RE	As-cast					140	242	6.4	[321]
Mg6Zn7Al4RE	As-cast					93	168	3.2	[321]

Mg8Zn5Al4RE	As-cast					95	174	3.1	[321]
Mg10Zn5Al4RE	As-cast					93	159	1.8	[321]
Mg8Zn4Al	As-cast					125	174	3.85	[322]
Mg8Zn4Al0.5Sn	As-cast					137	185	4.05	[322]
Mg8Zn4Al1Sn	As-cast					149	194	4.32	[322]
Mg8Zn4Al2Sn	As-cast					163	180	3.13	[322]
Mg1Zn0.2Sr	Backward-extrusion	SBF		0.53	1.8	89	187	11	[140]
Mg1Zn0.5Sr	Backward-extrusion	SBF		0.71	2.8	93	211	11.8	[140]
Mg1Zn0.8Sr	Backward-extrusion	SBF		2.4	3.9	117	210	11.5	[140]
Mg1Zn1Sr	Backward-extrusion	SBF		5.1	6.3	130	249	12.6	[140]
Mg2Zn0.1Sr	As-cast	SBF; 37 °C	0.025Fe; <0.001Cu; <0.001Ni; 0.065Al	8.9	6.4	58	179	11.5	[141]
Mg2Zn0.2Sr	As-cast	SBF; 37 °C	0.033Fe; <0.001Cu; <0.001Ni; 0.058Al	7.6	5.6	66	186	14.4	[141]
Mg2Zn0.3Sr	As-cast	SBF; 37 °C	0.018Fe; <0.001Cu; <0.001Ni; 0.072Al	9.5	6.8	66	179	10.7	[141]
Mg2Zn0.4Sr	As-cast	SBF; 37 °C	0.026Fe; <0.001Cu; <0.001Ni; 0.061Al	13.1	7	64	176	10.4	[141]
Mg2Zn0.5Sr	As-cast	SBF; 37 °C	0.033Fe; <0.001Cu; <0.001Ni; 0.074Al	14.9	7.5	52	153	6.3	[141]
Mg2Zn0.5Sr	Aging	HBSS		0.2		62	142	8.9	[143]
Mg4Zn0.5Sr	Aging	HBSS		0.4		104	169	3	[143]
Mg6Zn0.5Sr	Aging	HBSS		10.6		128	209	3.6	[143]
Mg4Zn1Sr	As-cast	SBF; 37 °C		9.4	2.3		250	5	[142]
Mg6Zn1Ag	Extrusion (at 275 °C)	3.5 wt.% NaCl saturated with $Mg(OH)_2$			33.3				[144]
Mg6Zn1Ag	Extrusion (at 350 °C)	3.5 wt.% NaCl saturated with $Mg(OH)_2$			48.1				[144]
Mg6Zn1Ag	Extrusion (at 275 °C) + Aging	3.5 wt.% NaCl saturated with $Mg(OH)_2$			88.4				[144]

Mg6Zn1Ag	Extrusion (at 350 °C) + Aging	3.5 wt.% NaCl saturated with $Mg(OH)_2$				106.2	[144]
Mg6Zn2Ag	Extrusion (at 275 °C)	3.5 wt.% NaCl saturated with $Mg(OH)_2$				40	[144]
Mg6Zn2Ag	Extrusion (at 350 °C)	3.5 wt.% NaCl saturated with $Mg(OH)_2$				58.5	[144]
Mg6Zn2Ag	Extrusion (at 275 °C) + Aging	3.5 wt.% NaCl saturated with $Mg(OH)_2$				97.8	[144]
Mg6Zn2Ag	Extrusion (at 350 °C) + Aging	3.5 wt.% NaCl saturated with $Mg(OH)_2$				111.2	[144]
Mg6Zn3Ag	Extrusion (at 275 °C)	3.5 wt.% NaCl saturated with $Mg(OH)_2$				42.7	[144]
Mg6Zn3Ag	Extrusion (at 350 °C)	3.5 wt.% NaCl saturated with $Mg(OH)_2$				66	[144]
Mg6Zn3Ag	Extrusion (at 275 °C) + Aging	3.5 wt.% NaCl saturated with $Mg(OH)_2$				85.4	[144]
Mg6Zn3Ag	Extrusion (at 350 °C) + Aging	3.5 wt.% NaCl saturated with $Mg(OH)_2$				102.9	[144]
Mg6Zn3Si0.4Ca	Extrusion	3.5 wt.% NaCl saturated with $Mg(OH)_2$	0.04Fe(max); 0.005Ni(max); 0.05Cu(max)	0.73			[281]
Mg6Zn5Si0.4Ca	Extrusion	3.5 wt.% NaCl saturated with $Mg(OH)_2$	0.04Fe(max); 0.005Ni(max); 0.05Cu(max)	0.42			[281]
Mg6Zn5Si0.6Ca	Extrusion	3.5 wt.% NaCl saturated with $Mg(OH)_2$	0.04Fe(max); 0.005Ni(max); 0.05Cu(max)	0.44			[281]
Mg6Zn5Si0.8Ca	Extrusion	3.5 wt.% NaCl saturated with $Mg(OH)_2$	0.04Fe(max); 0.005Ni(max); 0.05Cu(max)	0.48			[281]
Mg6Zn10Si0.4Ca	Extrusion	3.5 wt.% NaCl saturated with $Mg(OH)_2$	0.04Fe(max); 0.005Ni(max); 0.05Cu(max)	0.4			[281]
Mg6Zn3Cu	Squeeze casting	Salt spray				11.7	[323]
Mg1.3Zn3.9La	Rapid solidification	1 wt.% NaCl	0.0229Fe		1.5		[228]
Mg2.6Zn3.9La	Rapid solidification	1 wt.% NaCl	0.0231Fe		2.3		[228]
Mg3.9Zn3.9La	Rapid solidification	1 wt.% NaCl	0.0234Fe		3.4		[228]

Mg5.2Zn3.9La	Rapid solidification	1 wt.% NaCl	0.0234Fe	6.3				[228]
Mg1.3Zn5.2Yb	Rapid solidification	1 wt.% NaCl	0.0237Fe	0.8				[228]
Mg2.6Zn5.2Yb	Rapid solidification	1 wt.% NaCl	0.0237Fe	1.4				[228]
Mg3.9Zn5.2Yb	Rapid solidification	1 wt.% NaCl	0.0237Fe	2.8				[228]
Mg5.2Zn5.2Yb	Rapid solidification	1 wt.% NaCl	0.0239Fe	4.1				[228]
Mg12Zn4Al0.5Ca	Gravity casting				118	151	1.3	[214]
Mg12Zn4Al0.5Ca	Squeeze casting				113	211	5.2	[214]

* means 0.2% yield strength

3. List of publications and conference

Papers:

1. **P.L. Jiang**, C. Blawert, R.Q. Hou, N. Scharnagl, J. Bohlen, M.L. Zheludkevich, Microstructural influence on corrosion behavior of MgZnGe alloy in NaCl solution, Journal of Alloys and Compounds, 783 (2019) 179-192. https://doi.org/10.1016/j.jallcom.2018.12.296
2. **P.L. Jiang**, C. Blawert, N. Scharnagl, M.L. Zheludkevich, Influence of water purity on the corrosion behavior of Mg0.5ZnX (X=Ca, Ge) alloys, Corrosion Science, 153 (2019) 62-73. https://doi.org/10.1016/j.corsci.2019.03.044
3. **P.L. Jiang**, C. Blawert, R.Q. Hou, J. Bohlen, N. Konchakova, M.L. Zheludkevich, A comprehensive comparison of the corrosion performance, fatigue behavior and mechanical properties of micro-alloyed MgZnCa and MgZnGe alloys, Materials & Design, 185 (2020) 108285. https://doi.org/10.1016/j.matdes.2019.108285
4. **P.L. Jiang**, C. Blawert, J. Bohlen, M.L. Zheludkevich, Corrosion performance, corrosion fatigue behavior and mechanical integrity of an extruded Mg4Zn0.2Sn alloy, Journal of Materials Science & Technology 59 (2020) 107-116. https://doi.org/10.1016/j.jmst.2020.04.042
5. **P.L. Jiang**, C. Blawert, N. Scharnagl, J. Bohlen, M.L. Zheludkevich, Mechanistic understanding of the corrosion behavior of Mg4Zn0.2Sn alloys: from the perspective view of microstructure, accepted by Corrosion Science.
6. **P.L. Jiang**, C. Blawert, M.L. Zheludkevich, The corrosion performance and mechanical properties of Mg-Zn based alloys—A review, Corrosion and Materials Degradation, 1(2020) 7. https://doi.org/10.3390/cmd1010007
7. R.Q. Hou, J. Victoria-Hernandez, **P.L. Jiang**, R. Willumeit-Römer, B. Luthringer-Feyerabend, S.B. Yi, D. Letzig, F. Feyerabend. In vitro evaluation of the ZX11 magnesium alloy as potential bone plate: Degradability and mechanical integrity, Acta Biomaterialia 97 (2019) 608-622. https://doi.org/10.1016/j.actbio.2019.07.053

Conference:

1. **P.L. Jiang**, C. Blawert, J. Bohlen, N. Konchakova, M.L. Zheludkevich, Influence of corrosion on the fatigue behavior and mechanical properties of micro-alloyed MgZnCa and MgZnGe alloys, EUROMAT 2019 – European Congress and Exhibition on Advanced Materials and Processes, September 2019, Stockholm, Sweden.

Acknowledgements

It is my honor here to express my sincere gratitude to those who have contributed in various ways to this thesis. I definitely cannot achieve it without the support and help from all sides.

First of all, I would like to thank my supervisor, Prof. Mikhail L. Zheludkevich, for giving me the opportunity to study at MagIC center in HZG and the chances to participate in international conferences and summer schools to exchange ideas with peer scientists. I appreciate all his contributions of time, idea and suggestions to make my study productive. I really enjoyed to be part of his group. His profound knowledge in electrochemistry and rigorous attitude towards scientific research gave me a deep impression and will benefit me for my future research career.

I would like to show my warm thank to my daily supervisor Dr. Carsten Blawert. His patience and guidance helped me to overcome many difficulties in my academic life. Every discussion with him was helpful and encouraging. Thanks to his wisdom and assistance, I have learned a lot of knowledge about materials science and gained much more experience in the area of corrosion.

I would like to thank Dr. Nico Scharnagl, Dr. Jan Bohlen, Dr. Natalia Konchakova and Dr. Silva Campos (Rosario) for their help in experiments and discussions about SKPFM, extrusion, fatigue tests and casting procedure, respectively. Many thanks to Mr. Ulrich Burmester, Mr. Gert Wiese, Mr. Volker Heitmann, Mr. Günter Meister and Dr. Gerrit Kurz for their kind and professional technical assistance through my PhD studies. My gratitude also goes to Dr. Darya Snihirova for sharing happiness and sorrows and giving me scientific suggestions. I would like to acknowledge all Chinese colleagues in HZG, especially those in WZK group. My sincere thanks go to Linqian Wang and Ting Wu for taking care of me when I was pregnant, and Min Deng for his valuable suggestions during writing of scientific papers and designing experiment. I also want to express my gratitude to all members of WZK group for their support and friendliness during my stay.

I gratefully acknowledge the financial support from China Scholarship Council (CSC) for my PhD study in Germany.

Finally, I would like to express my deepest appreciation to my parents, my sisters and my brother for their selfless support. I also want to sincerely thank my husband, Ruiqing Hou, for his accompany, support, encouragement and understanding during our daily life and my work days. It is so nice to go through the master and doctoral studies with him together. More importantly, I really appreciate the birth of my daughter, Yile Hou. She is a special gift in my life and I hope she will be healthy and happy during her entire life.